

USS 10 / Libran

WDL-TR4223
70 Jul 15

N70-38190

FLIGHT DATA ANALYSIS OF POWER SUBSYSTEM DEGRADATION AT NEAR SYNCHRONOUS ALTITUDE

FINAL REPORT

CONTRACT NASW-1876

PREPARED FOR:

NATIONAL AERONAUTICS AND SPACE ADMINISTRATION
OFFICE OF ADVANCED RESEARCH AND TECHNOLOGY
HEADQUARTERS, WASHINGTON, D.C.

PHILCO



Philco-Ford Corporation
Western Development Laboratories Division
Palo Alto, California 94303

ABSTRACT

A study of the solar arrays on 19 Air Force IDSCS satellites in near-synchronous orbit has been completed. The best- and worst-case degradations projected to 5 years, encompassing all cell and noncell (i.e. coverslide system) losses are 12.5% and 16.8% for short-circuit current and 1.7 and 5.5% for open-circuit voltage. Distribution appears Gaussian over these ranges.

Calculated cell degradations, due to residual electrons and flare protons under the 20 mil coverslide shield, indicate that maximum damage regions appear at electron energies near 0.7 MeV and at proton energies near 3 MeV. The ratio of calculated electron to proton cell damage is about 5 to 2.

When these results and calculations are integrated with an understanding of the statistical uncertainties involved and a knowledge of ground cell irradiation data, a number of conclusions logically follow: noncell losses affecting I_{sc} range from 6 to 12% while cell loss, per se, is only about 6% (projected to 5 years). Basic V_{oc} loss is about 2% but an additional 0 to 3% is observed and tentatively credited to low-energy proton damage. The best equivalent fluence for the 5 year projection is 1.2×10^{14} 0.8 MeV electrons.

FLIGHT DATA ANALYSIS OF
POWER SUBSYSTEM DEGRADATION
AT NEAR SYNCHRONOUS ALTITUDE

FINAL REPORT

Contract NASW - 1876

Approved by:


Prepared by:



R. J. Grant
Program Manager

W. T. Picciano

R. A. Reitman



D. L. Reynard, Manager
Power & Control Engineering Dept.

Prepared For

National Aeronautics and Space Administration
Office of Advanced Research and Technology
Headquarters
Washington, D. C.

FOREWORD

This report concerns the electrical power subsystem performance of the Initial Defense Satellite Communication System.* In particular, it details the on-orbit degradation of the satellite solar arrays. The work is sponsored by the National Aeronautics and Space Administration under contract NASW-1876.

The study was conducted in the Power and Control Engineering Department of the Philco-Ford Western Development Laboratory Division at Palo Alto, California. This department is managed by Mr. D. L. Reynard. The program was under the overall technical direction of Mr. R. J. Grant. Mr. W. T. Picciano was responsible for all the physical analysis and mathematical techniques employed in the study. Mr. R. A. Reitman implemented the computer programming and the automatic computer plotting of the program output.

This Final Report contains, in addition to the work performed in the fourth quarter, all the material published in the previous three quarterly reports.** Minor exceptions occur where previously published material has been updated, corrected, or consolidated.

*Formerly Initial Defense Communication Satellite Program (IDCSP).

**Flight Data Analysis of Power Subsystem Degradation at Near Synchronous Altitude, First Quarterly Report, Philco-Ford Technical Report TR-DA2124, 3 October 1969; Second Quarterly Report, TR-DA2159, 5 January 1970; Third Quarterly Report, TR-DA2179, 2 April 1970.

TABLE OF CONTENTS

PART I - SUMMARY REPORT

<u>Section</u>		<u>Page</u>
1.0	SUMMARY OF OBJECTIVES	1-1
2.0	SUMMARY OF METHODS	1-1
3.0	SUMMARY OF RESULTS	1-2
4.0	SUMMARY OF CONCLUSIONS AND RECOMMENDATIONS	1-7

PART II - DETAILED REPORT

<u>Section</u>		<u>Page</u>
1	INTRODUCTION AND OBJECTIVES	1-1
1.1	Background	1-2
1.2	Objectives	1-3
1.3	Task Descriptions	1-3
1.3.1	Documentation of Achieved Orbits and Altitudes	1-3
1.3.2	Document Satellite Design Details	1-3
1.3.3	Document Instrumentation and Telemetry Design and Capability	1-5
1.3.4	Develop Analytical Techniques for I_{sc} and V_{oc} Degradation Determination	1-5
1.3.5	Develop Analytical Technique for I-V Curve Shape Determination	1-6
1.3.6	Convert Raw T/M Data to Computer Input Tapes	1-7
1.3.7	Review Environmental Data	1-7
1.3.8	Significance of Telemetry Parameters	1-7
1.3.9	Development of Computer Processing Techniques	1-7
1.3.10	Development of Computer Plotting Routines	1-7
1.3.11	Perform Error Analysis	1-7

TABLE OF CONTENTS (Continued)

<u>Section</u>		<u>Page</u>
	1.3.12 Output of Array and Cell Degradation Data	1-8
	1.3.13 Perform Curve Fitting and Statistical Analysis	1-8
	1.3.14 Perform Equivalent Circuit Analysis	1-8
	1.3.15 Perform Physical Parameter Analysis	1-9
	1.3.16 Compare Degradation Results with Environmental Models	1-10
	1.3.17 Study Solar Flare Degradation	1-10
	1.3.18 Perform Cell Failure Analysis	1-10
	1.3.19 Comparison of IDSCS Degradation with other Flight Data	1-10
	1.3.20 Perform Analysis of Source of Anomalous Seasonal Variation	1-11
	1.3.21 Generalize Degradation Prediction Methods	1-11
	1.3.22 Document Program Results	1-12
2	DETAILED METHODS AND ANALYSIS	2-1
	2.1 Approach and Logic of Degradation Studies	2-2
	2.2 Significance of Telemetered Parameters	2-5
	2.3 Extraction of Degradation Data From Telemetry	2-7
	2.3.1 Basic Method	2-7
	2.3.2 The Detailed Calculations	2-9
	2.4 Extraction of Array I-V Characteristics From Eclipse Entrance Data	2-16
	2.5 Curve Fitting and Statistical Analysis	2-22
	2.5.1 Linear Regression	2-22
	2.5.2 Nonlinear Regression	2-22
	2.5.3 Correlation Coefficient	2-25
	2.5.4 Confidence Limits	2-25
3	DETAILED RESULTS	3-1
	3.1 Satellite Geometry and Orbit Definition	3-2
	3.2 Degradation Plots of Cell I_{sc} and V_{oc} Versus Time	3-4

TABLE OF CONTENTS (Continued)

<u>Section</u>	<u>Page</u>
3.3 Functional Dependence of Radiation Degradation	3-46
3.4 Statistical Results	3-49
3.4.1 Projection Degradation to Five Years	3-49
3.4.2 Telemetry Error Analysis	3-58
3.4.3 Statistical Analysis of 5 year I_{sc} Distribution	3-61
3.5 Array I-V Characteristics from Eclipse Entrance Data	3-63
3.6 Environmental Data	3-71
3.7 Degradation Mechanisms and Calculational Methods	3-75
3.7.1 Calculated Radiation Degradation	3-75
3.7.2 Variation of Cell Equation Parameters to Express Solar Cell Degradation	3-80
3.7.3 Time Dependence of Noncell Losses	3-95
3.8 Study of Anomalous Seasonal Variations and Variations Due to Cell Failures	3-100
3.8.1 Seasonal Variations	3-100
3.8.2 Variations Due to Cell Failures	3-107
3.9 Comparison of Other Flight Data	3-114
4 CONCLUSIONS AND RECOMMENDATIONS	4-1
APPENDICES	
A Satellite Documentation	
B Derivation of an Explicit Function Function for I(V)	
C Extraction of Parameters From I/V Data	
D Temperature Dependence of the Parameters	
E Description of the Computer Programs Developed	

PART I

SUMMARY REPORT

The intent of this section is to present a concise summary of the results and highlights of the study for the benefit of readers unconcerned with technical detail. Four subsections follow: a summary of objectives, a summary of methods, a summary of results, and a summary of conclusions and recommendations.

1.0 SUMMARY OF OBJECTIVES

Twenty-six identical satellites have been orbiting at near-synchronous altitudes as part of the Air Force Defense Communications Network (IDSCS). The first seven satellites, launched 16 June 1966, have been exposed to the synchronous environment for over four years, to date. The prime objective of this study was to process the large accumulation of available high quality telemetry data on the first 19 satellites* and to attempt to extract a maximum amount of information on the degradation and behavior of the solar arrays. A secondary objective was to compare these results and calculational methods with others currently available, attempting to derive generalizations and recommendations which can ultimately benefit future programs.

2.0 SUMMARY OF METHODS

The IDSCS satellites were not instrumented to provide solar array degradation information, per se, but the quantity, quality, and nature of the telemetry data is readily amenable to computer processing toward this end. Current and voltage data on the steady-state status at two operating points of the array, together with temperature and angle-sensor data, were punched onto computer tape for every 10th orbital day. Theoretical undegraded states of these two points were compared with actual (telemetered) values, and the differences used to generate degradation information applicable to a single cell on the array. The computer plotter printed a series of dots, versus time, representing I_{sc} and V_{oc} behavior.

The basic "dot-plot" data were further analyzed, utilizing portions of the best-available environmental and ground test cell data, in an attempt to synthesize a consistent statement of degradation behavior in space. A four parameter "degradation function" was derived and regression techniques developed to extract parameter values from the dot-plot data. Comparisons of observed and calculated functions were studied in an effort to separate cell and coverslide-assembly losses.

*Actually only 18 satellites; telemetry on satellite No. 9331 ceased after 75 days. Included in the study was the Despun Antenna Test Satellite (DATS) which is not considered as one of the 26. It is designated No. 9334.

3.0 SUMMARY OF RESULTS

The first two IDSCS payloads — a total of 15 satellites — were launched on 16 June 1966 and 18 January 1967, respectively. These satellites are orbiting at an average altitude of 18,320 nmi and inclination of 0.24° (true synchronous is 19,370 nmi and 0°) and appear to have been on orbit long enough for consistent degradation trends to emerge.

Figure 1-1 presents best- and worst-case cell short-circuit current degradation curves, extrapolated to five years, for the first two payloads. All cell and noncell (i.e., coverslide-assembly) losses are included. The best- and worst-case endpoints are 0.875 and 0.832. Figure 1-2 presents similar open-circuit voltage curves; the best- and worst-case endpoints are 0.984 and 0.945. Figure 1-2 also includes a curve which corresponds to the theoretically calculated V_{oc} degradation, based on the updated radiation environment and best available damage coefficient data. This curve is observed to present an average path between the measured extremes.

Figure 1-3 presents the calculated I_{sc} degradation to cell alone due to radiation. Comparing this curve with the two extreme curves of Figure 1-1, we present the best- and worst-case estimates of noncell losses projected to five years; the curves indicate endpoints of 0.933 and 0.887.

The distribution of I_{sc} and V_{oc} values between best and worst cases appears to be random, as the inserts on Figures 1-1 and 1-2 indicate. A similar random distribution is observed for initial (time = 0) values, despite the supposedly "identical" nature of the satellites.

Assuming that on-orbit degradation primarily translates the I-V curve (i.e., no "knee rounding"), we calculate P_{max} degradation for the above best- and worst-case satellites and present these curves in Figure 1-4. An examination of eclipse-entrance data at start- and end-of-life, which enables a nearly complete array I-V curve to be constructed, appears to substantiate the translation approximation.

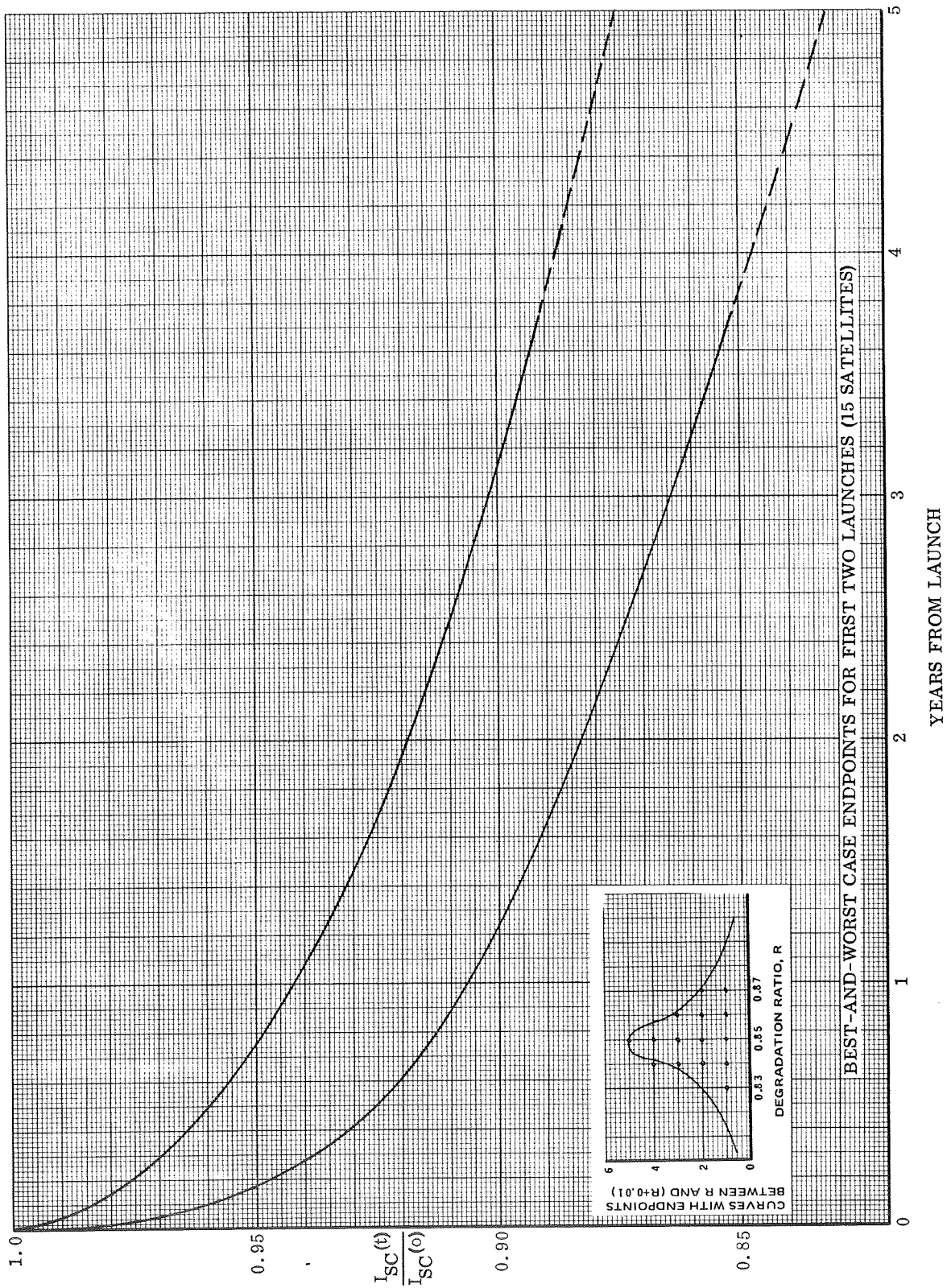


Figure 1-1 Observed and Projected Cell Short-Circuit Current Degradation

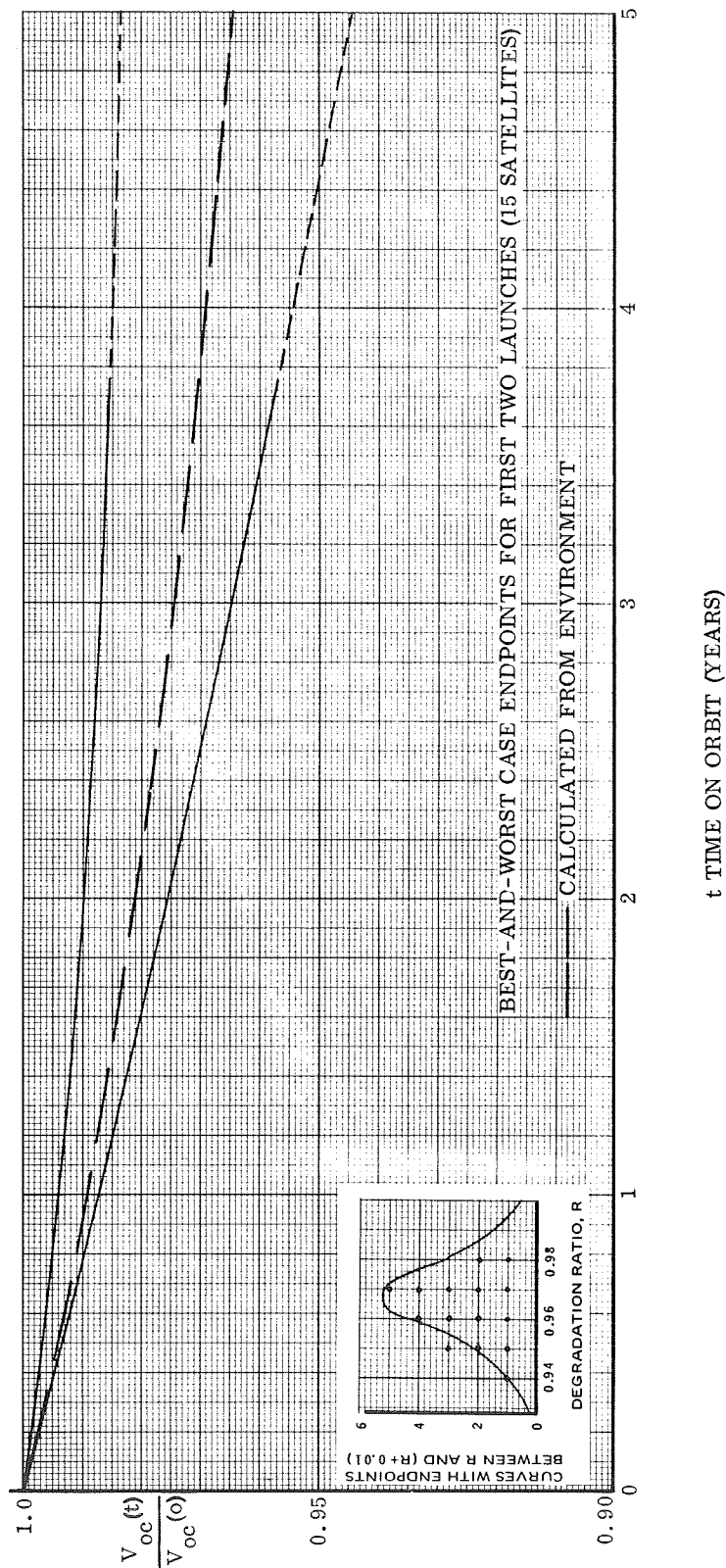


Figure 1-2 Observed, Projected and Calculated Cell Open-Circuit Voltage Degradation

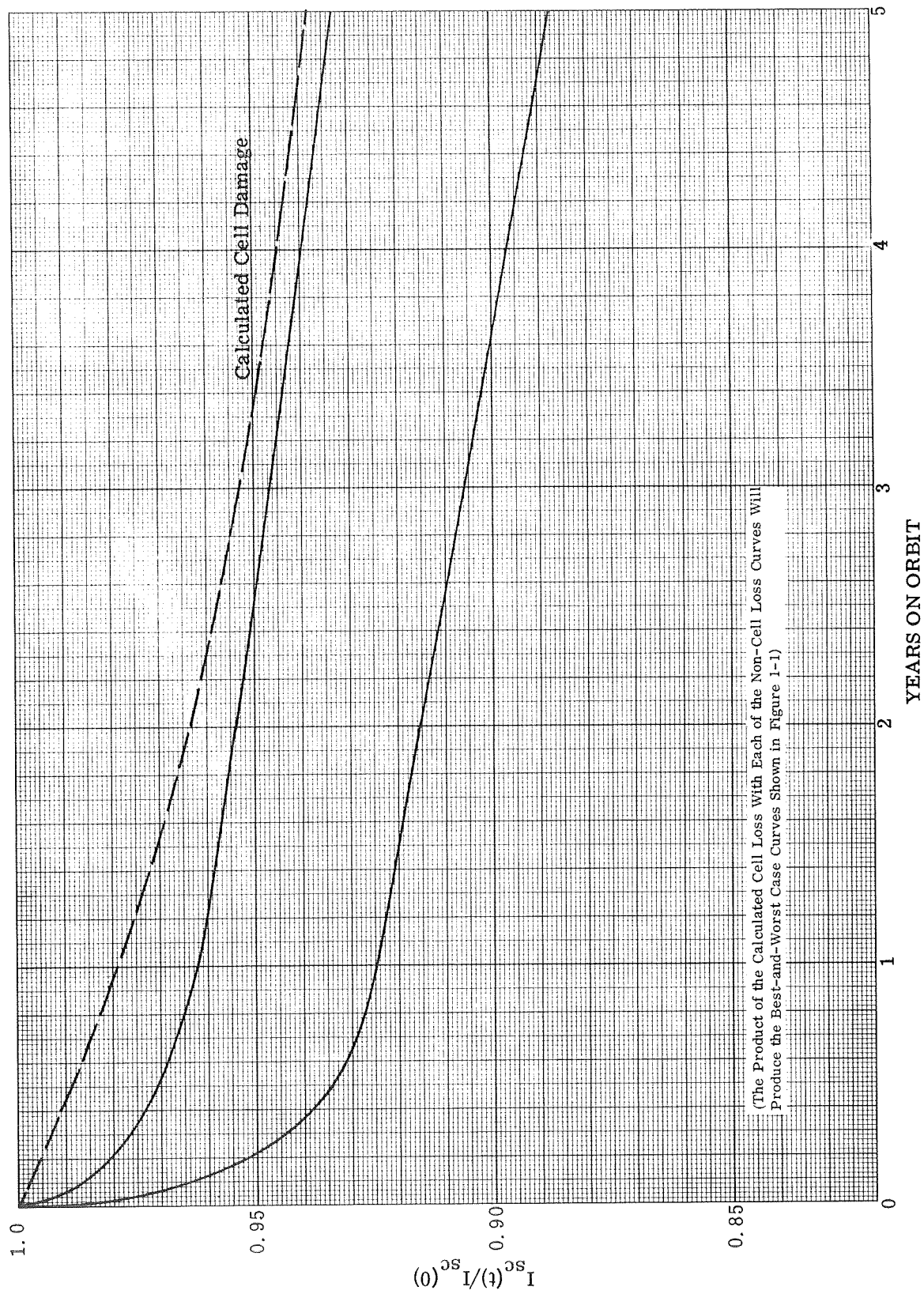


Figure 1-3 Estimated Noncell (Coverslide System) Losses and Calculated Cell Short-Circuit Current Loss

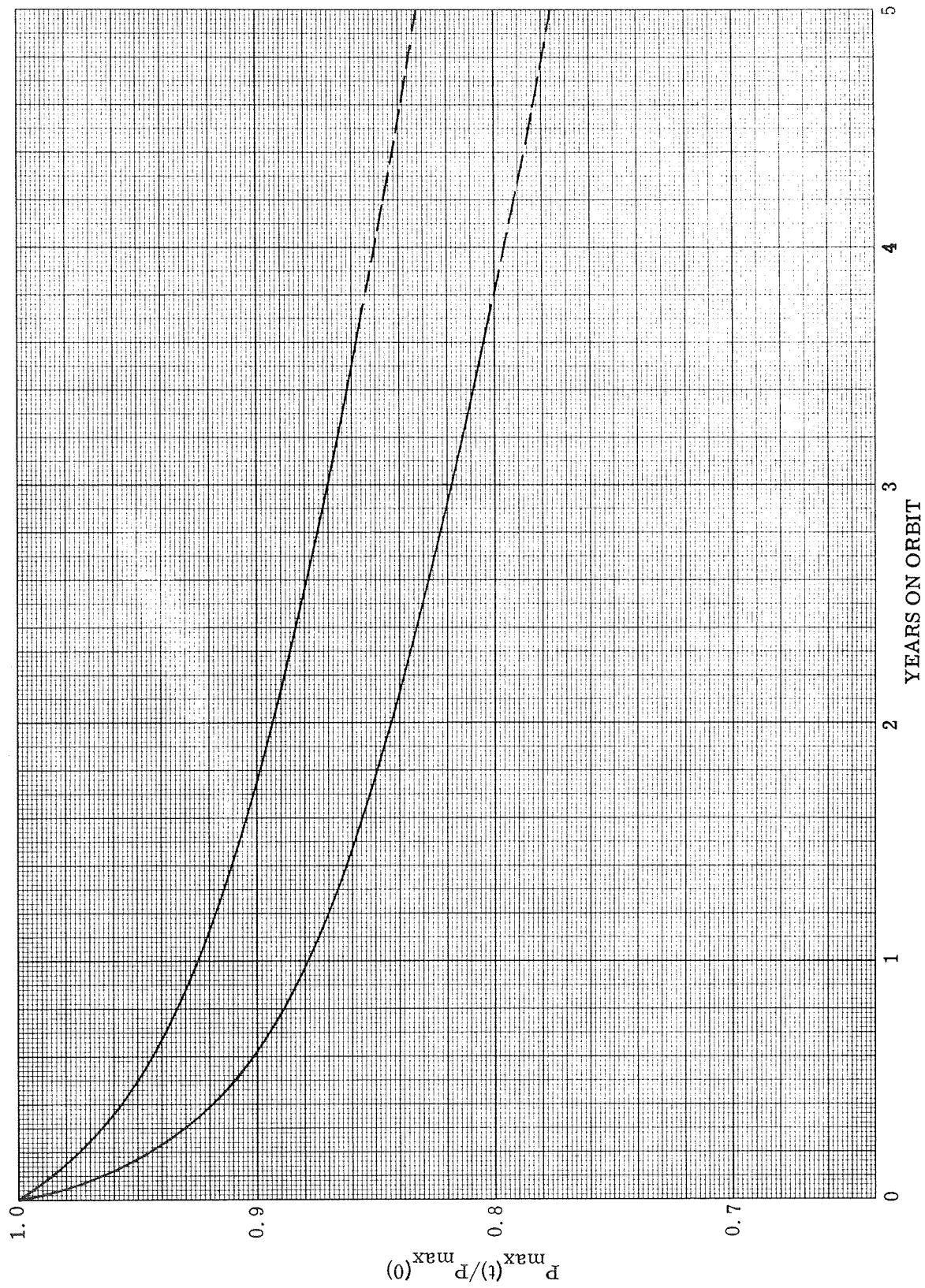


Figure 1-4 Calculated Best- and Worst-Case Degradation to the Maximum Power Point

The products of the damage coefficients and residual spectra under the 20-mil coverslide indicate regions of maximum damage; for the on-orbit electrons this region is near 0.7 MeV, and for the protons near 3 MeV. The ratio of electron-to-proton damage appears to be about 5:2.

Figures 1-5 through 1-7 show the best available collection of other synchronous flight data on I_{sc} , P_{max} , and V_{oc} degradations. The comparison, unfortunately, is somewhat hampered by the variety of coverslide shield thicknesses. One of the great uncertainties observed in this study is the behavior of the coverslide assembly on orbit, both as to the total light loss versus time and to the dependence of light loss on thickness. For the IDSCS satellites, there appears to be some evidence that slide-assembly losses of 2 to 5% occur within the first 100 days on orbit (possibly due to UV) followed by a more uniform loss producing an overall 5-year loss of 6.7 to 11.3%.

4.0 SUMMARY OF CONCLUSIONS AND RECOMMENDATIONS

The above degradation levels and the observed behavior appear to be explained by the following conclusions:

- a. Radiation damage to the solar cell due to all trapped particles and flare protons degrades I_{sc} by about 6% , and V_{oc} by about 2%, over five years.
- b. Coverslide-assembly transmission losses over 5 years range from 6 to 12% with a random distribution over that range. A 2 to 5% loss occurs within the first 100 days on orbit.
- c. Another interaction, probably low-energy proton damage, degrades V_{oc} an additional 0 to 3% over 5 years with a random distribution over fluence. Concurrent degradation to I_{sc} is negligible.

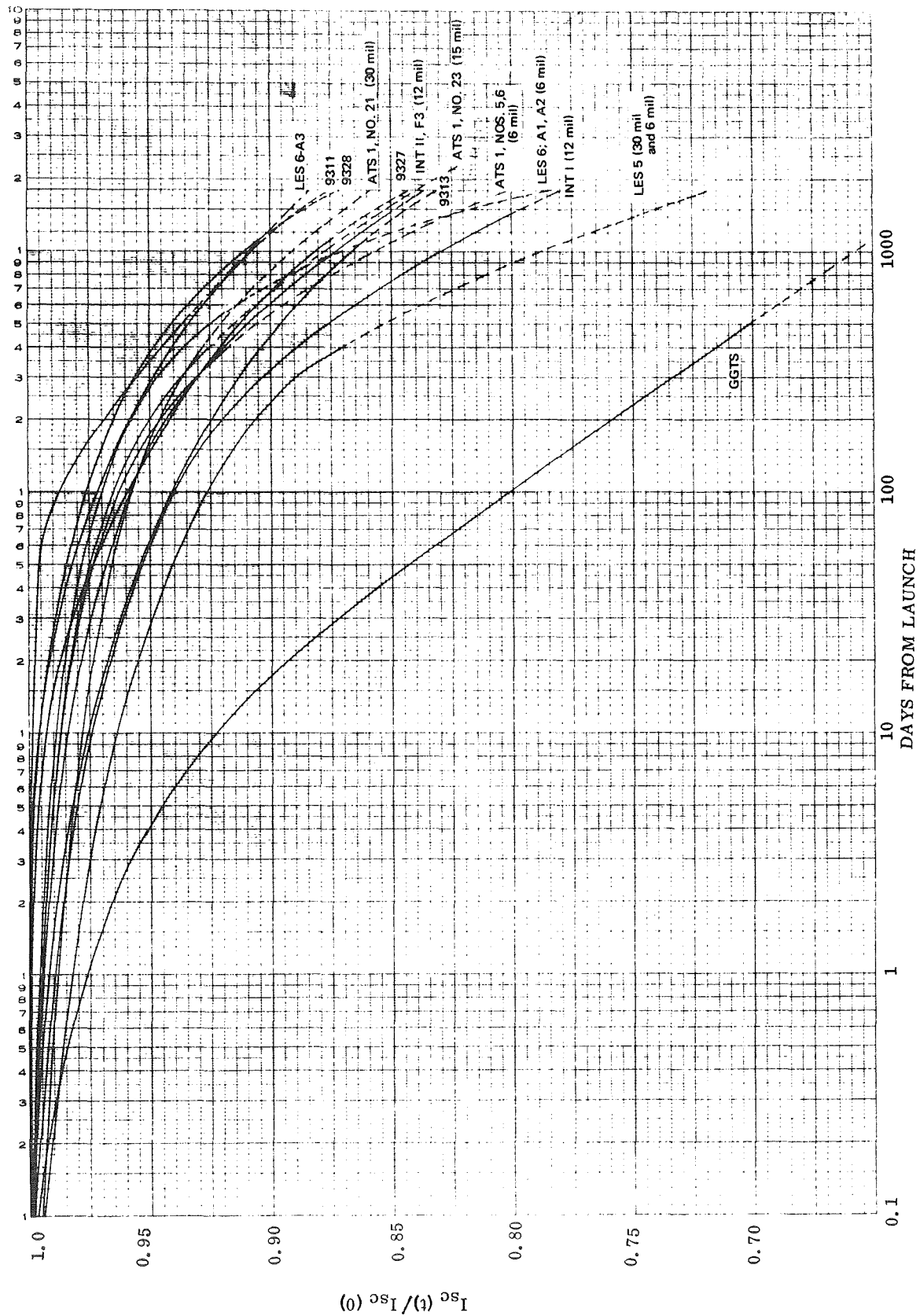


Figure 1-5 Comparison of Available Flight Data: Normalized Short-Circuit Degradation

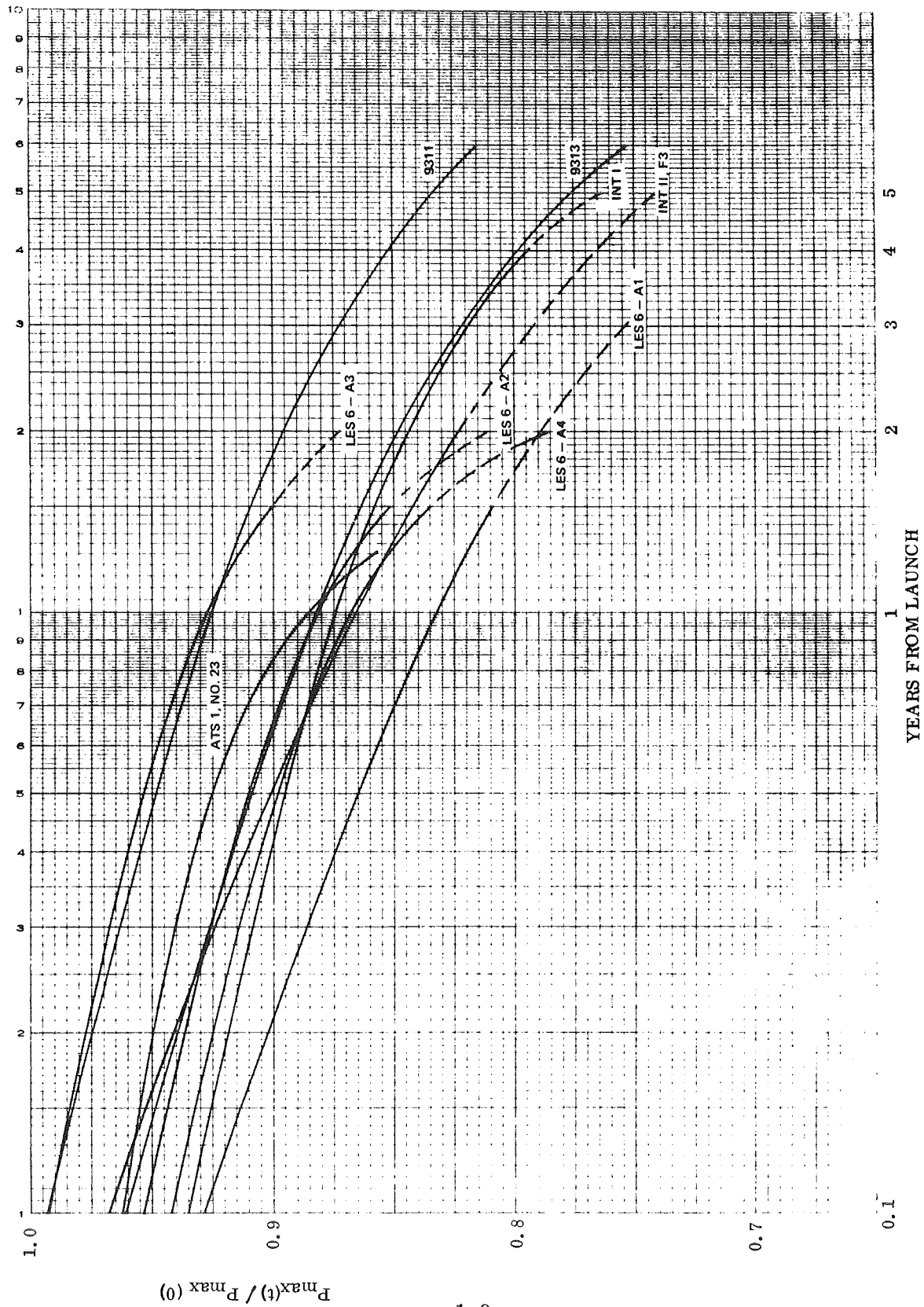


Figure 1-6 Comparison of Available Flight Data: Normalized Maximum Power Point Degradation

EUBENE DIETZGEN CO.
MADE IN U. S. A.

NO. 340R-M DIETZGEN GRAPH PAPER
MILLIMETER

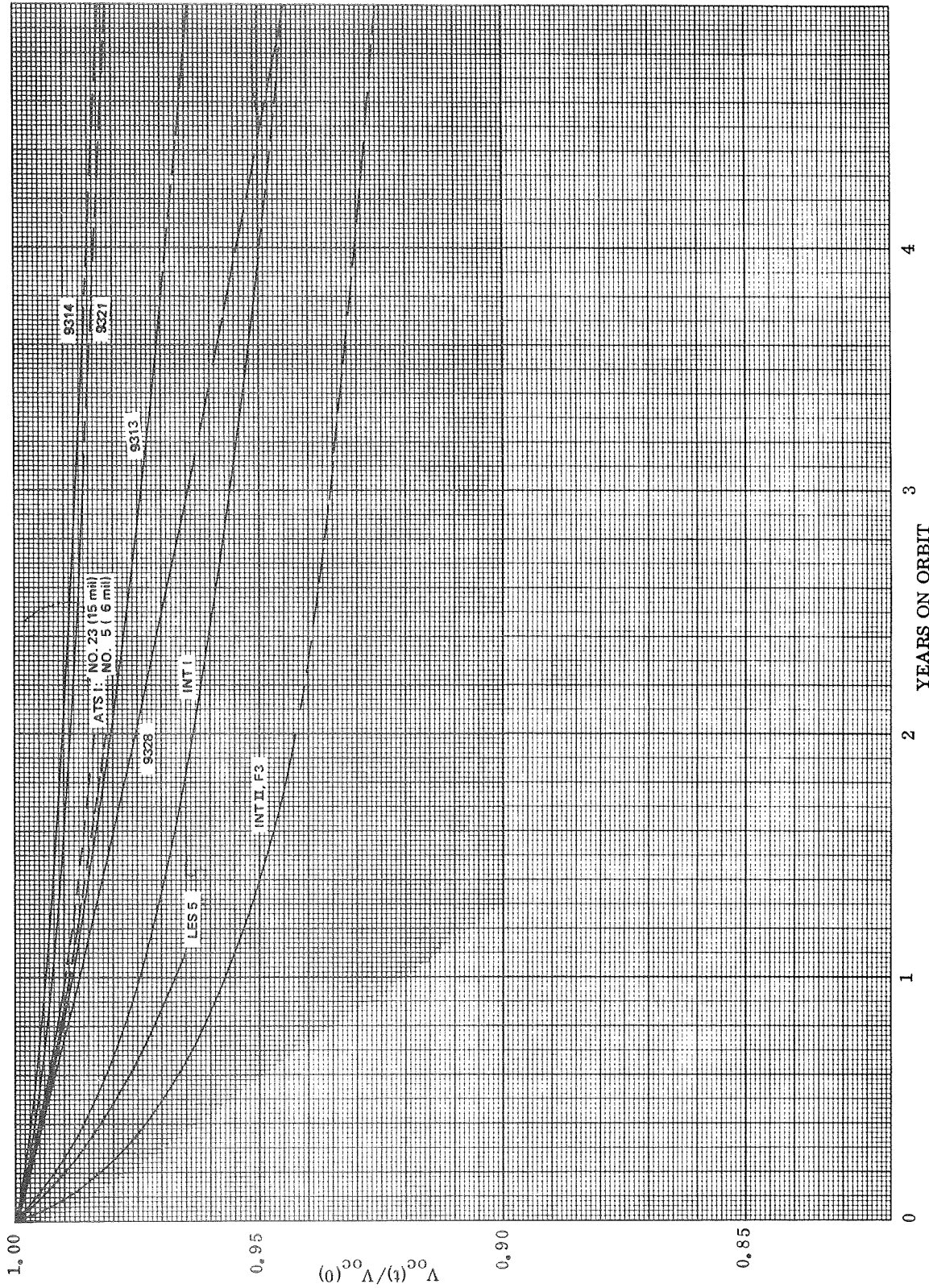


Figure 1-7 Comparison of Available Flight Data: Normalized Open-Circuit Voltage Degradation

Conclusion (a) results from an examination of ground irradiation data, the present estimation of the orbital environment, and accepted radiation damage coefficients. Conclusion (b) appears to explain the phenomenon of large I_{sc} losses with minimum V_{oc} loss. Similar behavior has been observed in ground tests on coverslides. Conclusion (c) results from ground irradiation data and appears to be the only explanation of a large V_{oc} loss coupled with a minimum I_{sc} loss which is observed in some satellites.

Additional interesting, but secondary, conclusions are:

- d. The apparent periodic seasonal variations, superimposed on the output data in the dot plots, primarily results from a slight ($\approx 3.5\%$) difference in the quality of the "average" solar cell used in the upper and lower zones of the solar array.
- e. The convenient, widespread, and somewhat arbitrary use of 1 MeV Equivalent Electron fluences as a measurement of particulate orbital environments should be discontinued. The peak damage energy for the dominant radiation type would be a far more accurate equivalence. We observe 5-year cell degradations corresponding to an equivalent fluence of about 1.2×10^{14} 0.8 MeV electrons. (In terms of 1 MeV equivalent electron fluences this corresponds to 1.1×10^{14} for I_{sc} , 8×10^{13} for P_{max} , and 4×10^{13} for V_{oc}).
- f. A useful computational technique, used throughout this study, is the definition of the solar cell equation in terms of the parameters A, B, R, and P (see Appendix B for definitions of terms):

$$I = I_L - \exp\left(\frac{-A}{B}\right) \left[\exp \frac{V + IR}{B} - 1 \right] - \frac{V}{P}$$

For modern cells, with large values of P, this simplifies to the expression:

$$V = A + B \ln(I_L - I) - IR$$

Temporal variations of these parameters for best- and worst-case satellites have been determined in this report.

g. The function,

$$R = R_0 [1 - a \ln(1 + bt)]$$

appears to represent the on-orbit radiation degradation ratio of cell I_{sc} or V_{oc} over a useful range of t . Uniform flux exposures are assumed for the equation derivation, which may imply a verification that dominant degradation is due to trapped electrons rather than the more erratic flare protons.

Recommendations evolved throughout this study are the following:

- a. Update the ground irradiation data on modern 2 x 2 cm solar cells for proton energies under 5 MeV and electron energies under 2 MeV.
- b. Consistent on-orbit degradation data is sparse. Every satellite launched should be required to carry sufficient monitors to derive some degree of cell degradation information.
- c. Coverslide degradation should be carefully investigated. The source (e.g., trace impurities) of the variable transmission loss behavior should be discovered and eliminated. Transmission losses versus slide thickness should be delineated. This recommendation is pertinent to the coverslide system, i.e., coverslide substrate, filters, adhesive, surface contamination, etc.

- d. Degradation calculation techniques should be re-examined. The correlation of total cell damage (i.e. $\int K \phi dE$) to I_{sc} or V_{oc} degradation should be unique and unambiguous, regardless of the damage source. A totally new approach, recommended by the authors, is to study energy depositions in selected regions of the solar cell and correlate them to changes in the cell equation parameters.
- e. A handbook for preliminary design purposes should be compiled. This document would incorporate radiation environmental data with accepted computational techniques to present solar array degradation levels as functions of altitude, inclination, coverslide thickness, temperature, and time on orbit. A periodic update could reflect improved solar cells, revised environments, and improved calculational techniques.

PART II

DETAILED REPORT

The four major sections presented here contain, in addition to the work performed in the fourth quarter, all the technical material generated and previously published on this program. The subsections of the earlier three quarterly reports have either been reproduced in their entirety or revised, updated, and reproduced (the quarterlies may thus be safely discarded).

SECTION 1

INTRODUCTION AND OBJECTIVES

This introductory section presents a brief background of the satellite launches and a description of the objectives and tasks of this study.

1.1 BACKGROUND

On 16 June 1966, seven IDSCS satellites were successfully placed in near synchronous equatorial orbit in a multiple launch by a single Titan III C booster. Twelve additional satellites were similarly orbited, eight on 18 January 1967 and four on 1 July 1967. Between the first and second successful launches there was a launch which self-aborted shortly after liftoff. The 18 January 1967 payload is sometimes referred to as the "third launch" although, throughout this report, we have numbered only the successful launches in order; hence "third launch" here is intended to mean the 1 July 1967 launch.

The existence of 19 identical satellites in very similar orbits near the synchronous altitude presented a unique opportunity to study solar array environmental degradation with a high degree of statistical confidence. In 1968, when Philco-Ford submitted its proposal to analyze the IDSCS flight data, there was widespread concern over the magnitude and frequency of solar flare proton damage at synchronous altitude. It was believed that a certain number of consistent "step" functions would appear among the satellites to enable extraction of these results. Such behavior was not observed, perhaps due to the benignness of the of the 20th solar cycle and/or the extremely conservative 20 mil fused silica coverslides on the IDSCS arrays.

All degradation results obtained were to be analyzed and discussed in terms of other flight data and of predicted behavior calculated from knowledge of the synchronous environment and ground irradiation data. Because of the importance of this orbit for both current and future missions, the ultimate objective of studies such as this appears to be to establish an environment, radiation interaction, and calculational technique which are mutually compatible and consistently able to produce accurate degradation predictions. This knowledge would permit more accurate sizing of future solar array designs.

1.2 OBJECTIVES

The primary objectives of this program were (1) to establish the quantitative degradation rates of the power subsystems of 18 IDSCS spacecraft, (2) to investigate the degradation of the I-V characteristics of their solar arrays, (3) to investigate any anomalous or unexpected behavior relating to environmental damage, and (4) to analyze all results such that the benefits of this flight experience could be applied to other current and future programs.

1.3 TASK DESCRIPTIONS

Figure 1-1 displays a block diagram/flow chart visual summary of the program. The unification of the individual tasks towards the overall program objectives is thus clarified. Each task block contains a reference to the location in this report of the detailed methods and results applicable to that task. A brief description of each task block follows.

1.3.1 Documentation of Achieved Orbits and Altitudes

All spacecraft achieved orbits which could be established by ground tracking data. On-board sun angle sensors provide precise data on spacecraft altitude relative to the sun and the orbit. These data are used to normalize seasonal variation in solar array output so that temporal environmental degradation phenomena can be isolated.

1.3.2 Document Satellite Design Details

The IDSCS spacecraft are primarily communications repeaters operating at X-band. They also contain a telemetry system for analyzing performance and for diagnostic purposes. The power subsystem consists of a body mounted solar cell array and a power control unit. The array produces a nominal beginning-of-life power of 45 watts. The power control unit provides a voltage-regulated bus by means of a partial shunt limiter, contains the necessary control circuitry for automatic load

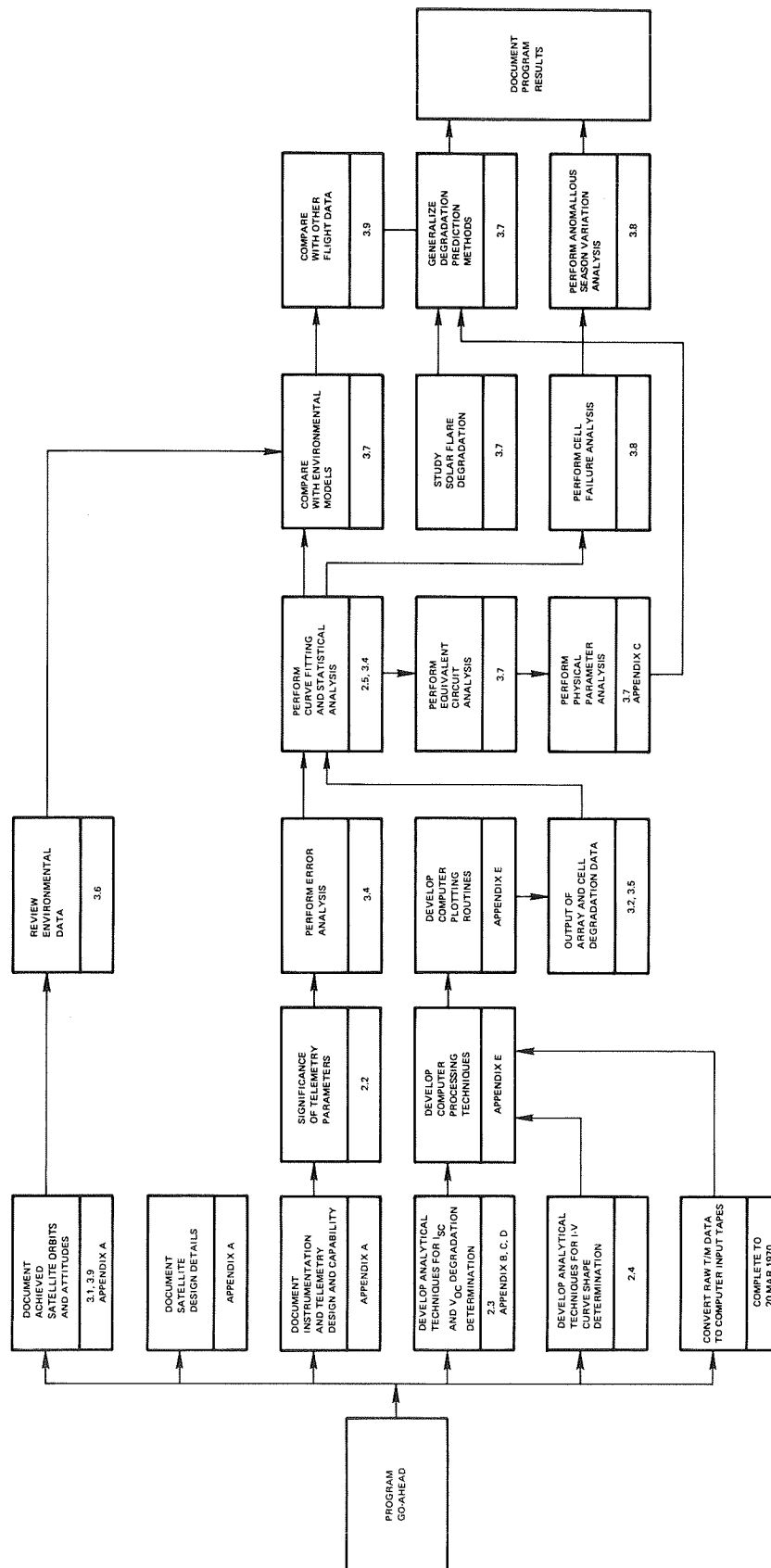


Figure 1-1 Task Description Flow Diagram (Includes Status and Reference Indications)

switching, and includes current, voltage and temperature monitors for assessing performance. This task provides a detailed summary of design data, specification performance requirements, and measured solar array characteristics for each spacecraft.

1.3.3 Document Instrumentation and Telemetry Design and Capability

Each of the power subsystem telemetry sensors provides a 0-3 volt analog signal which is encoded into one of 64 digital words. The digital format is transmitted, received, decoded and printed out by computer in engineering units.

The monitors are specified to be initially accurate to $\pm 3\%$ and stable to within $\pm 2\%$. By observing such parameters as control bus current and voltage and main bus current and voltage, it is possible to determine with high precision the magnitude and changes in array short-circuit current and open-circuit voltage. Array temperature is also telemetered and permits normalization of these parameters. An error analysis establishes the credibility of the data as it is received for processing.

1.3.4 Develop Analytical Techniques for I_{SC} and V_{OC} Degradation Determination

Telemetry data is received every two seconds and automatically converted to electrical units. Extractions of temperature stabilized array data must be carried out to obtain a sufficient number of inputs for the required sampling statistics. After preparing a detailed check of the array output as calculated from purely geometrical, astronomical, and thermal considerations, we compare these theoretical values with telemetry data to establish "difference data" which include the results of all degradation mechanisms (i.e., cell, plus noncell losses). The difference data is then processed to extract maximum significant information on the behavior of array and cell short-circuit currents.

Since the sum of the unshunted and shunted (control bus) array voltages is regulated to 29.4 Vdc, any degradation in the unshunted half of the array must be exactly compensated by an increase in the shunted half, which is a telemetered parameter.

By applying iteration techniques to vary cell V_{oc} and I_{sc} , the two calculated array points can be brought into coincidence with the two telemetered array points. The validity of this technique depends on a condition of minimum knee softening or a fortuitous location of the two array points safely outside of the knee region. Eclipse entrance data is used to analyze these assumptions.

1.3.5 Develop Analytical Technique for I-V Curve Shape Determination

Partial I-V curves can be obtained from telemetry data by examining eclipse entrance data. As intensity drops during passage of the satellite through the penumbra, the power control unit attempts to counteract current and voltage changes to provide all available power at 29.4 (± 0.2) Vdc. Thus, I-V data can be extracted by the following equations for either the unshunted or shunted values of the array:

$$\begin{aligned} I_{UN} &= I_{MB} \\ V_{UN} &= V_{MB} - V_{CB} \\ I_{SH} &= I_{MB} + I_{CB} \\ V_{SH} &= V_{MB} - V_{UN} = V_{CB} \end{aligned}$$

where the subscripts are defined as:

UN = Unshunted
SH = Shunted
MB = Main Bus
CB = Control Bus

The quantities I_{MB} , I_{CB} , V_{MB} , and V_{CB} , are telemetered parameters. Any changes in I-V curve shape (especially the knee) can thus be detected.

1.3.6 Convert Raw T/M Data to Computer Input Tapes

Equilibrium values of the above electrical parameters, plus satellite zone temperatures and angle sensor data, are manually punched onto computer tape.

1.3.7 Review Environmental Data

The best available measured flare proton data and the published spectral data of the Vette group on the trapped radiation environment at synchronous altitude is summarized in graphical form. The electron and proton fluence at the cell junction, shielded by coverslide and adhesive, is computer calculated at a number of angles (due to the omnidirectionality of the flux) and presented on the same graphs. This information is used to compare predicted with actual array degradation.

1.3.8 Significance of Telemetry Parameters

The interaction of the partial shunt regulator with the solar array is described.

1.3.9 Development of Computer Processing Techniques

Required aspects of solar cell theory and mathematics are converted into practical and efficient computer algorithms and programs. Input and output, as well as editing, efficiency is considered.

1.3.10 Development of Computer Plotting Routines

Techniques were developed to use computer calculated outputs directly for automatic graphical display.

1.3.11 Perform Error Analysis

Systematic and random error was investigated through all telemetry links. Worst-case as well as RMS magnitudes are determined.

1.3.12 Output of Array and Cell Degradation Data

Output data is graphically displayed by the computer. Consideration has been given to the casual or nontechnical reader in an effort to communicate results with maximum clarity.

1.3.13 Perform Curve Fitting and Statistical Analysis

The selection of a proper degradation function should be aided by the large number of identical satellites in the IDSCS program. Aspects of cell degradation theory were also examined to determine the form of a general degradation function. Linear and nonlinear regression techniques were studied for data fitting.

Once a function has been applied and its regression parameters determined, statistical analysis proceeds readily. Of particular interest is the determination of 95% confidence limits.

1.3.14 Perform Equivalent Circuit Analysis

The lumped-parameter equivalent circuit equation for the solar cell is usually written as:

$$I = I_L - I_O \left[\exp \left\{ \frac{q(V + IR_S)}{nKT} \right\} - 1 \right] - \frac{V}{P} \quad (1)$$

If this equation is solved for $V = V(I)$, shunt resistance (P) neglected, and $I \neq I_L$, a simplified explicit relationship results:

$$V = A + B \ln (I_L - I) - IR_S \quad (2)$$

or, equivalently,

$$I = I_L - \exp \left\{ -\frac{A}{B} \right\} \left[\exp \frac{V + IR_S}{B} - 1 \right], \quad (3)$$

which defines the new parameters in terms of the old.

The effect of radiation on solar cell output power is usually presented in terms of degradation to short-circuit current, $I_{sc} = I(V = 0)$; open-circuit voltage, $V_{oc} = V(I = 0)$; and the maximum power point, $P_M = (IV)_{MAX}$. Such three-point presentation concisely summarizes the total effect of radiation damage to Equation (1), but requires the design engineer to tediously reconstruct the total I-V curve before he can utilize this knowledge. Not knowing the location of either the voltage or current points at the value of maximum power, he must resort to certain approximations or trial-and error curve reconstructing.

One solution to this problem is the presentation of radiation degradation as changes to the "fixed" parameters, A, B, I_L , and R_S , in Equations (2) or (3). Thus, assuming the accuracy of Equation (1) over a portion (at least) of the I-V curve of interest, the exact translations and shape changes (e. g., "knee softening") will all be accommodated.

1.3.15 Perform Physical Parameter Analysis

Methods of extracting cell parameters from laboratory I-V curves have been described in the literature, but as far as is known, none is so general as to include shunt resistance when and if it is required. Techniques are developed for general parameter extraction using either a few or many data points. Least-squares regression techniques are explored.

Part of this analysis concerns the relation and conversion of the degradation functions for I_{sc} , V_{oc} , and P_M into degradation functions for A, B, R, and P. Verification of the final parameter curves with the more standard degradation curves has been carried out to check any simplifying assumptions or approximations involved. The parameter degradation curves should eventually encompass all particulate radiation effects, coverslide (i. e. noncell) temporal losses, temperature, and seasonal intensity effects. Presentation of degradation data, even on such a purely phenomenological basis, provides a number of previously discussed advantages to the design engineer who is interested in fast, accurate, and complete I-V curves.

1.3.16 Compare Degradation Results with Environmental Models

Based on currently established analytical methods, a degradation prediction is recalculated using established radiation models. Differences between actual IDSCS rates are discussed and interpreted in the light of present knowledge. Suggestions for improving conventional calculational techniques are offered.

1.3.17 Study Solar Flare Degradation

Data on flare proton spectra and intensity variations were collected and summarized. It had been originally proposed to study flare pulse degradation effects in detail and correlate observations with solar cycle activity and geomagnetic shielding. Final analysis, however, produced no indication of flare damage step functions. An averaged, uniform flare spectrum was introduced and found to suffice.

1.3.18 Perform Cell Failure Analysis

Data points are available at different positions around the satellite spin axis, and reductions of short-circuit current are available for periods greater than one year (over $\pm 23^\circ$) providing variations about the "equatorial axis". Waveform patterns are analyzed to ascertain cell failures and panel output variations. Waveform amplitudes are correlated to single and multiple cell open-circuit failures.

1.3.19 Comparison of IDSCS Degradation with Other Flight Data

For the sake of completeness in presenting a comprehensive study of solar arrays at this very important altitude, data is collected on other NASA and DOD programs and experiments in the synchronous orbit environment. Discrepancies have been discussed to the best of current knowledge.

1.3.20 Perform Analysis of Source of Anomalous Seasonal Variation

Preliminary analysis indicated an anomalous sinusoidal pattern in the annual degradation waveforms of two IDSCS satellites. The expected pattern has two distinct slopes per year, corresponding to the $\pm 23^\circ$ exposure to the top and bottom "hemispheres" of the satellite. The anomalous patterns are studied in an effort to explain their waveforms.

1.3.21 Generalize Degradation Prediction Methods

The prime motivation in examining telemetered degradation rates is for the purpose of comparing and verifying predictions based on ground irradiation data and established calculation techniques. If either of the latter are deficient, alternatives should be established as rapidly as possible. Recommendations are offered for supplemental experiments and alternative calculational methods. The study proceeded with an examination of the following basic items:

- (1) Comparison of omnidirectional space irradiation with monodirectional ground irradiation.
 - (a) Short-Circuit Current
 - (b) Open-Circuit Voltage
 - (c) Maximum Power Points
- (2) Comparison of degradation predictions based on:
 - (a) Experimental data only.
 - (b) Diffusion-length degradation calculations with established damage coefficients.

- (3) Degradation of light transmission due to ultra-violet and particulate radiation exposure of coverslide, adhesive, and coatings.
- (4) Comparison of total space degradation with sum (or product) of individual component degradations.

Based on the reduction of existing IDSCS flight data and knowledge of the environmental model, degradation of the solar arrays is calculated out to five years.

1.3.22 Document Program Results

The Final Report presents material on increasing levels of technical complexity, such that the casual or nontechnical reader can quickly find results or simple verbal descriptions of methods. The Final Report is also inclusive; all interim reports may be discarded.

SECTION 2

DETAILED METHODS AND ANALYSES

This section presents the detailed logic and mathematics used in the study. The first subsection discusses the basic logic of our approach; the second describes the significance of the telemetered parameters; the third presents the mathematics of the basic analysis program; the fourth presents the method of extracting complete array I-V characteristics from eclipse entrance data; and the fifth discusses statistical methods.

Other derivations and analyses, by their nature, qualify to be designated "results"; this material is presented in Section 3.0.

2.1 APPROACH AND LOGIC OF THE DEGRADATION STUDY

The detailed Task Description Diagram presented in Figure 1-1 (Part II) is organized in a somewhat broadened form to clarify the methodology of this study. Two general study directions proceeded simultaneously: One direction analyzes the reduced telemetry data to induce the degradation mechanisms responsible for the observations, and the other applies established environments and calculational methods to deduce expected observations. Both paths currently suffer some imprecision, missing links, and ambiguities. The working hypothesis might best be characterized as an iteration between induction and deduction in which a common, consistent path is established. Figure 2-1 indicates the general mechanics of the system studied.

The inductive approach begins with the collection of reduced data points and attempts to discover by regression and correlation analyses the "best" function to represent this data. (Functions with highest probabilities have been deduced from established theory; the term "reduction" also unfortunately implies "deduction". The "iteration" process is observed to have begun.) The reduced data represents the combined manifestation of cell degradations and noncell degradations; the analysis attempts to separate these two mechanisms. Once separated, the study of the interrelationships between the I_{sc} , P_m , and V_{oc} cell degradation functions produces a "signature" which is unique to the mixture of particles and energies causing the damage. Insight would be gained toward the environment, providing ground irradiation data was available and valid. (The question of validity has again risen concerning the measured degradation between irradiated lit and unlit cells.)

The deductive approach begins with an accepted orbital environment and calculates degradation using the best techniques currently available. These techniques include shielding routines for omnidirectional irradiation, estimates of noncell losses, and cell degradation calculations (based on ground irradiation data). The mixture of electrons and protons at various energies is observed to produce ambiguous values of I_{sc} , P_m , and V_{oc} when the best method currently available

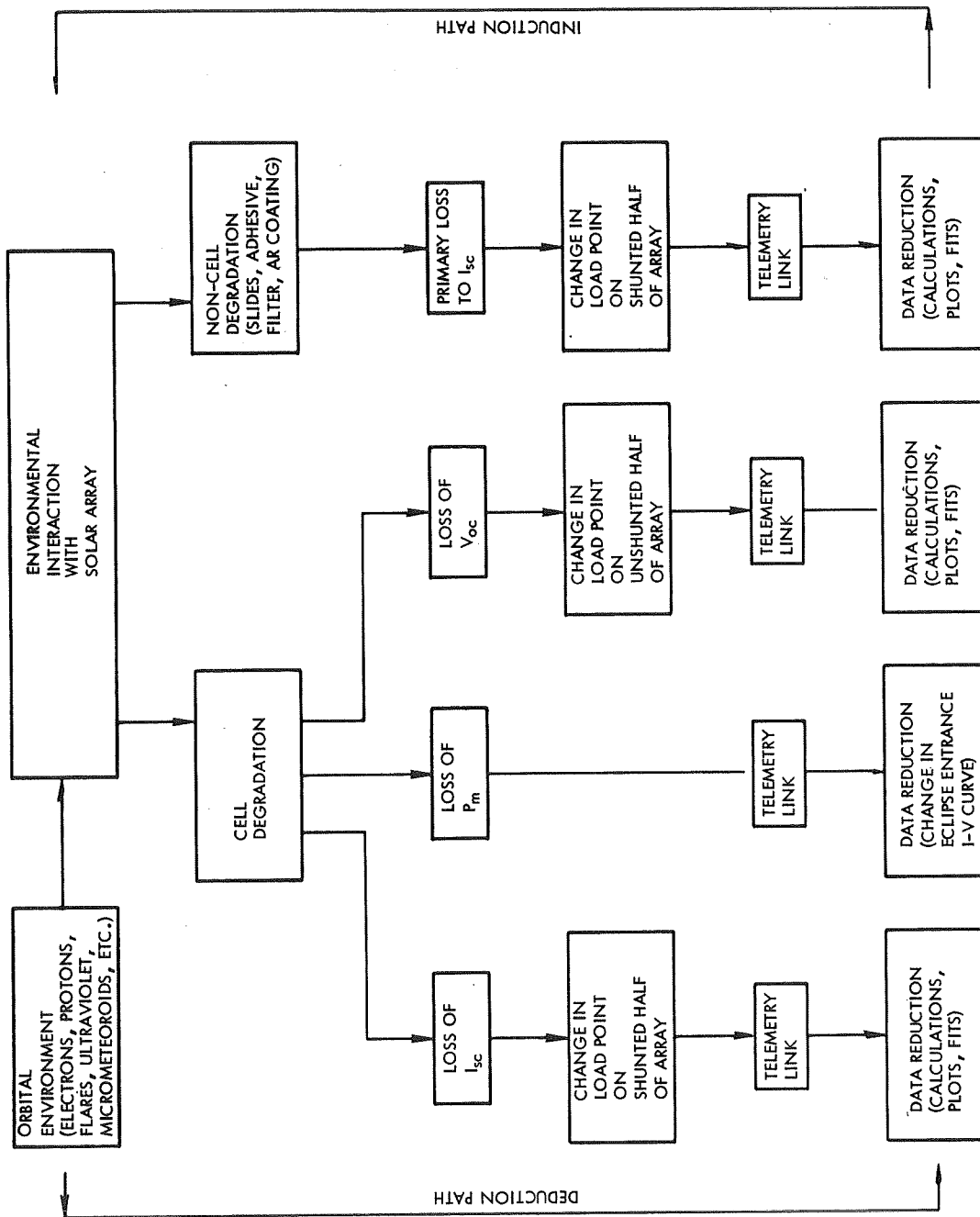


Figure 2-1 General Mechanics of the System

is used. Damage coefficients, discovered either phenomenologically or by energy deposition considerations, might better be functions of a number of environmental variables which ultimately lead to a unique value of a cell parameter; different damage functions may, in addition, be required for each cell parameter.

If these approaches have established a common and consistent path through the system, new insight and knowledge concerning each item has been gained. This type of iteration process can hopefully extend the ultimate limits of our accuracy.

2.2 SIGNIFICANCE OF TELEMETERED PARAMETERS

To properly interpret the telemetered parameters as they relate to solar array performance, it is necessary to understand the interaction of the partial shunt regulator with the solar array. Figure 2-2 presents a simplified block diagram of the regulation scheme and a graphical representation of the solar array and its typical operating points. The parameters of significance are as follows:

I_{MB} = Main bus current

V_{MB} = Main bus voltage (29.4 ± 0.2 Vdc)

I_{CB} = Control bus current

V_2 = Control bus voltage

V_1 = Unshunted array voltage ($V_1 = V_{MB} - V_2$)

The primary purpose of the partial shunt regulator is to limit the bus to a predetermined voltage; in this case, 29.4 ± 0.2 Vdc. Voltage is regulated by sensing the voltage across the main bus, comparing it to a reference voltage, and generating an error signal which is amplified and supplied to the shunt element. This variable impedance shunt element adjusts V_2 such that the sum of V_1 and V_2 equals the main bus regulation set point, 29.4 ± 0.2 Vdc.

From Figure 2-2, it can be seen that changes in I_{CB} are indicative of changes in the current capability of the solar array, assuming the main bus current and the voltage capabilities of the array are held constant. Correspondingly, changes of V_2 are indicative of changes in the voltage capability of the array assuming the current capability is held constant.

By properly interpreting these telemetered parameters, it is possible to determine the array current and the voltage characteristics. It is also possible to construct the entire knee of the I-V curve by detailed investigation of eclipse entrance data. Knee characteristics are developed in subsequent sections of this report.

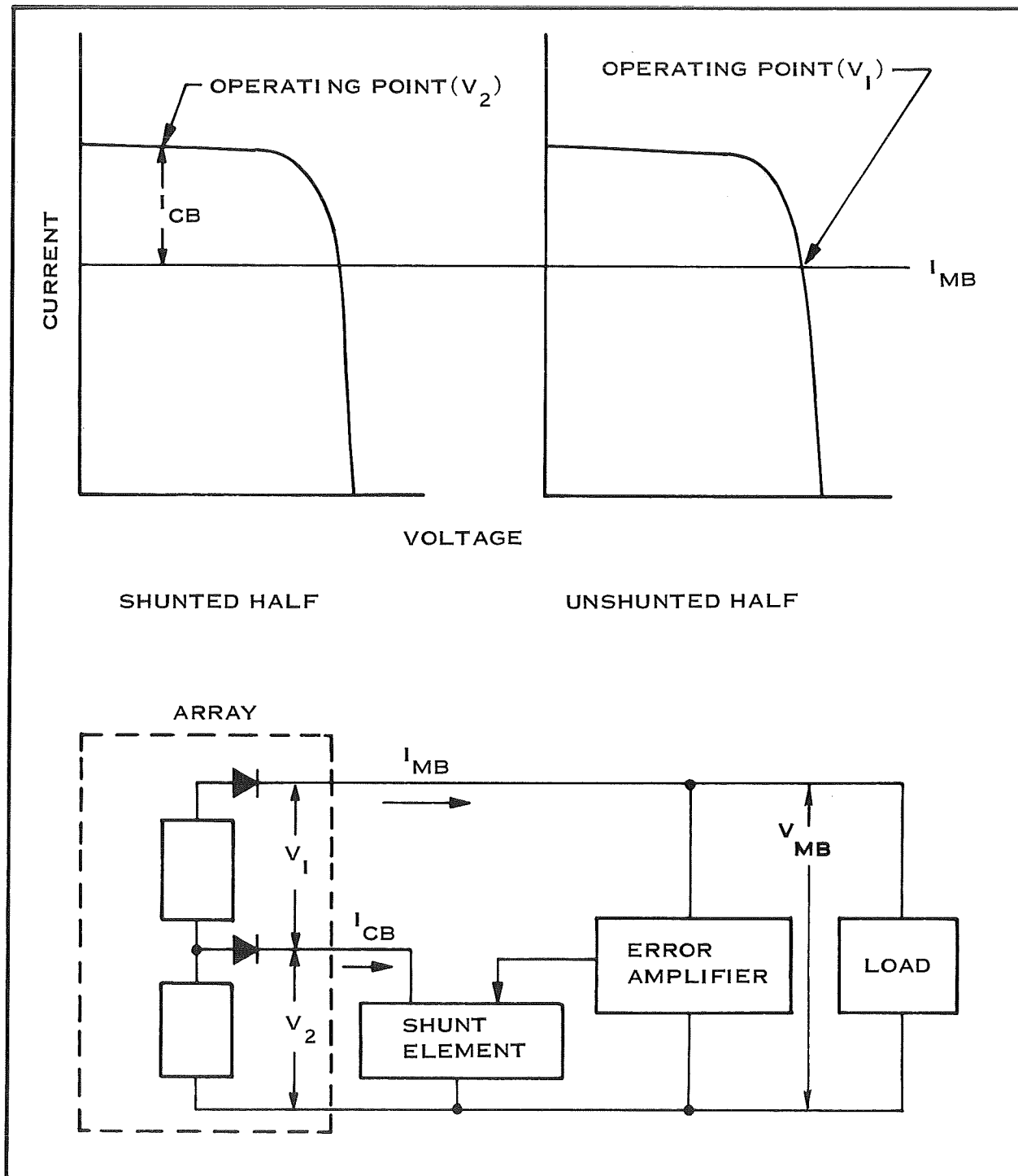


Figure 2-2 Solar Array Regulator Schematic - Simplified

2.3 EXTRACTION OF DEGRADATION DATA FROM TELEMETRY

2.3.1 Basic Method

Stated most simply, the approach followed in this study is the determination of the difference between actual (telemetered) and theoretical undegraded current and voltage points on the array I-V curve as a function of time on orbit. This difference is used to generate degradation information applicable to a single solar cell on the array.

The theoretical array output is developed on the basis of an assumed typical solar cell manufactured for the IDSCS program. This cell is a 1 x 2 cm, N on P boron doped silicon cell of 1964 vintage with a base resistivity ranging between 7 and 13 ohm-cm. Figure 2-3 presents the I-V characteristic of this cell at 77°F. All cells are shielded by 20 mils of fused silica applied with Dow XR-6-3489 adhesive. A five-parameter (including shunt resistance) single-cell I-V equation is used to develop the total array I-V characteristic considering satellite geometry, sun angle, earth orbit ellipticity and operating temperatures. Temperature dependences (for this vintage of solar cells) are incorporated in each of the cell equation parameters.

Two points on the array I-V curve are effectively monitored by telemetry due to the different loading on the shunted and unshunted halves of the array. The shunted portion produces a data point close to the short-circuit point and the unshunted portion produces a point between maximum power and open-circuit voltage. The degradation of these two operating points can thus be tracked, versus time, by comparing them with the same points on the theoretical array I-V curve.

A more sophisticated technique is applied to extract single-cell degradation versus time of the two interesting parameters, I_{sc} and V_{oc} . An iteration scheme is introduced into the theoretical array I-V computation that finds the corresponding degraded value of the cell I_{sc} , which is required to remove the difference between the theoretical and observed array data point near the array short-circuit point. With this degraded value in place, a second iteration is performed to determine the required cell V_{oc} necessary to remove the difference present in the other array data point near the array open-circuit voltage location.

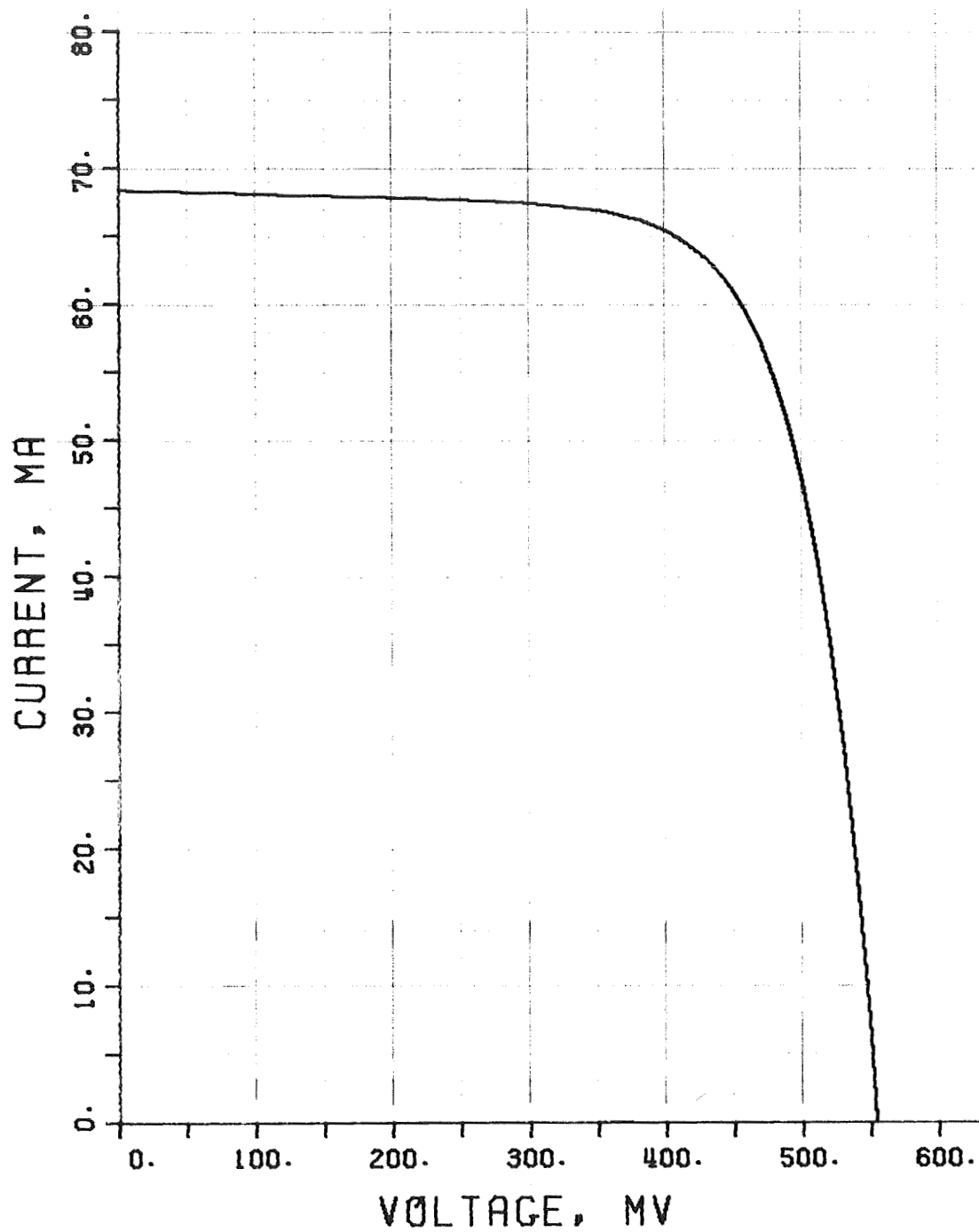


Figure 2-3 Assumed Average Solar Cell I-V Characteristics
(Bare New Cell at 25°C (77°F), 1 Sun AMO)

2.3.2 The Detailed Calculations

The assumed basic solar cell equation for forward characteristics is the conventional lumped-parameter expression* written as follows:

$$I = I_L - I_0 \left[\exp \frac{V+IR}{B} - 1 \right] - \frac{V}{P} \quad)1)$$

The implicit relationship between I and V has been approximated by a semi-iterative explicit expression for I(V):

$$I(V) = I_L - E \exp \frac{R(I_2 + I_3)}{2B} - \frac{V}{P}$$

$$\text{where } I_3 = I_L - E \exp \frac{R I_2}{B}$$

$$I_2 = I_L - E \exp \frac{R I_1}{B}$$

$$I_1 = (I_L - E) \left(\frac{1}{1 + \frac{RE}{B}} \right)$$

$$E = \exp \frac{V' - A}{B} ; V' = V \left(1 - \frac{R}{P} \right)$$

$$A = -B \ln I_0$$

The derivation and accuracy of the explicit relation for I(V) is presented in Appendix B; agreement is excellent (better than 0.01%) over 90% of the I-V curve, with a maximum error of 0.33% as current approaches the open-circuit voltage point.

Assignment of the cell parameters depends on the selected average cell assumed in the makeup of the array. Methods applicable to determining parameters from empirical I-V data are presented in Appendix C. Temperature dependences of the parameters are determined similarly, and analytical functions are finally assigned to each parameter to produce smooth variation with temperature. Appendix D

*Notation and definition of the terms are listed in Appendix B.

presents the list of functions and resultant I-V plots used on this program. Test cases indicate that degradation rates of cells are not too sensitive to operating temperature assignments (within "reasonable" excursions) but absolute values and starting points differ.

Light-generated current, I_L , of a cell is assumed to vary directly with incident light intensity and with the cosine of the angle between the cell normal and the incident light direction. The satellite array is constructed with 24 planar panels, or "facets", each panel containing a series string of 76 or 84 submodules and each submodule containing 4 parallel cells. The light-generated current of each cell on facet j , where $j = 1$ to 24, is thus,

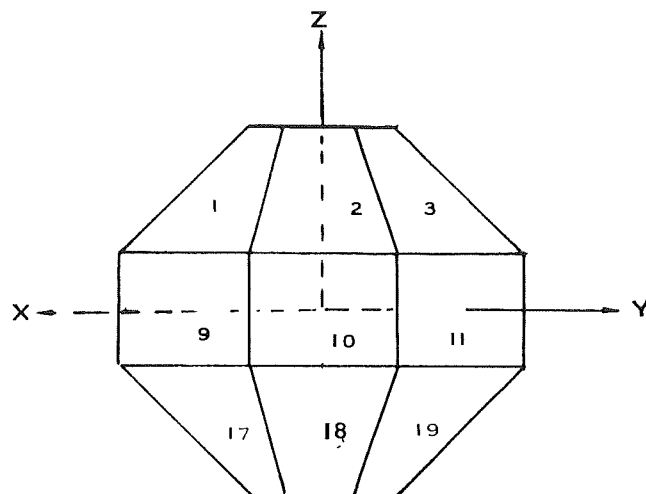
$$(I_L)_j = K I_L \cos(n_j, s)$$

where K is an intensity factor and $\cos(n_j, s)$ is the cosine of the angle between the sun direction and the normal to panel j . If the spin axis of the satellite is designated as the z axis of a satellite coordinate system and arbitrary (but consistent) x and y axes assigned relative to it, we may write:

$$\begin{aligned} \cos(n_j, s) &= \cos(n_j, x) \cos(s, x) \sin(s, z) \\ &+ \cos(n_j, y) \sin(s, x) \sin(s, z) \\ &+ \cos(n_j, z) \cos(s, z) \end{aligned}$$

where the $\cos(n_j, x)$, $\cos(n_j, y)$, and $\cos(n_j, z)$ are the direction cosines of the 24 facets, the angle (s, x) a satellite rotation position angle, and (s, z) the angle between the spin-axis and the sun. The direction cosines for the IDSCS geometry are listed in Table 2-1. As the satellite spins around its z -axis (to gyroscopically maintain a "fixed" orientation in space), the power output ripples sinusoidally eight times per rotation as each subsequent facet faces the sun. Since the telemetry data sampling (once every 2 seconds) is not an exact multiple of the spin rate (approximately 2.7 Hz), readout is assumed random on the power ripple. In this analysis, therefore, the angle (x, s) is fixed at 11.24° to provide an approximate

TABLE 2-1
LIST OF DIRECTION COSINES



Facet j	$\cos(n_j, x)$	$\cos(n_j, y)$	$\cos(n_j, z)$	Temp. Zone
1	0.735	0.000	0.680	I
2	0.520	0.520	0.680	
3	0.000	0.735	0.680	
4	-0.520	0.520	0.680	
5	-0.735	0.000	0.680	
6	-0.520	-0.520	0.680	
7	-0.000	-0.735	0.680	
8	0.520	-0.520	0.680	
9	1.000	0.000	0.000	II
10	0.707	0.707	0.000	
11	0.000	1.000	0.000	
12	-0.707	0.707	0.000	
13	-1.000	0.000	0.000	
14	-0.707	-0.707	0.000	
15	0.000	-1.000	0.000	
16	0.707	-0.707	0.000	
17	0.735	0.000	-0.680	III
18	0.520	0.520	-0.680	
19	0.000	0.735	-0.680	
20	-0.520	0.520	-0.680	
21	-0.735	0.000	-0.680	
22	-0.520	-0.520	-0.680	
23	0.000	-0.735	-0.680	
24	0.520	-0.520	-0.680	

ripple-average output level. The angle (z, s) is a telemetered parameter and actual satellite data is used in each theoretical calculation.

The value of the intensity factor, K , is as follows:

$$K = 0.94 (1 + 0.0167255 \cos Q)^2$$

where $Q = S + 0.033444 \sin S$ radians

$$S = 0.017203 (t + t_L) \text{ radians}$$

t_L = number of days from Jan 1 to launch date.

The 0.94 factor is due to coverslide and filter losses in the basic solar cell assembly; the time dependent function expresses intensity variation ($\pm 3.5\%$) caused by the slight ellipticity of the earth's orbit around the sun.

The value of I_L is restricted to be positive or zero. The presence of a negative $\cos(s, n_j)$ merely indicates that a facet is in darkness and I_L must be set identically equal to zero. The value of the current output for facet j , I_j , is also restricted to be positive or zero due to the presence of a blocking diode between each cell string and the satellite main bus. This diode also causes a voltage drop of approximately 1 volt in each string.

The facet angles of the satellite geometry cause a temperature variation between various sets of facets. Due to the high spin rate, the satellite is effectively divided into three temperature zones (with the assigned facet numbers indicated in Table 2-1). These zone temperatures are also telemetered parameters and actual values are used to determine cell parameters valid in each of the I_j calculations.

Referring to the previous section on the significance of the telemetered parameters, we obtain different load points on the array I-V characteristic by considering the shunted and unshunted halves separately:

$$V_{UN} = V_{MB} - V_{CB}$$

$$I_{UN} = I_{MB}$$

$$V_{SH} = V_{CB}$$

$$I_{SH} = I_{MB} + I_{CB}$$

The expected undegraded theoretical currents are thus calculated as follows:

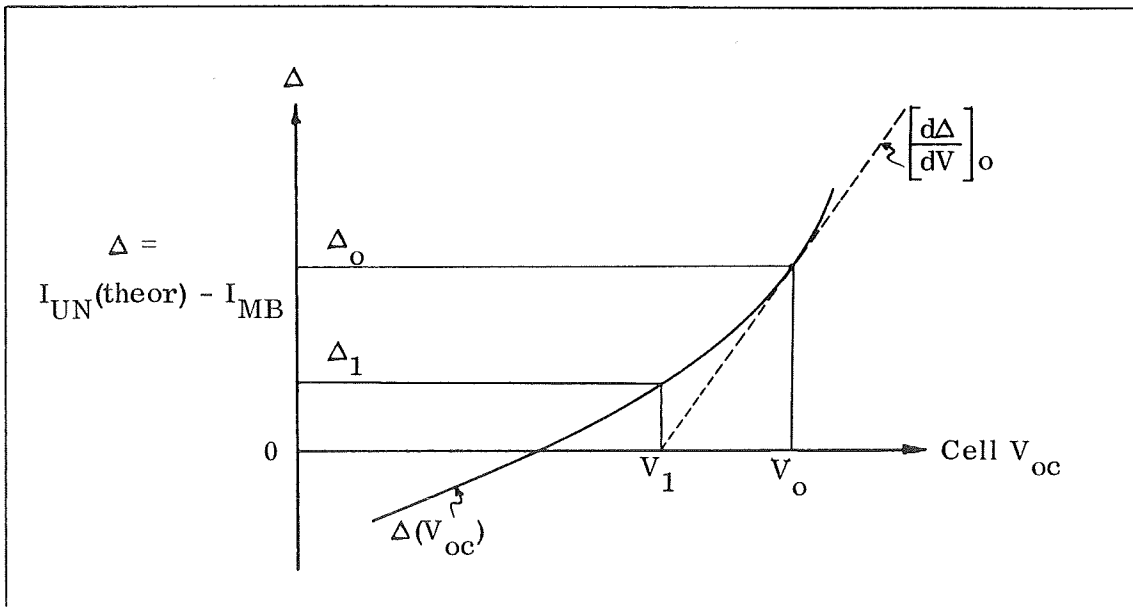
$$\begin{aligned} I_{UN} \text{ (theor.)} &= 4 \sum_{j=1}^8 I_j \left(t, T_1, \frac{V_{UN}}{42} \right) \\ &+ 4 \sum_{j=9}^{16} I_j \left(t, T_2, \frac{V_{UN}}{38} \right) \\ &+ 4 \sum_{j=17}^{24} I_j \left(t, T_3, \frac{V_{UN}}{42} \right) \end{aligned}$$

$$\begin{aligned} I_{SH} \text{ (theor.)} &= 4 \sum_{j=1}^8 I_j \left(t, T_1, \frac{V_{SH}^{+1}}{42} \right) \\ &+ 4 \sum_{j=9}^{16} I_j \left(t, T_2, \frac{V_{SH}^{+1}}{38} \right) \\ &+ 4 \sum_{j=17}^{24} I_j \left(t, T_3, \frac{V_{SH}^{+1}}{42} \right) \end{aligned}$$

The differences between the above theoretical currents and the observed telemetered currents are the most direct degradation outputs of this study. Since $V_{CB} \approx 8$ volts, it is observed that the degradation of the I_{SH} load point must be very close to the degradation of the array short-circuit current point. If no shape changes occur in the array I-V curve, it is further observed that the degradation of V_{UN} , which produces the change in the I_{UN} load point, must be very close to the degradation of the array open-circuit voltage point.

Of more significance to any degradation analysis is the change in I_{sc} and V_{oc} of a single solar cell, since all ground irradiation tests are made at this level. Iteration algorithms have thus been carried out to determine what factors of initial cell I_{sc} and V_{oc} (at room temperature) must be inserted to remove the differences between theoretical and observed current values. These factors are plotted as dots in Section 3.2.

The iteration scheme assumes that the current difference is a linear function of cell I_{sc} or V_{oc} :



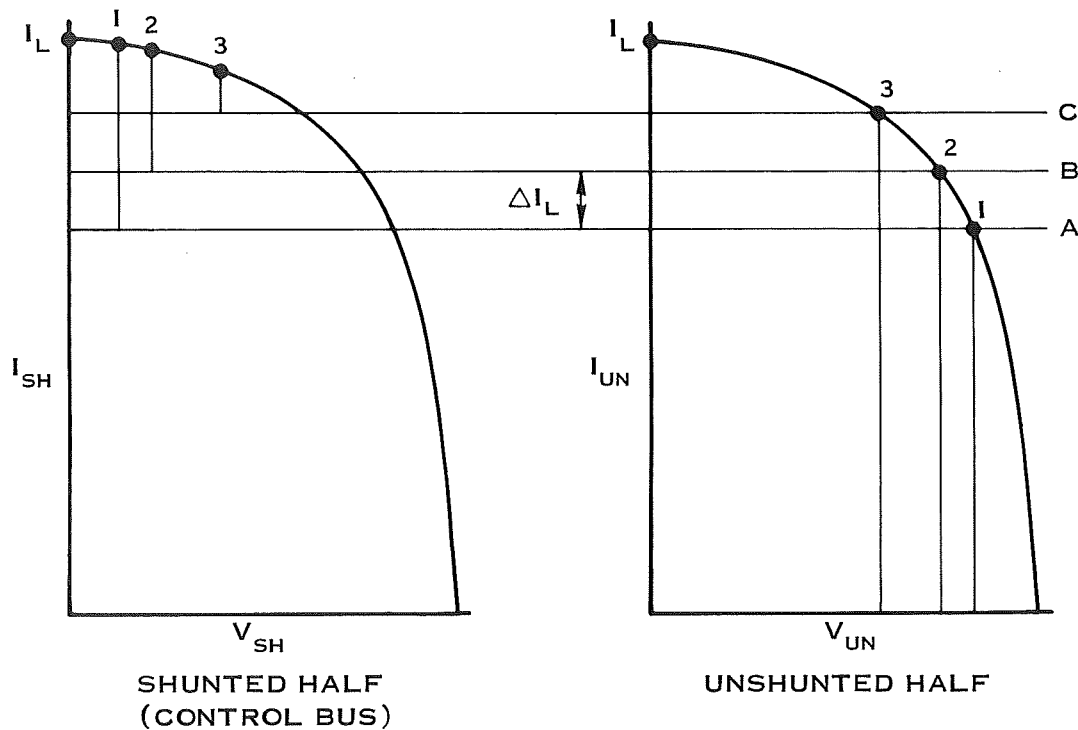
The slope of the function $\Delta(V_{oc})$ at Δ_o is determined by a small test variation in V_{oc} at its initial value, V_o . The first, and subsequent, iterative values aimed at reducing $\Delta(V_i)$ to 0 ± 0.001 are calculated as follows:

$$V_i = V_{i-1} - \left[\frac{dV}{d\Delta} \right]_{i-1} \Delta(V_{i-1})$$

In practice, $\Delta(I_{sc})$ was reduced to less than 0 ± 10^{-10} amps within two iterations and $\Delta(V_{oc})$ to less than 0 ± 0.0005 amps within seven. (Note that in both cases Δ is a current difference treated as a dependent function, first of I_{sc} and then of V_{oc}).

2.4 EXTRACTION OF ARRAY I-V CHARACTERISTICS FROM ECLIPSE ENTRANCE DATA

Twice a year, during the equinox periods, the IDSCS satellites pass through the penumbra region of the earth's shadow into eclipse. The partial shunt regulator maintains the main bus at 29.4 Vdc as long as there is sufficient array capacity to support the loads. Telemetry monitoring of control bus current and voltage through the penumbra provides data from which a portion of the array I-V curve can be constructed. The sketch below indicates the pattern of events.



At full light intensity the array is operating at point 1; as intensity drops, the relative array operating point moves through points 2 and 3 and so on until power and voltage demands cannot be met. (Actually, I_L moves downward and the lines A, B, and C remain coincident and fixed at a constant current.) The following equations govern the two halves of the array:

$$V_{SH} + V_{UN} = 29.4 = MBV$$

$$I_{SH} - CBI = MBI = I_{UN}$$

$$V_{SH} = CBV.$$

The quantities CBI, CBV, MBV, and MBI are telemetered parameters.

To obtain I vs V for the unshunted half of the array, where the maximum power point "knee" resides, we plot

$$I_{UN} = MBI + |\Delta I_L|$$

versus

$$V_{UN} = 29.4 - CBV$$

To determine ΔI_L , we must consider the slope, dI/dV , of the array I-V curve near I_L due to the cumulative shunt resistances of the cells in the array.

$$\begin{aligned} I_L &= I_{SH} - (dI/dV) V_{SH} \\ &= MBI + CBI - (dI/dV) CBV \end{aligned}$$

thus

$$\Delta I_L = \Delta CBI - (dI/dV) \Delta CBV$$

and this is the true separation between lines A and B, B and C, etc., as long as CBV does not approach too closely to the knee. Figure 2-4 shows the array I-V output as calculated at the autumnal equinox. The equation for ΔI_L is valid for $0 \leq CBV \leq 12$ (for half of the array); and $dI/dV = -1.33 \text{ mA/V}$ for the full array voltage axis or -2.67 mA/V for the half array axis.

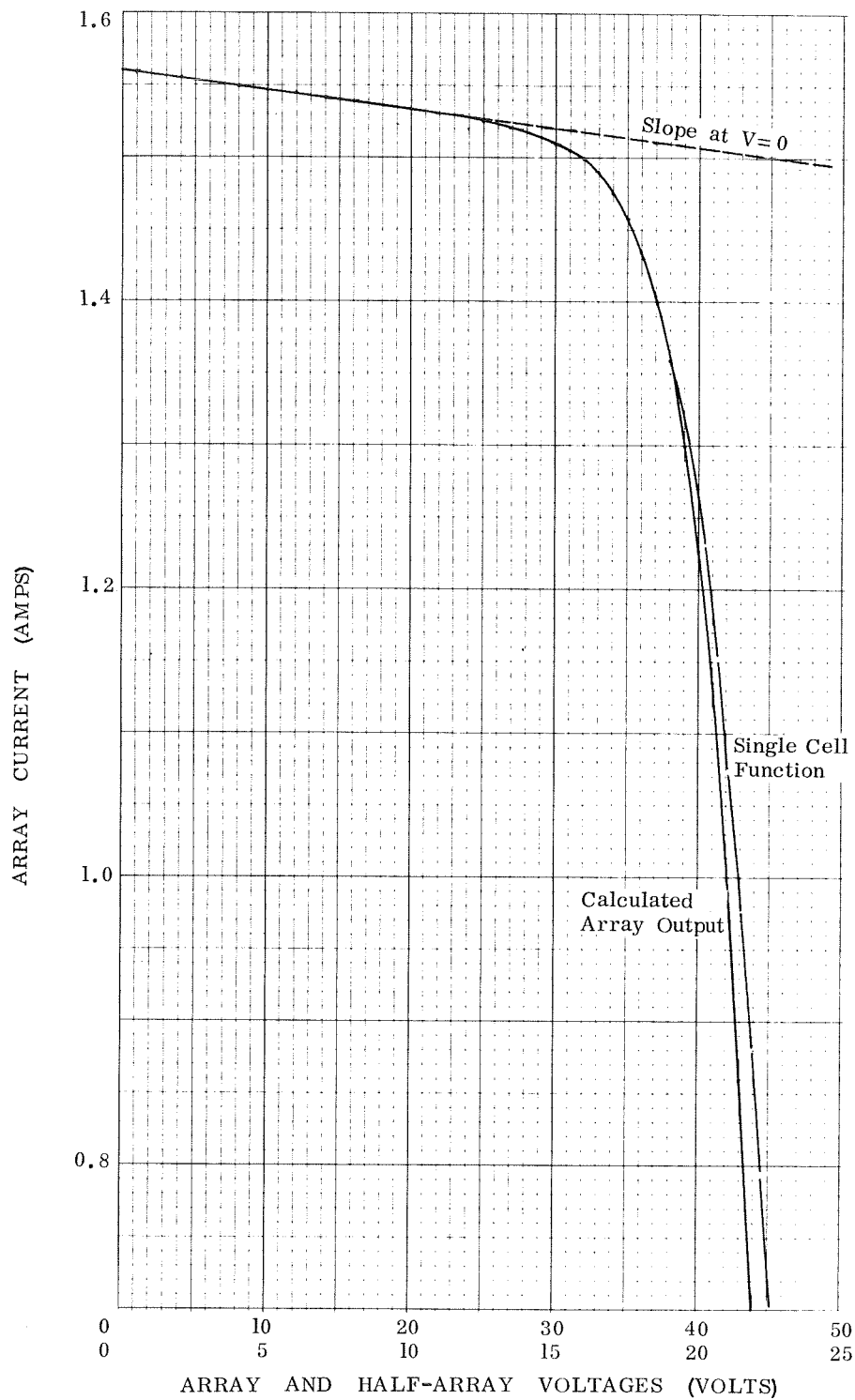


Figure 2-4 Calculated Array Output Compared with Theoretical Single-Cell Function

Typical eclipse entrance telemetry data is shown in Figure 2-5. In order to obtain an impartial curve thru the CBV data, a function was derived from theory to indicate the expected dependence with time. The array I-V curve was assumed to follow the functional shape of a single cell I-V curve, with appropriate parameters. Figure 2-4 indicates that this assumption is a good approximation in the vicinity of the knee and above.

Let

$$V = (29.4 - CBV)$$

$$I = I_L - I_o \left[\exp \frac{V + IR}{B} - 1 \right] - \frac{V}{P}$$

$$= CBI = a + bt$$

The last equality follows from the observed data (cf. Figure 2-5). Dropping the insignificant 1 in the brackets and rearranging terms, we obtain,

$$V = A + B \ln (I_L - a - bt - V/P) - Ra - Rbt$$

$$CBV = (29.4 - A + Ra) - B \ln (I_L - a - bt - V/P) + Rbt$$

and, dropping the small V/P term, we produce a function of the form,

$$CBV = C_1 - B \ln (k - bt) + C_3 t,$$

at $t = 0$, $CBV = CBV(0) = C_1 - B \ln K$, whence

$$CBV = CBV(0) - B \ln (1 - C_2 t) + C_3 t$$

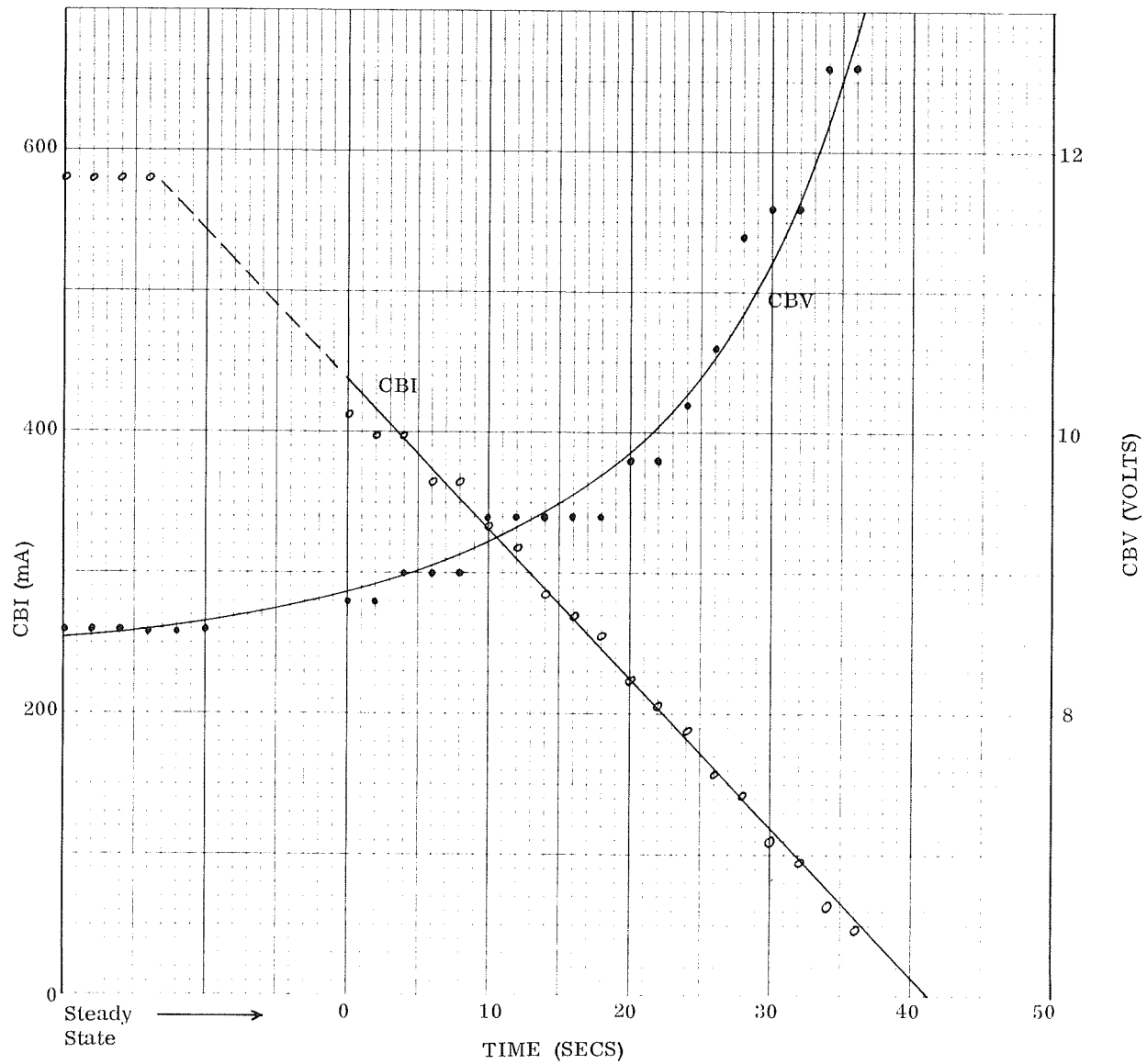


Figure 2-5 Example of Eclipse-Entrance Telemetry Data with Least-Squares Fitted Functions (Satellite No. 9312)

The value of t reaches a maximum when CBI reaches zero. At this point, and for purposes of mathematical simplification, $CBV \rightarrow \infty$ and $C_2 t_{\max}$ must approach unity. We can estimate,

$$C_2 \approx 1/t_{\max}$$

and rewrite the CBV functional dependence in a further state of approximation as

$$CBV = CBV(0) - B \ln (1-t/t_{\max}) + Ct.$$

This equation is amenable to linear regression techniques since the logarithmic term does not contain a parameter. The CBI function produces a reasonable value of t_{\max} . Given N data pairs of CBV vs t , and using the following substitutions:

$$y = CBV$$

$$A = CBV(0)$$

$$b = \ln (1-t/t_{\max})$$

we minimize the sum of the squared differences with respect to A , B , and C and produce three solvable equations in three unknowns:

$$\begin{aligned} AN + B \sum b_n + C \sum t_n &= \sum y_n \\ A \sum b_n + B \sum b_n^2 + C \sum t_n b_n &= \sum y_n b_n \\ A \sum t_n + B \sum t_n b_n + C \sum t_n^2 &= \sum y_n t_n \end{aligned}$$

An example of this function is plotted in Figure 2-5.

Five eclipse-entrance array I-V curves from the first launch satellite have been reconstructed by this method for the 1966 autumnal and 1970 vernal equinox periods. The plots are displayed in Section 3.5.

2.5 CURVE FITTING AND STATISTICAL ANALYSIS

The techniques used in fitting functions to the plotted I_{sc} and V_{oc} degradation, as well as the inferences and relative tests on the fits, are described in this section.

2.5.1 Linear Regression

Initially the functions describing I_{sc} and V_{oc} degradation were assumed to be linear; that is, they could be described either by a straight line or could be linearly transformed into a straight line. The functions considered, based on the general shape of the dot or scatter plots, were:

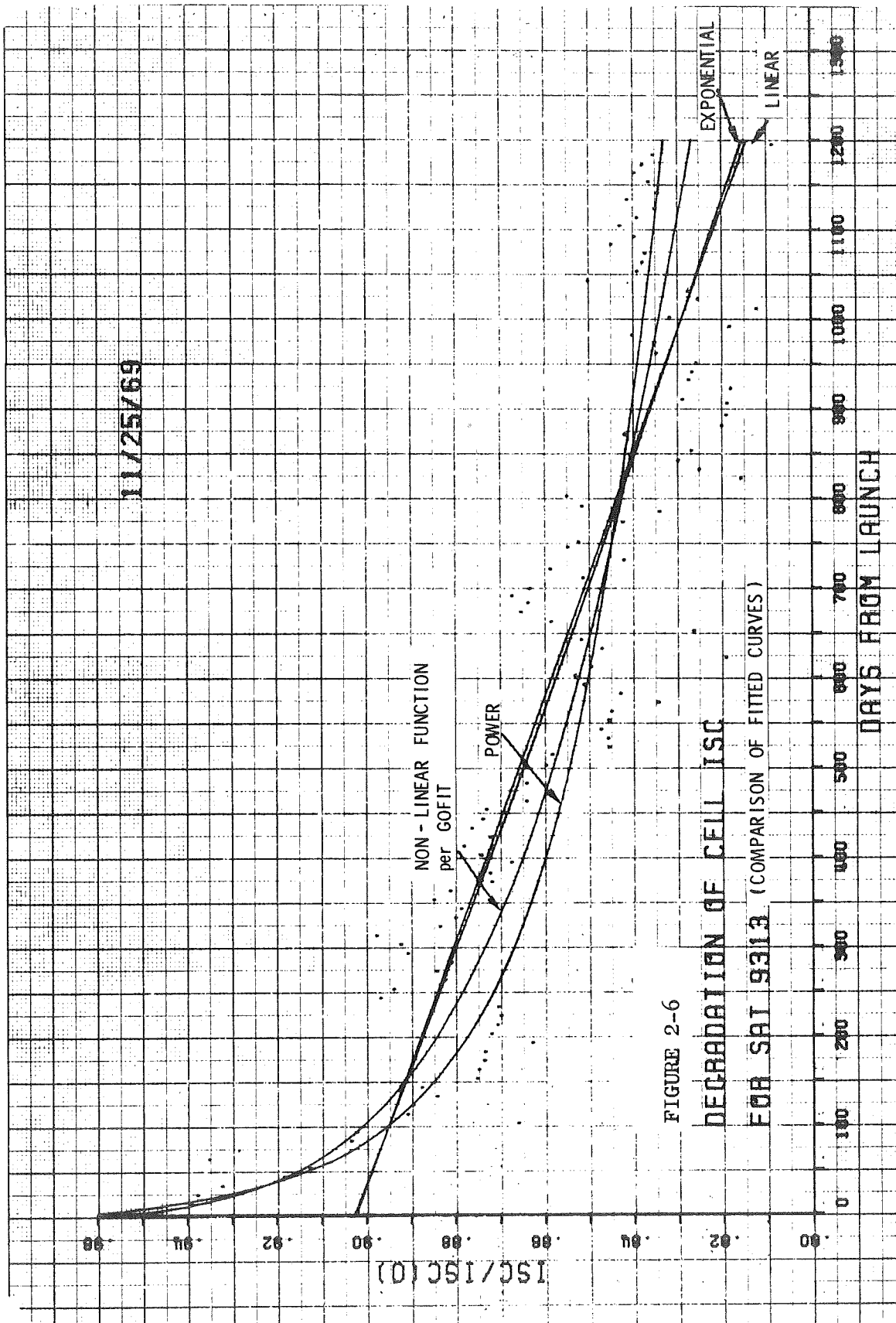
- (a) $y = ax + b$
- (b) $y = ae^{bx}$
- (c) $y = ax^b$

The dependent variable y was either $I_{sc}/I_{sc}(0)$ or $V_{oc}/V_{oc}(0)$, and the independent variable x was the number of days from launch.

A linear regression of y on x was performed on both I_{sc} and V_{oc} data for several satellites using LINREG (a program in our timesharing library). The exponential fit generally produced higher correlation coefficients than did either the linear or power functions for both I_{sc} data and V_{oc} data. A typical comparison of these fits is shown in Figure 2-6. The nonlinear regression curve, as discussed in the following section, is included for reference.

2.5.2 Nonlinear Regression

Though the function obtained from the linear regression indicated a high degree of association of the dependent variable on the independent variable (high correlation coefficients at least for I_{sc}), they did not satisfactorily link what is known of the degradation phenomena to a function which allowed the parameters influencing degradation to be included in its form. In Section 3.3 the development of a



hypothetical degradation function is described. The functions examined are:

$$I_{sc}(t)/I_{sc}(0) = R_o \left(1 - A \ln(1 + Bt) \right) (1 - Mt)$$

$$\text{and } V_{oc}(t) (V_{oc}(0) = R_o' \left(1 - A' \ln(1 + B't) \right))$$

These functions have no linear transform and thus cannot be treated by linear regression analysis. A program, called GOFIT, was developed which performs a nonlinear regression to an arbitrary function on a set of data pairs (x,y) for up to several thousand observations. Having inputted the data set, the function, and the number of data points in the data set, a starting point for the regression parameters is inputted to the computer. From this starting point, a search is made along the n-dimensional regression parameter space, where the total square error is the dependent variable. The search is based on minimizing the square error and continues until an inputted square error is reached or until an actual minimum on the surface of the parameter contour is found. (Refer to Appendix C, Method 4, for a further description of this type analysis.) When either criteria is met, a set of regression parameters and the resulting total square error is outputted along with a histogram of the resulting errors.

One of the assumptions made in all regression analysis is that data population follows a normal distribution about some mean. For true random data, the mean is developed as the fitted function. Therefore, the variation in the data should follow a normal or gaussian distribution about the function developed in GOFIT. The histogram developed for each final choice of regression parameters provides information on how close to a gaussian the error distribution actually is and how random the data actually is.

Some of the fits obtained from the nonlinear regression did not exhibit apparent good fits or gaussian shaped histograms. There were small clusters of points detached from the main group; these points contributed large errors to the total square error. A facility within GOFIT was introduced which allowed an absolute error to be set and to eliminate all stray points larger than the set absolute error.

Elimination of these "strays" improved the fits considerably although they only accounted for less than 5% of the total number of points.

2.5.3 Correlation Coefficients

The correlation coefficients provide a relative measure of the degree of association between two variables. For linear regressions the correlation coefficient is calculated automatically. For the nonlinear cases, the program CORR evaluates the coefficient, as given by the equation:

$$r = \sqrt{1 - \frac{\sum (y_i - y_{\text{calc}})^2}{\sum (y_i - \bar{y})^2}}$$

where y_i = the value of y for the i^{th} data pair

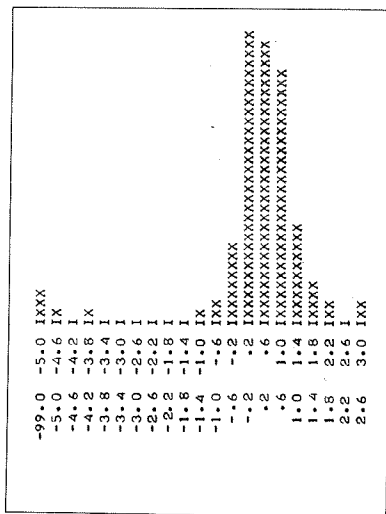
y_{calc} = the value of the fitted function for the i^{th} value of the independent variable x_i

\bar{y} = the mean value of y over all data pairs

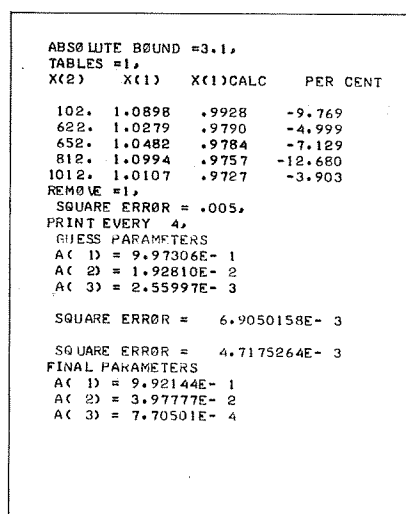
As might be expected, there is good correspondence between decreasing square error, tightly packed histograms centered about zero error and higher correlation coefficients. The histograms in Figure 2-7 illustrate the improvements found with the refinements introduced into the regression analysis.

2.5.4 Confidence Limits

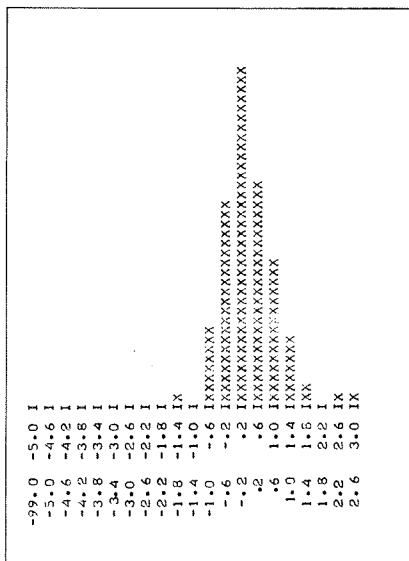
Confidence intervals about fitted functions provide a measure of how accurately the regression functions can serve as predictors in describing a phenomena. The 95% confidence limits describe the boundaries around a fitted function within which one can expect 95% of the data points to fall if the observations are repeated many times. The analytic description of the 95% confidence interval is given by:



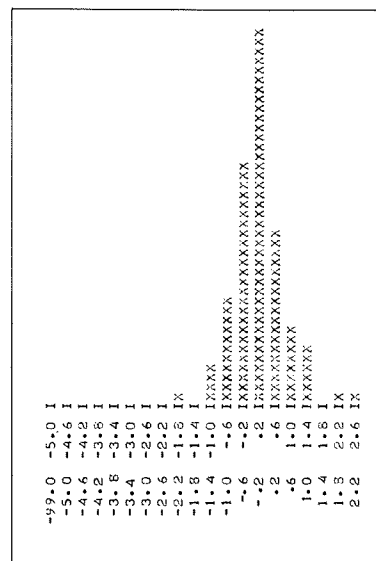
A. Histogram printout after three iterations, no points removed; square error = .04032



B. GOFIT output indicating choice of absolute error bound and removal of five "stray" data points, and final parameters resulting from four additional iterations.



C. Resultant histogram; square error = .0047175



D. Histogram after 20 additional iterations; square error = .0042754

FIGURE 2-7 REFINED GOFIT REGRESSION PROGRAM

$$y_{\text{calc}} \pm \frac{2}{n-2} \sum_{i=1}^n (y_i - y_{\text{calc}})^2 \sqrt{\frac{1}{n} + \frac{(X_o - \bar{X})^2}{\sum (X_i - \bar{X})^2}}$$

where $n \simeq 100$ and equal to the number of observations

y_{calc} = the value of the fitted function at X_o

y_i = the value of the observation at X_o

\bar{X} = the mean value of X

X_i = the i^{th} value of X in the set of observations

The CONLIM program was used to evaluate the confidence limits for several satellites. The results are presented in Section 3.4.

SECTION 3

DETAILED RESULTS

This section presents the collection of graphs, tables, derivations, and figures which comprise the detailed results of this study. Some ambiguous entries, such as a presentation of methods attempted in an effort to separate cell and noncell damage and a presentation of the analysis of anomalous seasonal variations, are treated as 'results'. Other analysis and technical detail appears in Section 2 and the Appendices.

3.1 SATELLITE GEOMETRY AND ORBIT DEFINITION

The IDSCS satellite, shown in Figure 3-1, is an active communication repeater. Its shape is a symmetrical polyhedron consisting of two octahedral truncated pyramids joined by an octagonal cylindrical center section. The height of the satellite body is 31 inches, and the diameter of the circle circumscribing the octagonal cylinder is 36 inches. The satellite weighs 97 pounds and employs passive thermal control. A detailed satellite description appears in Appendix A.

Three launches have been considered in this study: The first (7 satellites) on 16 June 1966; the second (8 satellites) on 18 January 1967; and the third or multiple payload (4 satellites) on 1 July 1967. An unsuccessful launch, between the first and the second, self-aborted shortly after liftoff due to structural failure of the booster fairing. The first and second successful launches achieved slightly subsynchronous circular equatorial orbits. The multiple payload orbit was similar, but inclined seven degrees due to the desire to increase the total payload weight.

The nominal orbits for the three launches are given in Table 3-1. The individual satellite orbits differ slightly because each has a slightly different initial velocity to insure separation and eventual distribution around the earth. More detailed orbital data appears in Appendix A and Section 3.9.

TABLE 3-1
SATELLITE ORBITS

Orbital Parameter	First Launch 16 June 1966	Second Launch 18 Jan 1967	Third Launch 1 July 1967
Apogee (nmi)	18,606	18,330	18,228
Perigee (nmi)	18,205	18,161	18,191
Eccentricity	0.0092	0.0039	0.00086
Inclination (degrees)	0.042	0.41	6.998
Period (minutes)	1350	1335	1332

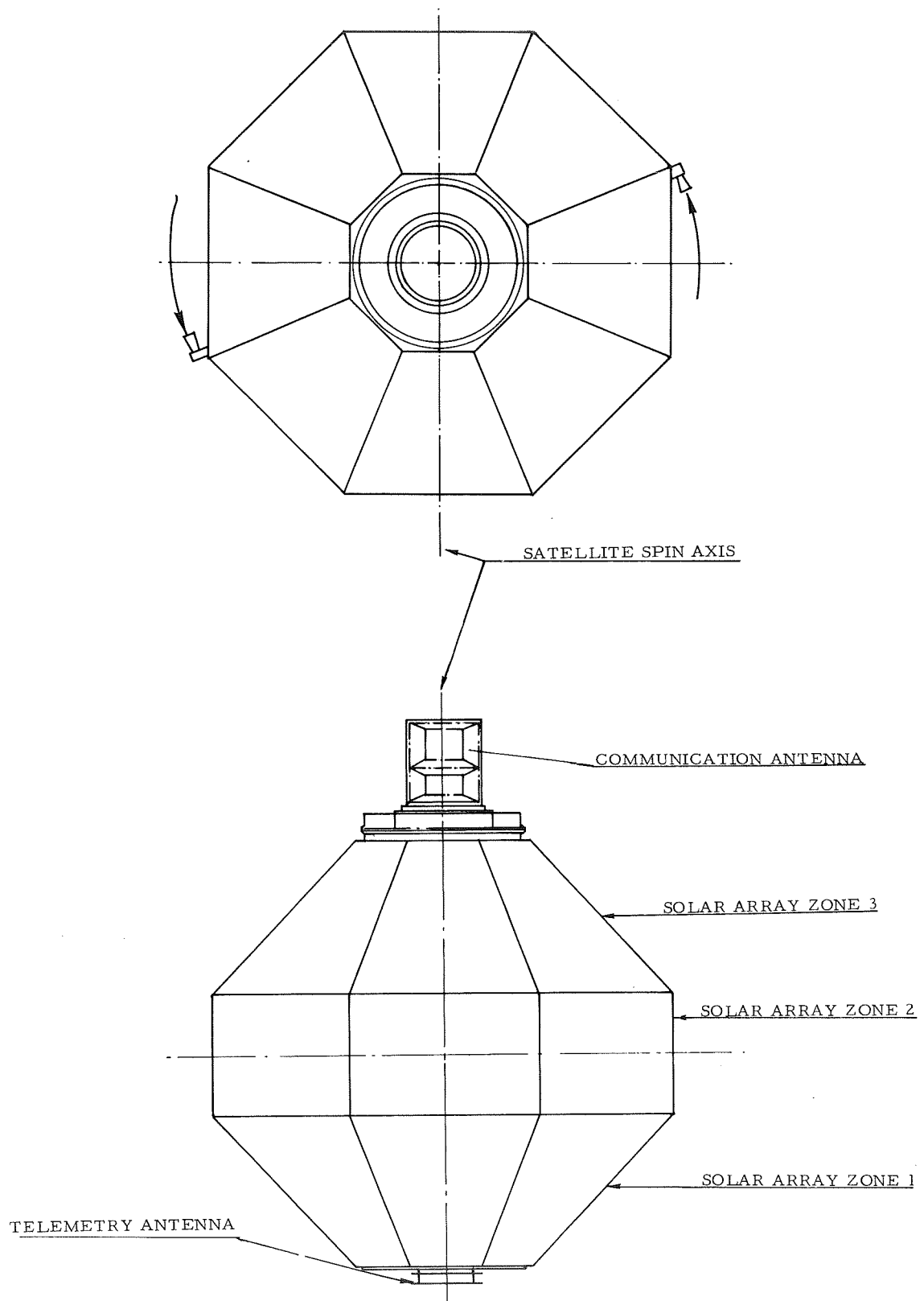


FIGURE 3-1 SATELLITE ENVELOPE CONFIGURATION

3.2 DEGRADATION PLOTS OF CELL I_{sc} AND V_{oc} VERSUS TIME

Figures 3-2 and 3-3 present the updated composites of normalized I_{sc} and V_{oc} degradation ratios. All cell and noncell losses are included. Five-year I_{sc} values range between 0.875 and 0.832 with a random (gaussian) distribution. Five-year V_{oc} values range between 0.984 and 0.945, but with a skewed-gaussian distribution.

Figures 3-4 through 3-22 present the detailed updated and previously published cell I_{sc} ratios calculated (generally) every ten days for the IDSCS satellites launches on 16 June 1966, 18 January 1967, and 1 July 1967.

Figures 3-23 through 3-41 present the corresponding cell V_{oc} ratios. The information shown has been derived from the temporal behavior of the operating points of the shunted and unshunted halves of the solar array. Variations due to solar intensity, temperature, and geometry are removed mathematically from the raw data to provide two array degradation points. Multipliers to individual cell values of I_{sc} and V_{oc} are then generated by iteration to produce degradation ratios of appropriate magnitude and combination to explain the observed array behavior.

Each graph contains a plotted curve which was least-squares fitted to the data using the functions

$$\begin{aligned} I_{sc}/I_{sc}(0) &= R_o \left[1 - A \ln(1 + Bt) \right] \left[1 - mt \right] \quad (1) \\ V_{oc}/V_{oc}(0) &= C \exp(kt). \end{aligned}$$

The implementation of the nonlinear regression to equation (1) has evolved thru a number of stages. The present program permits outlying data points (which unrealistically influence the curve) to be discovered, examined, and removed. The function is derived from observed cell behavior and actually applies to the V_{oc} ratio as well as to the I_{sc} ratio, but the computer time required for the V_{oc} runs were so great that a simpler exponential function was used for the previously published data. The drawback of the exponential

function was the almost linear nature of the resultant fit. This does not appear to accurately represent the data pattern in the plots.

The present nonlinear regression program has been made more efficient but the scattered V_{oc} data evidently presents a broad minimum in parameter space which inhibits a least-squares solution. The collection of updated V_{oc} curves presented here has thus been visually fitted with the approximate shape of equation (1).

The wide breaks in the data display of satellite 9314 are due to intermittent operation of the satellite telemetry system. Telemetry on satellite 9331 is totally absent after 75 days.

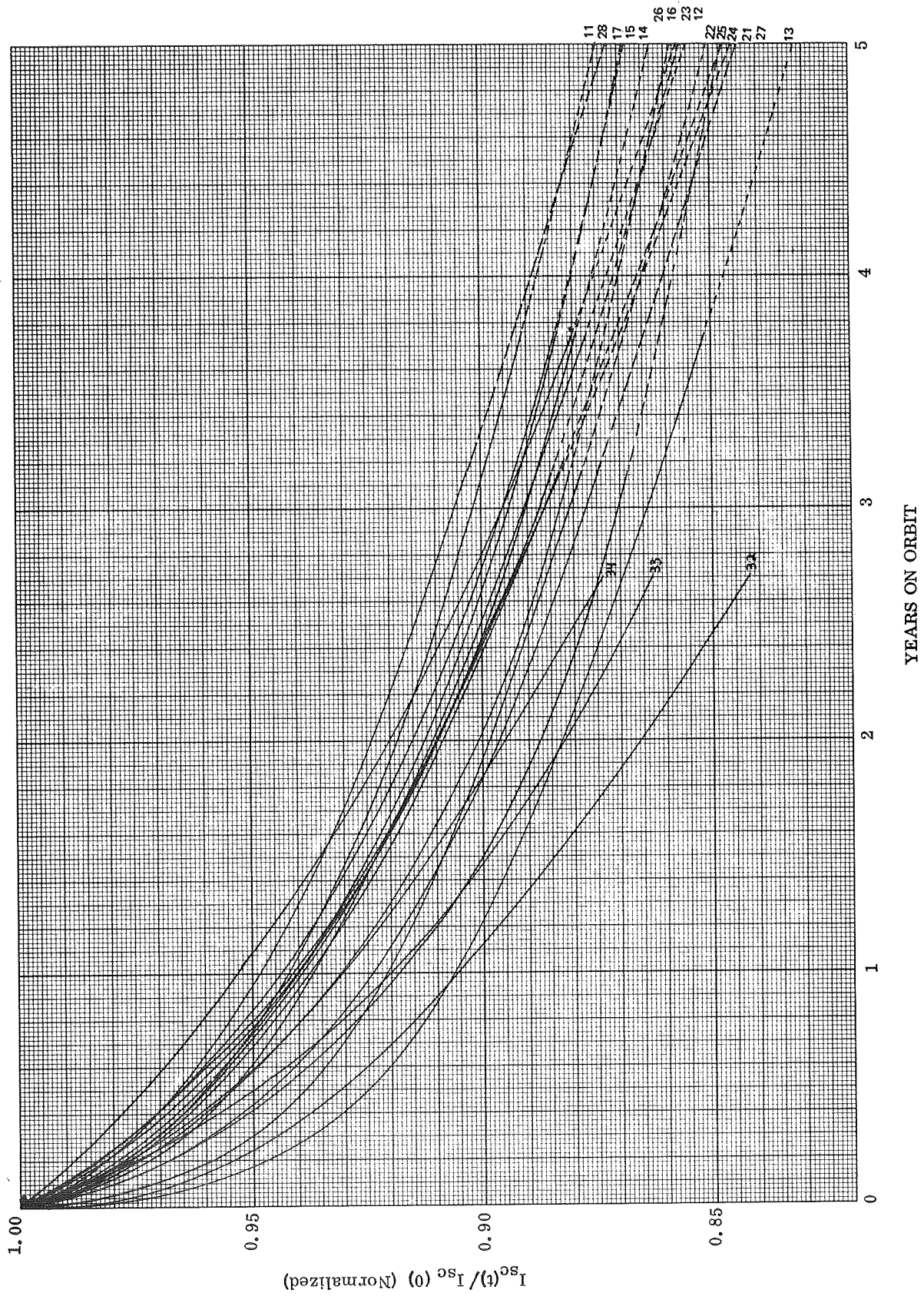


Figure 3-2 Normalized Summary of Cell Short-Circuit Current Degradation

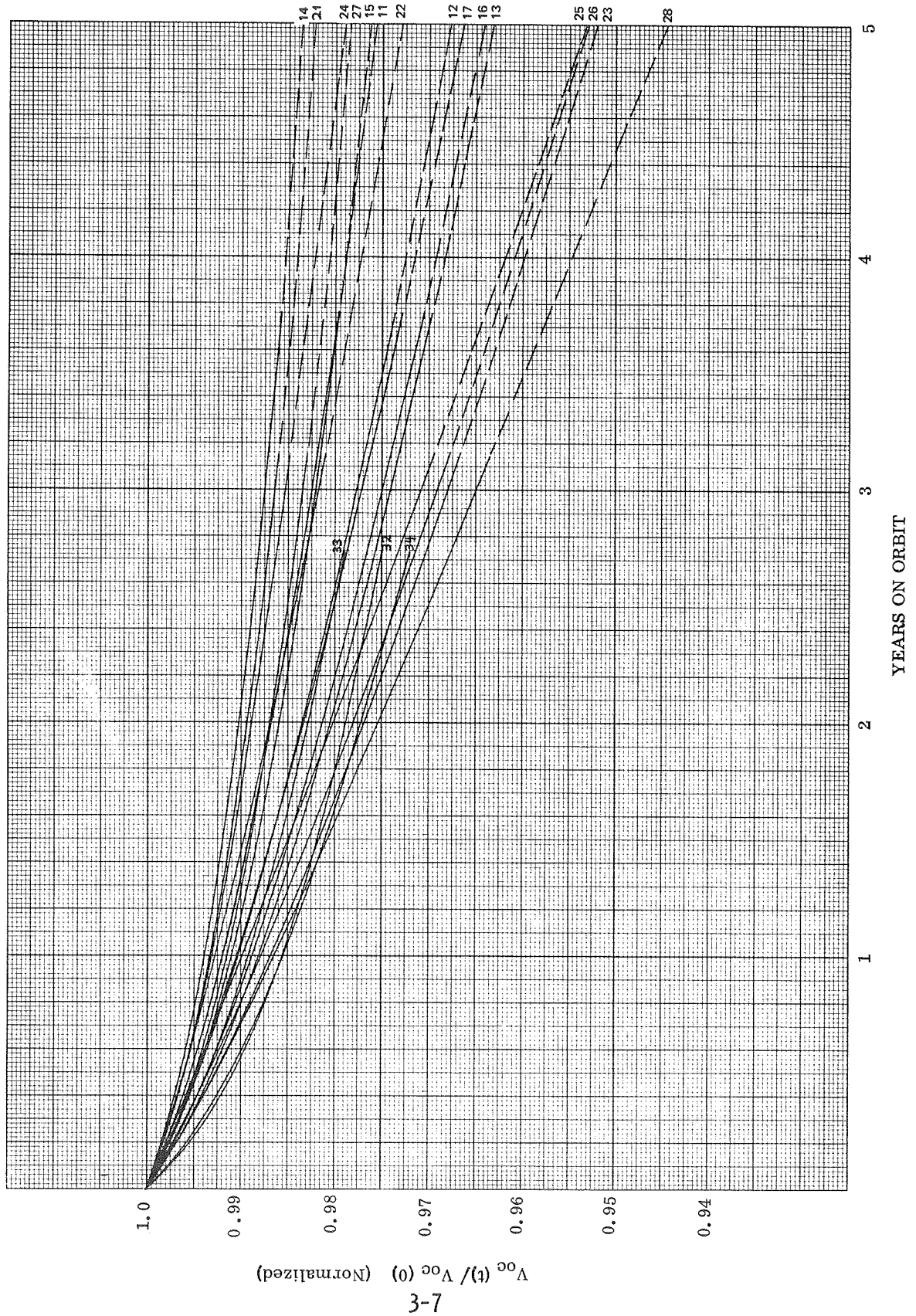
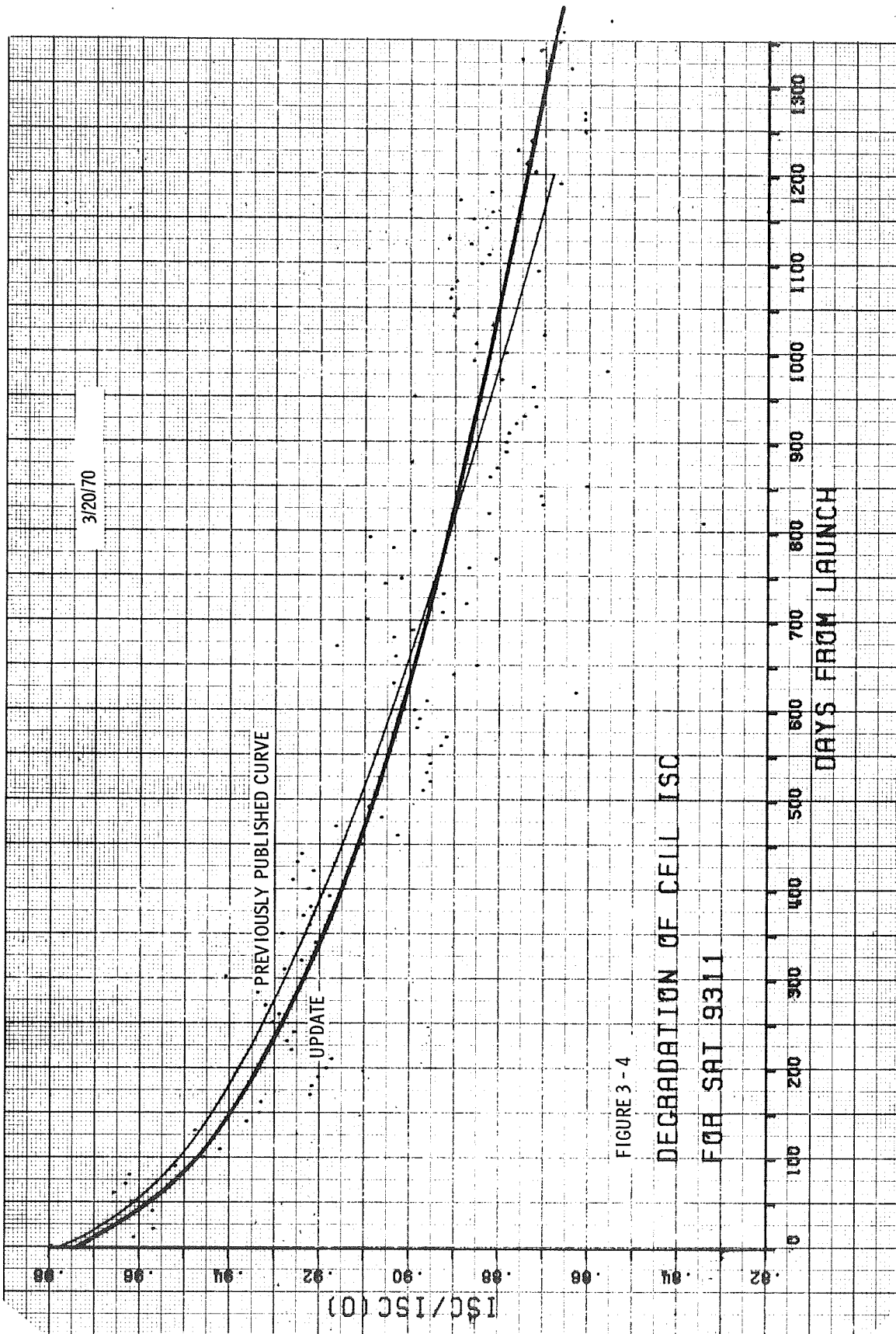
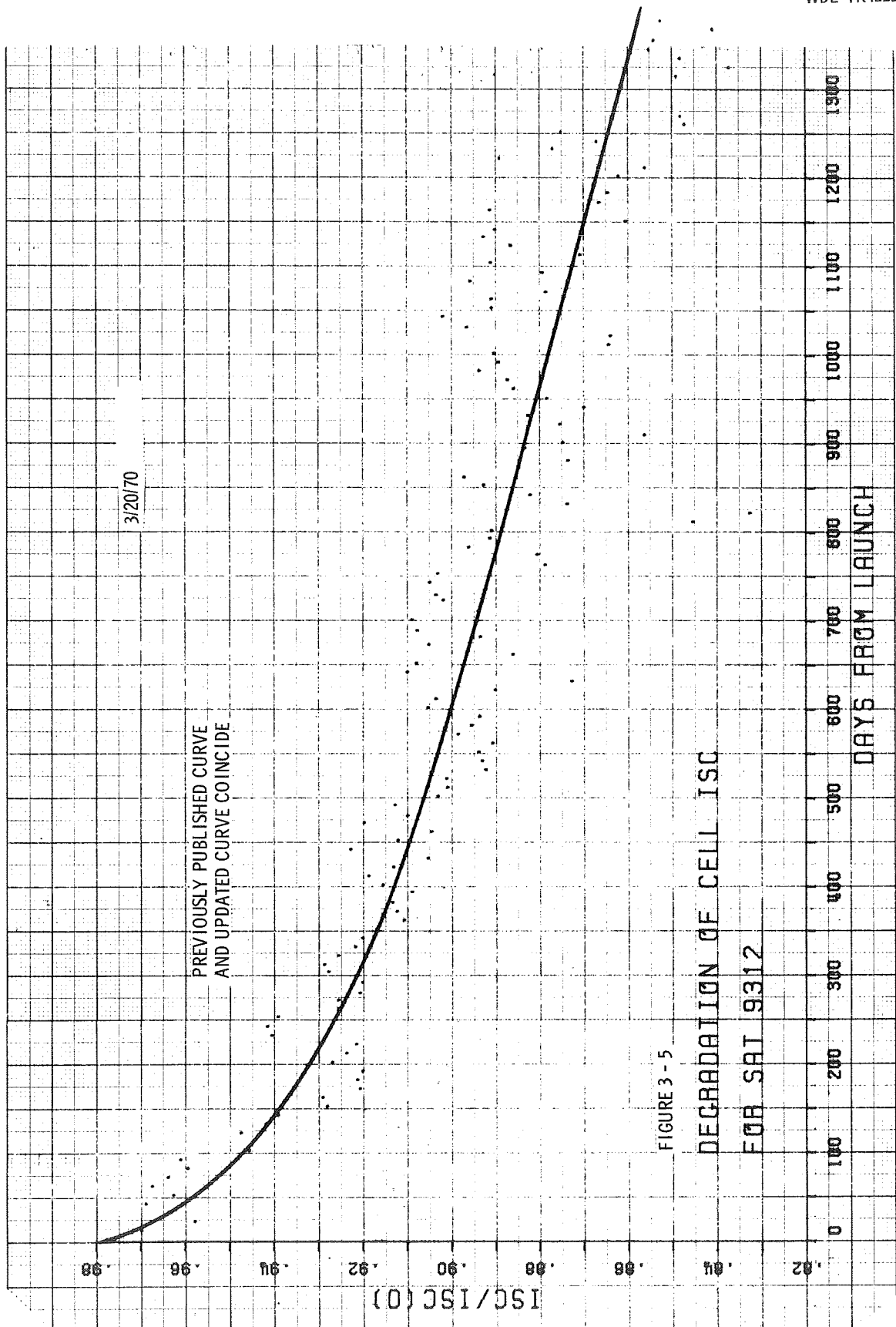
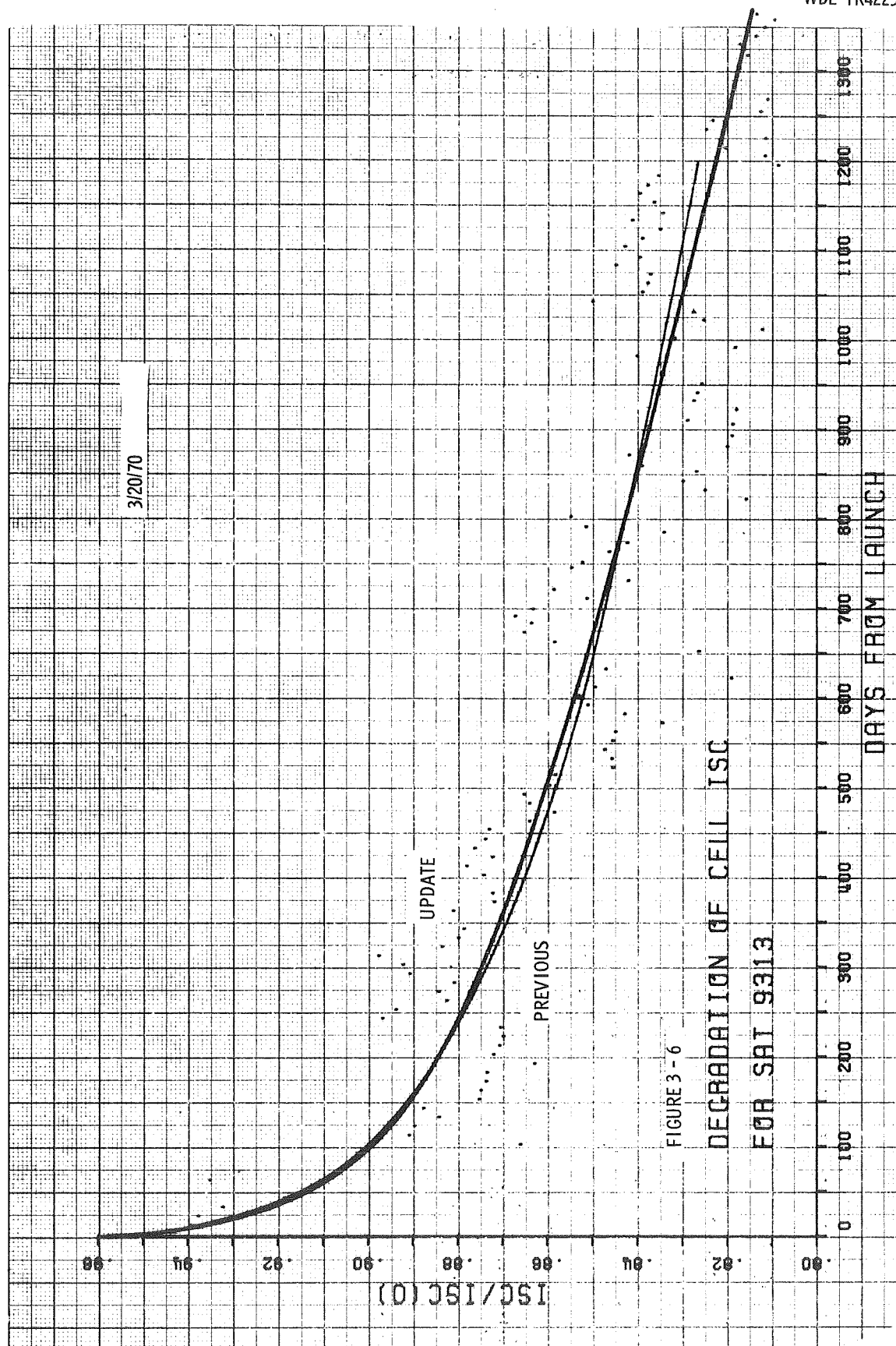
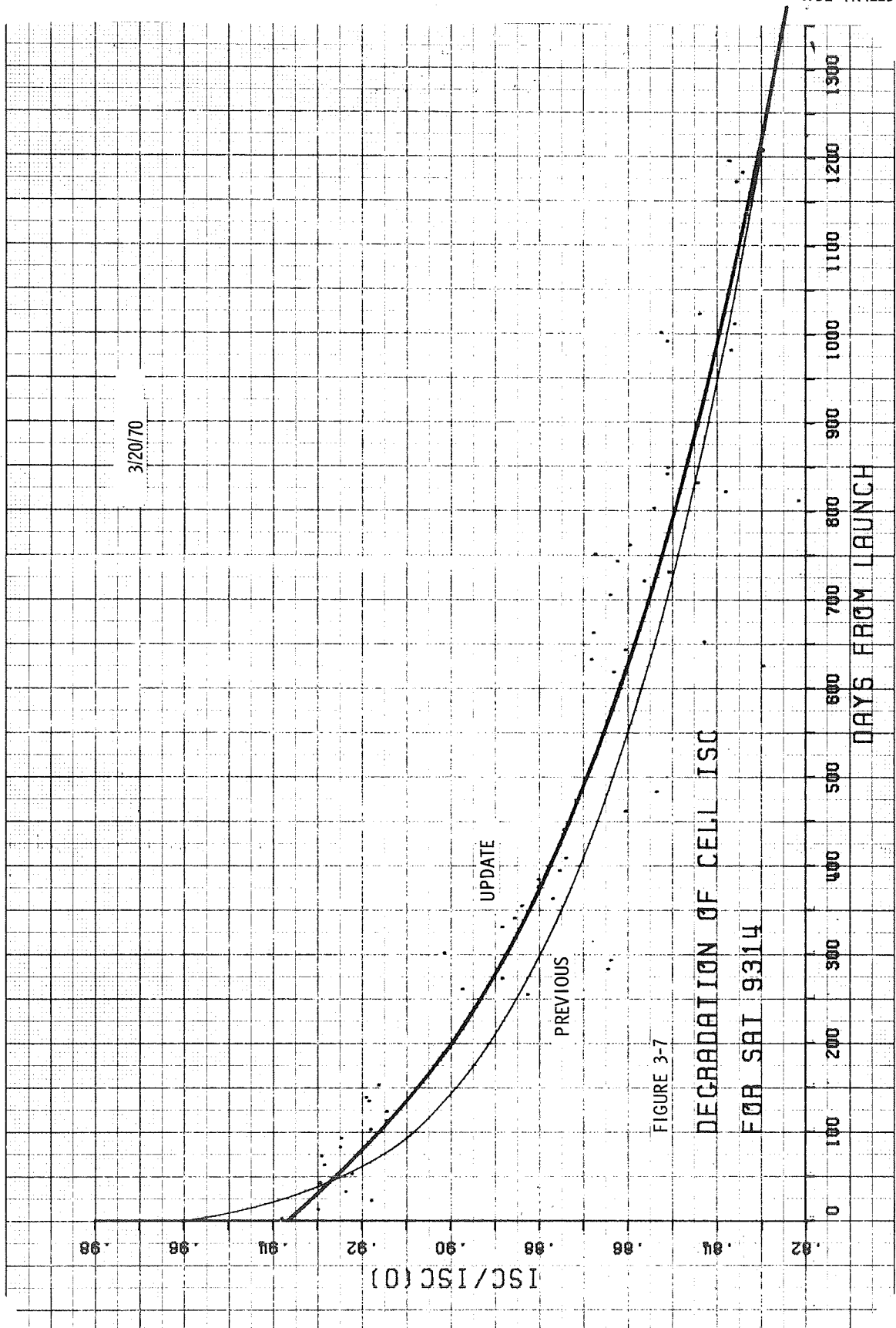


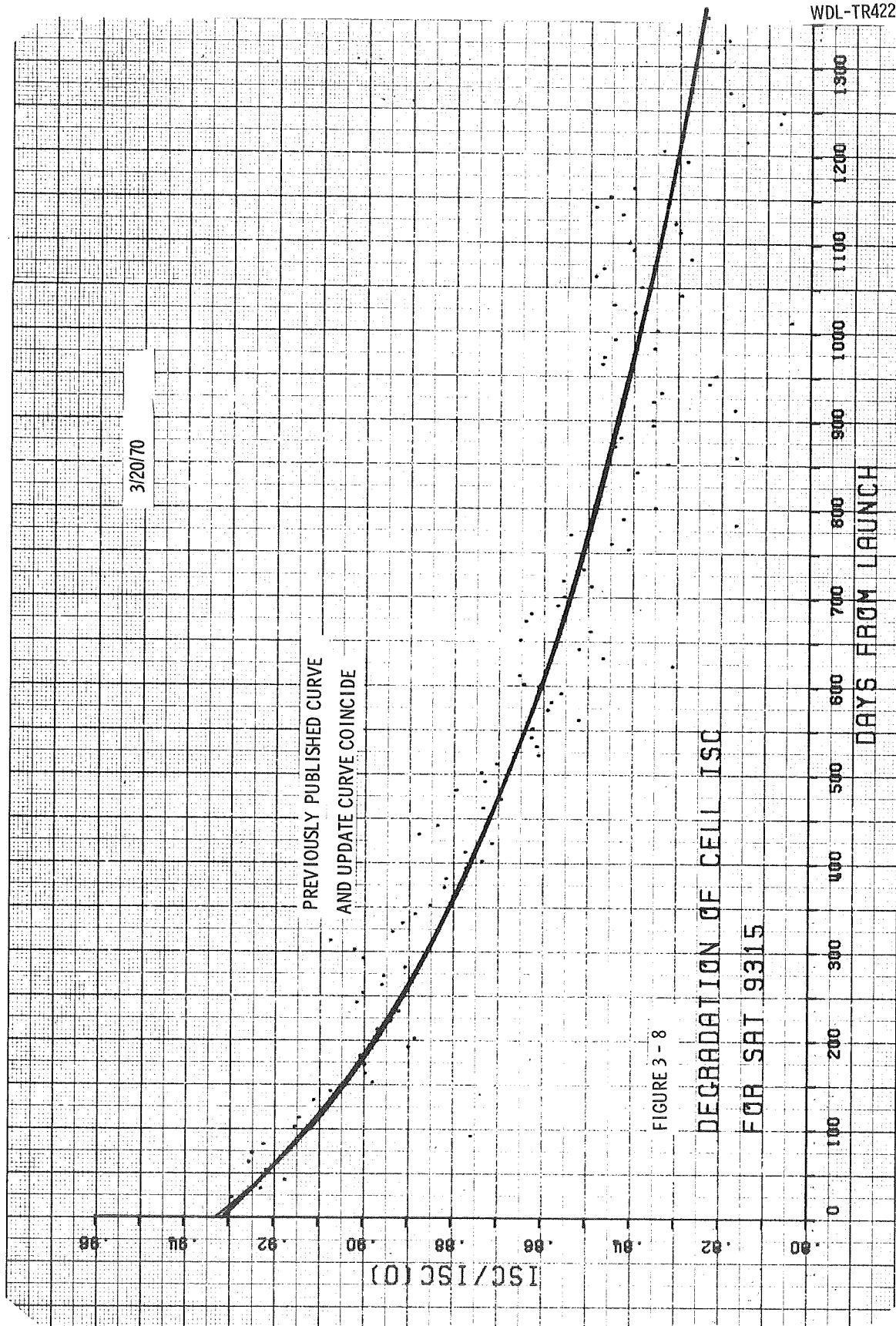
Figure 3-3 Normalized Summary of Cell Open-Circuit Voltage Degradation

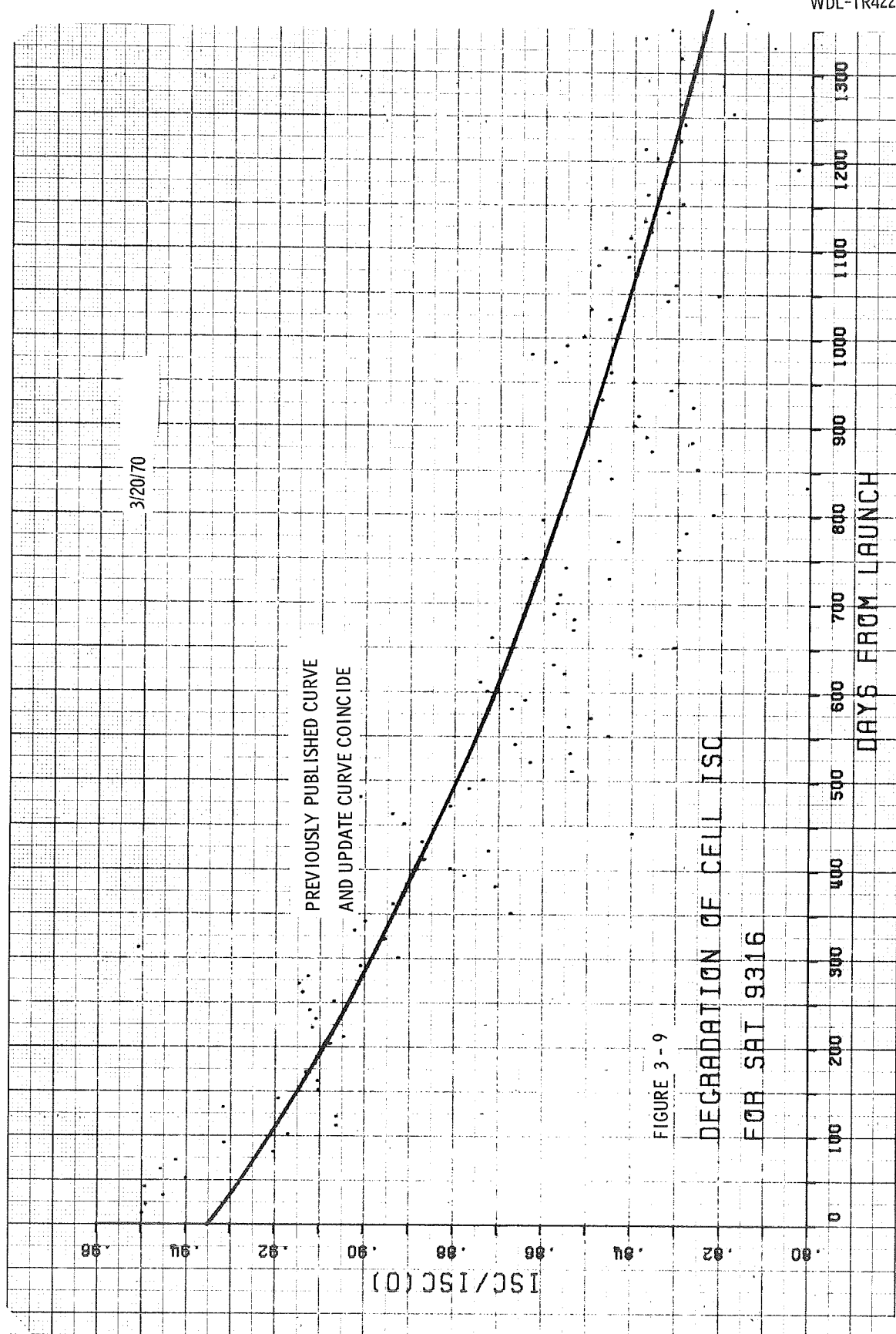


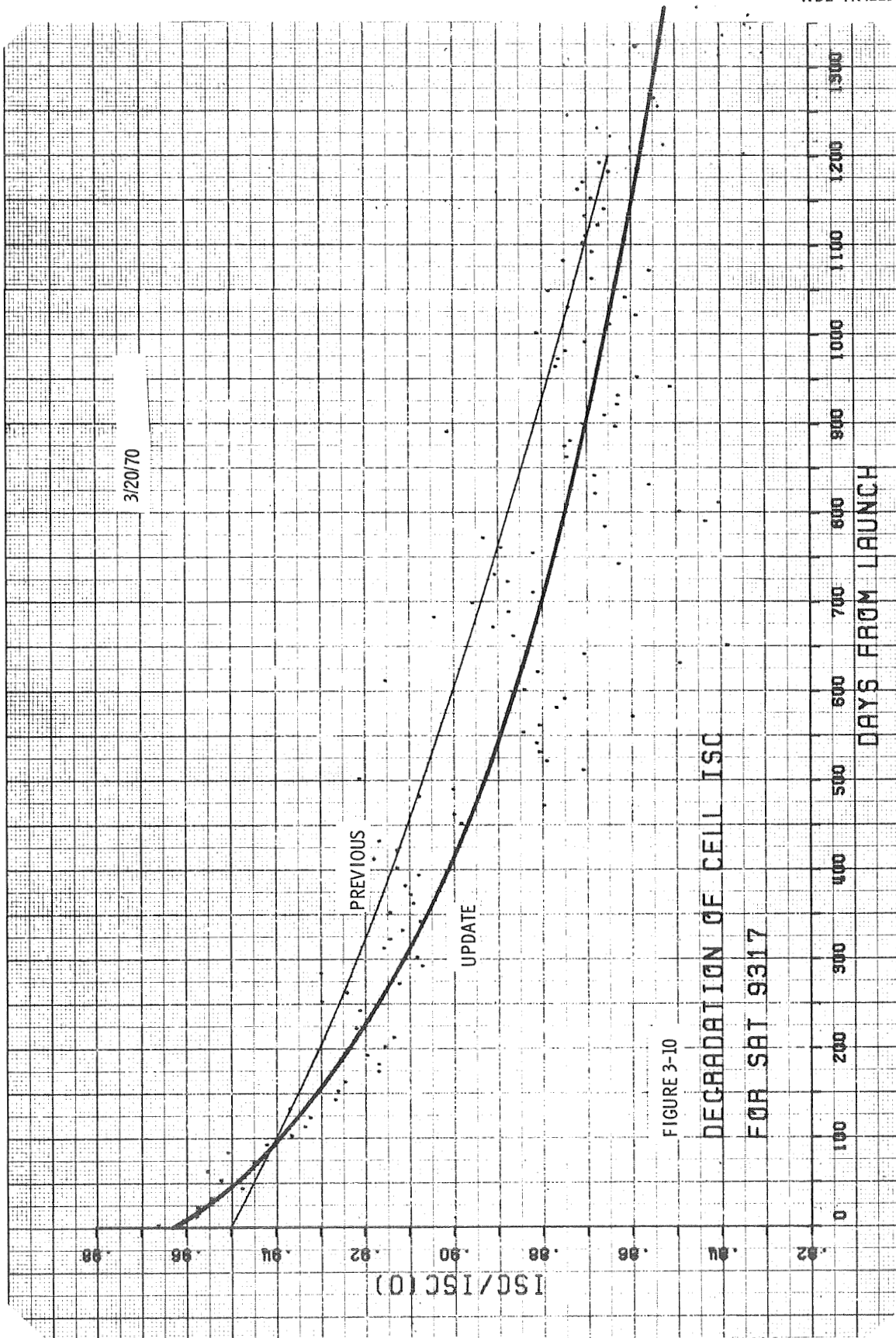


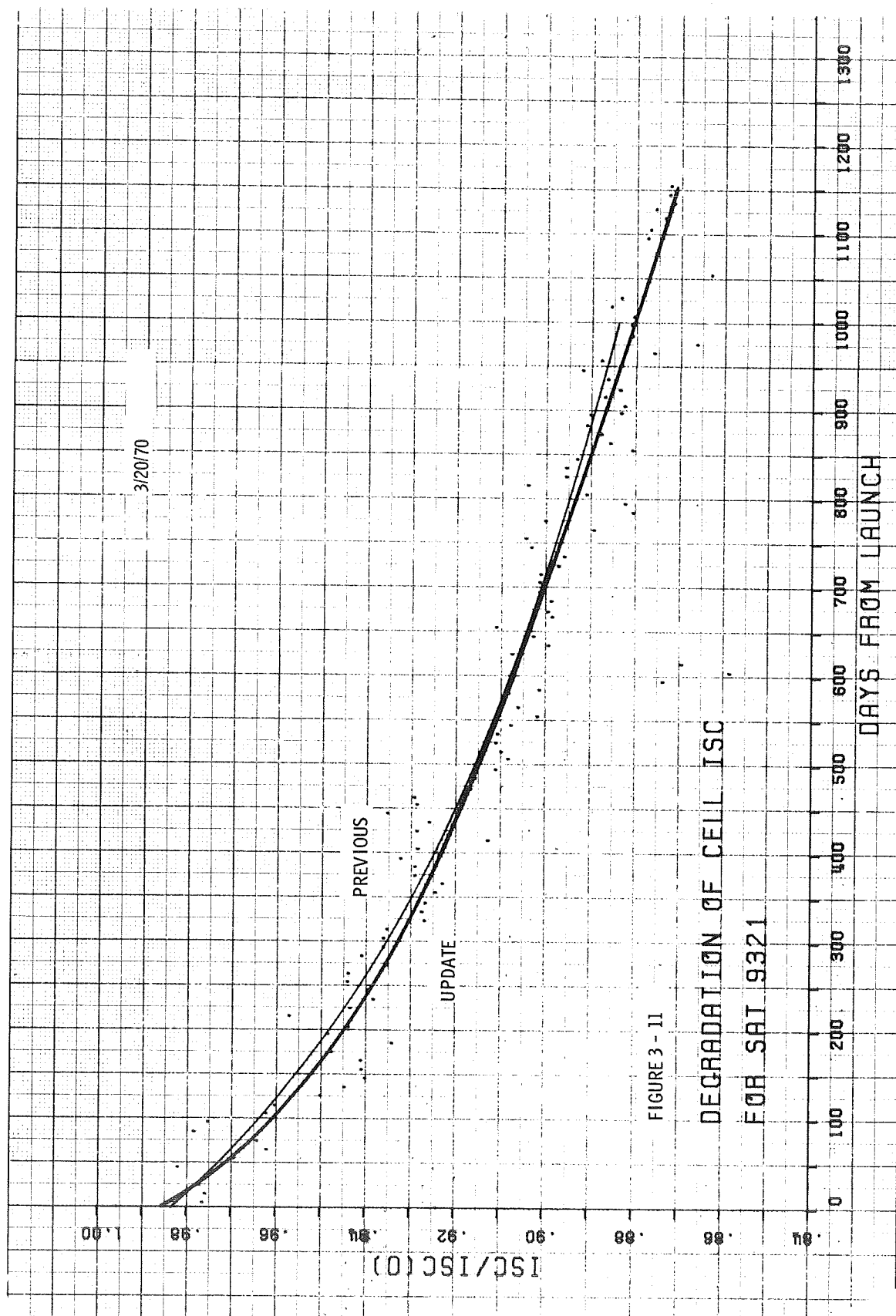


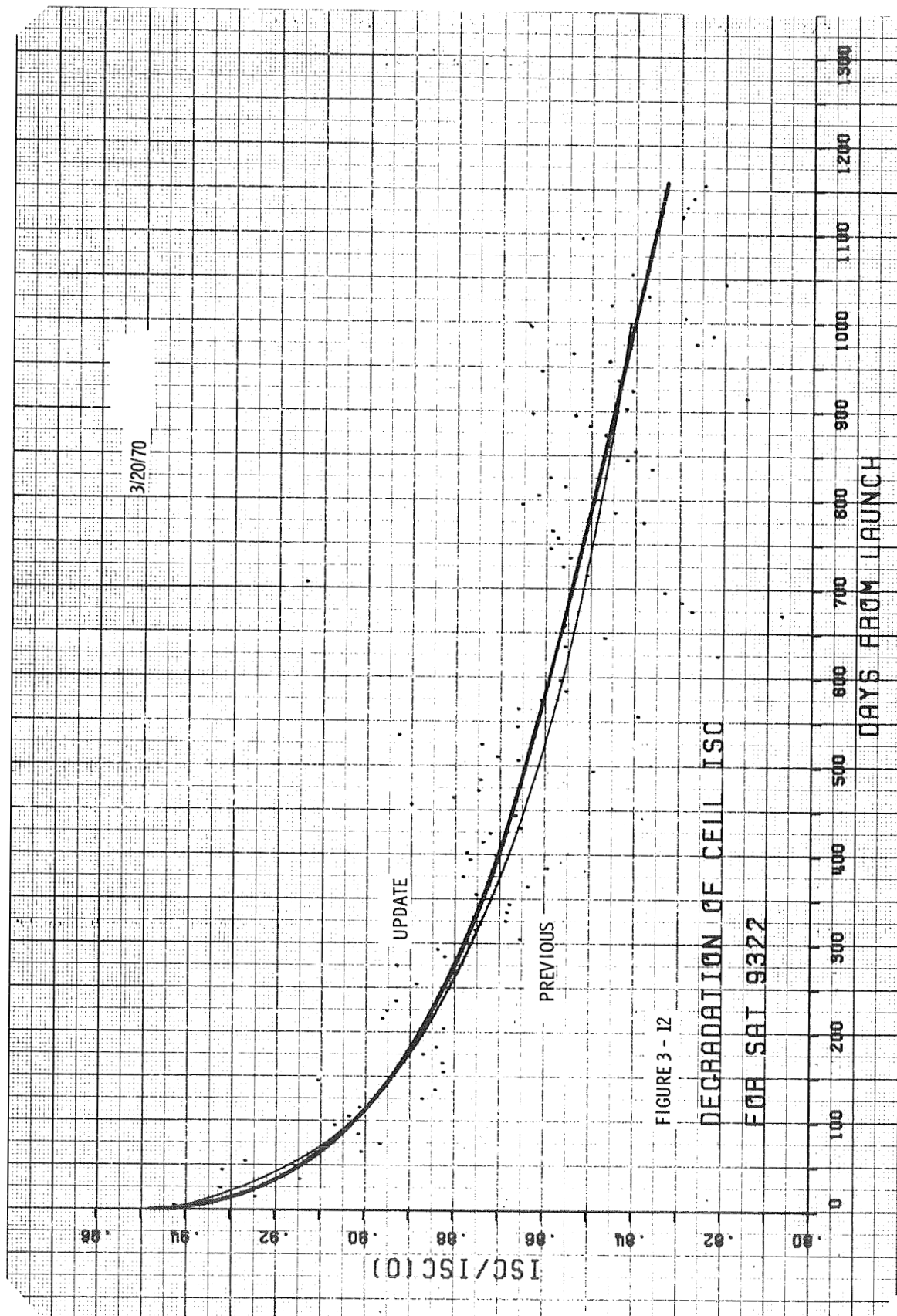


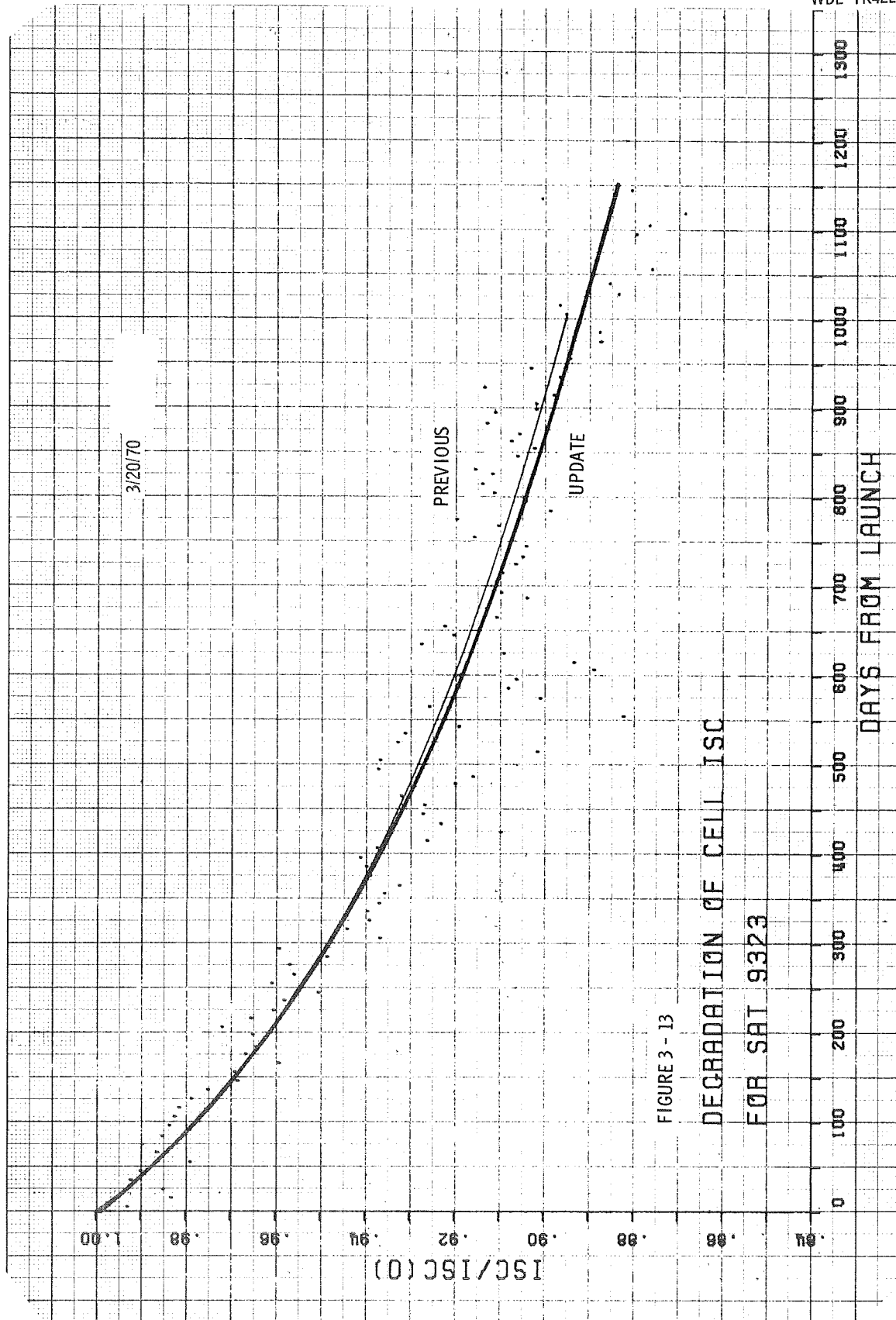


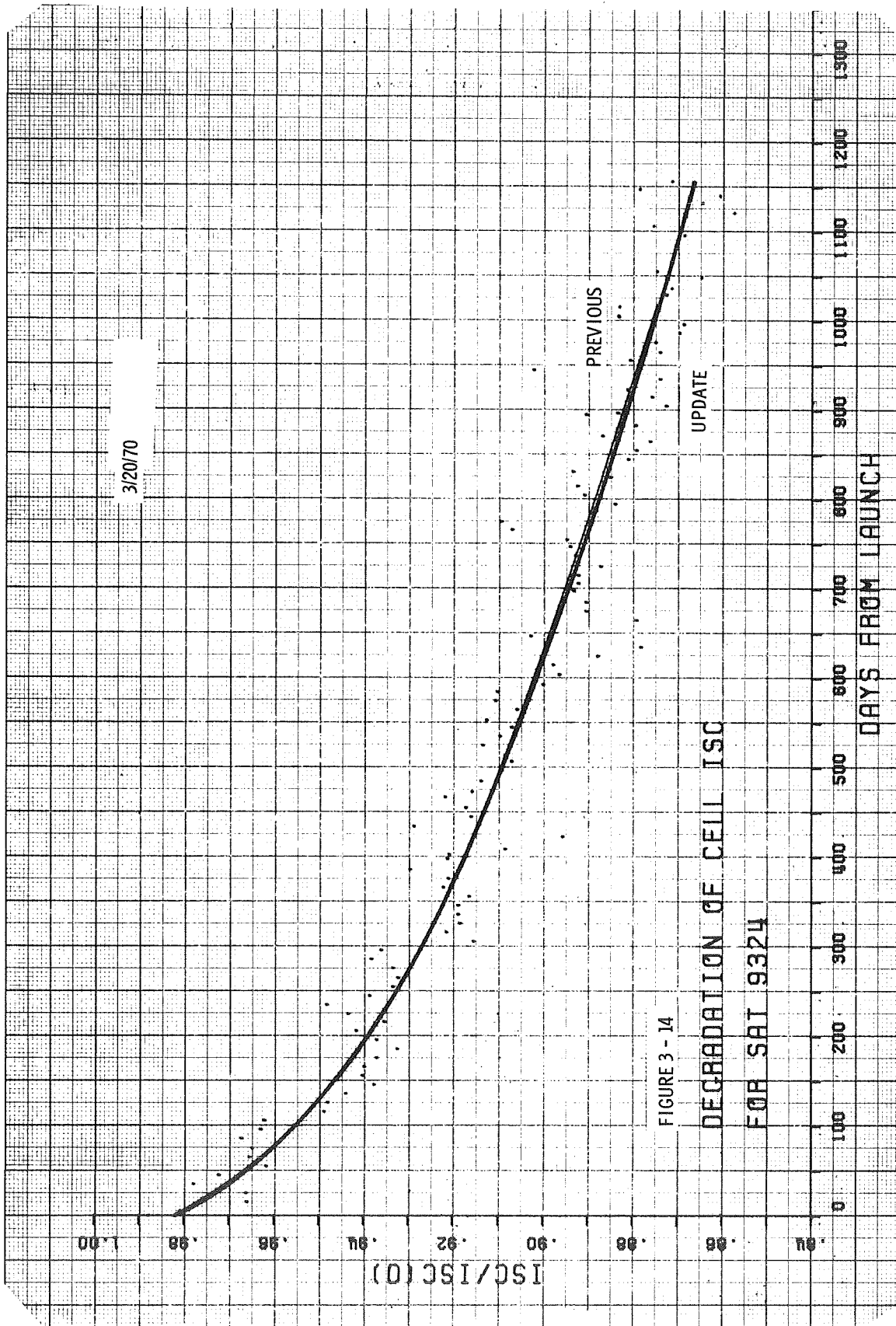


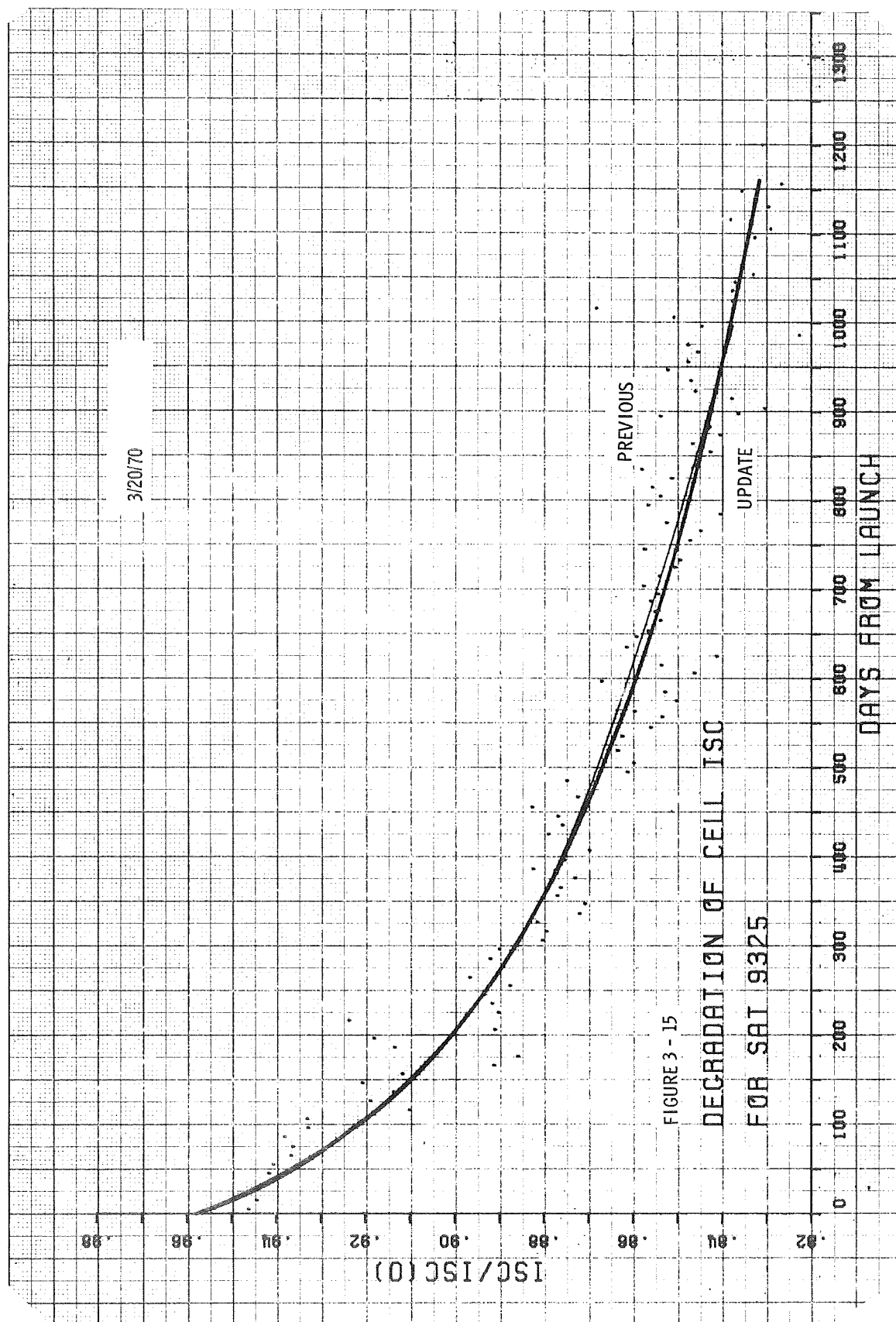


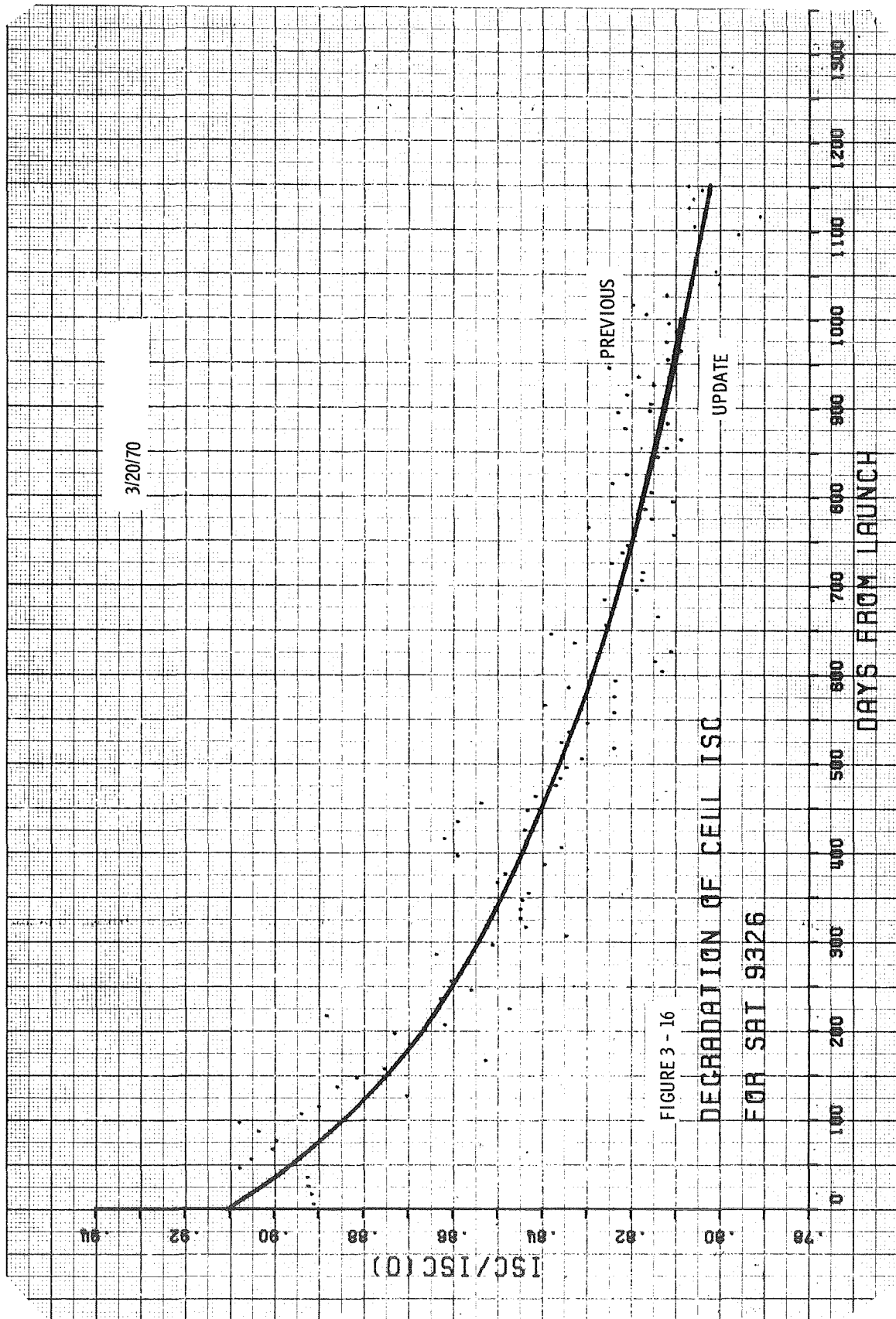


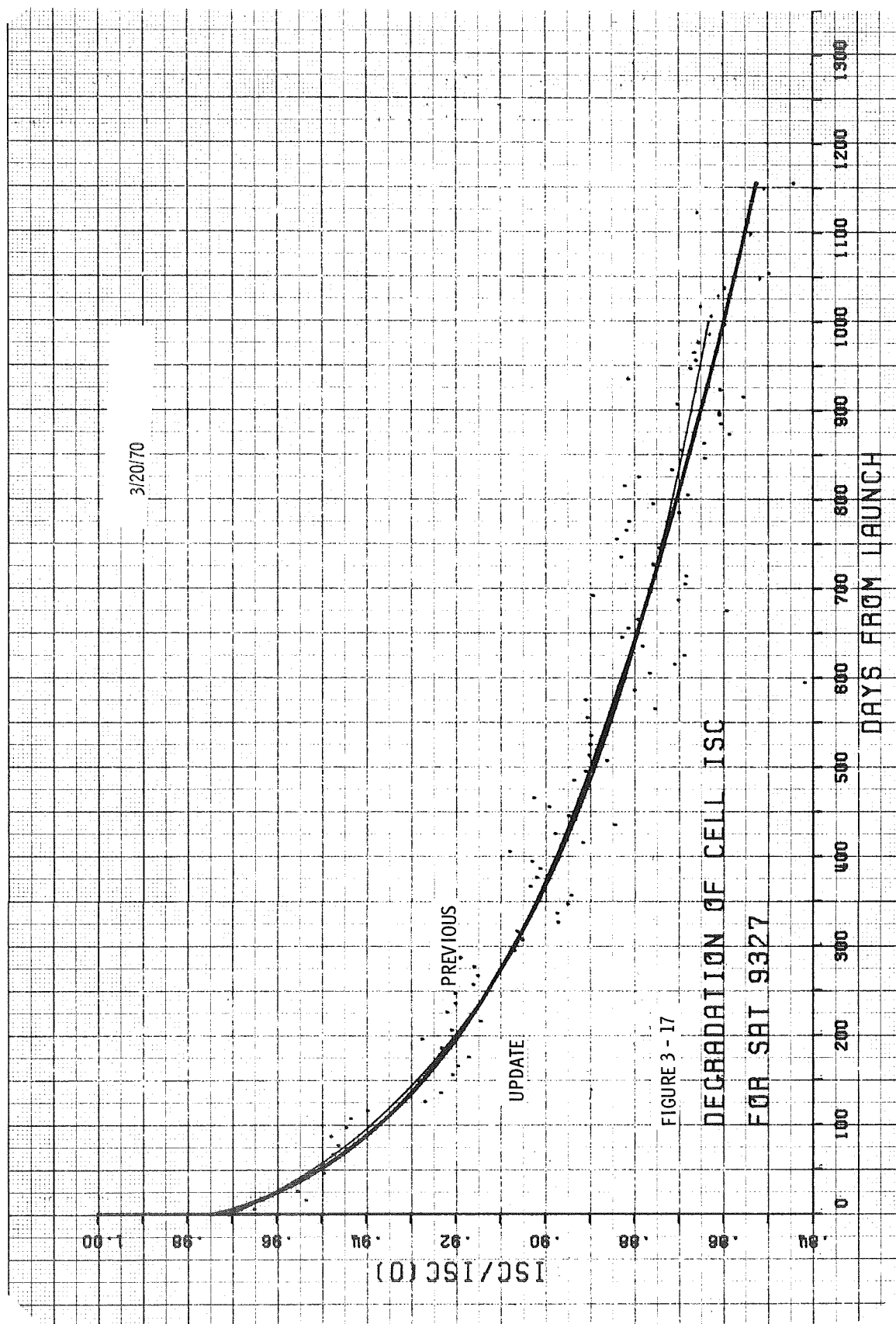


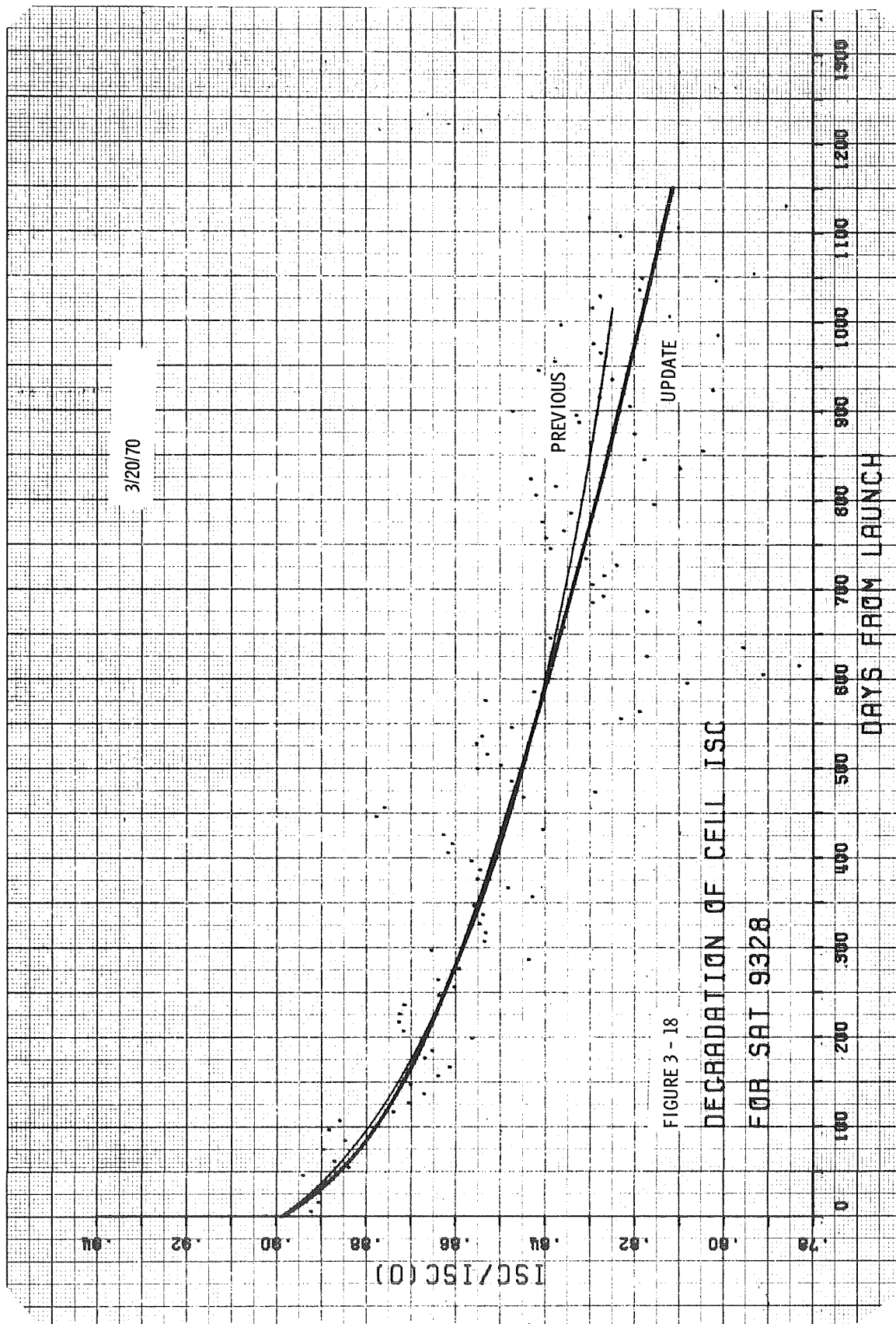


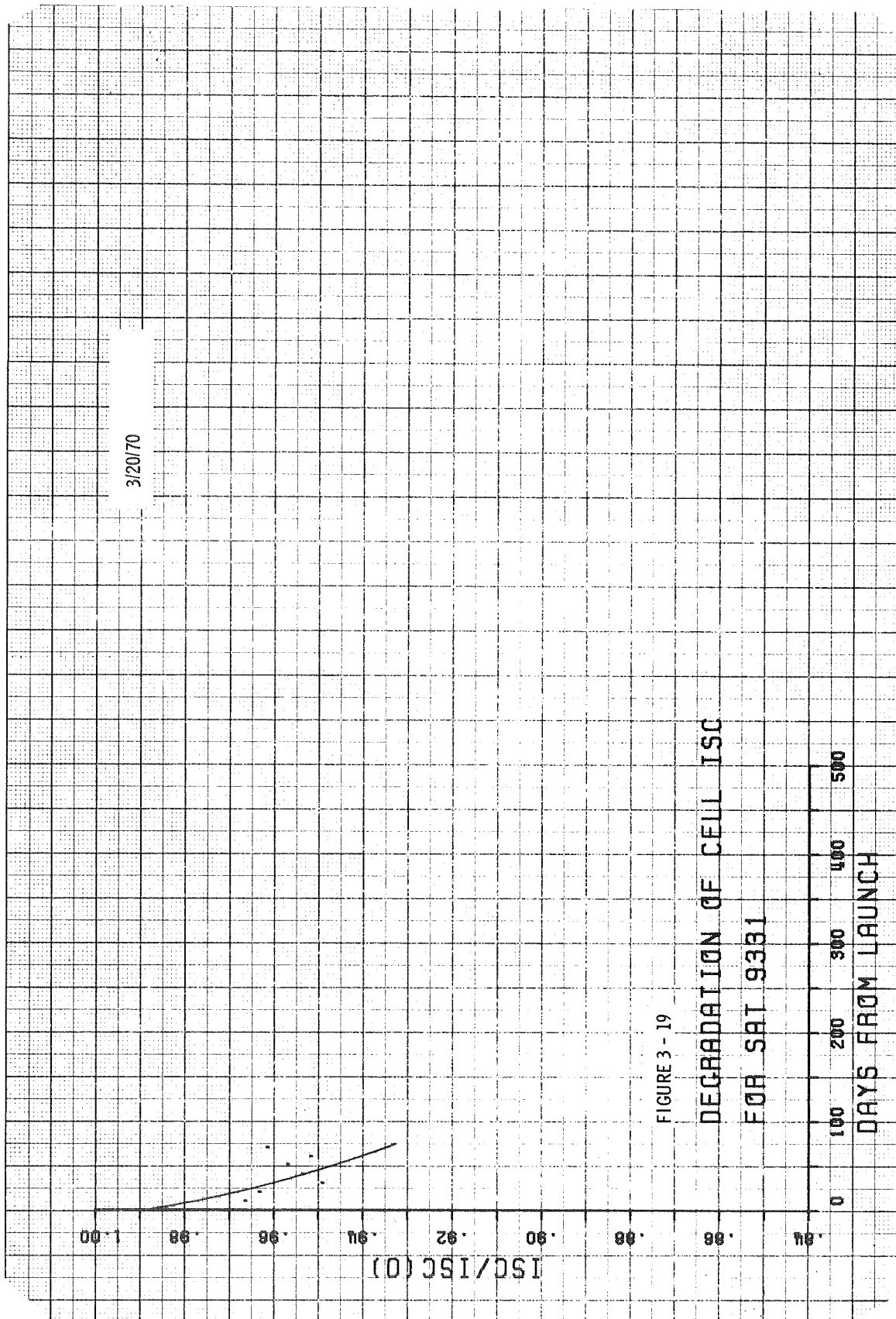


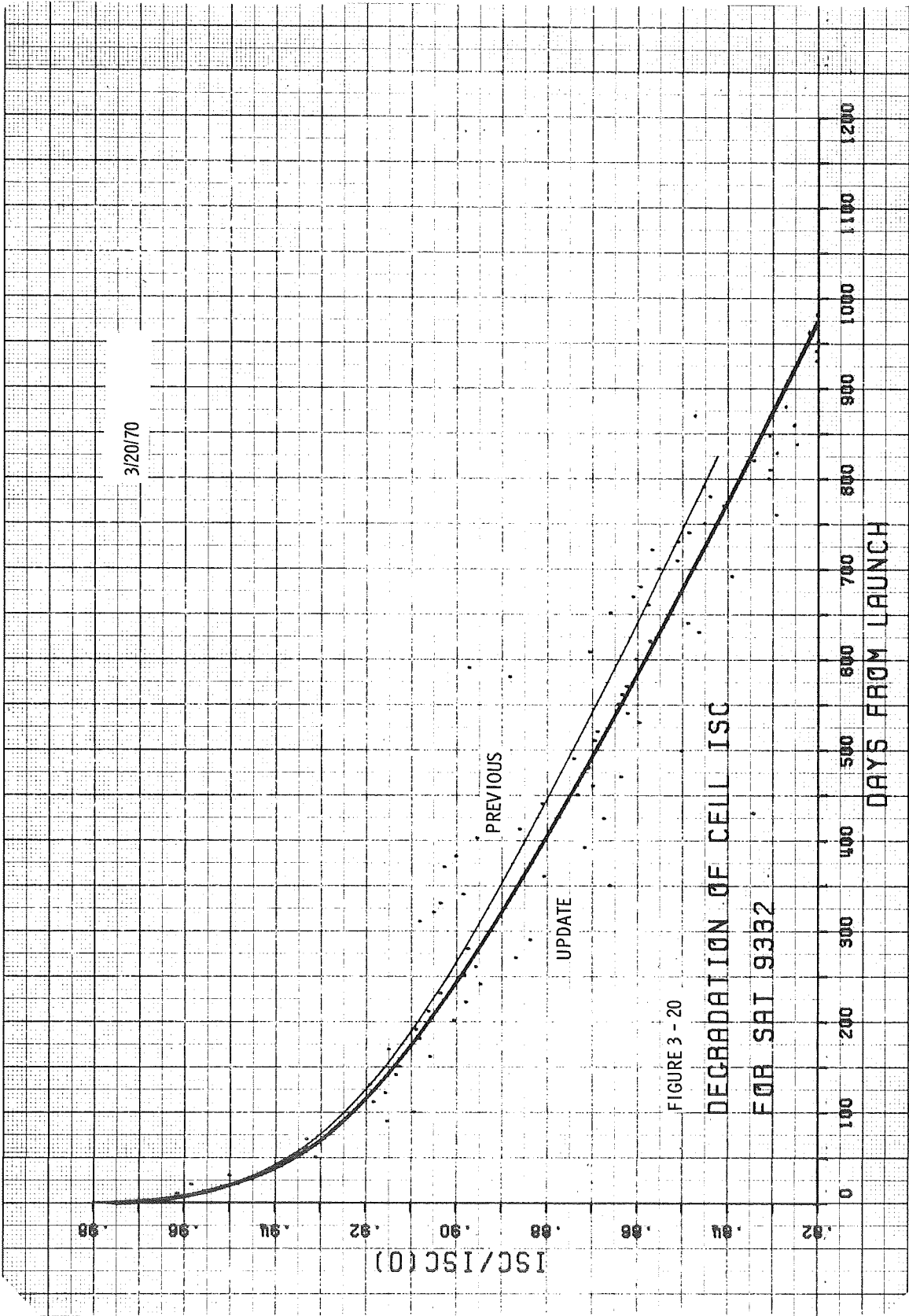


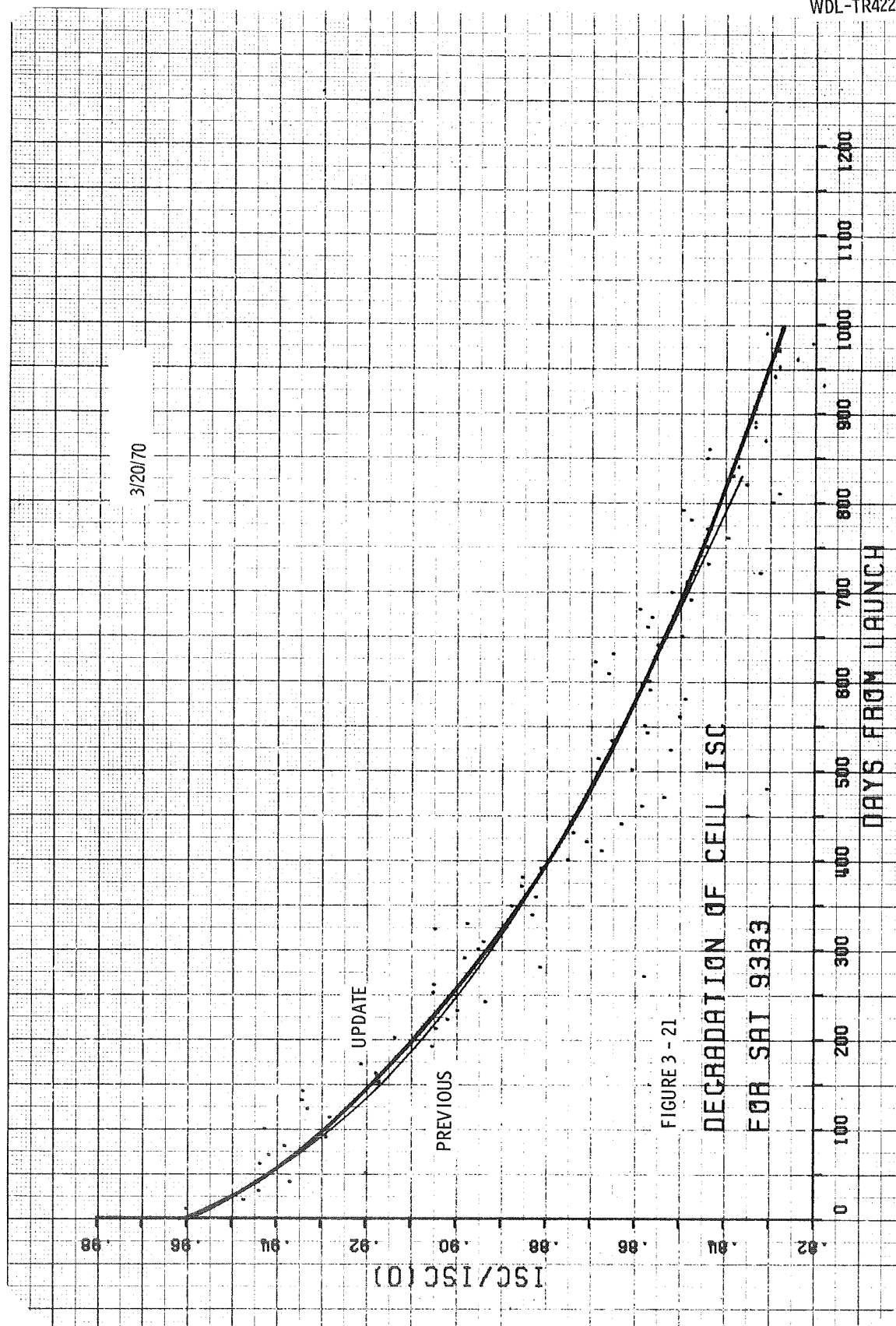


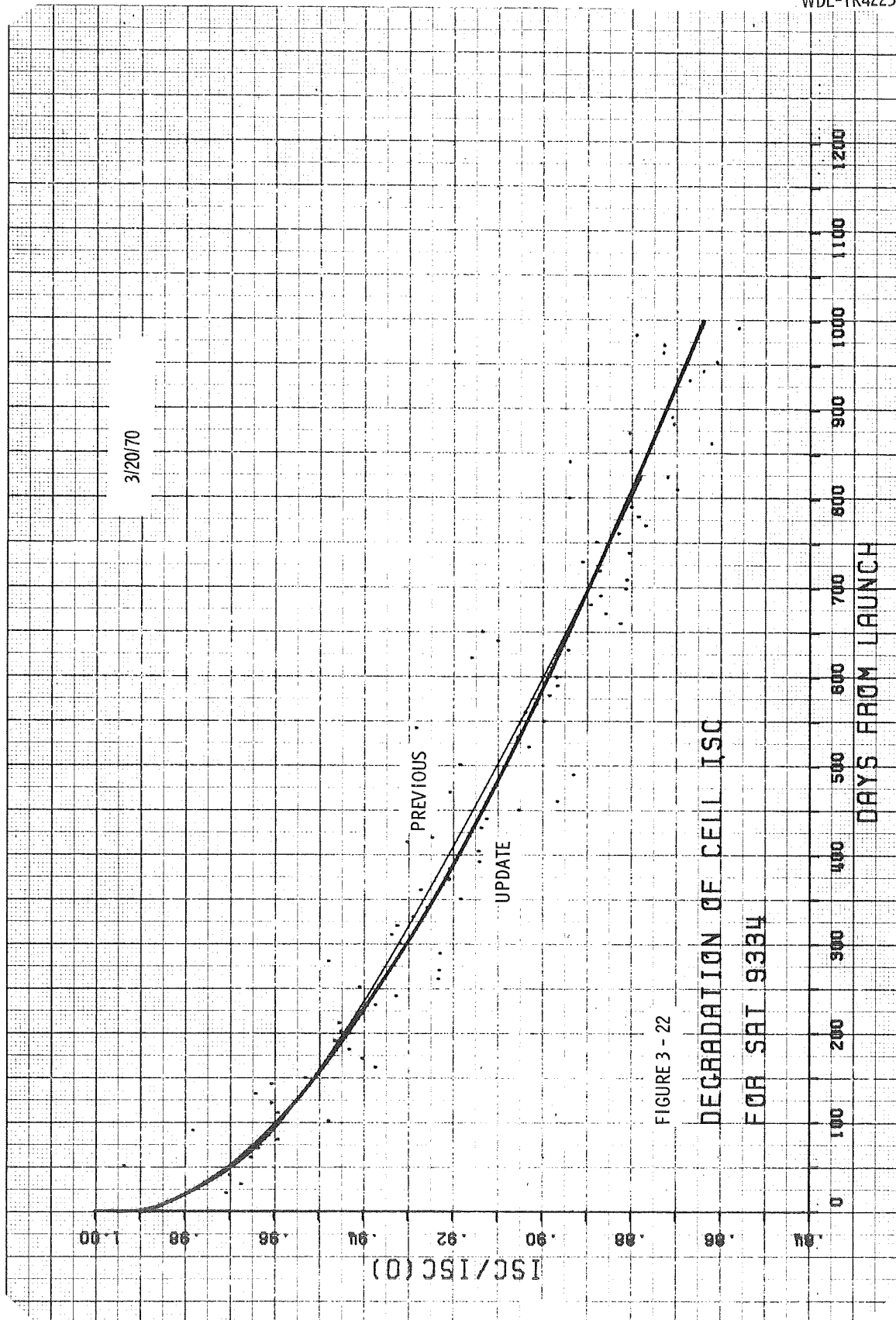












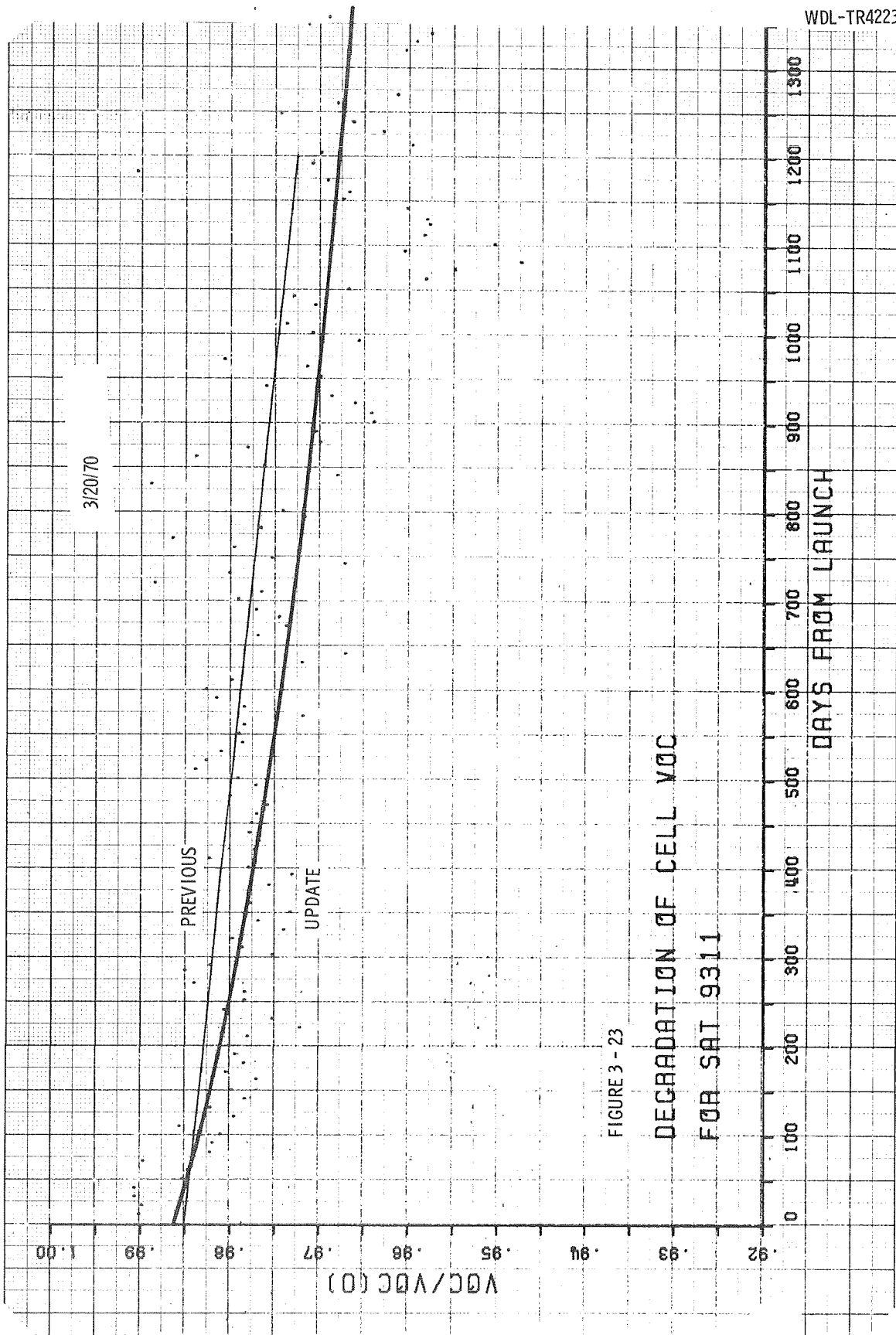
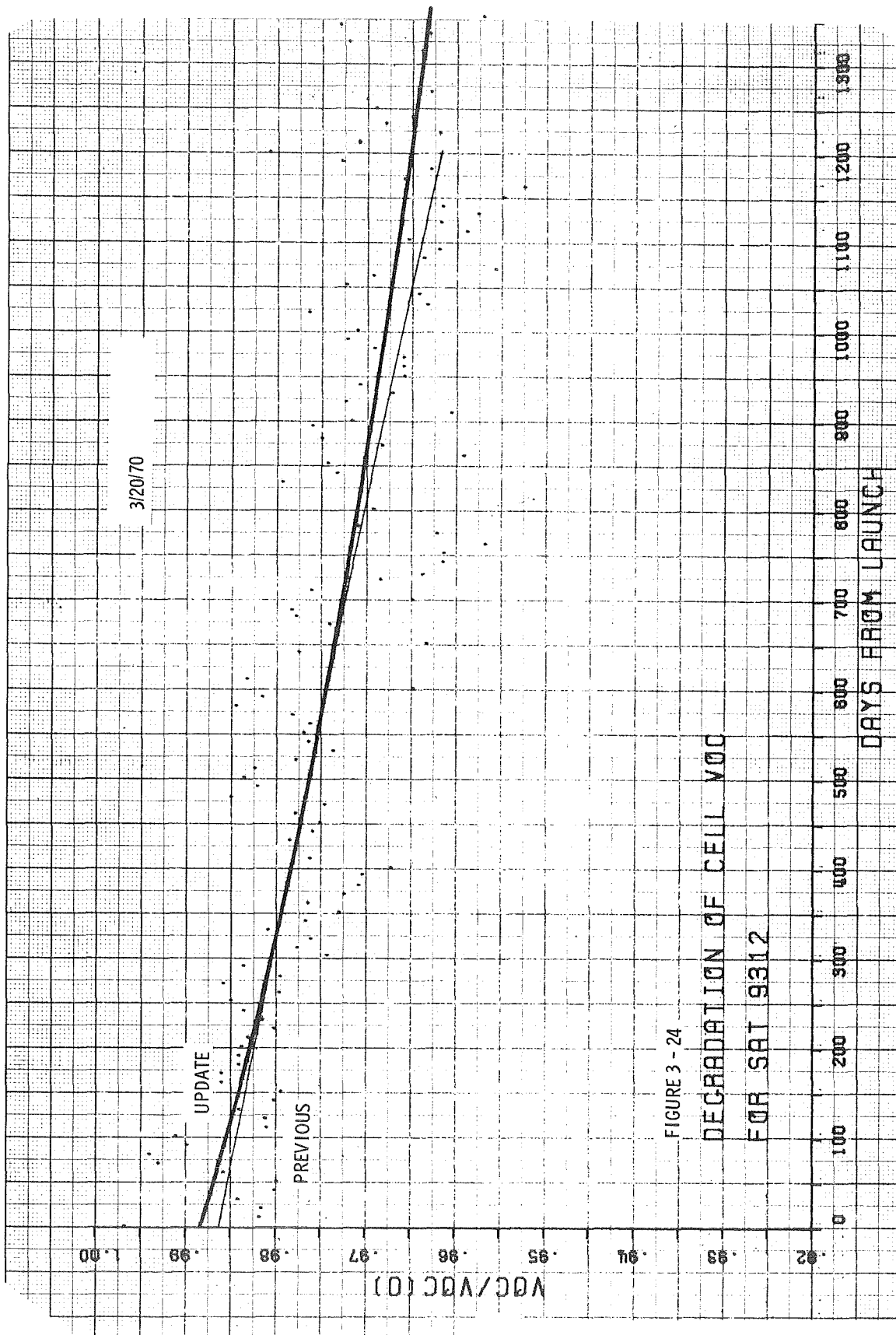
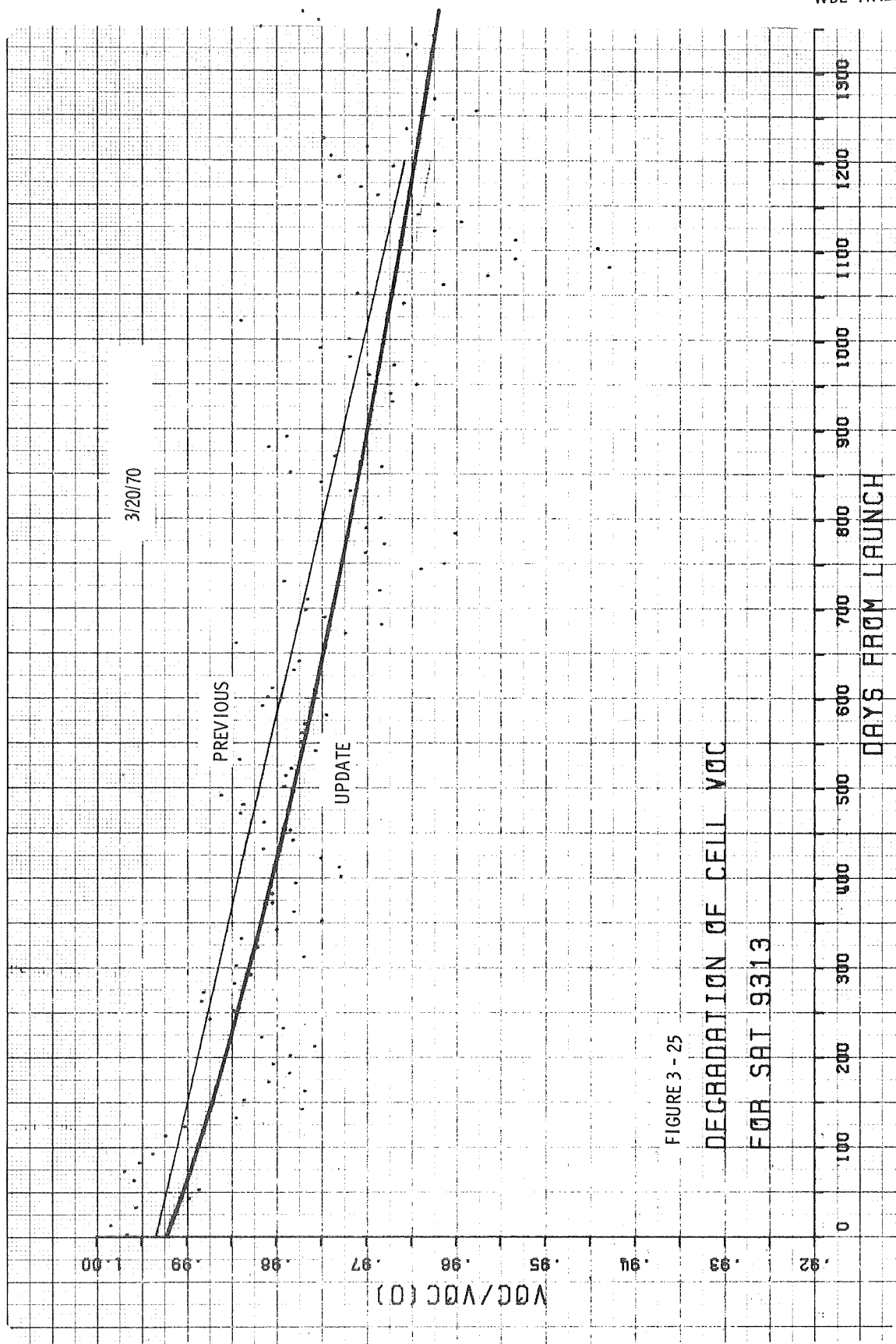


FIGURE 3 - 23

DEGRADATION OF CELL VOC
FOR SAT 9311





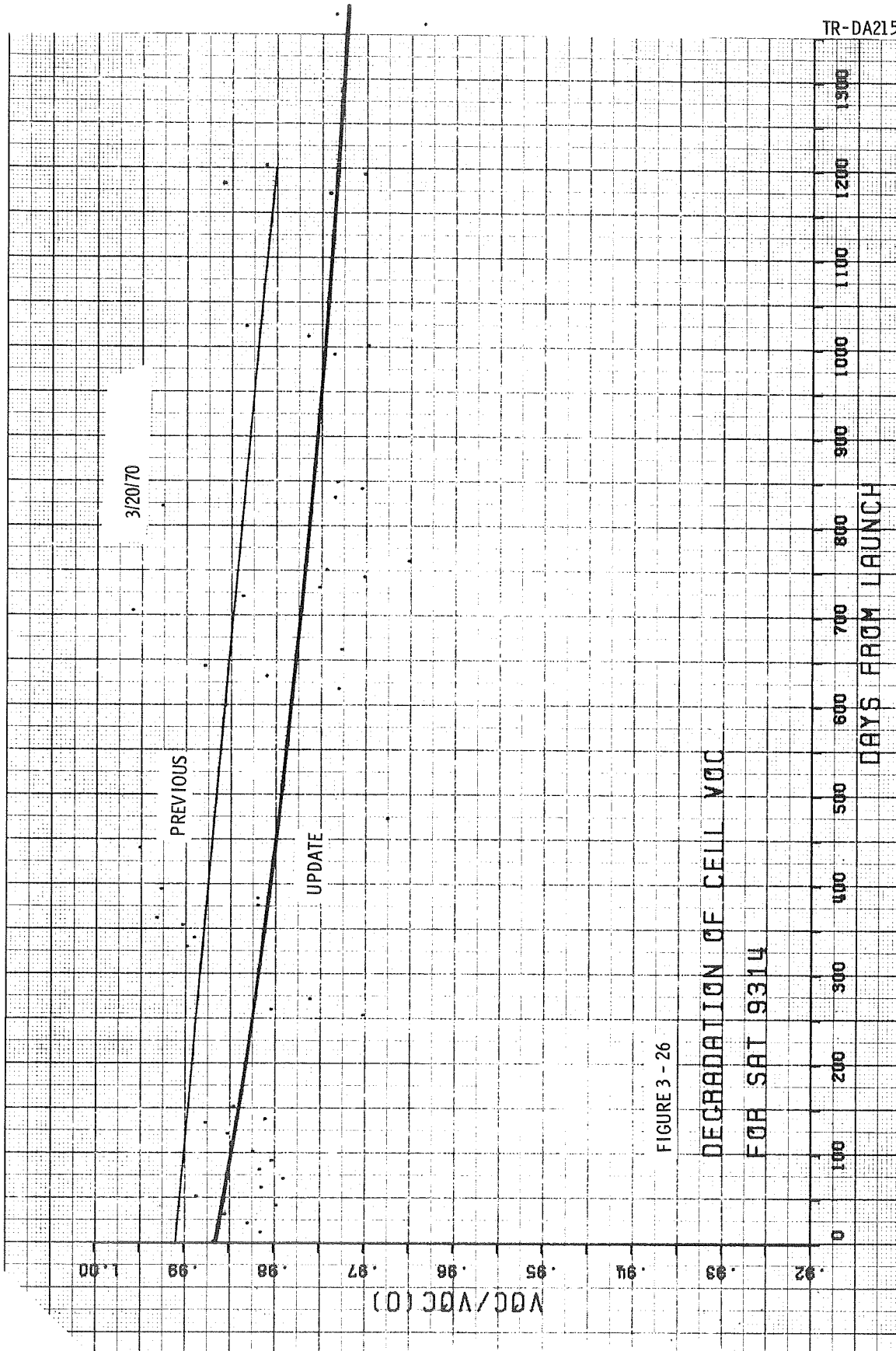
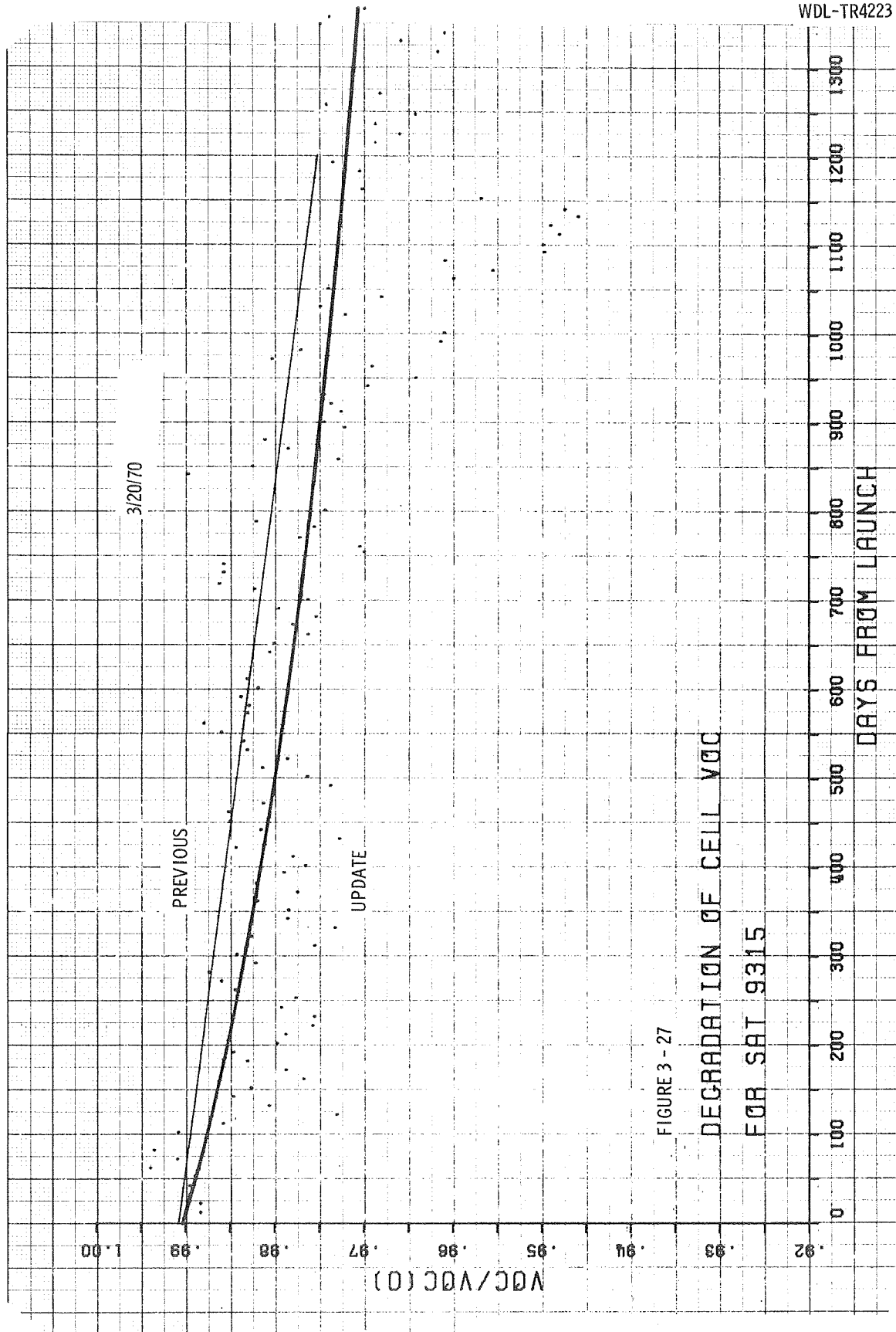
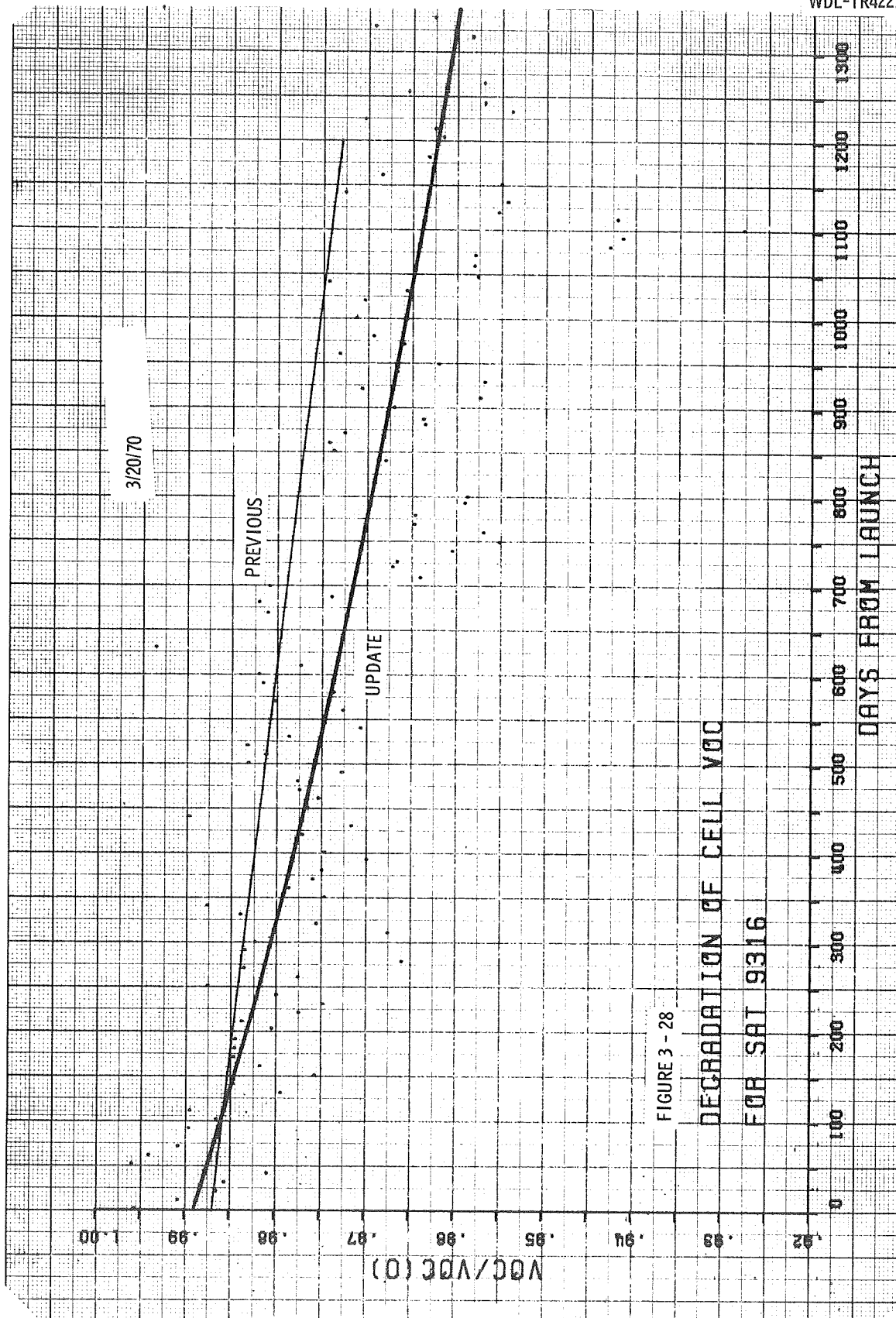
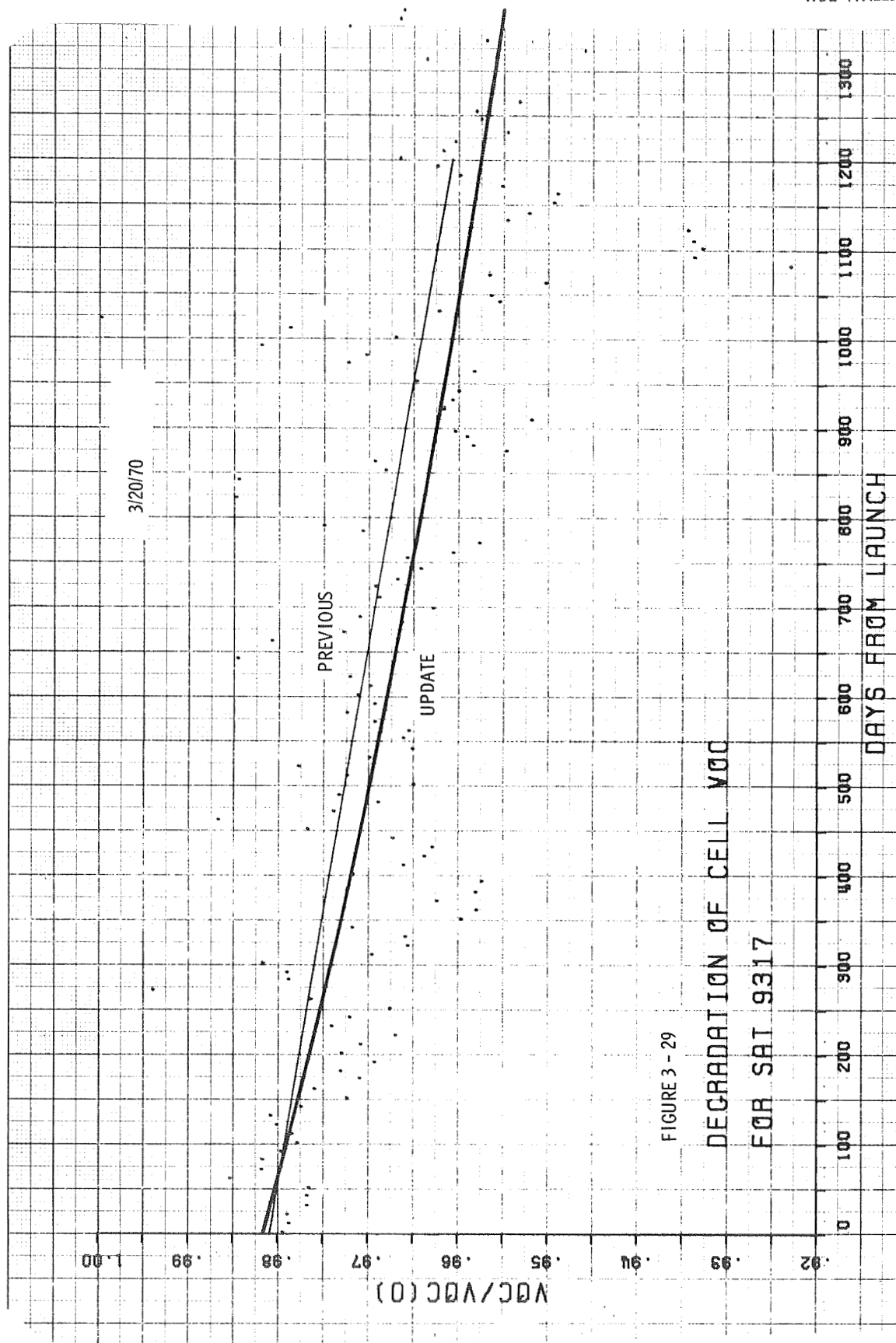
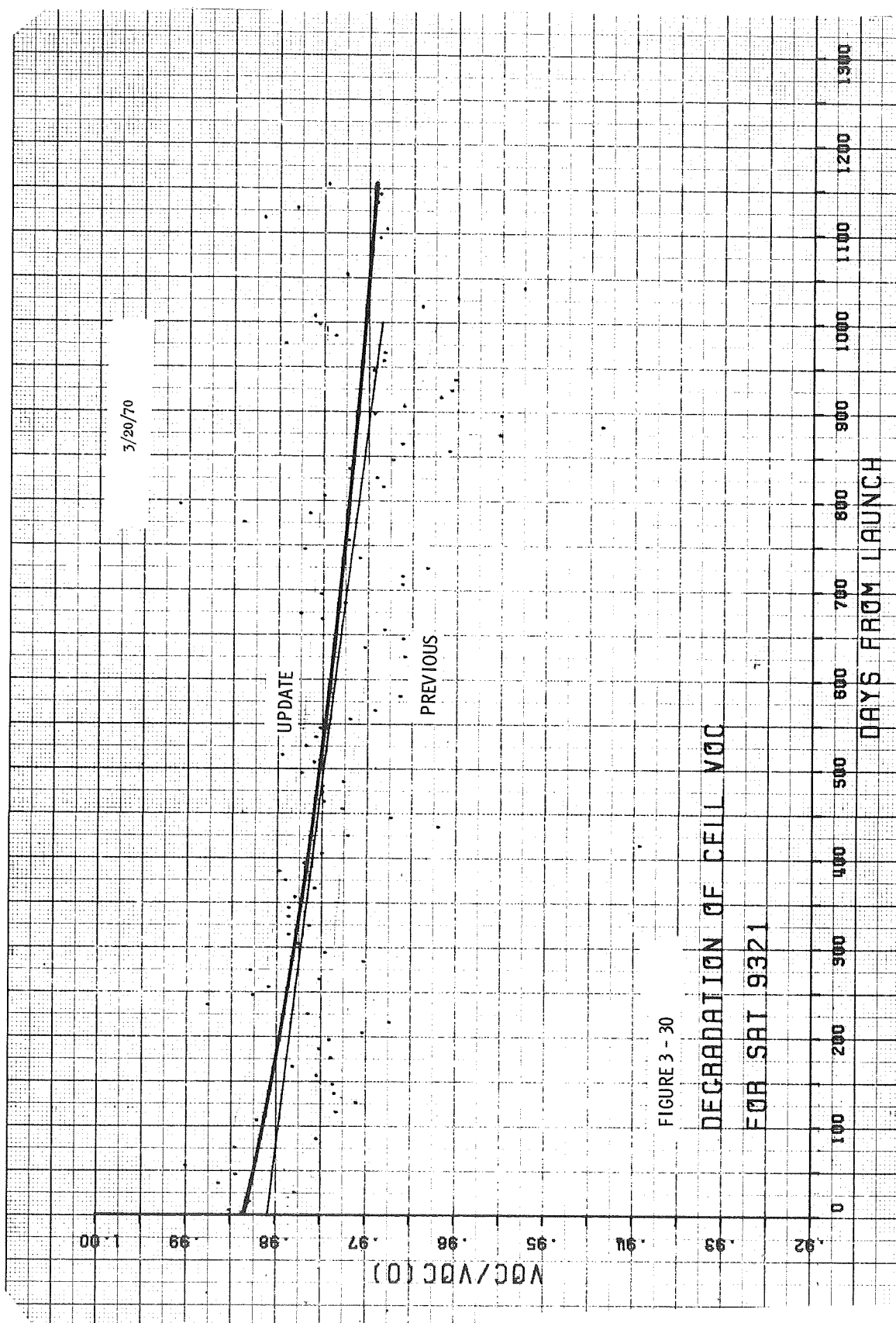


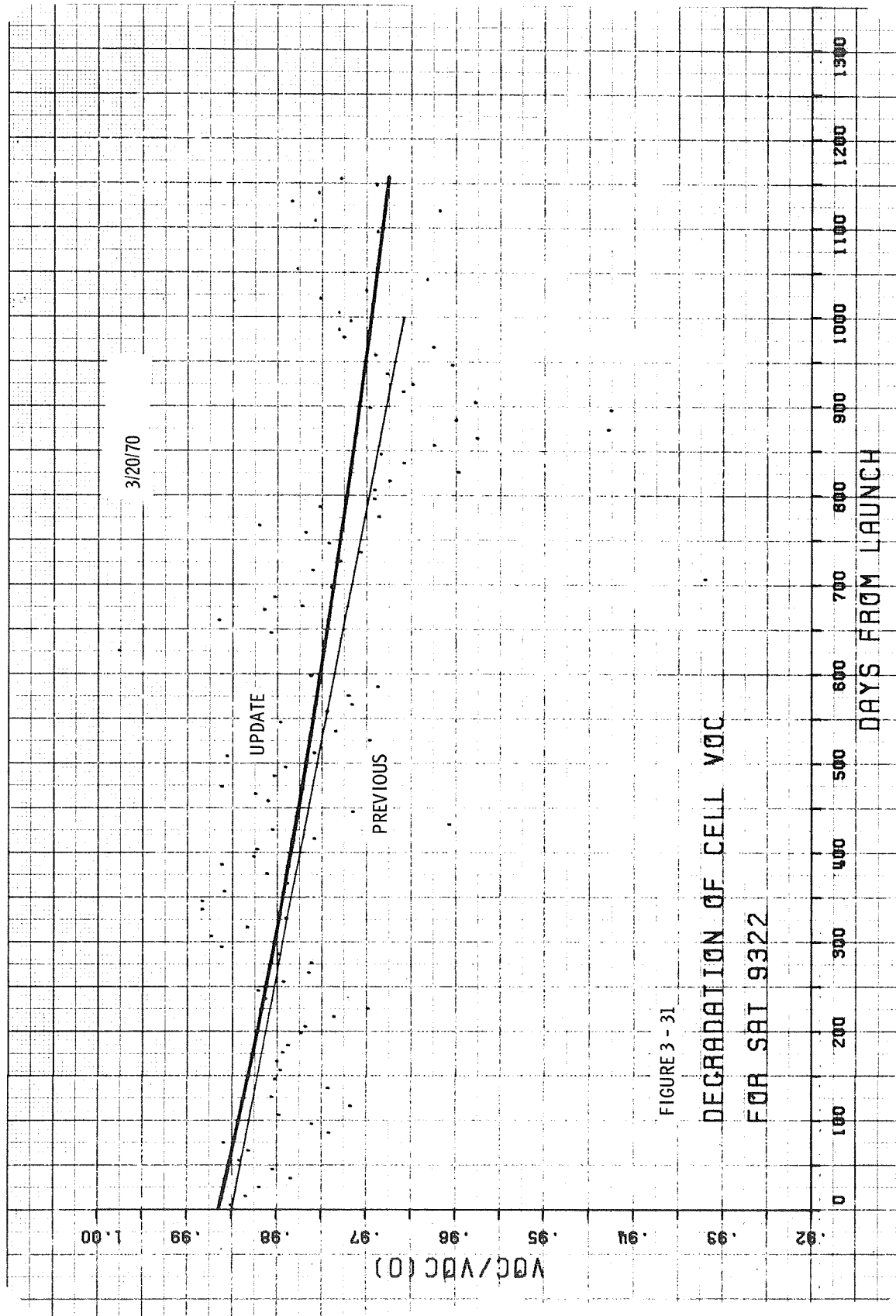
FIGURE 3 - 26

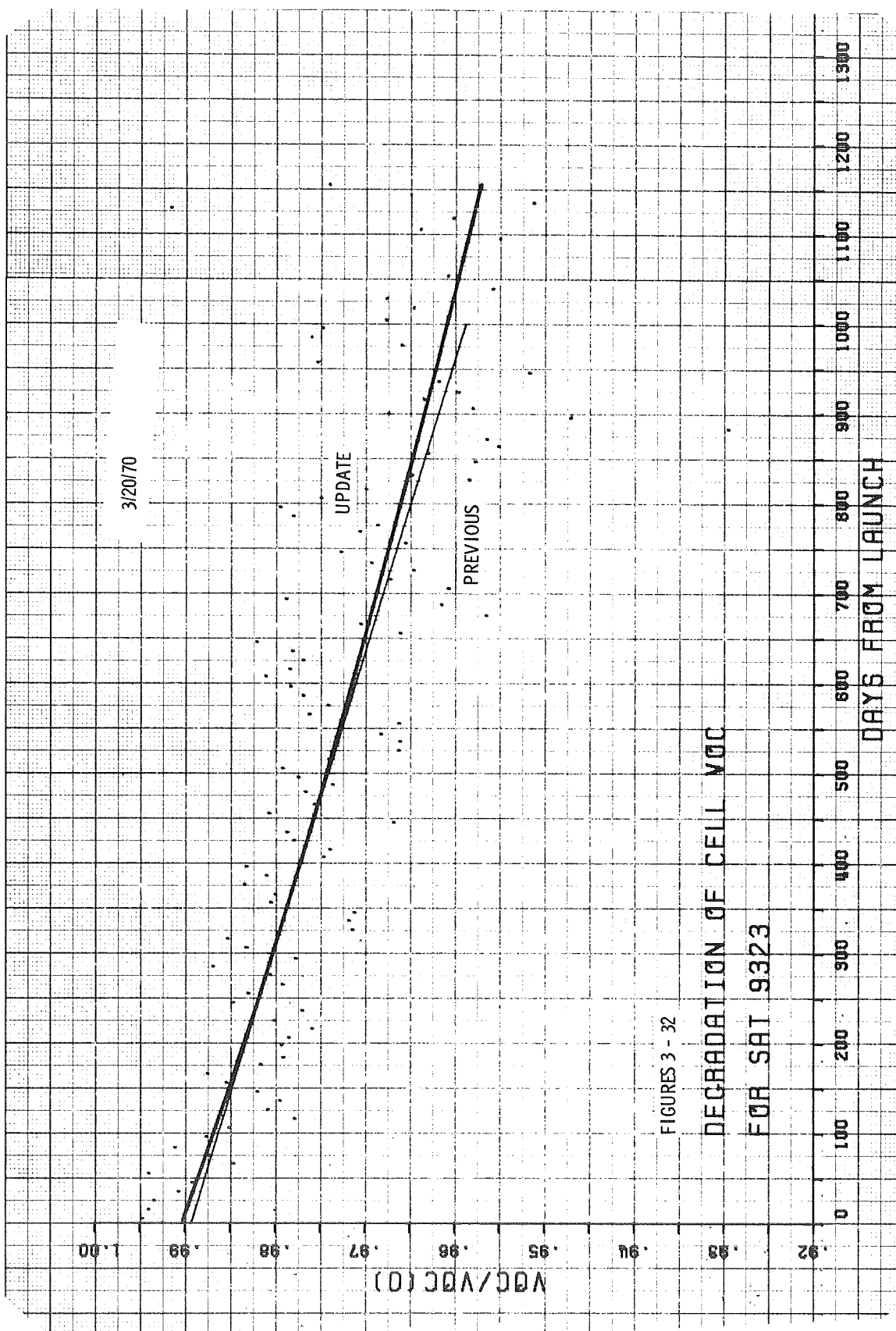


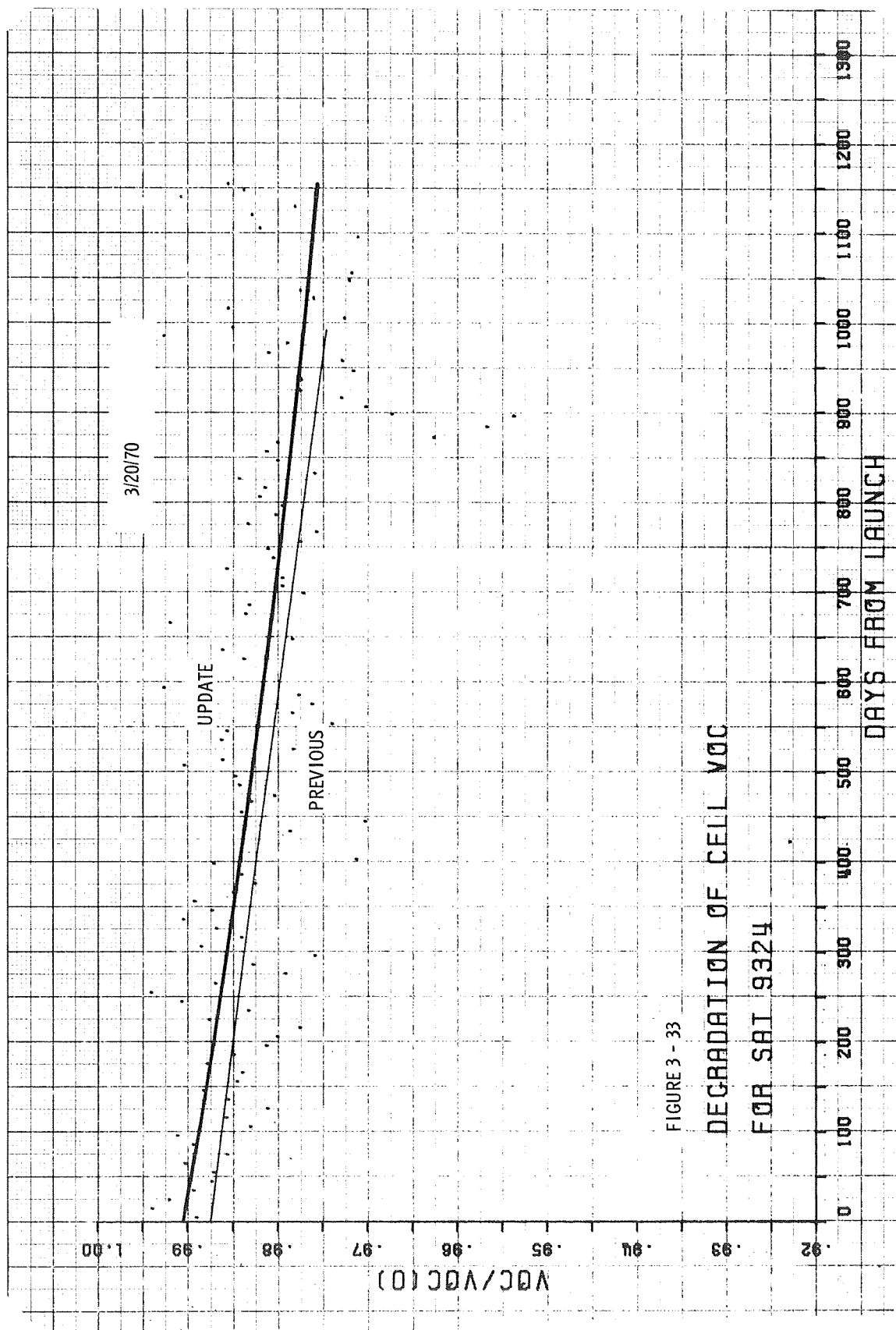












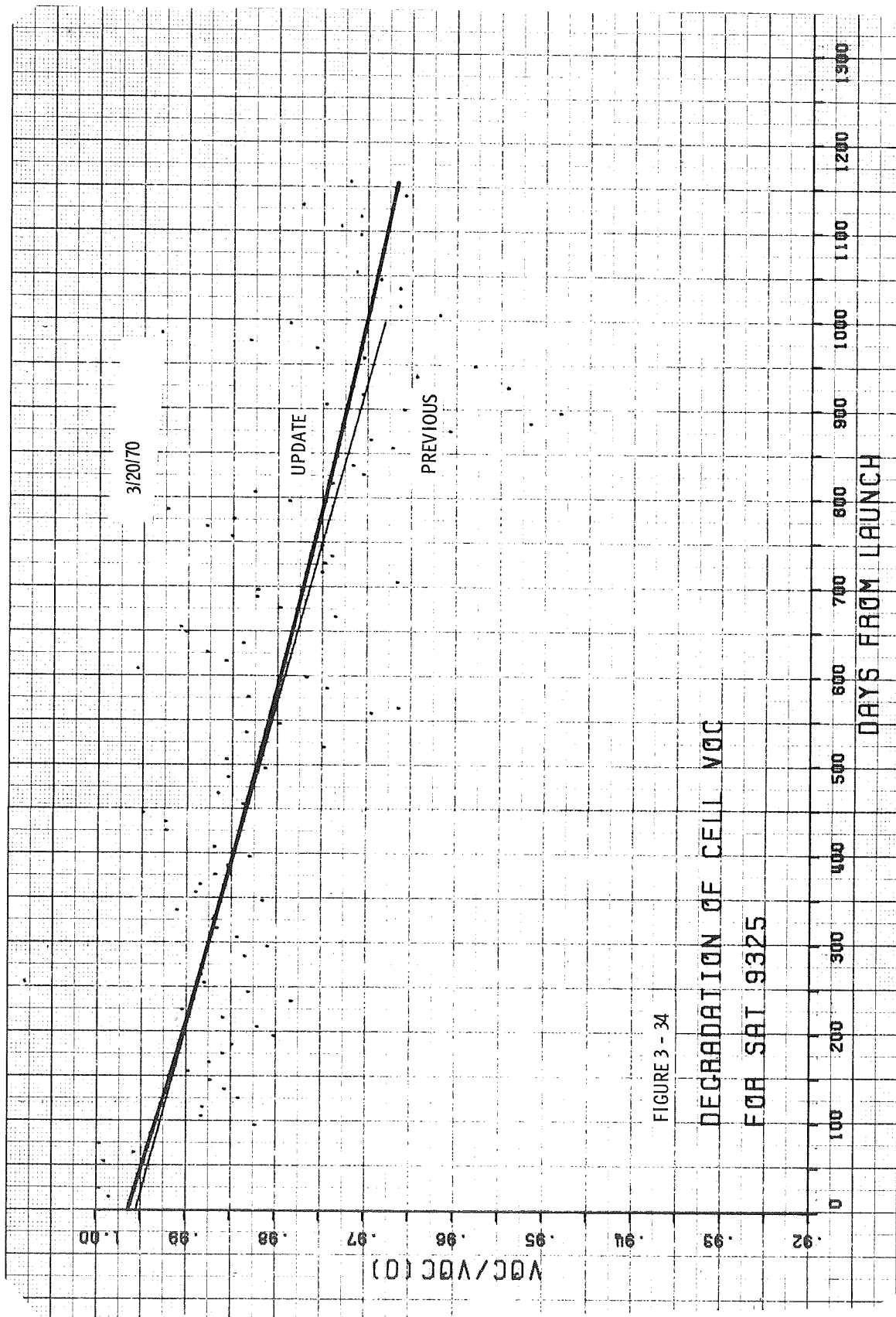
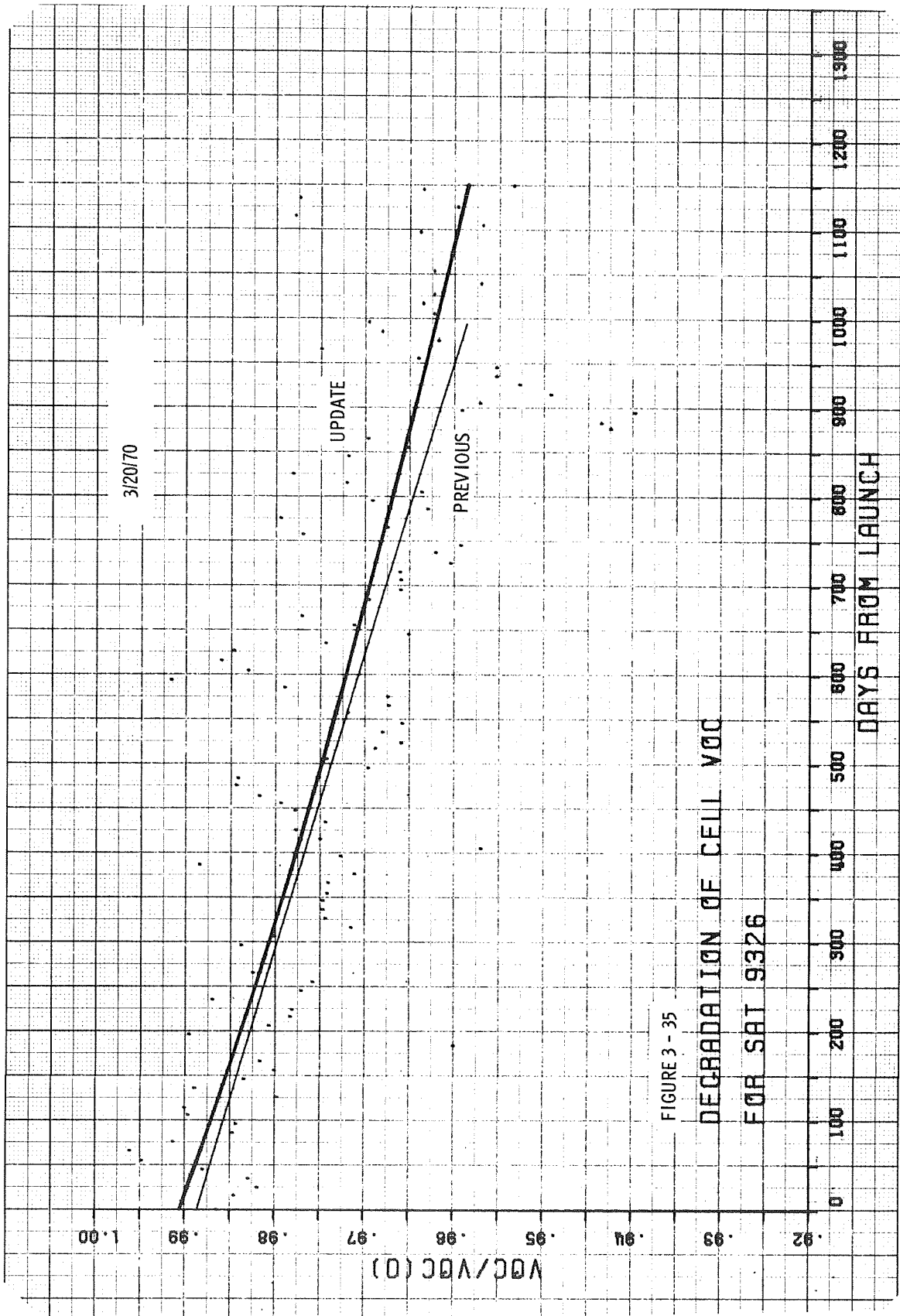
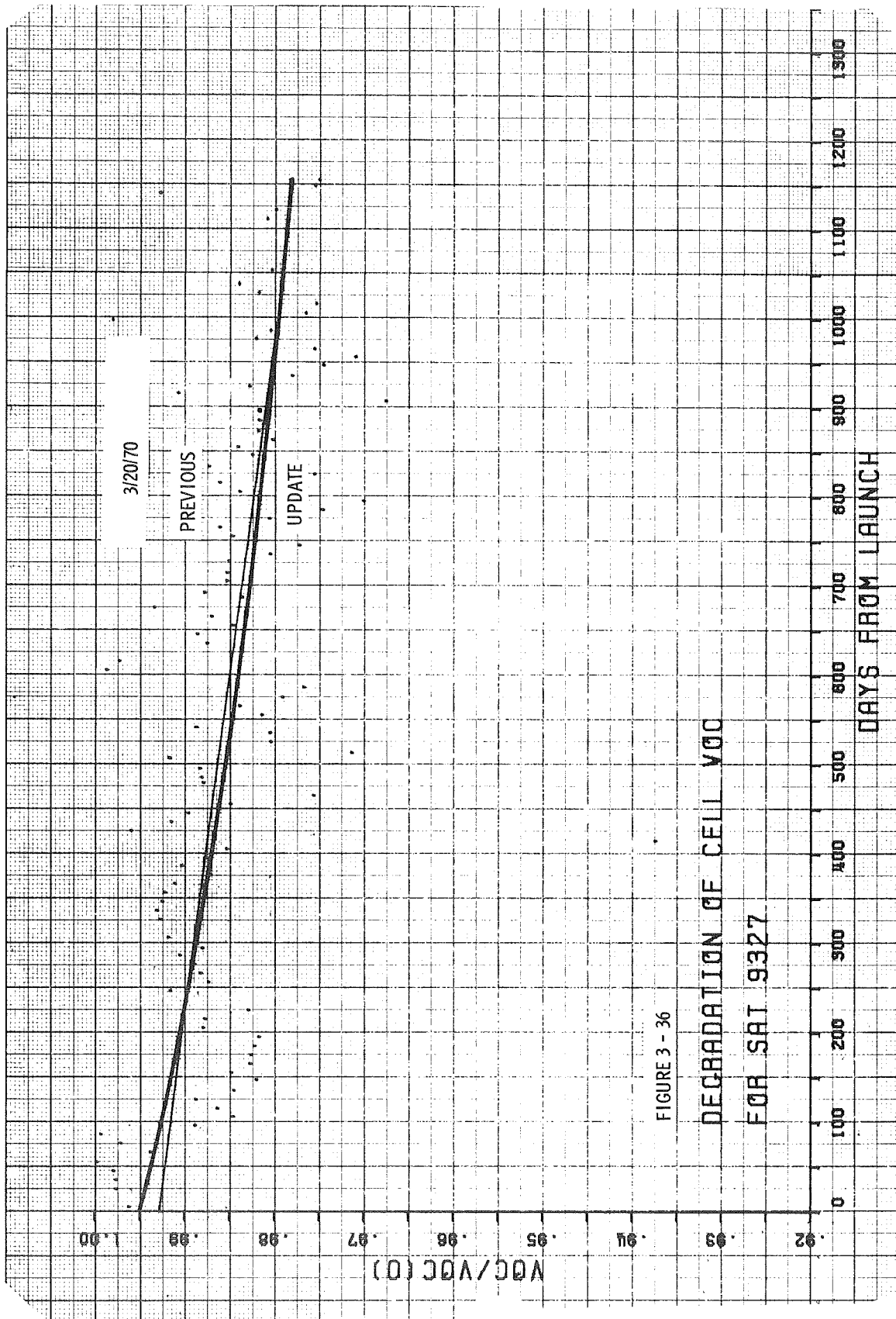


FIGURE 3 - 34





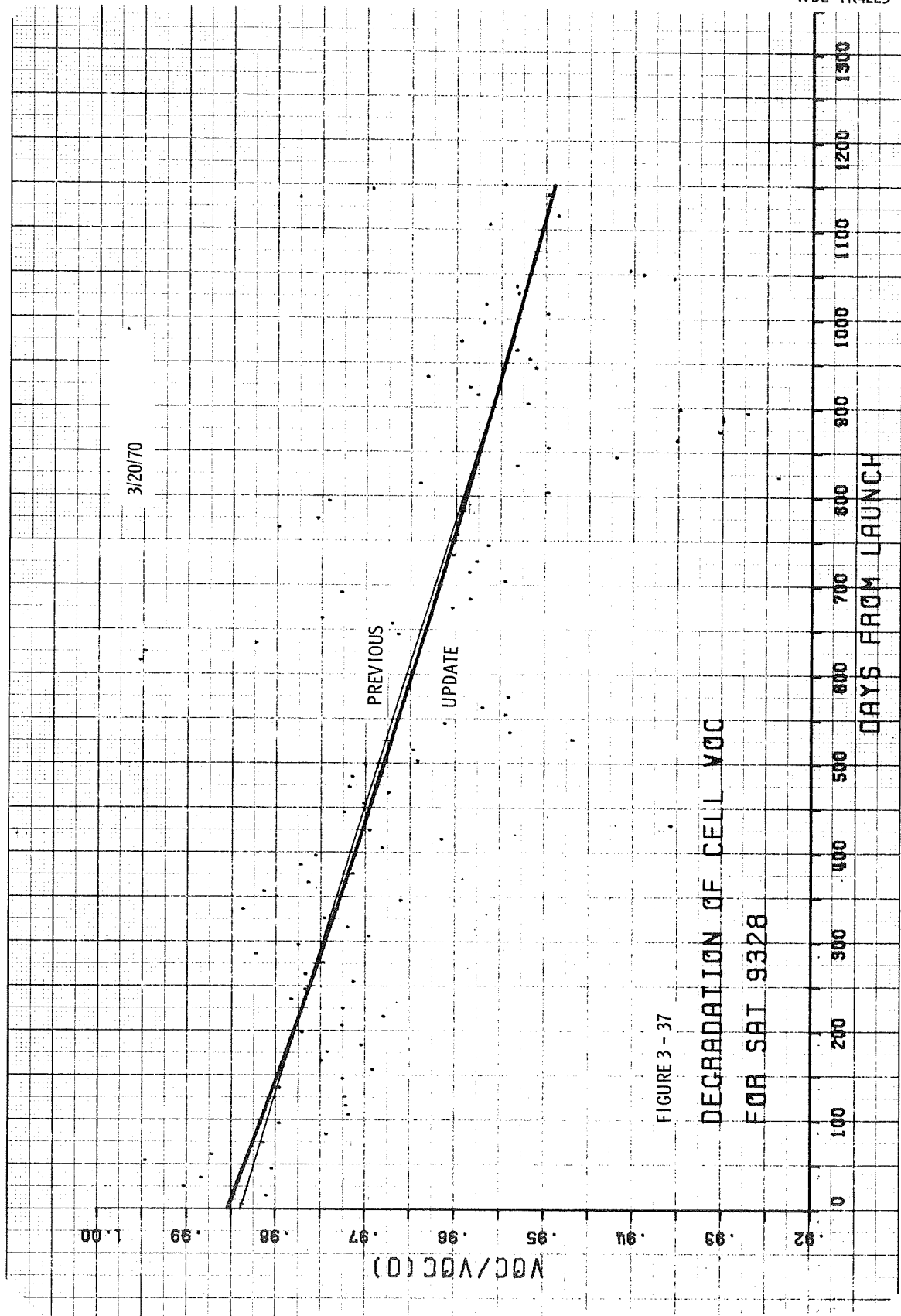
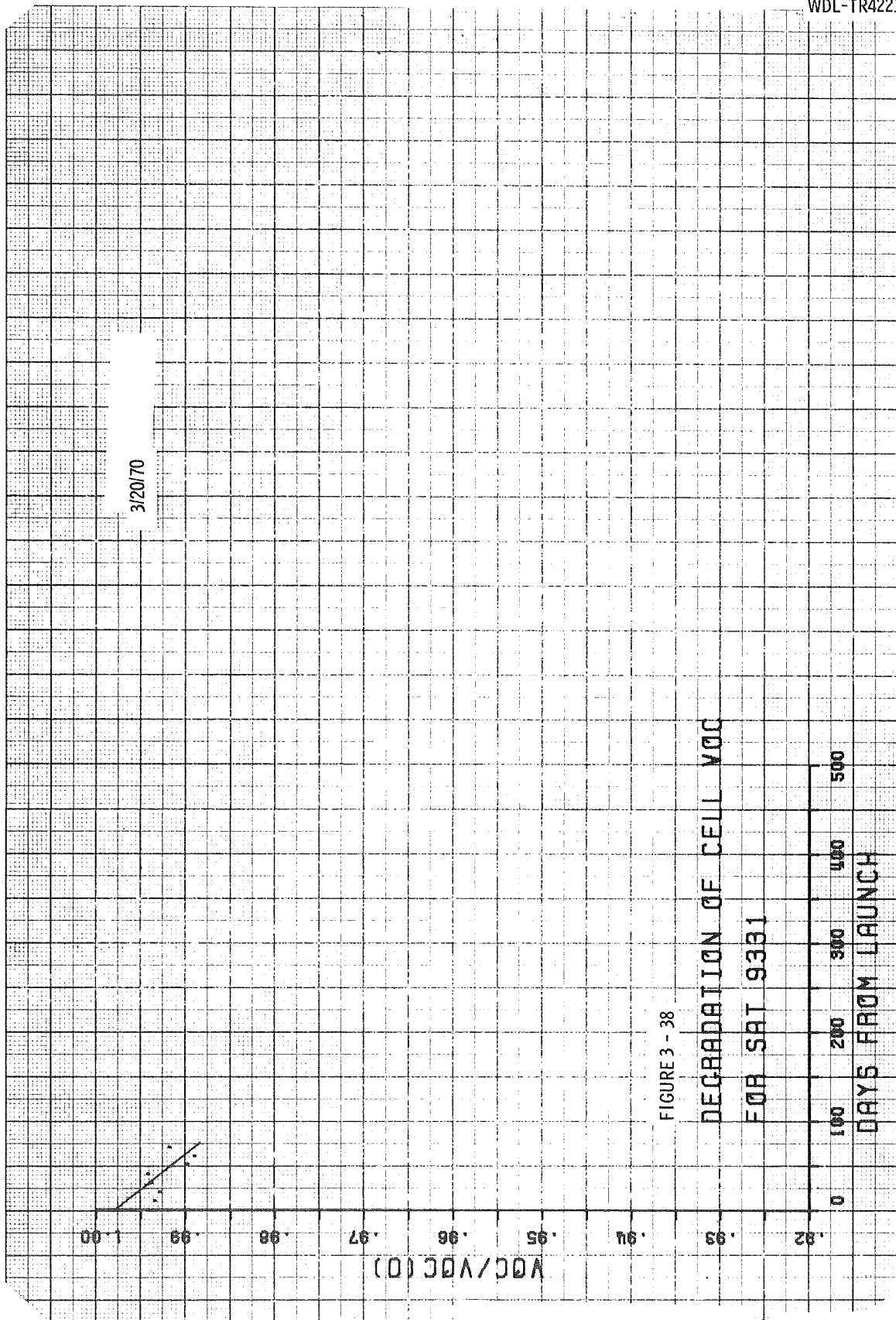
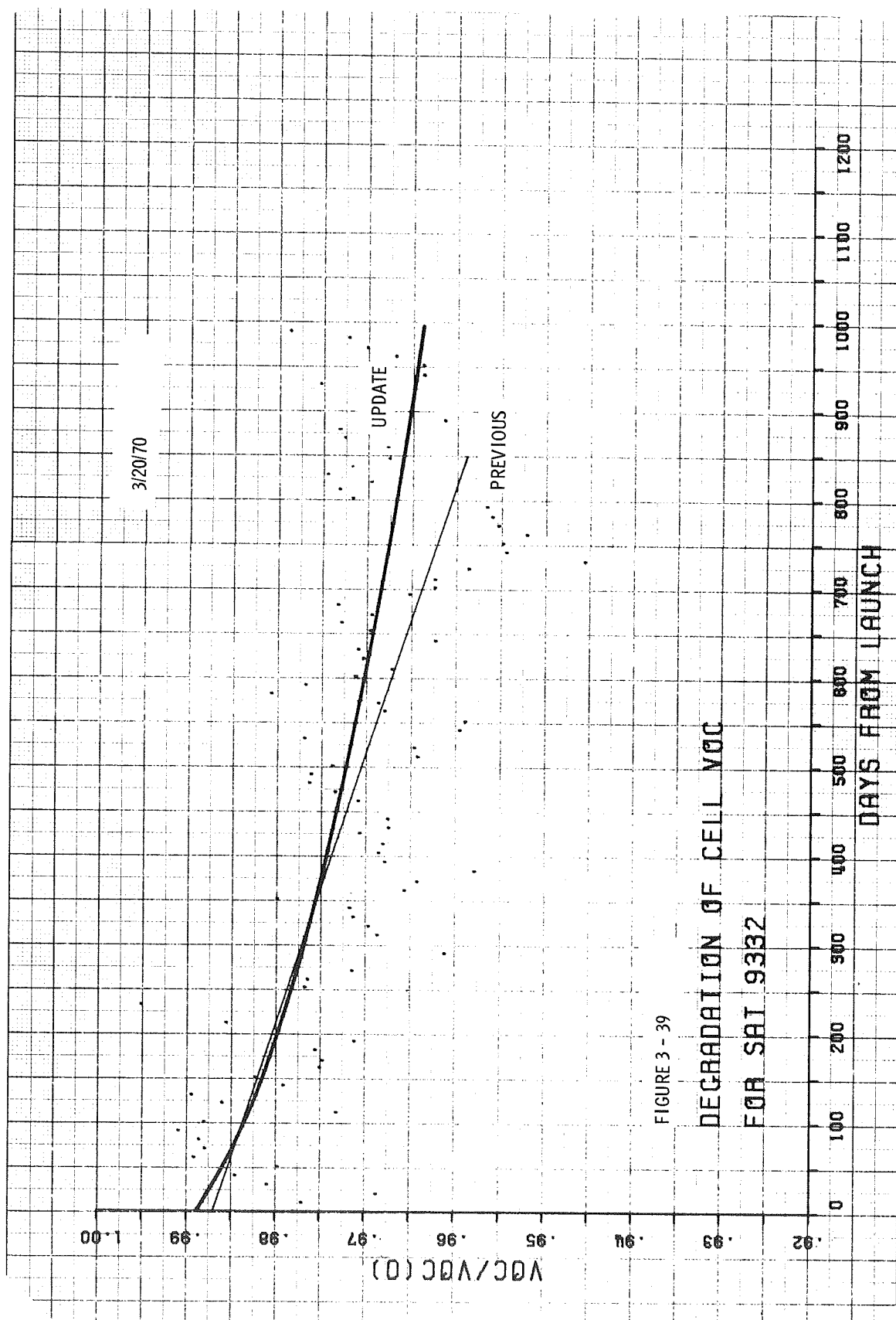
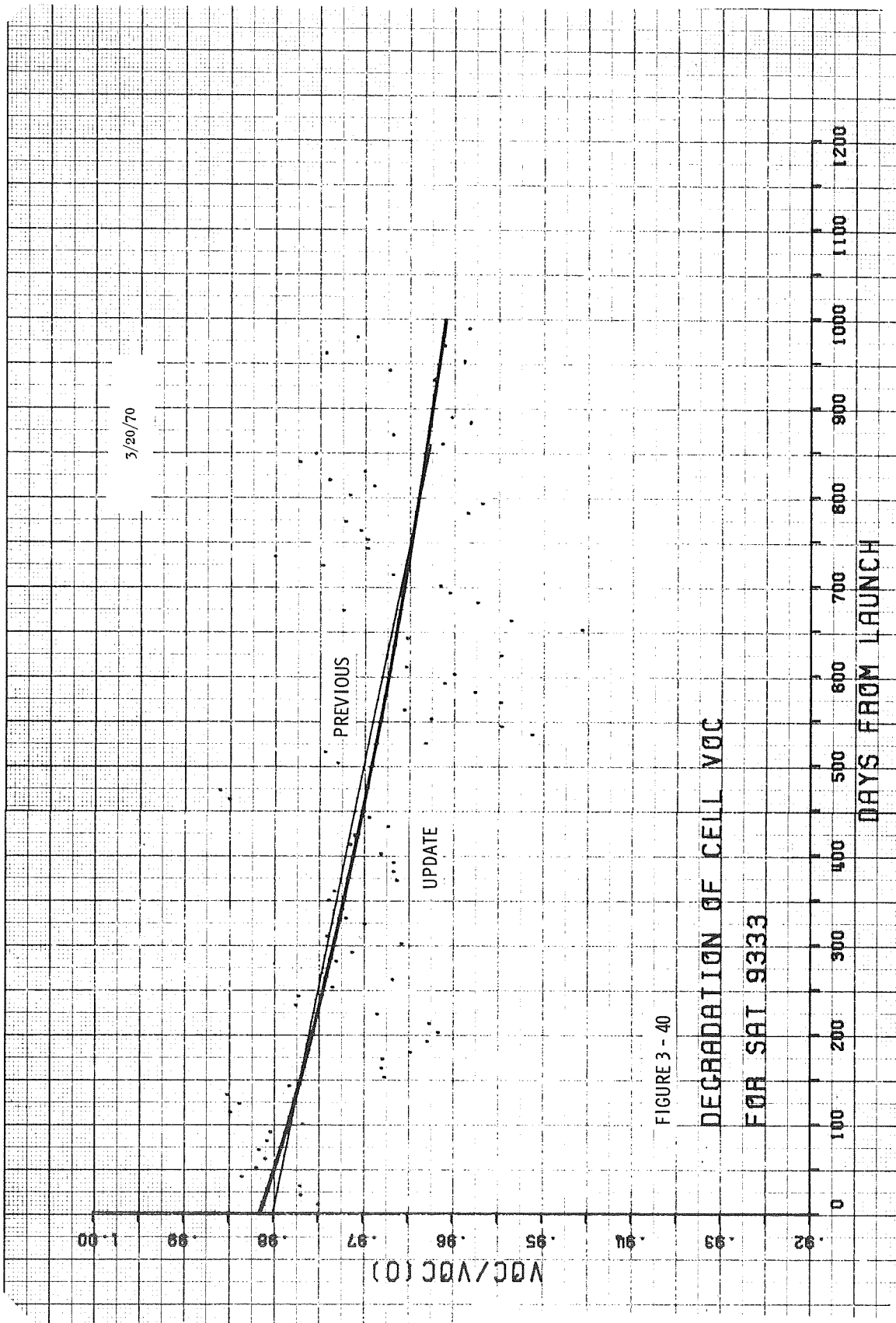


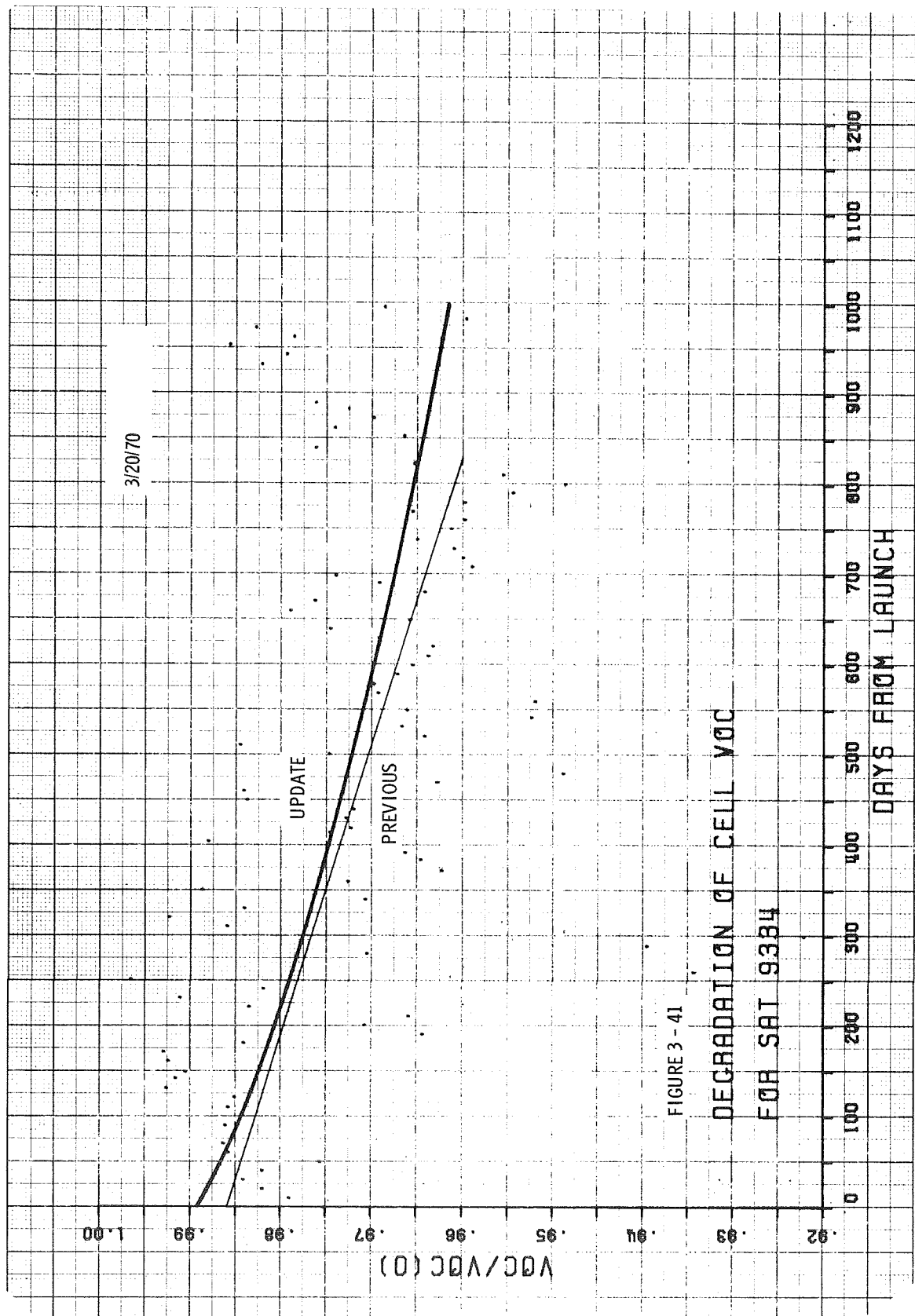
FIGURE 3 - 37

DEGRADATION OF CELL VOC
FOR SAT 9328









3.3 FUNCTIONAL DEPENDENCE OF RADIATION DEGRADATION

In order to present a smooth and impartial curve through the degradation ratio points calculated and plotted in this study, an approximate functional dependence (with time) was sought from theory. To simplify the derivation, the following assumptions were incorporated:

- a. Exposure to damaging radiation was assumed uniform and constant
- b. Degradation ratios for I_{sc} and V_{oc} were linear with the log of the diffusion length for "light" exposures to electrons and protons

The first assumption appears to be verified by the measured environmental data collected in Section 3.6; the uniform trapped electron belt appears to dominate over erratic solar flare proton influences. The second assumption is fairly exact for penetrating radiation and not too bad an approximation for low exposure non-penetrating radiation. This is indicated in Figure 3-42, which is extracted from the handbook by Cooley and Barrett ⁽¹⁾, the most general current reference on this calculation method.

Using R to designate either the ratio $V_{oc}/V_{oc}(0)$ or $I_{sc}/I_{sc}(0)$, we write

$$R = a + k \ln L .$$

The dependence of L on radiation, and thus on time, is

$$L^{-2} = L_0^{-2} + Kt$$

or

$$L = L_0 \left(1 + L_0^2 Kt \right)^{-1/2} .$$

1. W. C. Cooley and M. J. Barrett, Handbook of Space Environmental Effects on Solar Cell Power Systems, NASA Contract NASW-1345, 1968.

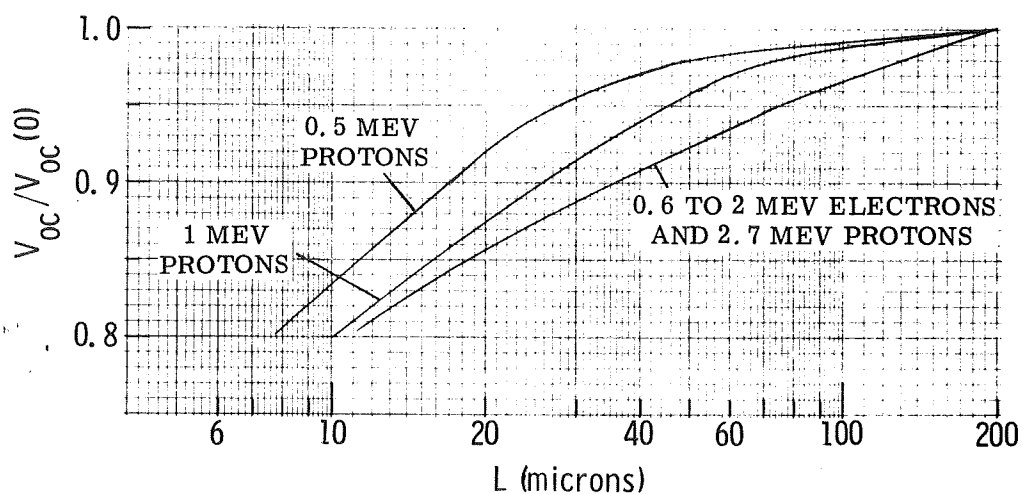
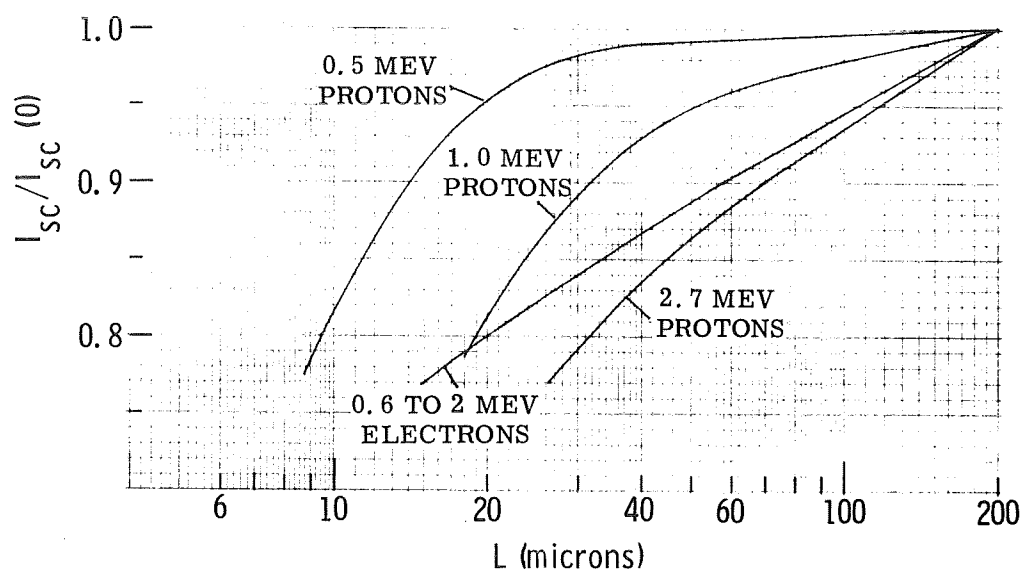


Figure 3-42 I_{sc} and V_{oc} Ratios vs. Diffusion Length
From the Cooley & Barrett Handbook⁽¹⁾

Substituting this function in the ratio equation, we obtain

$$R = a + k \ln \left[L_o \left(1 + L_o^2 K t \right)^{-1/2} \right]$$

which can be written in the form

$$R = R_o \left[1 - A \ln (1 + B t) \right] .$$

Non-cell transmission losses are known to diminish the I_{sc} ratio beyond the pure cell degradation indicated in the above function. Not knowing the nature of this loss function, a simple linear multiplier, $(1 - mt)$, was tentatively incorporated into the regression program (GOFIT) for the preliminary fits to the data. In some cases the parameter m was so small ($\approx 10^{-9}$) that it was set identically to zero to avoid singularities in the matrices of the GOFIT program. The complete table of regression parameters is presented in Section 3.4 and the resultant curves are plotted over the data in Section 3.2.

3.4 STATISTICAL RESULTS

Table 3-2 presents the updated regression parameters, R_0 , A, B, and M, for the regression curves of $I_{sc}/I_{sc}(0)$ on t (days from launch). These results express data through March 20 1970. Also included in the table are 3 satellites with regression parameters fitted with the first 100 days of data missing; these parameters are used in Section 3.7 for an experimental approach to separate aspects of noncell behavior from total behavior.

Table 3-3 presents the previously published regression parameters for I_{sc} and V_{oc} . For I_{sc} the function fitted is:

$$I_{sc}(t)/I_{sc}(0) = R_0 (1 - A \ln(1 + Bt)) (1 - Mt)$$

and for V_{oc} the function fitted is:

$$V_{oc}(t)/V_{oc}(0) = C e^{-kt}$$

The extraction of correlation coefficients and confidence limits was performed on the 25 November 1969 data update. The addition of 14 more points is not expected to significantly alter these results.

Figures 3-43 through 3-48 are representative of the 95% confidence limits found on the fitted functions. The tightness of these limits indicates that the given functions are quite good predictors. As might be expected from the greater scatter in the V_{oc} dot plots, the confidence limits on the V_{oc} functions are not quite as tight as on I_{sc} plots.

3.4.1 Projected Degradation To Five Years

The 15 IDSCS satellites, launched on 16 June 1966, and 18 January 1967, have been analyzed with telemetry information spanning 3.75 and 3.16 years, respectively. The study has produced I_{sc} and V_{oc} ratios (e.g., $I_{sc}(t)/I_{sc}(0)$) of the output of an average individual solar cell assumed to be used throughout each array.

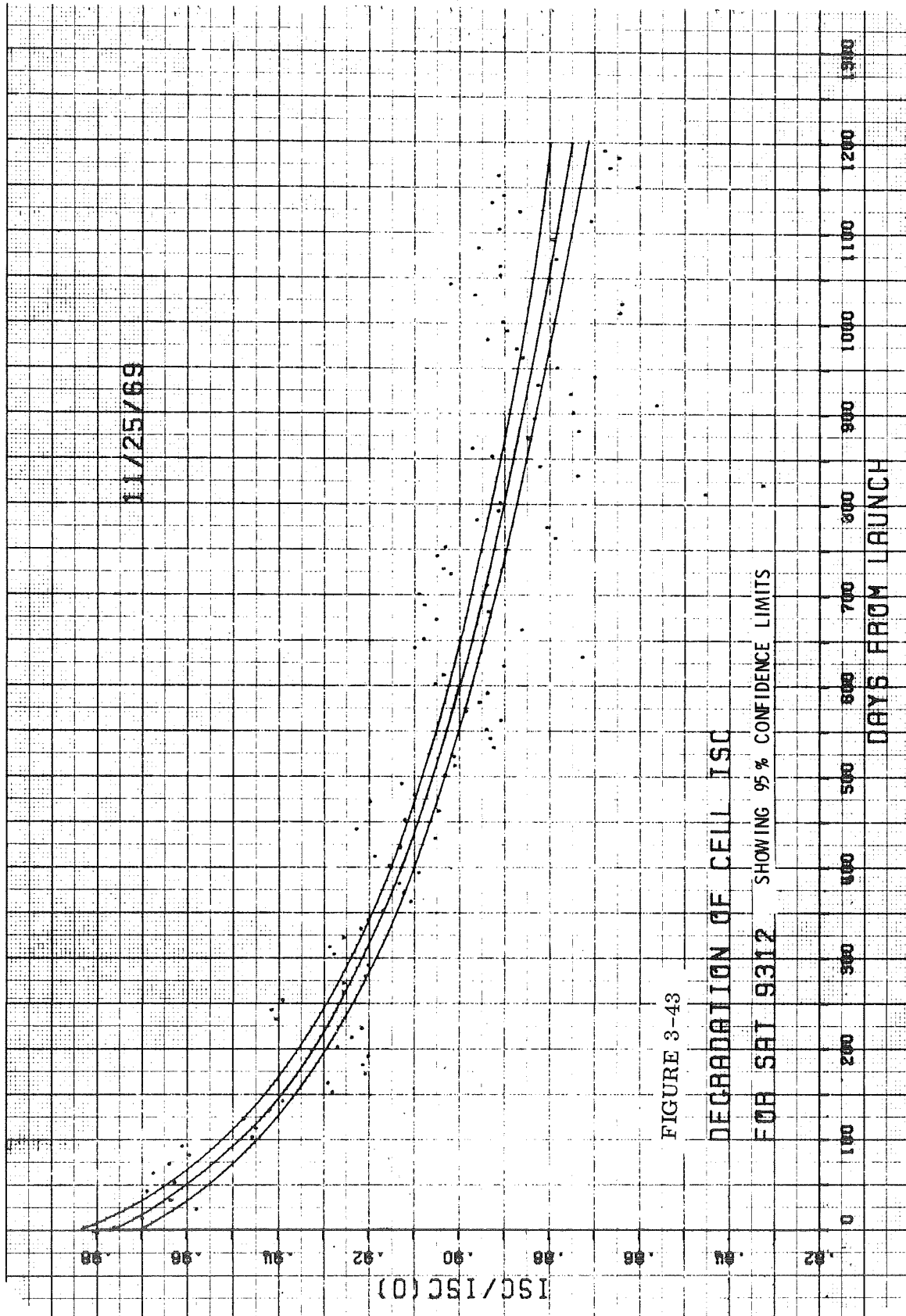
TABLE 3-2
20 MARCH 1970 UPDATE OF REGRESSION PARAMETERS

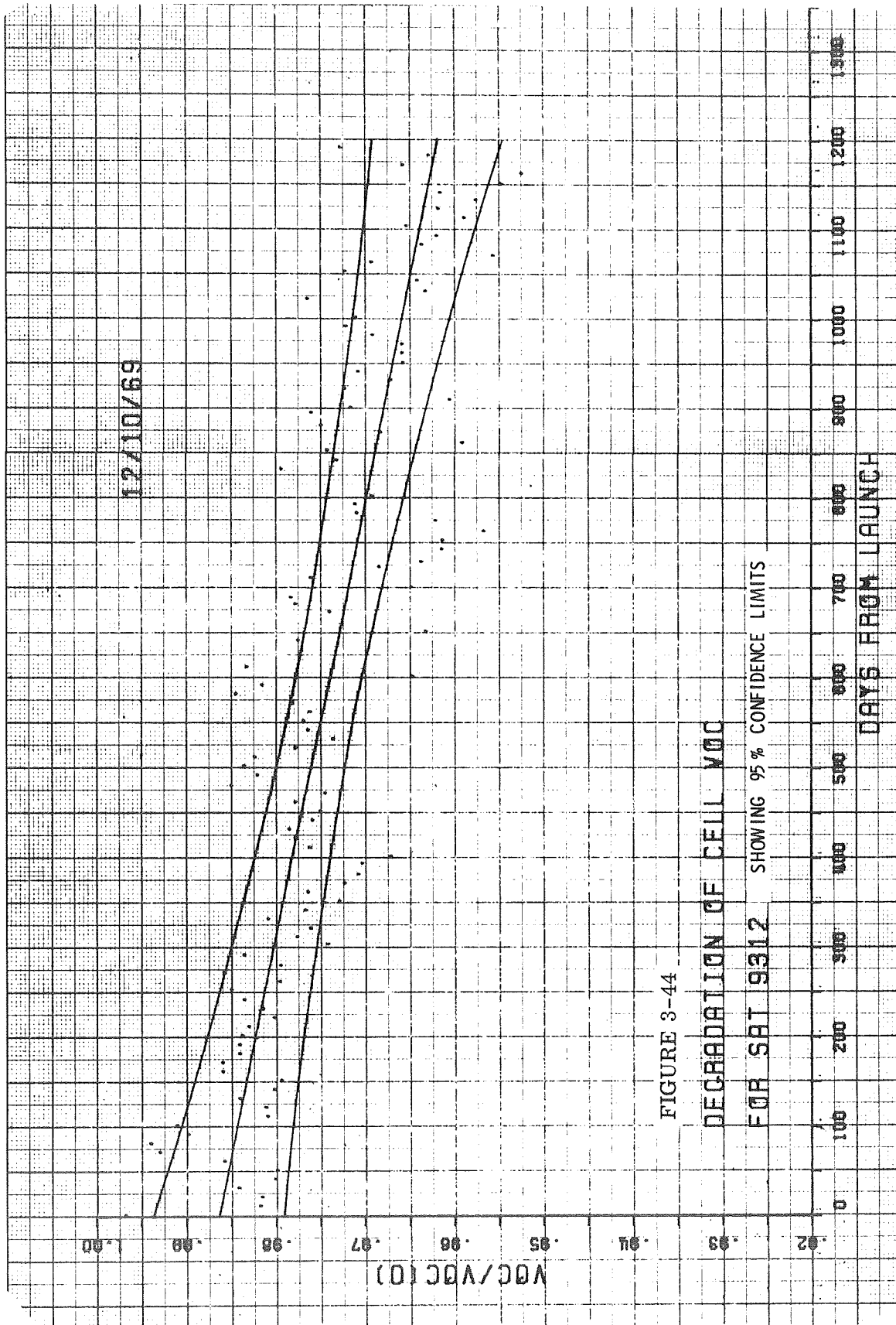
Satellite No.	No. of Points	R _o	A	B	M	Total Square Error
9311	134	0.97386	0.0258305	0.0162537	2.21509 E-5	1.030246 E-2
9312	134	0.97964	0.0179982	0.0410728	3.996170 E-5	1.342733 E-2
9313	134	0.95869	0.020323	0.157739	3.26352 E-5	1.893364 E-2
9314	67	0.93724	0.0621888	0.0044020	3.06236 E-11	3.415818 E-3
9315	133	0.93234	0.0625068	0.0040032	3.4537 E-10	1.734776 E-2
9316	133	0.93540	0.112	0.00141	0.	2.080061 E-2
9317	133	0.96354	0.0454935	0.0069688	7.38541 E-6	1.921652 E-2
9321	114	0.98704	0.023847	0.0155683	4.43964 E-5	4.406652 E-3
9322	114	0.94824	0.178786	0.11724	3.23560 E-5	1.250398 E-2
9323	113	0.99912	0.0743762	0.0032225	3.00737 E-10	8.699752 E-3
9324	114	0.98278	0.0265283	0.0147543	3.86412 E-5	6.157174 E-3
9325	112	0.95910	0.0486362	0.0122890	0	5.861288 E-3
9326	111	0.91133	0.052745	0.0075012	1. E-9	8.519808 E-3
9327	115	0.97507	0.027079	0.0277944	2.98648 E-5	4.831811 E-3
9328	116	0.89855	0.0191877	0.0161359	3.63765 E-5	1.489192 E-2
9332	96	0.97554	0.0117326	0.413301	9.89322 E-5	5.973742 E-3
9333	97	0.95978	0.0790191	0.0047149	5.06982 E-10	5.151958 E-3
9334	96	0.98993	0.0180555	0.0265268	7.1891 E-5	6.681930 E-3
-1st 100 days						
9312	124	0.94642	0.158878	5.79756E-4	0.	1.3339976 E-2
9313	124	0.89672	0.159593	5.69128E-4	0.	1.5118374 E-2
9321	104	0.96737	0.108157	0.0012909	0.	3.5622298 E-3

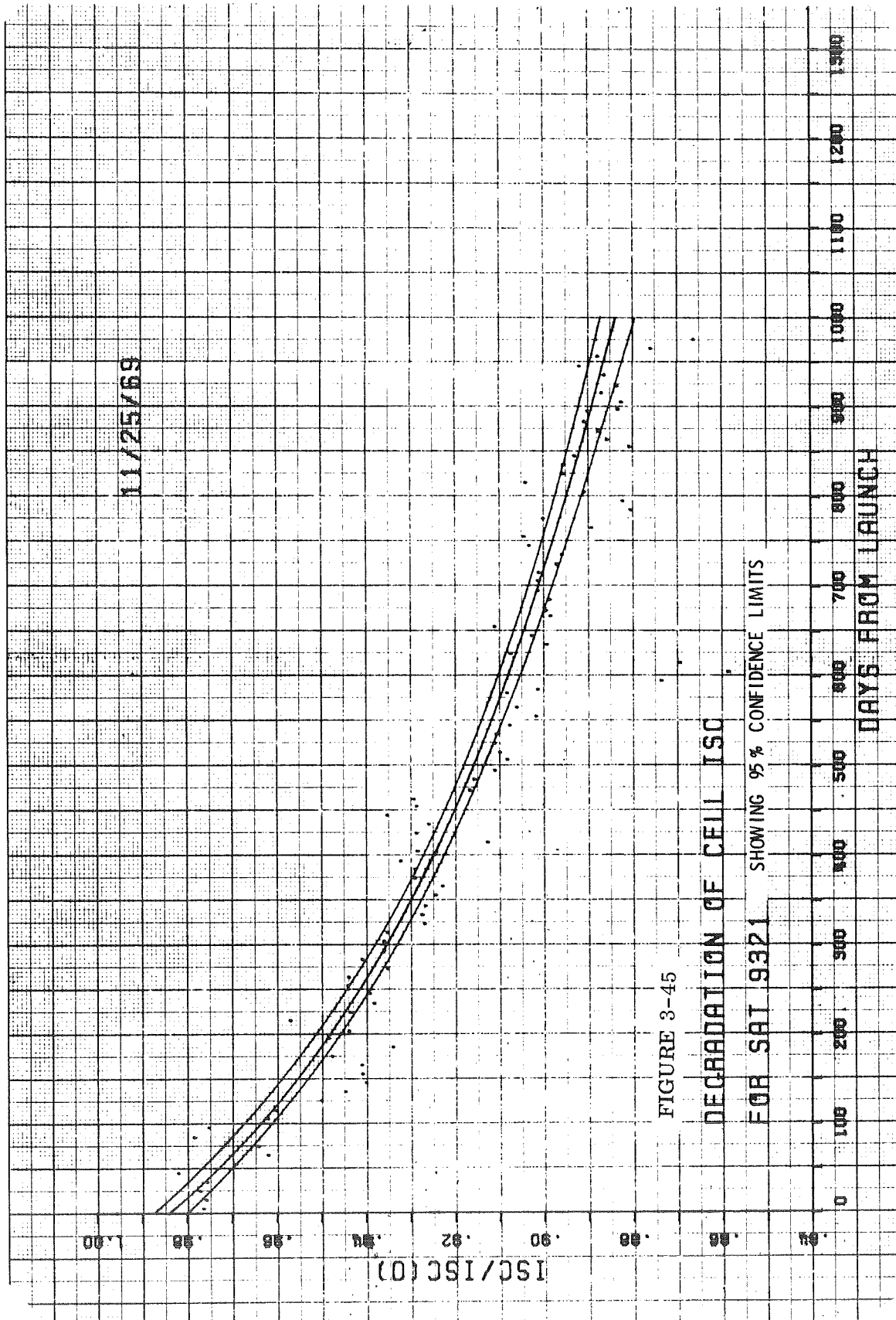
TABLE 3-3
REGRESSION PARAMETERS FOR PREVIOUSLY PUBLISHED REGRESSION CURVES (25 NOV 1969)

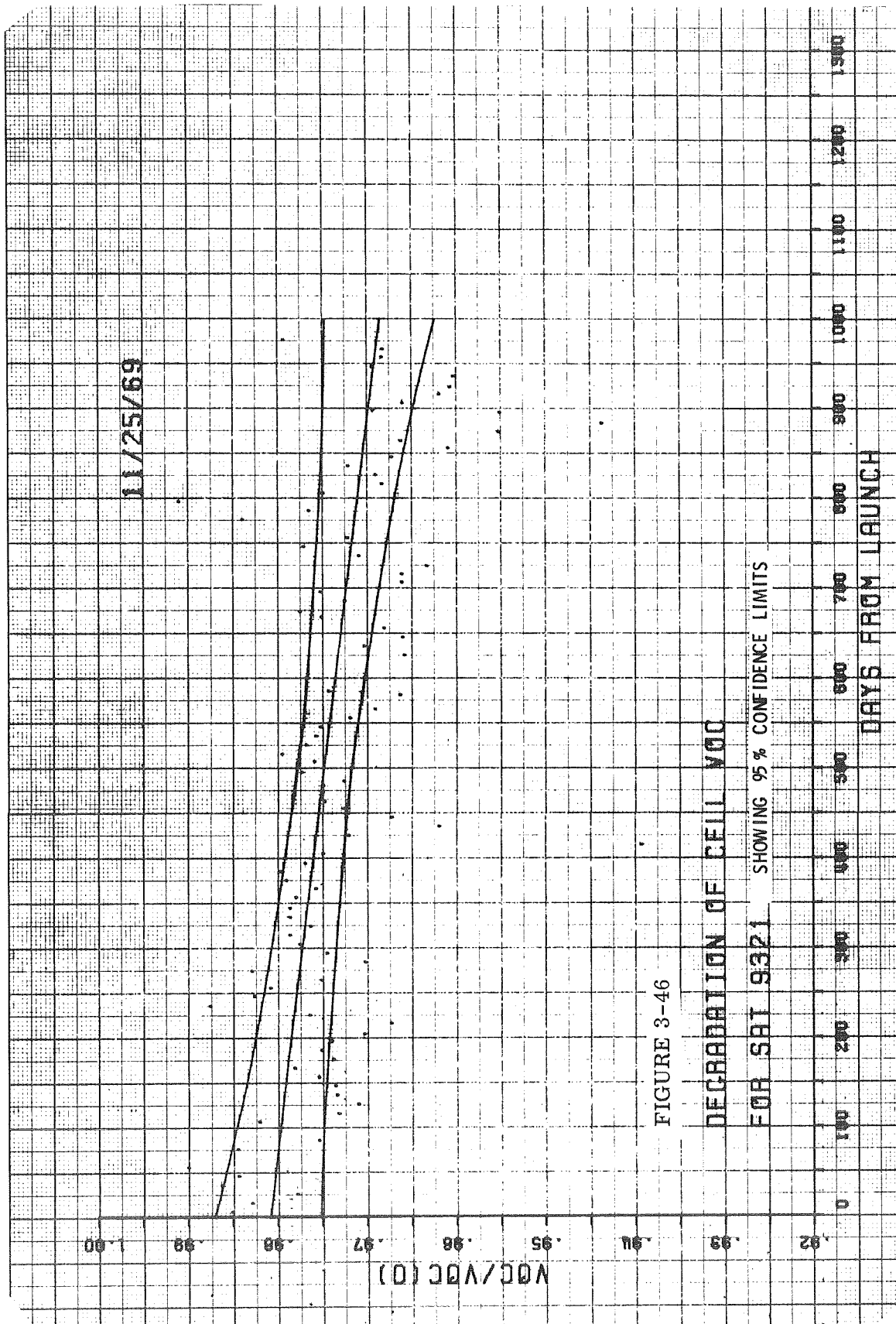
Sat. No.	No. of Points	R _o	A	B	M	Corr. Coeff.	Square Error	C	K	Corr. Coeff.
9311		0.97894	0.0170906	0.0301294	4.6E-5	0.8961		0.98523	-1.09E-5	-0.23024
* 9312	120	0.977313	0.084813	0.0130859	5.7664E-6	0.91480312	7.46E-3	0.98653502	-2.1143E-5	-0.7948
(-1st 100 days)		0.95465	0.059844	2.63098E-3			7.868042E-3			
9313	120	0.956	0.0245	8.6E-2	2.0E-5	0.8854	2.37E-2	0.9935	-2.36E-5	-0.410
(-1st 100 days)		0.900442	0.0970194	1.13873E-3			1.269E-2			
9314	61	0.96	0.0277	5.4E-2	1.8E-5	0.9267	8.8E-3	0.991	-9.2E-6	-0.1302
(-1st 152 days)		0.912696	0.0655155	0.00218011			0.002988974			
9315	119	0.9337	0.05389	5.05E-3	5.29E-6	0.8761	2.9E-2	0.991	-1.34E-5	-0.194
9316	120	0.9354	0.112	1.41E-3	7.334E-10	0.8819	4.18E-2	0.987	-1.198E-5	-0.156
9317	120	0.9501	0.1221	9.04E-4	1.771E-8	0.8374	3.16E-2	0.981	-1.73E-5	-0.276
9321	100	0.9845	0.0645	3.76E-3	2.51E-6	0.9451	9.67E-3	0.981	-1.2702E-5	-0.236
(-1st 100 days)		0.967373	0.108157	0.00129089			2.3671822E-3			
9322	100	0.944	0.0288	3.39E-2	8.71E-6	0.8308	2.66E-2	0.985	-1.96E-5	-0.509
* 9323	99	1.00026	0.061752	4.64486E-3	0.0	0.94868836	4.16E-3	0.9896	-3.15E-5	-0.7888
* 9324	99	0.982417	3.01126E-2	1.22619E-2	3.24663E-5	0.965984148		0.9877	-1.34E-5	-0.3072
* 9325	97	0.959099	4.86362E-2	1.2289E-2	0.0	0.97150334		0.9957	-2.8E-5	-0.723
* 9326	97	0.911331	5.2745E-2	7.50123E-3	0.0	0.9501903		0.9888	-3.1E-5	-0.731
* 9327	100	0.971330E-1	4.48526E-2	1.11578E-2	0.0	0.96463641		0.993	-1.35E-5	-0.3322
* 9328	100	0.898968	4.0419E-2	6.86838E-3	0.0	0.83381766		0.984	-3.21E-5	-0.4184
9331	8	0.989	8.63E-2	1.24E-2	1.0E-10		1.25E-3	0.998	-1.33E-4	-0.745
9332	81	0.97746	1.2E-2	4.145E-1	8.91E-5	0.9405	9.9E-3	0.987	-3.4E-5	-0.492
9333	82	0.96244	3.0E-2	1.7E-2	6.5E-5	0.9372	1.27E-2	0.98	-2.02E-5	-0.288
9334	82	0.995	9.3E-3	1.68E-1	9.17E-5	0.8901	1.77E-2	0.986	-3.23E-5	-0.468

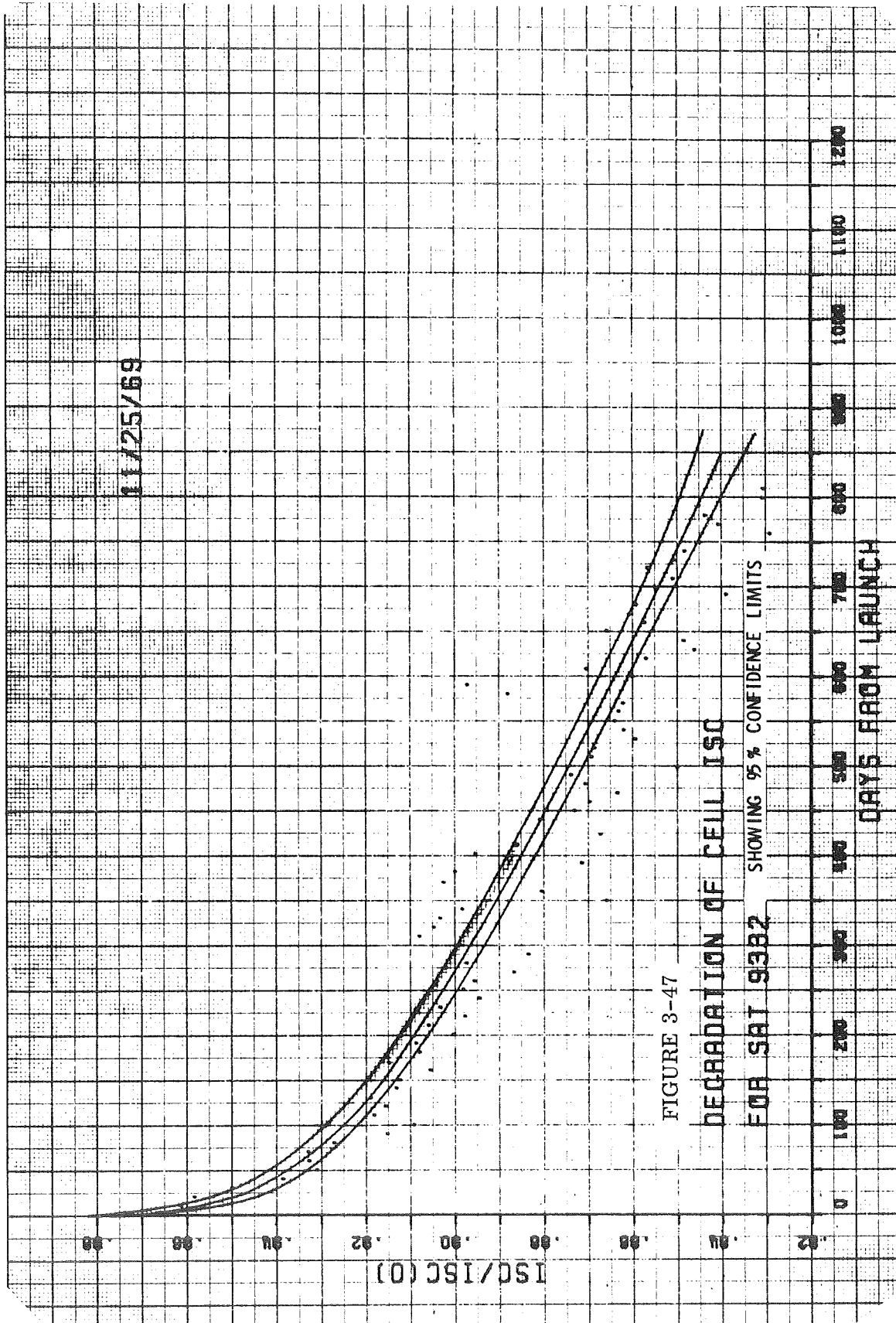
*Satellites have been run through revised non-linear regression for I_{sc} data.

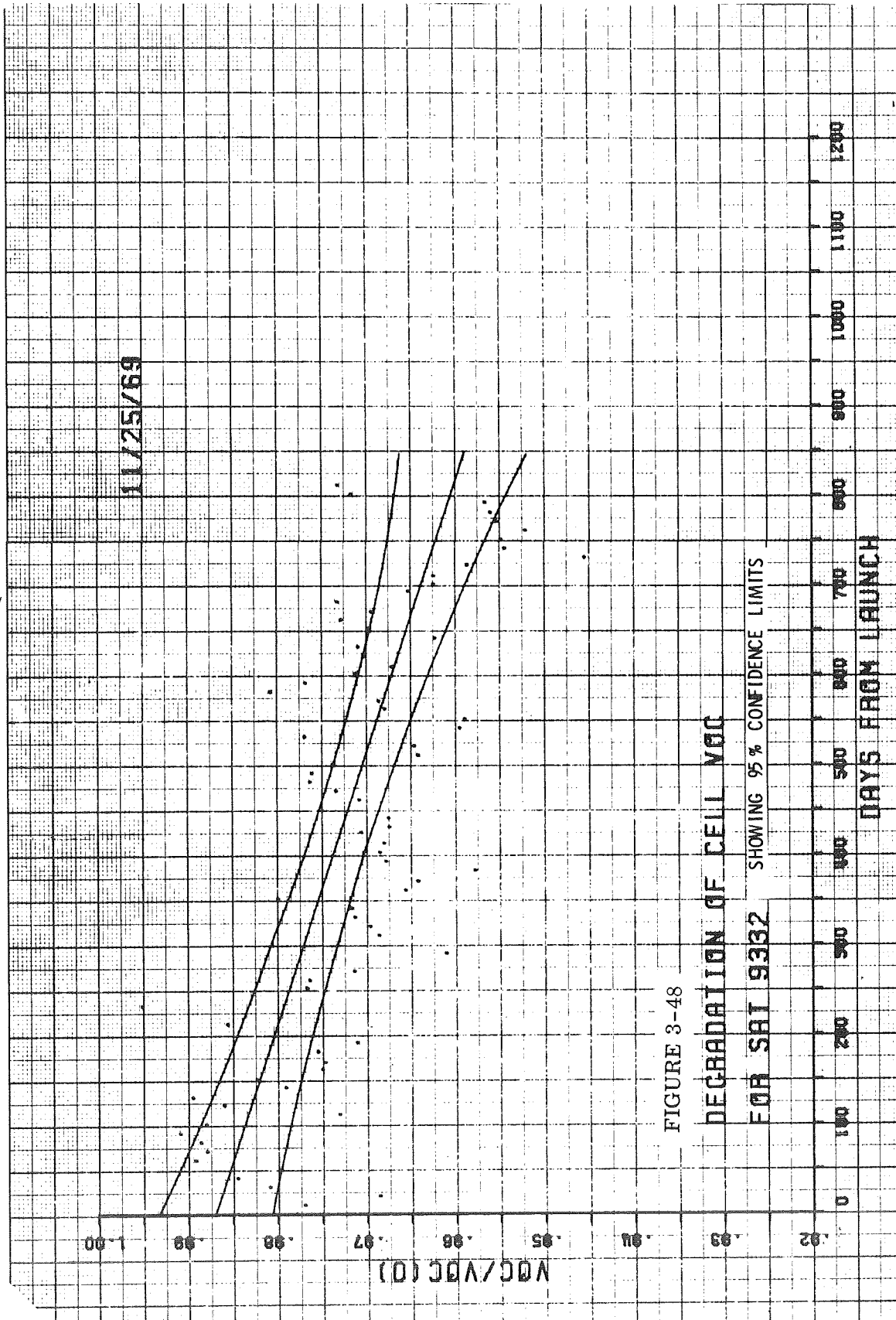












The functions and the regression parameters enable an extrapolation to be made which is dependent on every data point in the collection. A consequence of this is that updating will not only affect the curve at its endpoint, but will slightly revise the curve in its entirety. Third-launch satellites (three are transmitting telemetry) currently appear to be degrading at an accelerated rate; 5-year projections of I_{sc} appear to be 0.76, 0.82, and 0.81. These low values are not currently understood. The third-launch satellites are orbiting slightly lower with an average period of 1313 minutes (compared to 1337 minutes), and with a 7.2° inclination (compared to near 0° for the first two launches). Future efforts might be directed towards correlating orbital differences with degradation.

Table 3-4 normalizes all functions to unity at time zero and presents tabular 1-, 3-, and 5-year degradation ratios, some of which are projected. The four-place entries reflect the consequences of a functional evaluation and should be rounded down to two places when ultimately applied or quoted. The notations X and N in the notation column refer to maximum and minimum 5-year values; 25 NI indicates that it is Satellite 9325 that has the minimum short-circuit current value of all second launch satellites. Averaged 1-, 3-, and 5-year values are included for interest at the end of each column.

3.4.2 Telemetry Error Analysis

Sources of Error

There are two types of error; systematic or fixed error and random error. The latter is of primary concern for this work. All degradation ratios are normalized to start-of-life, so systematic errors will influence only absolute quantities, while the random errors can affect the degradation ratio points.

Our task is further simplified by the results of using a reference analog voltage as a means of testing the stability of the telemetry system. Data show the reference signal to be constant to within $\pm 0.78\%$ for the resolution of the system; thus, we can assume the errors introduced by the telemetry system are negligible. Therefore, we must concern ourselves with the stability of the sensors of each data channel providing information used in the degradation analysis.

TABLE 3-4
TABULATED DEGRADATION RATIOS
(Normalized to Unity at Time Zero)

Satellite No.	$I_{sc}(t)/I_{sc}(0)$: for t=			$V_{oc}(t)/V_{oc}(0)$: for t=			Notation
	1	3	5 (years)	1	3	5 (years)	
9311	0.9423	0.9018	0.8747	0.9917	0.9823	0.9757	11 X I
9312	0.9362	0.8903	0.8548	0.9906	0.9779	0.9677	
9313	0.9063	0.8632	0.8321	0.9890	0.9740	0.9632	13 NV NI
9314	0.9404	0.8904	0.8631	0.9942	0.9870	0.9836	14 X V
9315	0.9437	0.8947	0.8676	0.9917	0.9824	0.9762	
9316	0.9535	0.8954	0.8573	0.9887	0.9746	0.9642	
9317	0.9399	0.8946	0.8690	0.9909	0.9771	0.9664	
9321	0.9392	0.8857	0.8448	0.9932	0.9865	0.9822	21 X V
9322	0.9214	0.8807	0.8506	0.9920	0.9822	0.9729	
9323	0.9421	0.8876	0.8565	0.9867	0.9680	0.9520	
9324	0.9374	0.8854	0.8473	0.9932	0.9853	0.9790	
9325	0.9172	0.8701	0.8466	0.9899	0.9708	0.9532	
9326	0.9304	0.8828	0.8582	0.9878	0.9691	0.9530	
9327	0.9245	0.8769	0.8444	0.9910	0.9835	0.9785	27 NI
9328	0.9502	0.9062	0.8724	0.9865	0.9650	0.9445	28 X INV
9332	0.9071	0.8276	(0.7556)	0.9855	0.9735	(0.9657)	32 NI
9333	0.9209	0.8563	(0.8212)	0.9892	0.9775	(0.9695)	33 X IXV
9334	0.9321	0.8646	(0.8075)	0.9855	0.9703	(0.9585)	34 NV
Averages	0.933	0.881	0.846	0.990	0.977	0.967	

Worst-Case Approach

All sensors operate within worst-case stability specifications as listed below:

- a. Voltage Sensors $\pm 2\%$ of full scale in 3 years
- b. Current Sensors $\pm 2\%$ of full scale in 3 years
- c. Temperature Sensors $\pm 3^\circ\text{C}$ in 3 years (negligible)
- d. Aspect Sensors $< 0.1^\circ$ in 3 years (negligible)

The RMS quantization error for a binary system is given by:

$$Q. E. = \pm \frac{1}{2^{n+1}\sqrt{3}}, \quad \text{where } n = \text{number of bits/word.}$$

$$Q. E. = - \frac{1}{2^7\sqrt{3}} = \pm 0.45\%$$

The total RMS error is then for each parameter:

$$\begin{aligned} \text{a. Voltage} \quad T_V &= \sqrt{2^2 + (.45)^2 + (.78)^2} = \pm 2.19\% \\ \text{b. Current} \quad T_I &= \sqrt{2^2 + (.45)^2 + (.78)^2} = \pm 2.19\% \end{aligned}$$

The electrical parameters of concern and associated instabilities in engineering units are as follows:

- a. Control Bus Voltage (25.0 vfs) $(\pm 2.19\%) = \pm 548 \text{ mV}$
- b. Control Bus Current (1000 ma) $(\pm 2.19\%) = \pm 22 \text{ ma}$
- c. Main Bus Current (2000 ma) $(\pm 2.19\%) = \pm 43.8 \text{ ma}$

Influence of Worst-Case Instabilities on Degradation Data

To establish stability bounds on the results of the I_{sc} and V_{oc} degradation analysis, the worst-case stability margins for the sensors in the above paragraph

were introduced in the analysis. The combined instabilities produce a translation of about $\pm 4\%$ in the function fitted to the I_{sc} degradation data. The V_{oc} degradation is translated by about $\pm 0.1\%$.

Observed Sensor Stabilities

During illuminated periods, the array sees essentially a constant power load. Telemetry data indicate no shift in either main bus current or voltage within the resolution limits of the system. This indicates sensor stability within the resolution of the system, or:

- a. $T_V = \pm 0.19\%$
- b. $T_I = \pm 0.19\%$
- c. $T_{Temp} = \pm 0.19\%$

This instability is considered negligible in its effect on degradation data.

Conclusions

The influence of telemetry and sensor instabilities on degradation information is negligible.

3.4.3 Statistical Analysis of 5 Year I_{sc} Distribution

The statistical significance of the 5-year endpoints found for the satellites in this study depends on two major factors:

1. How well defined are the individual endpoints for each satellite?
2. How representative is the distribution of endpoints?

In section 3.4 above, the confidence limits were typically defined for general satellites. From these confidence limits, it is clear that the uncertainty in each

endpoint is one the order of tenths of one percent. Thus, only the endpoint distribution itself need be considered; this is done here for the fifteen satellites in the first two launches. The comparison is made between this fifteen element sample and a projected population of many satellites.

Based on the sample distribution of endpoints and the sample statistics associated with this distribution, it is possible to project, for any specified degree of confidence, the expected range of the population mean. If we think of the population as being very large compared to the number of samples, this is, these satellites are chosen at random from a large number of satellites, the confidence limits on the population mean give a measure of how much faith we can have that the samples are a good representation of the population.

The table reproduced below presents the sample statistics and confidence limits found for this distribution. The 95% confidence level indicates that we can be 95% sure of finding the population mean between 0.8493 and 0.8626, or within a range of about 1% about the sample mean. Thus, the sampling provides a satisfactory representation of the entire population and the distribution of endpoints is real.

VALUES OF SAMPLE STATISTICS:

SIZE OF SAMPLE	15
SAMPLE MEAN VALUE	.85596
VARIANCE OF SAMPLE	.0001337
SAMPLE STD DEVIATION	.0115635
ESTIMATED POPN STD DEV	.0119694
STANDARD ERROR OF MEAN	.0030905

CONFIDENCE LIMITS ON POPULATION MEAN:

CONF LEVEL	LOWER LIM	UPPER LIM
50	.8538201	.8580999
75	.8522511	.8596688
90	.8505178	.8614021
95	.8493345	.8625854
99	.8467746	.8651453
99.9	.8432306	.8686893
99.99	.8395826	.8723373
99.999	.8356993	.8762207

3.5 ARRAY I-V CHARACTERISTICS FROM ECLIPSE ENTRANCE DATA

Telemetry data received during eclipse entrance has been processed to produce portions of the array I-V curve. The upper portions of these curves for five satellites of the first launch are shown in Figures 3-49 through 3-53. All data is representative of the first experienced eclipse, the autumnal equinox of 1966, and the most recent eclipse permitted during the contract period, the vernal equinox of 1970. The time span is thus restricted to 3.5 years.

The purpose in calculating array I-V curves is to examine curve shapes and maximum-power point degradations between start-of-life and elapsed times on orbit.

The methods developed in Section 2.4 were computerized and applied to data on satellites 9311, 9312, 9313, 9315, and 9316. These were the only five satellites on which both start-of-life and end-of-life eclipse data were available.

A convenient approximation in studying degradation effects on cell I-V curves is the assumption that I_{sc} and V_{oc} losses simply translate the I-V curve along these two axes. If the array I-V curves obtained here demonstrate the validity of this assumption, we can probably safely assume that single cell I-V curves will also obey the trend.

Table 3-5 lists numerical P_{max} information from the 10 array I-V curves. The earlier I-V curves are translated (as shown in the figures) and the resultant numerical P'_{max} values compared with the measured values. The differences range from -1.8% to +2.7%, with an average difference of +0.7%. The current translation, ΔI_{sc} , was obtained from the figures; the voltage translation, ΔV_{oc} , was obtained from the dot plots in Section 3.2.

The errors inherent in the above I-V curve reconstructions can be estimated by examining the data scatter about the CBV and CBI fitted curves shown in Section 2.4. Current scatter is as great as ± 0.01 amps, and voltage scatter as great as ± 0.3 volts. The possible power scatter could thus be as great as $\pm 2.5\%$ for each final IV curve. Our conclusion regarding the comparison can only be that, within

experimental error, the following assumption is valid: that translations along the current and voltage axes reasonably express total I-V curve degradations for the satellites studied.

TABLE 3-5
COMPARISON OF MEASURED AND TRANSLATED P_{MAX} VALUES
(Autumn 1966 and April 1970) Eclipse Periods

Satellite Launch	9311			9312			9313			9315			9316		
	Oct 1966	April 1970		Oct 1966	April 1970		Oct 1966	April 1970		Oct 1966	April 1970		Oct 1966	April 1970	
I_{max}	1.3865	1.2860		1.4206	1.2687		1.3168	1.1610		1.3588	1.1909		1.3361	1.1841	
V_{max}	18.7616	18.0926		18.5713	18.0122		19.0208	18.2503		19.0737	18.2833		19.2460	18.1552	
P_{max} from (eclipse data)	26.0133	23.2679		26.3827	22.8528		25.0470	21.1882		25.9165	21.7740		25.7147	21.4977	
P'_{max} (trans- lated)		23.1866			22.4489			21.3069			22.3300			22.0678	
$\frac{P'_{\text{max}} - P_{\text{max}}}{P_{\text{max}}}$		-0.003403			-0.01767			0.005602			0.02554			0.02652	
Average Percentage Difference: +0.73%															

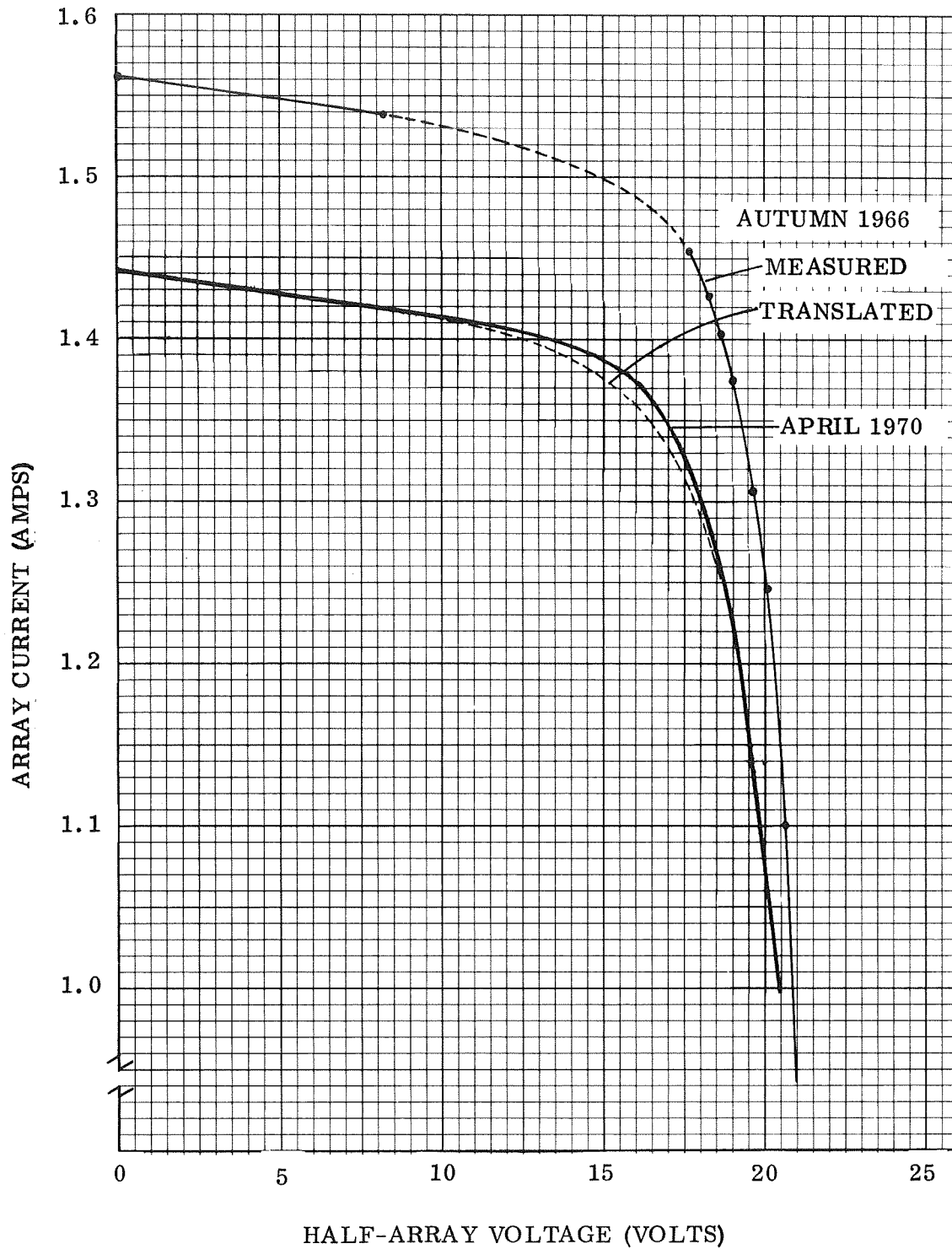


Figure 3-49 Eclipse Entrance Array I-V Curve for Satellite 9311

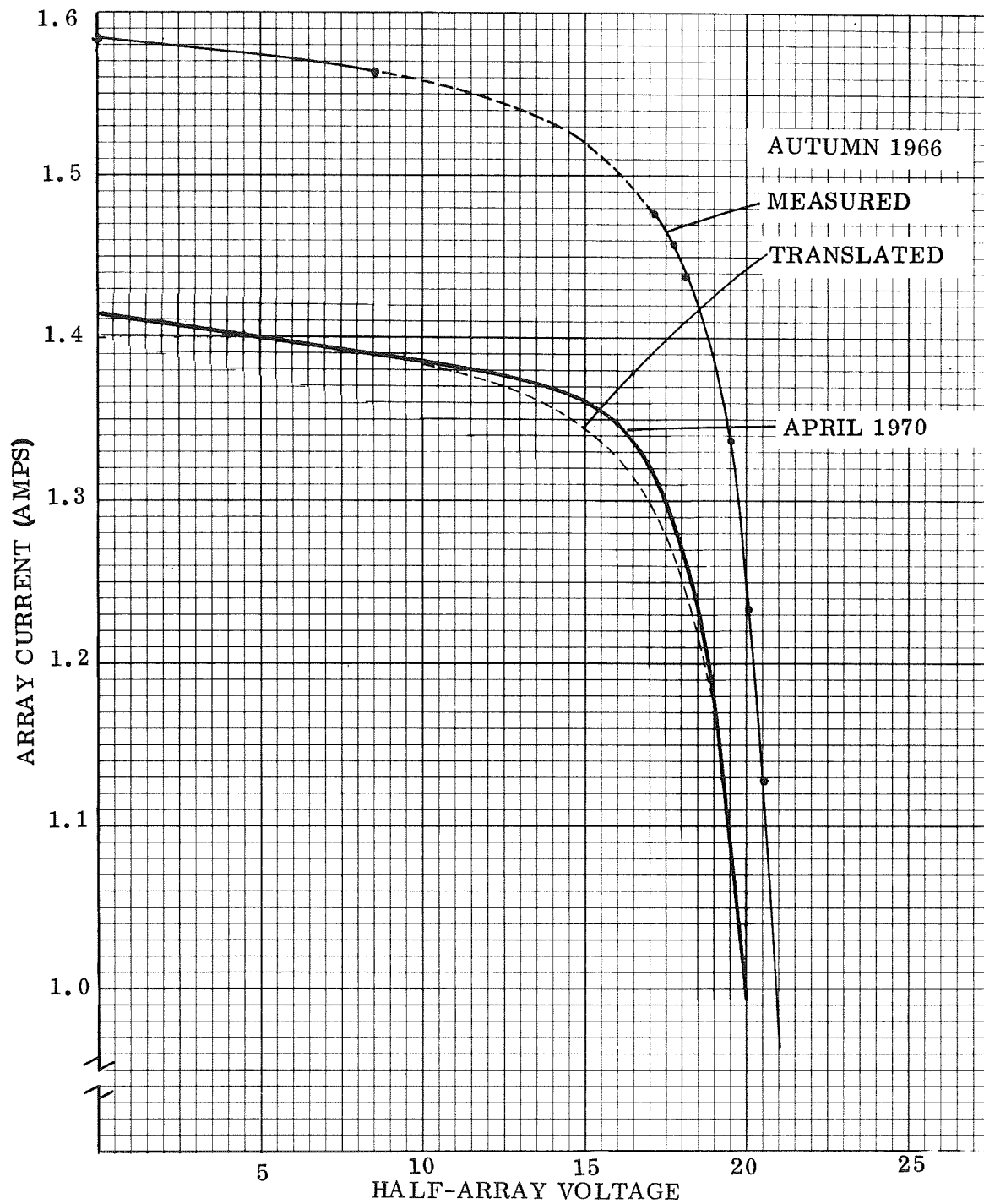


Figure 3-50 Eclipse Entrance Array I-V Curve for Satellite 9312

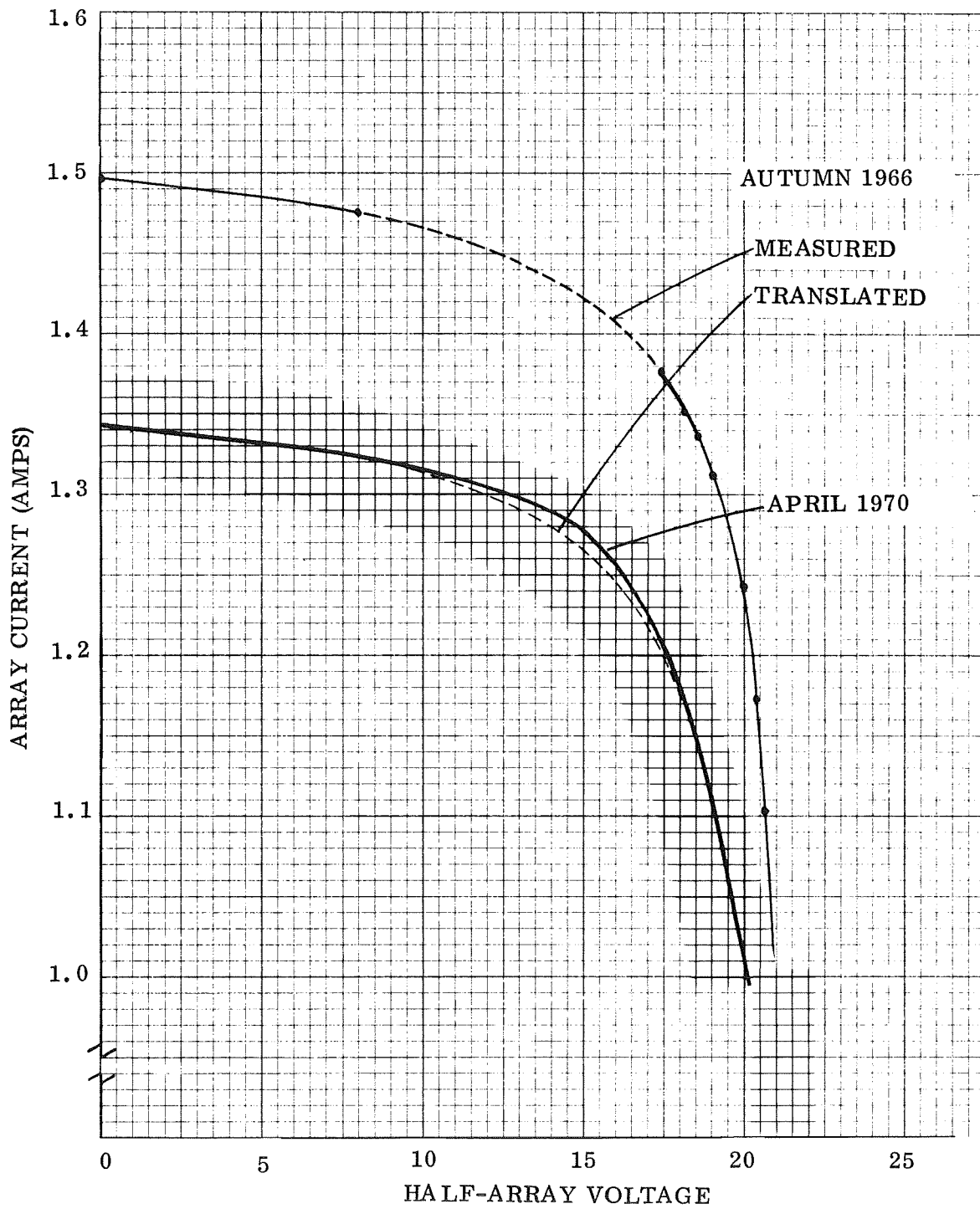


Figure 3-51 Eclipse Entrance Array I-V Curve for Satellite 9313

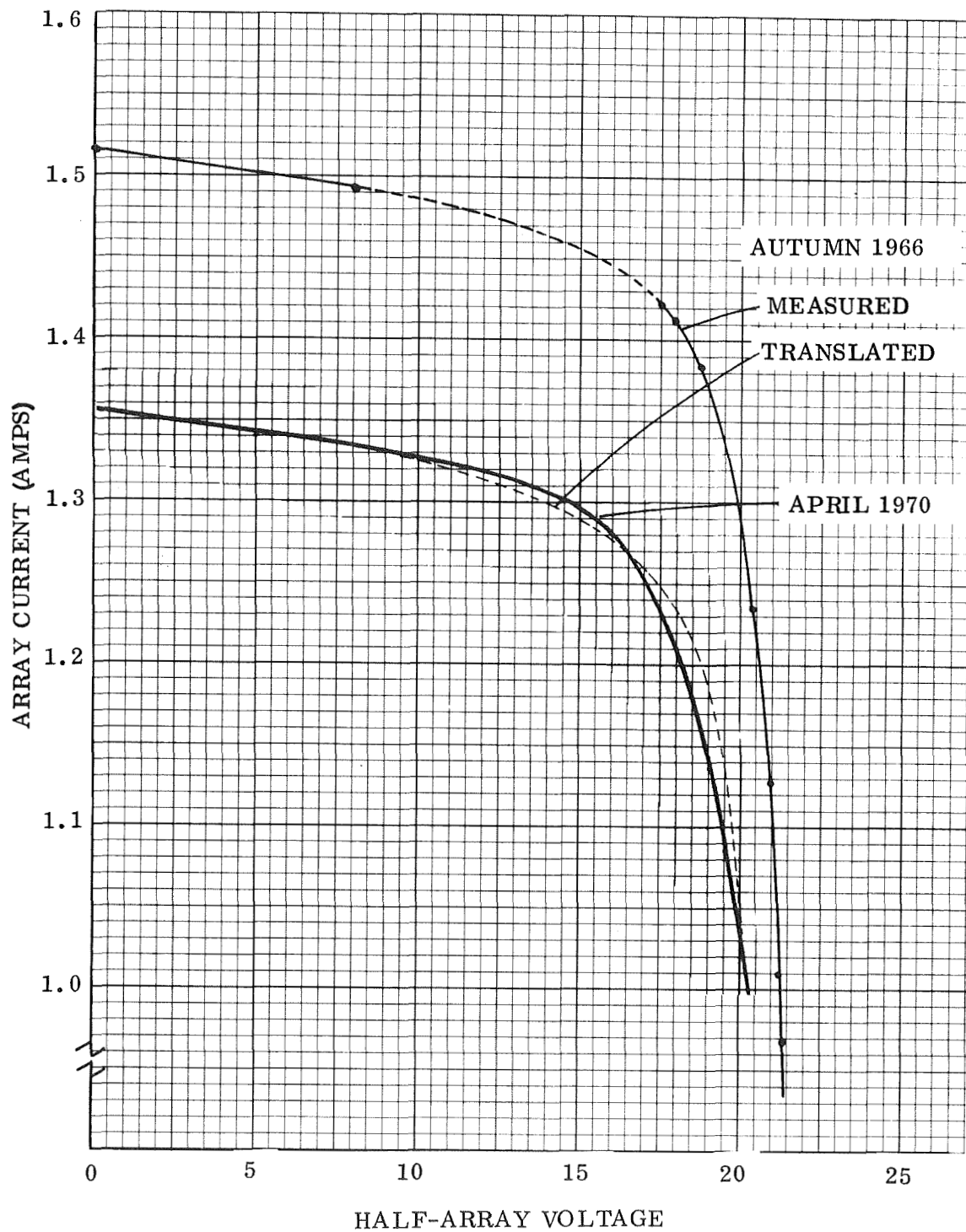


Figure 3-52 Eclipse Entrance Array I-V Curve for Satellite 9315

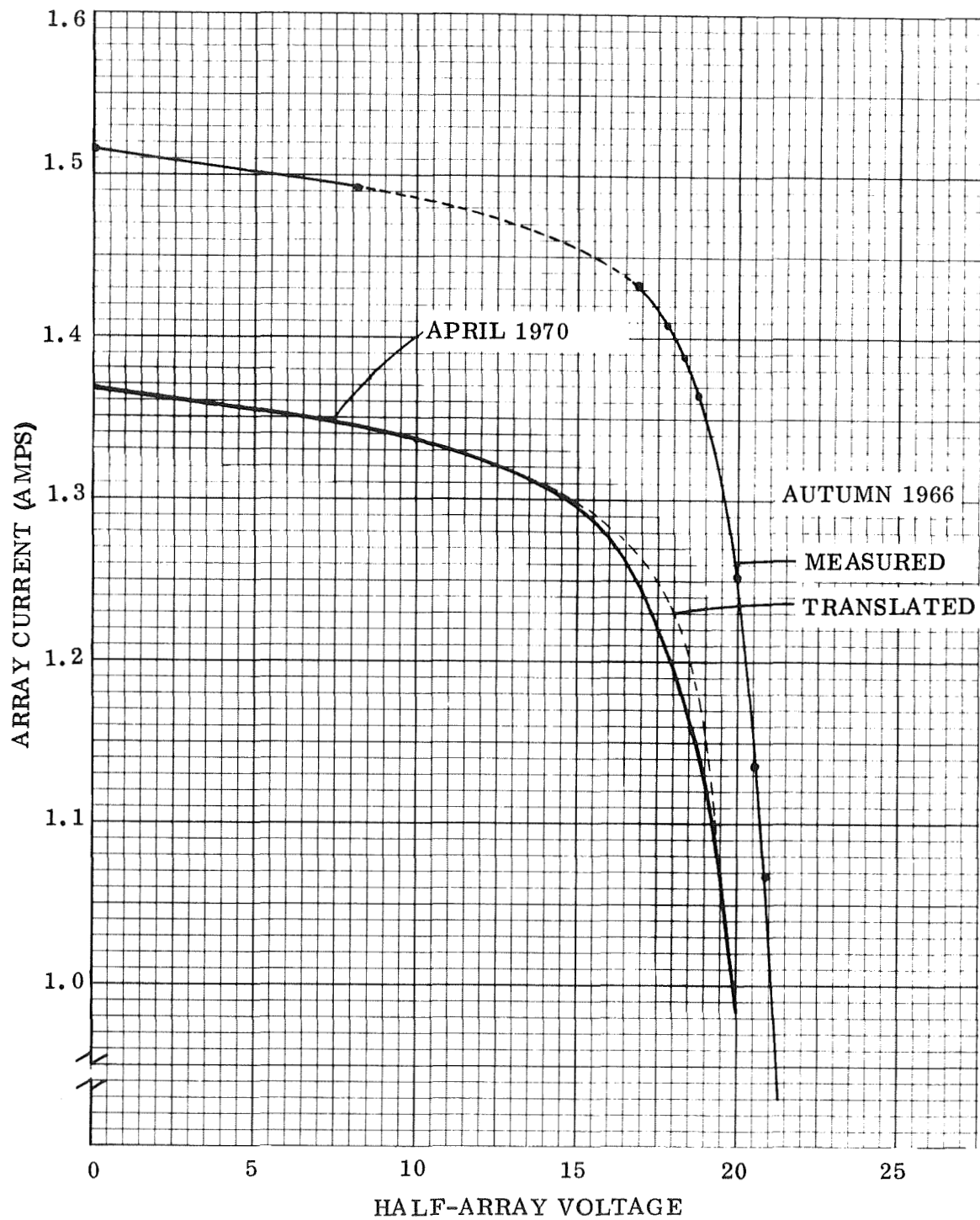


Figure 3-53 Eclipse Entrance Array I-V Curve for Satellite 9316

3-70

3.6 ENVIRONMENTAL DATA

Trapped electron and proton spectra as compiled by Vette⁽¹⁾ are displayed in Figures 3-54 and 3-55. The measured flare proton environment of 1967 and 1968, as compiled by Paulikas,^(2,3) is displayed in Figure 3-56. The following table summarizes the available flare data:

Energy, E	Omnidirectional Fluence Greater than E (C_m^{-2})		
	1967	1968	2-Year Total
5 MeV	1.37×10^9	3.71×10^9	5.08×10^9
21 MeV	3.44×10^8	3.94×10^8	7.38×10^8

The extreme extrapolations shown in Figure 3-56 were made for the purpose of solar cell degradation calculations but, as the following section will show, fluences at energies above 20 MeV are negligible contributors to cell damage. The 5-year average flare environment was assumed to be 5/2 as great as the 2-year total shown above.

Residual spectra under the 20 mil fused silica coverslide are shown in the same figures. Omnidirectional incidence and total back-shielding has been assumed. Residual energies have been calculated from range-energy tables with particle intensities of the incident energy groups assumed unchanged during penetration.

- (1) J. I. Vette, A. B. Lucero, and J. H. King, Models of the Trapped Radiation Environment, Vols. III and IV, NASA SP-3024, 1967.
- (2) G. A. Paulikas and J. B. Blake, Solar Proton Observations at Synchronous Altitude During 1967, Aerospace Corporation Report No. TR-0200(4260-20)-2, Sept. 1968.
- (3) G. A. Paulikas and J. B. Blake, Solar Observations at Synchronous during 1968, Aerospace Corporation Report No. TR-0066 (5260-20)-13, December 1969.

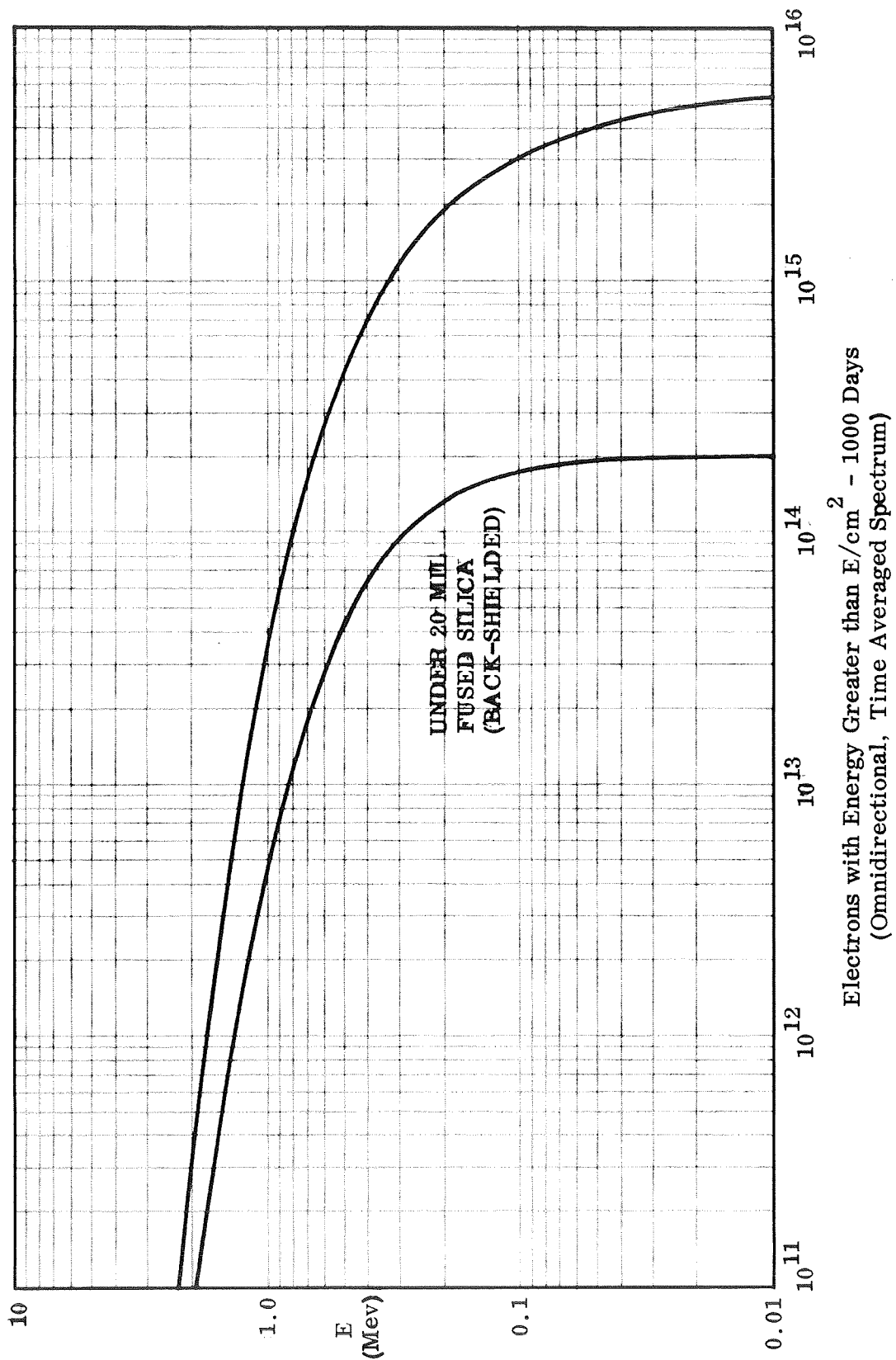


Figure 3-54 Electron Environment

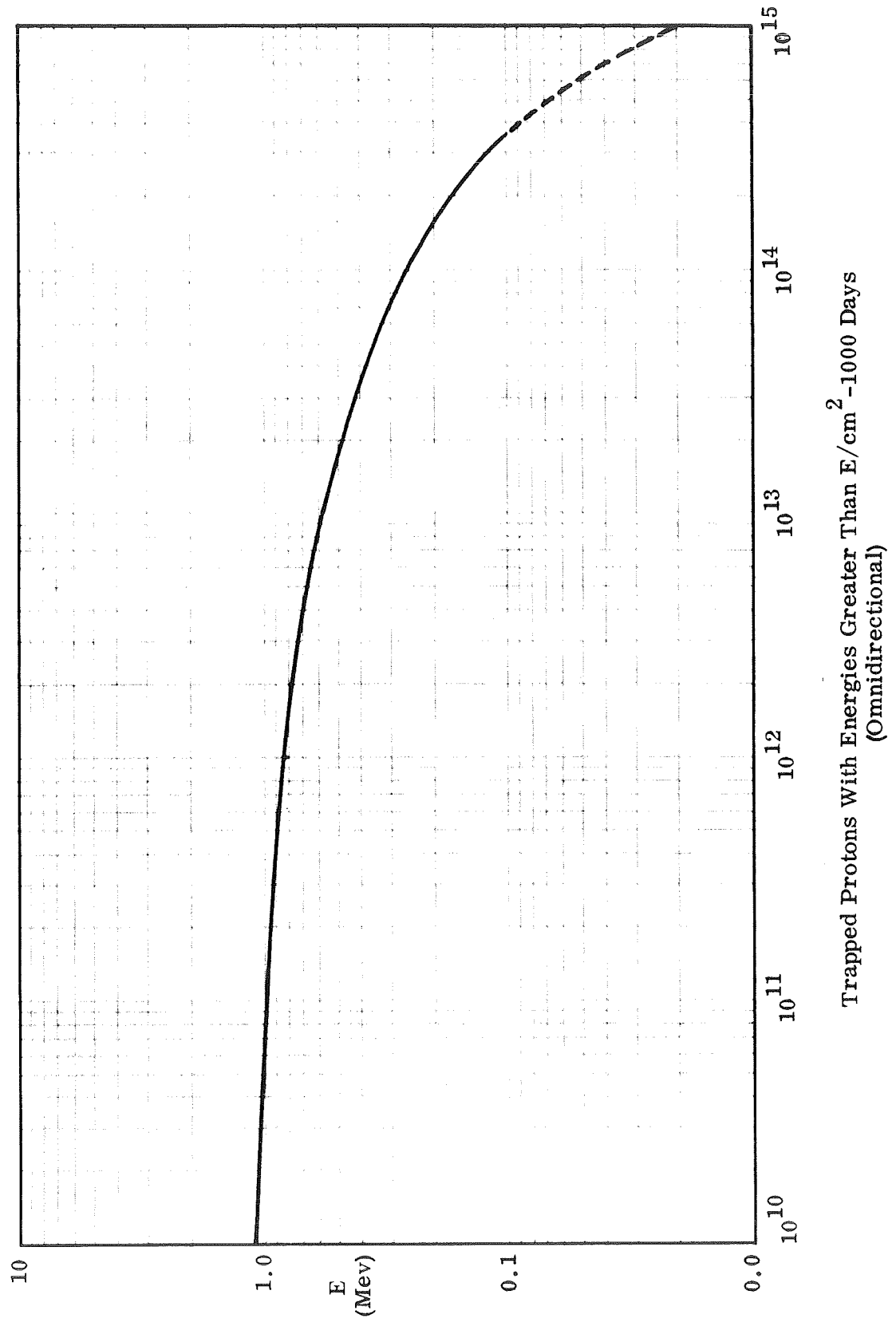


Figure 3-55 Trapped Proton Environment

3-73

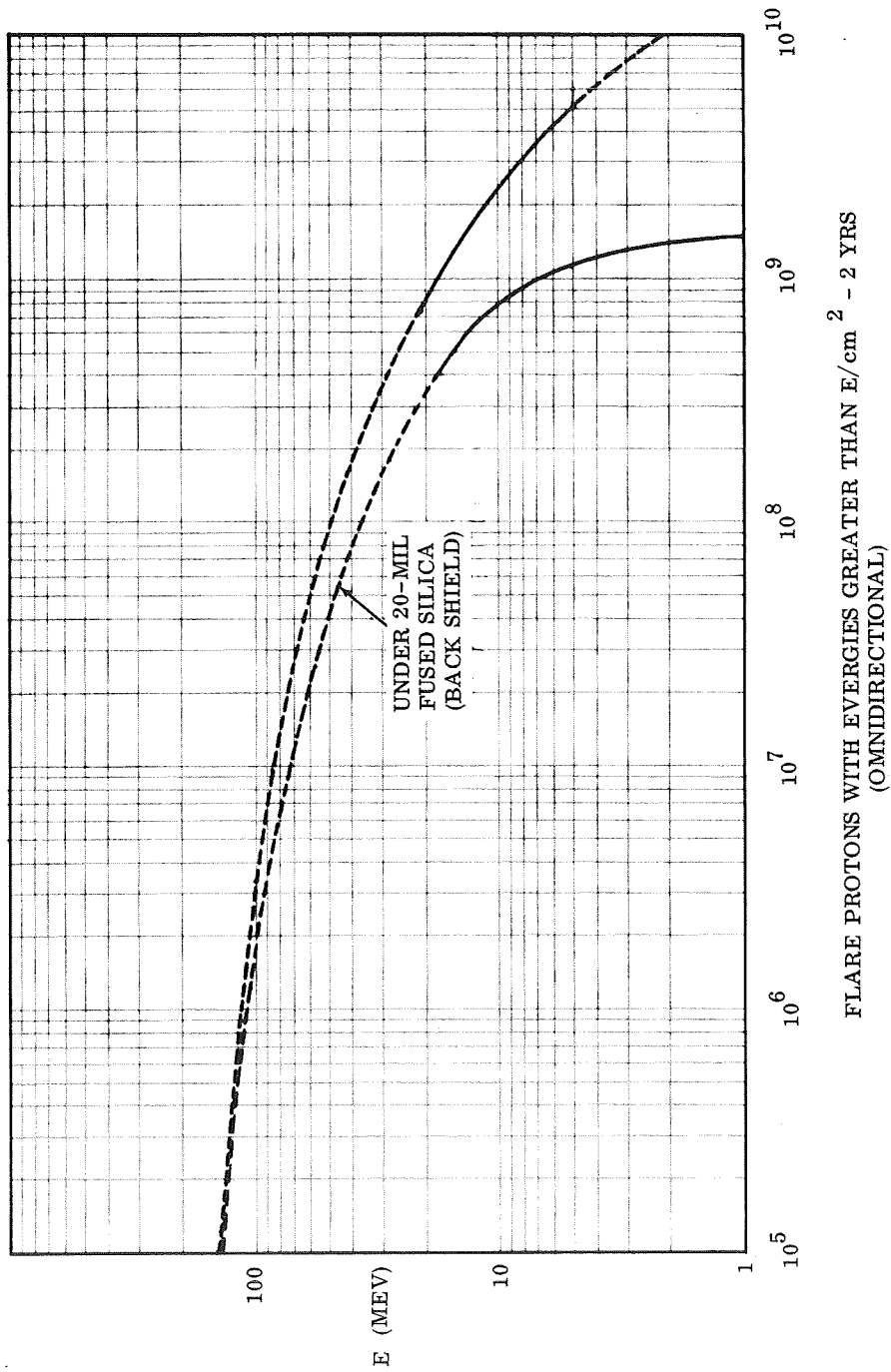


Figure 3-56 Average Flare Proton Environment for 1967 and 1968

3.7 DEGRADATION MECHANISMS AND CALCULATIONAL METHODS

3.7.1 Calculated Radiation Degradation

Incident particulate radiation, which sufficiently penetrates the solar cell, causes displacement damage in the crystal lattice which may be correlated to V_{oc} and I_{sc} degradation. Radiation is assumed to change the base region minority carrier lifetime which reduces the diffusion length L according to the rela-

$$\frac{1}{L^2} = \frac{1}{L_o^2} + K\phi.$$

K is an empirical damage constant which is dependent on energy and the type of radiation. When the incident radiation is a spectrum of energies, rather than monoenergetic, the simple product $K\phi$ is best replaced by an integral or summation over the energy range. Values of the damage constants, and the correlations of L to V_{oc} and I_{sc} are taken from Cooley and Barrett⁽¹⁾. L_o is assumed to be 200 microns.

Figure 3-57 and 3-58 shown residual electron and proton spectra under the 20-mil coverslide in differential form. The plots present the number of particles/ cm^2 in the energy region dE at E , as obtained from the previously published electron integral spectrum and the updated proton spectrum in Section 3.6.

Figure 3-59 and 3-60 shown the product $K\phi$ as a function of energy; the maximum damage regions appear at energies near 0.7 meV for electrons and near 3 meV for protons. The areas under these curves represent the damage integral and have been evaluated by graphical summations. Five-year values appear below:

Radiation	$\int K \phi dE$	L (5 yrs)	$I_{sc}/I_{sc}(o)$	$V_{oc}/V_{oc}(o)$
Electron	5600	111.1	0.954	0.972
Proton	2000	149.1	0.973	0.986
Combined	7600	99.5	0.940	0.965

Electron damage dominates by a factor of roughly 5 to 2.

(1) W. C. Cooley and M. J. Barrett, Handbook of Space Environmental Effects on Solar Cell Power Systems, NASA Contract NASW-1345, 1968.

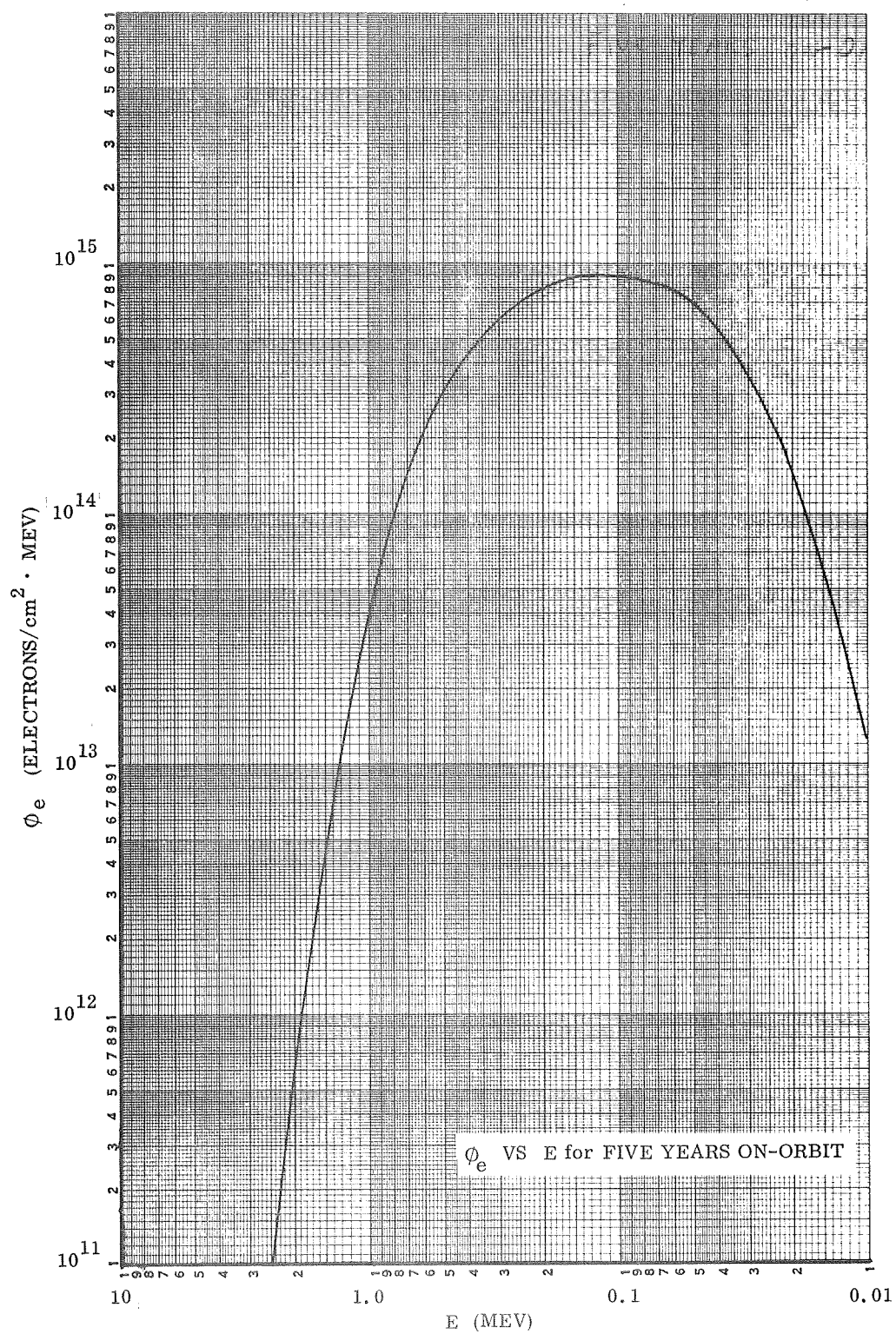


Figure 3-57 Residual Electron Differential Spectrum

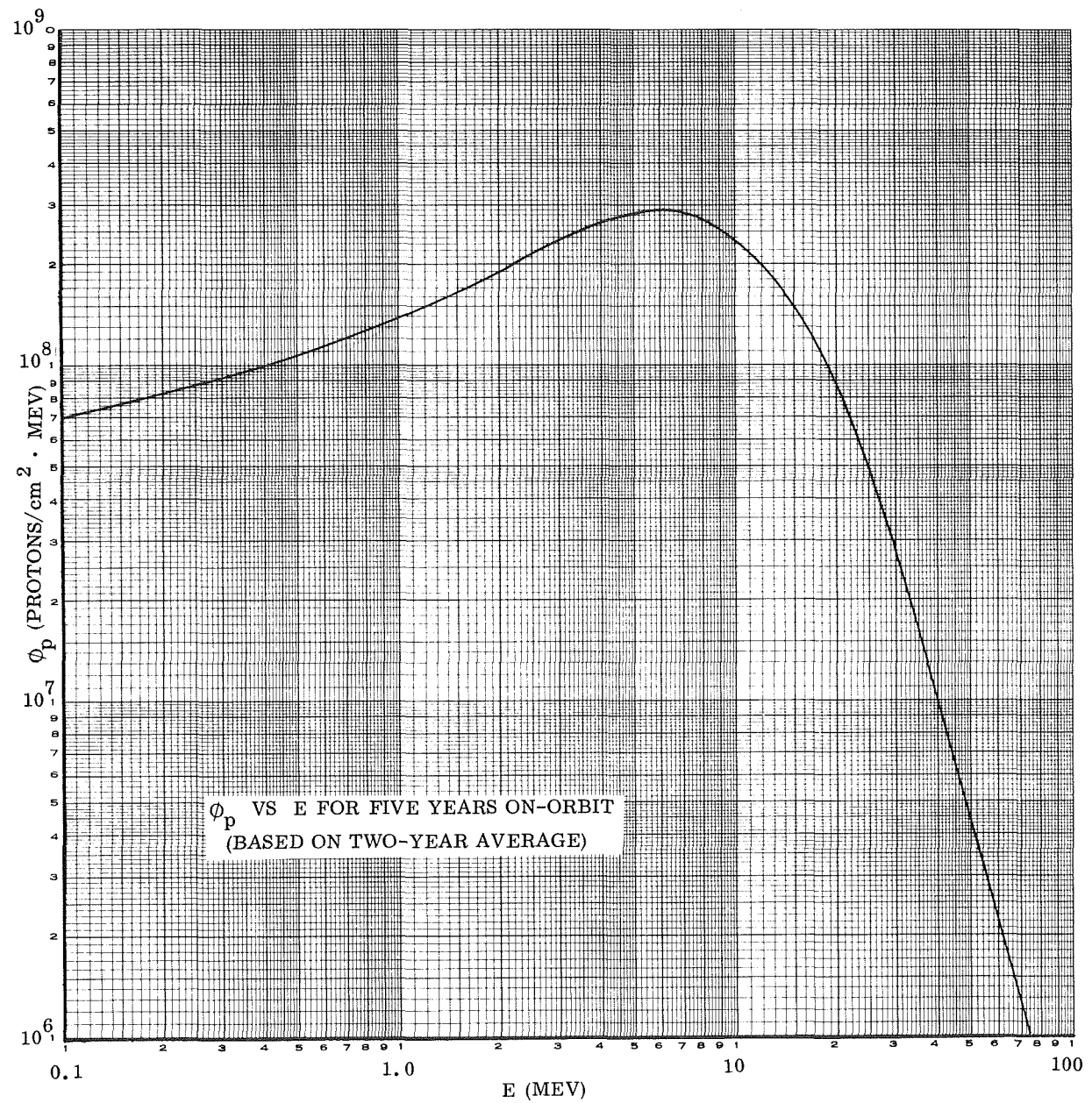


Figure 3-58 Residual Proton Differential Spectrum

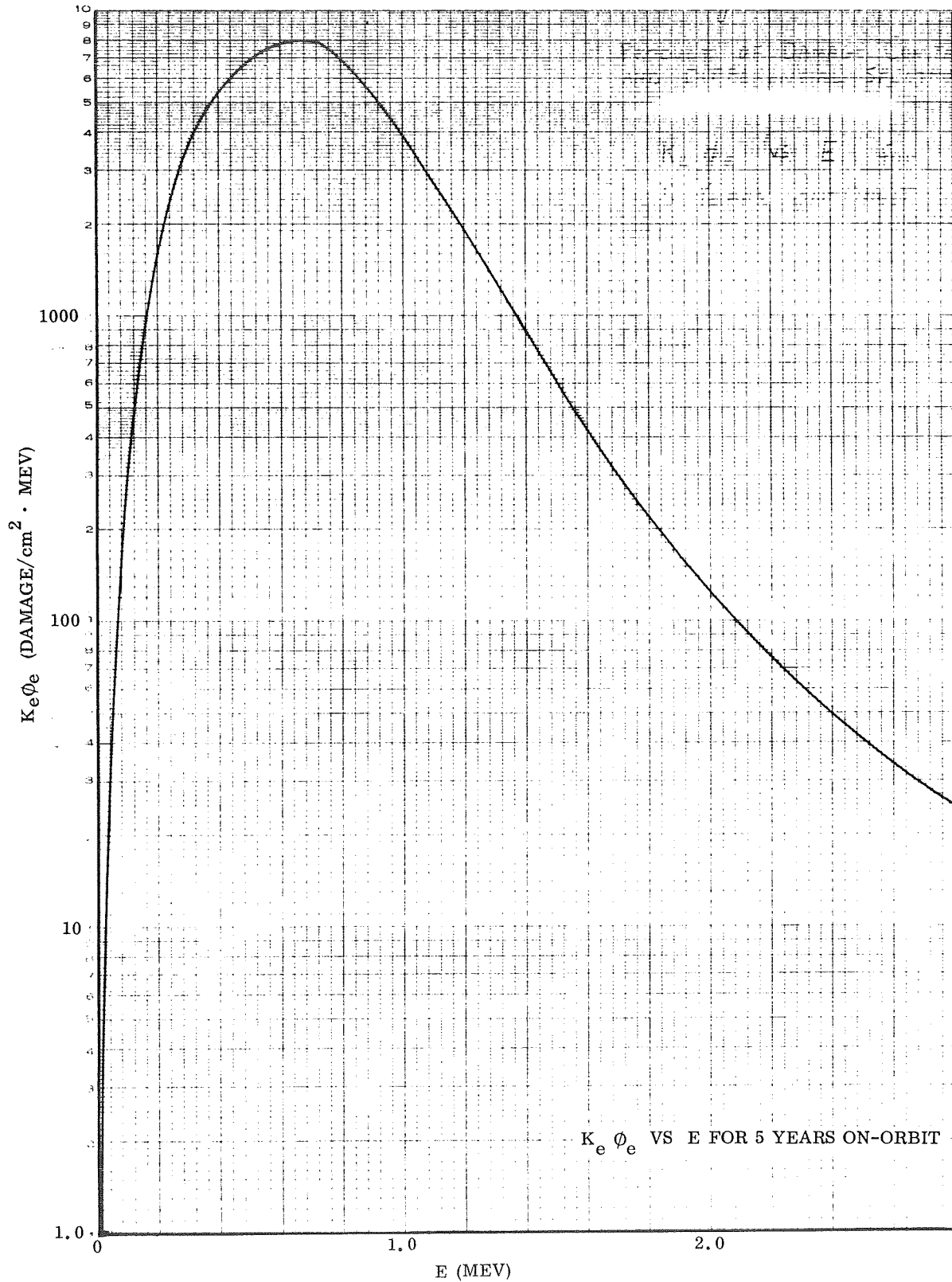


Figure 3-59 Product of Damage Constant and Differential Spectrum for Electrons

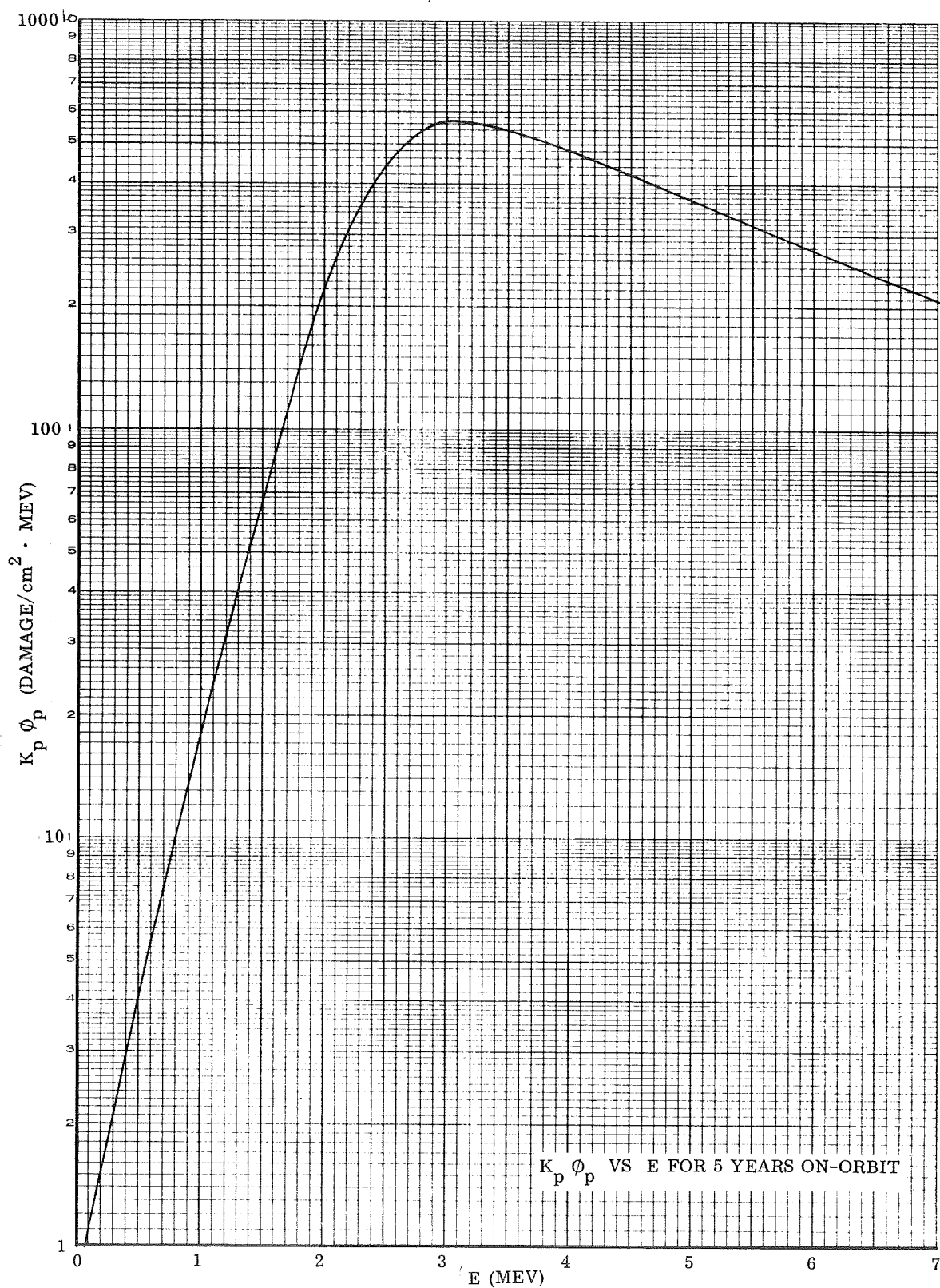


Figure 3-60 Product of Damage Constant and Differential Spectrum for Protons

3.7.2 Variation of Cell Equation Parameters to Express Solar Cell Degradation

This subsection presents the current status of the concept and formulation of a calculational technique which involves the expression of degradation data in parametric form. The parameters referred to are the fixed constants which appear in the solar cell equation and which, as a group, establish a unique shape for a cell I-V curve. The term solar cell equation means any of the forms, inversions, or approximations of the mathematical model which adequately expresses the current versus voltage behavior of a particular solar cell to the required degree of accuracy. The intent of this effort was to develop an alternative method of presenting solar cell degradation information, a method which particularly simplifies the task of the array design engineer.

The standard lumped-parameters equation for silicon solar cells is usually written,

$$I = I_L - I_o \left\{ \exp \left[\frac{q (V + IR)}{nkT} \right] - 1 \right\} - \frac{V}{p},$$

where the notation is as defined in Appendix B. The material which follows includes a brief discussion of two other useful solar cell equations to which parameterized degradation data might ultimately be applied. The IDSCS behavior, as observed in this study, is then presented in terms of parameters which vary with time on-orbit. Because complete I-V curves cannot be obtained from the IDSCS telemetry data, the previously discussed "translation approximation" is introduced to enable exploratory calculations of the satellite parameters to be made. When this assumption is checked against known ground irradiation data, it proves to be quite accurate, especially for the low fluences of interest to this program. One of the consequences of applying this assumption to satellite data, however, is that noncell losses (i. e., coverslide-assembly darkening) will unavoidably be included in the same process. This aspect is briefly addressed and the presentation concludes with an examination of the possibility of utilizing the parametric approach as a new tool in the task of separating cell and noncell degradations.

Other Solar Cell Equations

When recent vintage 2 x 2 cm silicon N/P cells are under consideration, the very simple inverted equation,

$$V = A + B \ln (I_L - I) - IR,$$

may suffice for preliminary design studies. The parameters, A and B, represent collections of the above standard parameters and have been defined elsewhere. Given A, B, I_L , and R as a function of time, a complete cell I-V curve and a complete array I-V curve may quickly be generated. Radiation degradations (both cell and noncell), temperature effects, and light variations may all be accommodated in these parameters. In the case of the inverted equation above, it can be shown that knowledge of I_{sc} , V_{oc} , and the values of the current and voltage at the maximum power point, I_m and V_m , is sufficient to compute all the equation parameters⁽²⁾.

IDSCS cells are 1 x 2 cm N/P boron-doped, phosphorous pentoxide-diffused silicon cells of 1964 vintage and, unfortunately, possess a shunt resistance of 350 to 500 ohms which cannot be neglected. A more general form of the cell equation,

$$I' = I_L - \exp \left[\frac{V(1 - R/P) - A + I'R}{B} \right],$$

discussed in Appendix B, will be assumed to apply. The above equation, with $I' = I + V/P$, can be written explicitly by a semi-iterative approximation to produce values of $I = I(V)$ which agree with the standard lumped-parameters equation to within ± 0.04 milliamps. Methods of calculating the equation parameters from I-V data have been presented in this study and elsewhere^(3, 4, 5).

(2) W. T. Picciano, Determination of the Solar Cell Equation Parameter From Empirical Data, Energy Conversion, Vol 9, pp. 106, March 1969.

Parameterized Satellite Data

Figures 3-61 through 3-65 present a compilation of IDSCS parameters applicable to the best- and worst-case updated V_{oc} and I_{sc} curves from the first two launches (15 satellites). We have assumed that no knee rounding occurs, i. e., that degradation on-orbit produces simple translations of the cell I-V curve along current and voltage axes. Evidence indicates that this approximation may actually be quite good; peak radiation damage regions appear to occur between residual electron energies of 0.5 and 1.0 MeV, and between residual proton energies of 2 and 4 MeV (see previous section). Published ground irradiation data indicate that cell degradations at these energies can be very adequately represented by simple curve translations. Figure 3-66 presents a derived result from the on-orbit parameter curves: the collection of best- and worst-case maximum power point curves, normalized to unity at time zero.

Verification of the Translation Assumption in Ground Data

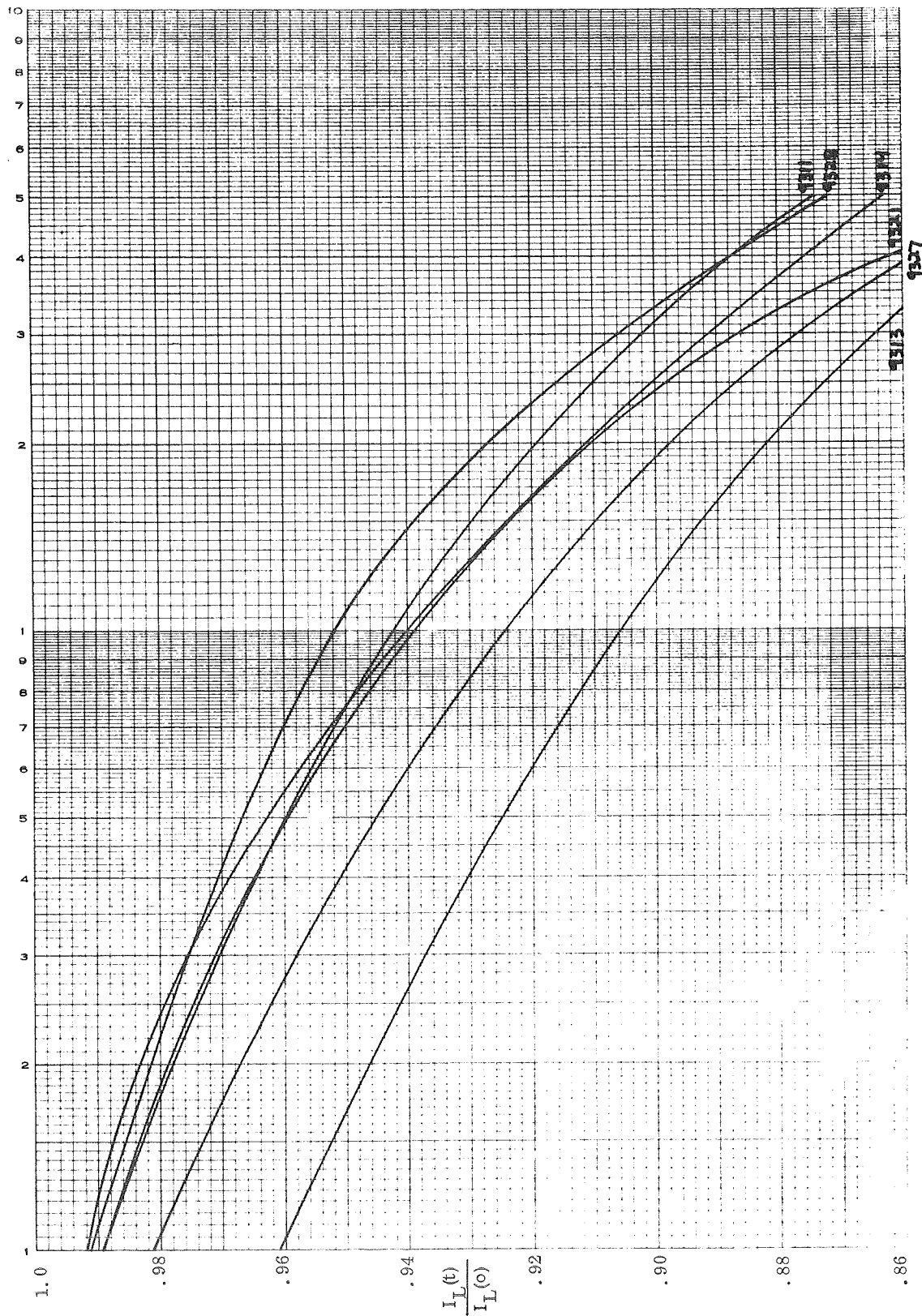
Figures 3-67 through 3-70 present the current status of a parametric representation of the Reynard⁽⁶⁾ data on 0.6, 0.8, and 1.0 MeV electron irradiations, and on 2.7 MeV proton irradiation. These curves have been derived from I_{sc} and V_{oc} data only, assuming the translation approximation. Figures 3-71 and 3-72 show the resultant V_{oc} and P_{max} behavior recalculated from the parameters. The agreement is excellent, especially at the low fluences of interest to this program. (Discrepancies of 0.5 to 2.0% are currently observed at the higher fluences because time has not permitted iterations within the error limits of the Reynard data.) The variations of the parameter B (Figure 3-69) are presented exactly as derived, but the presence of the very small negative dip in the electron curves might prove fallacious.

(3) Appendix C

(4) K. L. Kennerud, A technique for Identifying the Cause of Performance Degradation in Cadmium Sulfide Solar Cells, Proc. 4th IECEC, September 22-26, 1969, p. 561.

(5) M. J. Barrett, Synthesis of Solar Cell Parameters (Sec. III), an Analytical Review of the ATS-1 Solar Cell Experiment, Second Periodic Progress Report, Contract NAS 5-11663, Exotech Corp., June 15, 1969.

(6) D. L. Reynard, Proton and Electron Irradiation of N/P Silicon Solar Cells, Contract AF 04(647)-787, Lockheed Rpt. LMSC 3-56-65-4, 12 April 1965.



YEARS ON ORBIT

Figure 3-61 IDSCS Parameter I_L

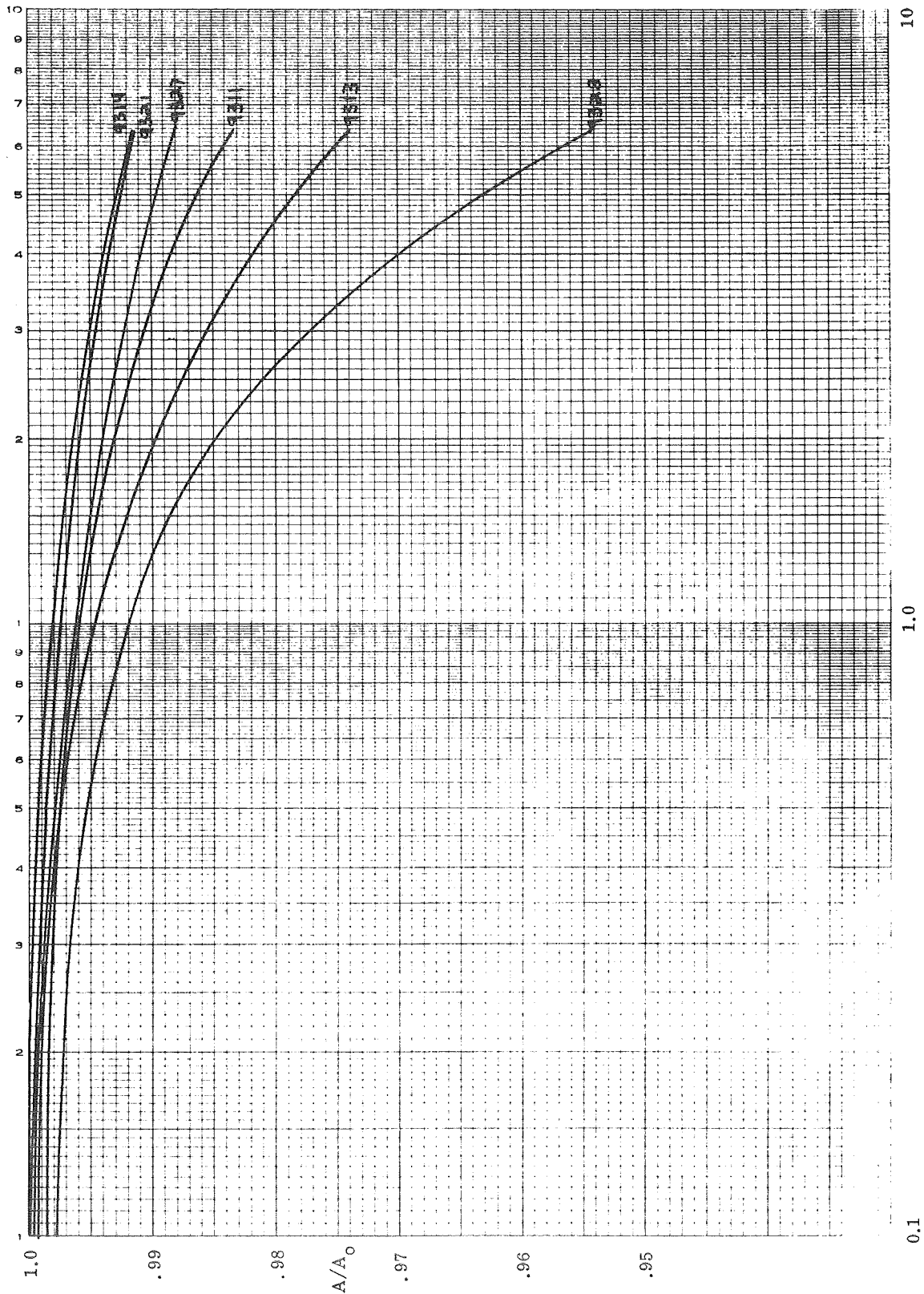
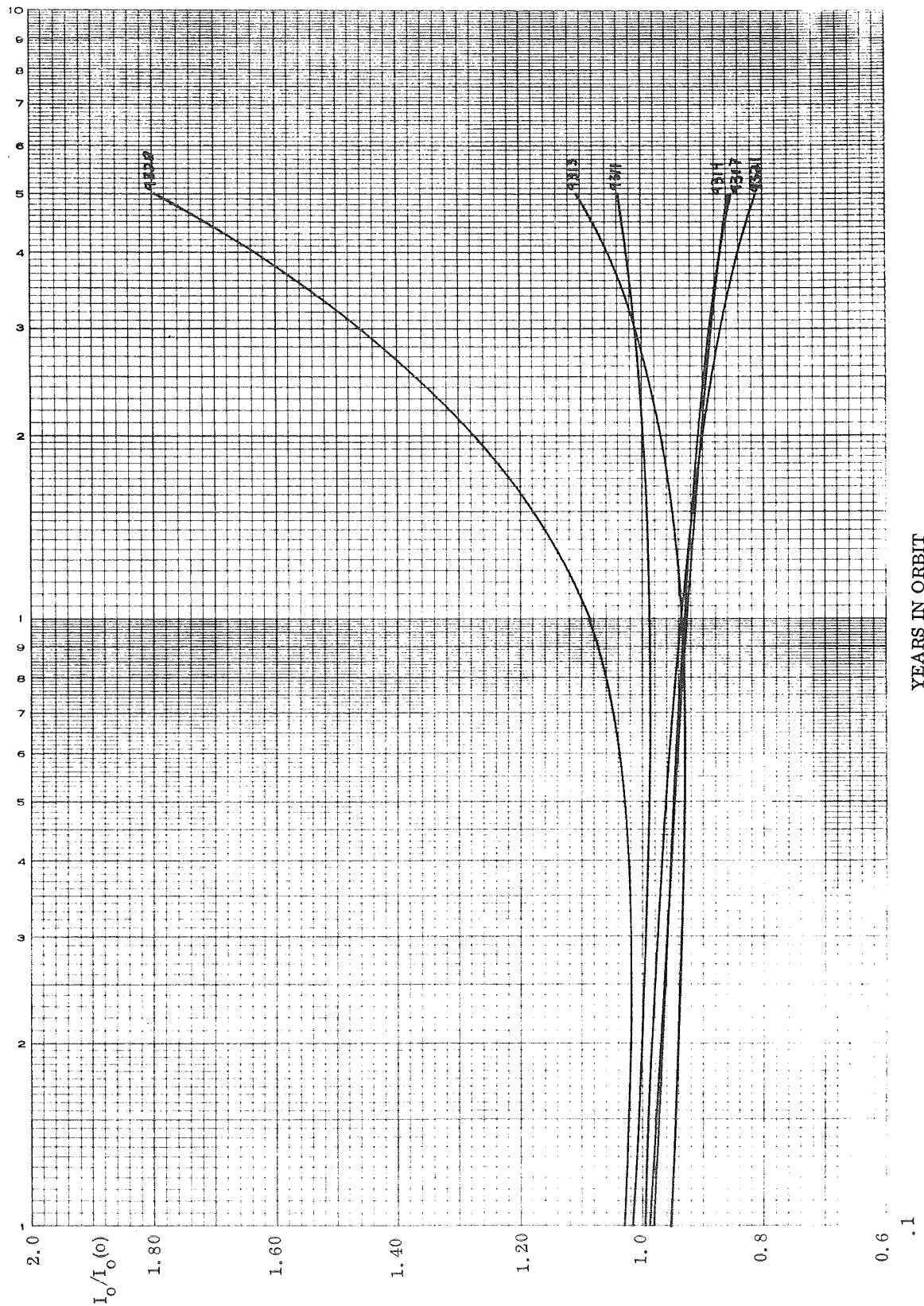


Figure 3-62 IDSCS Parameter A



YEARS IN ORBIT

Figure 3-63 IDSCS Parameter I_o

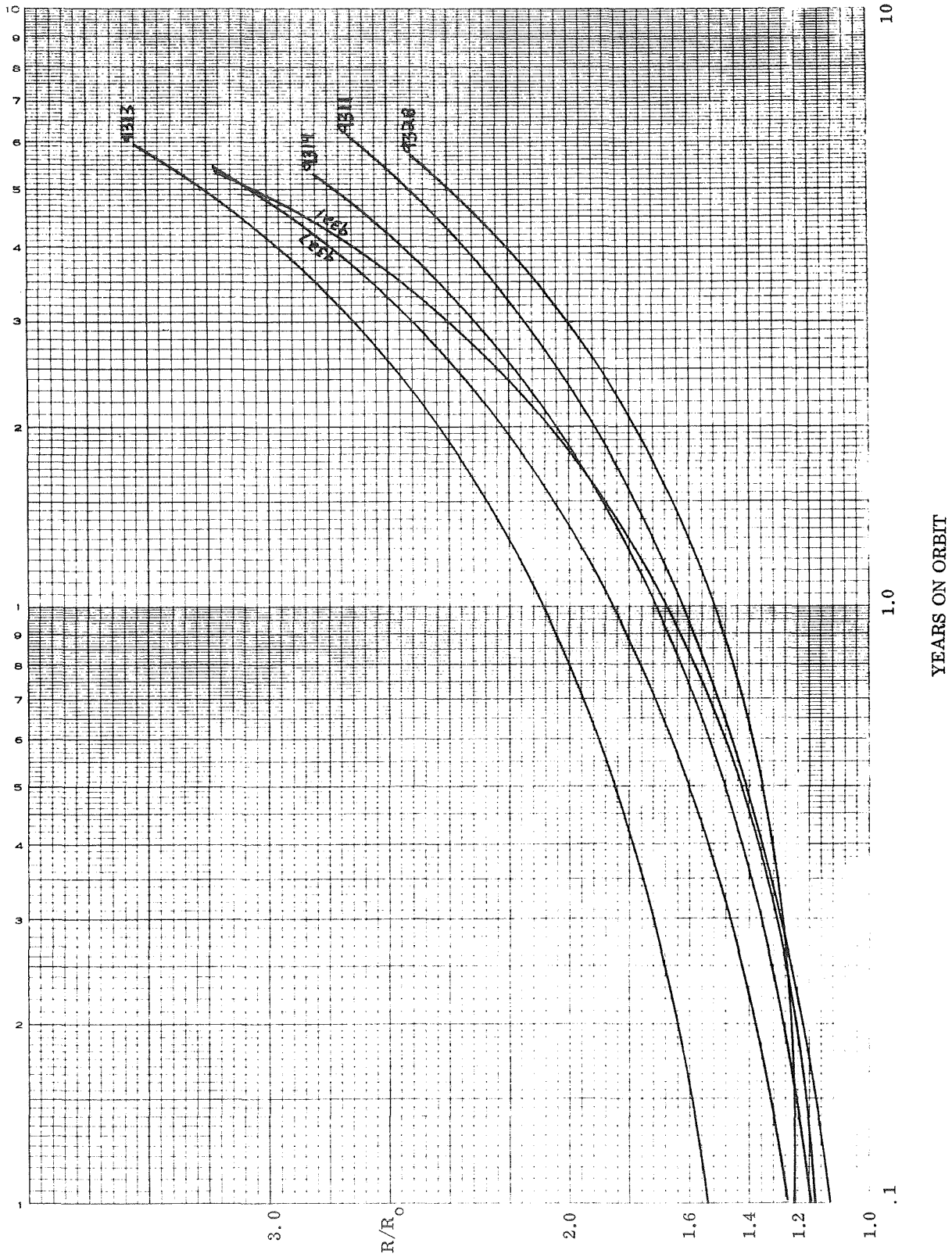


Figure 3-64 IDSCS Parameter R

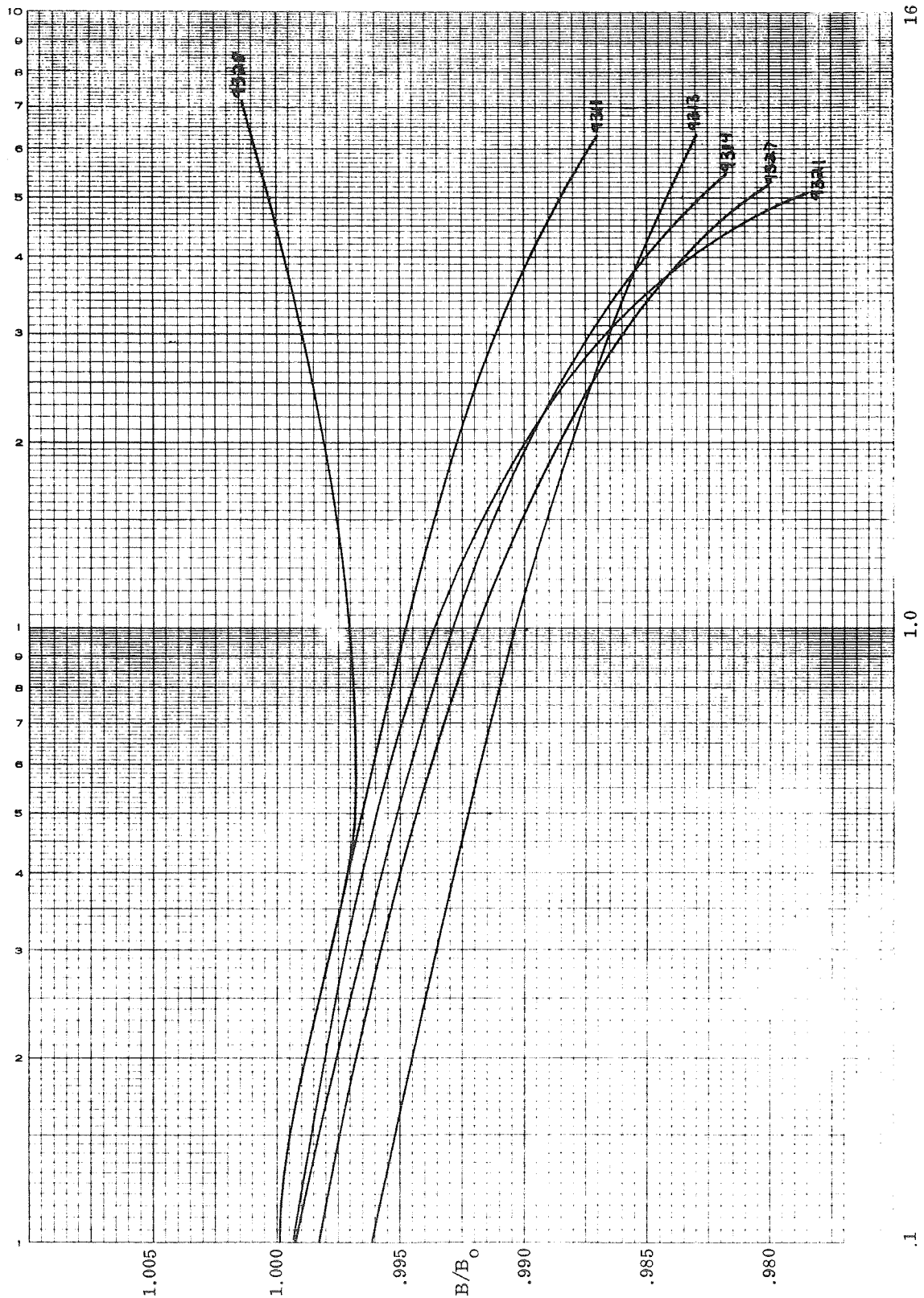


Figure 3-65 IDSCS Parameter B

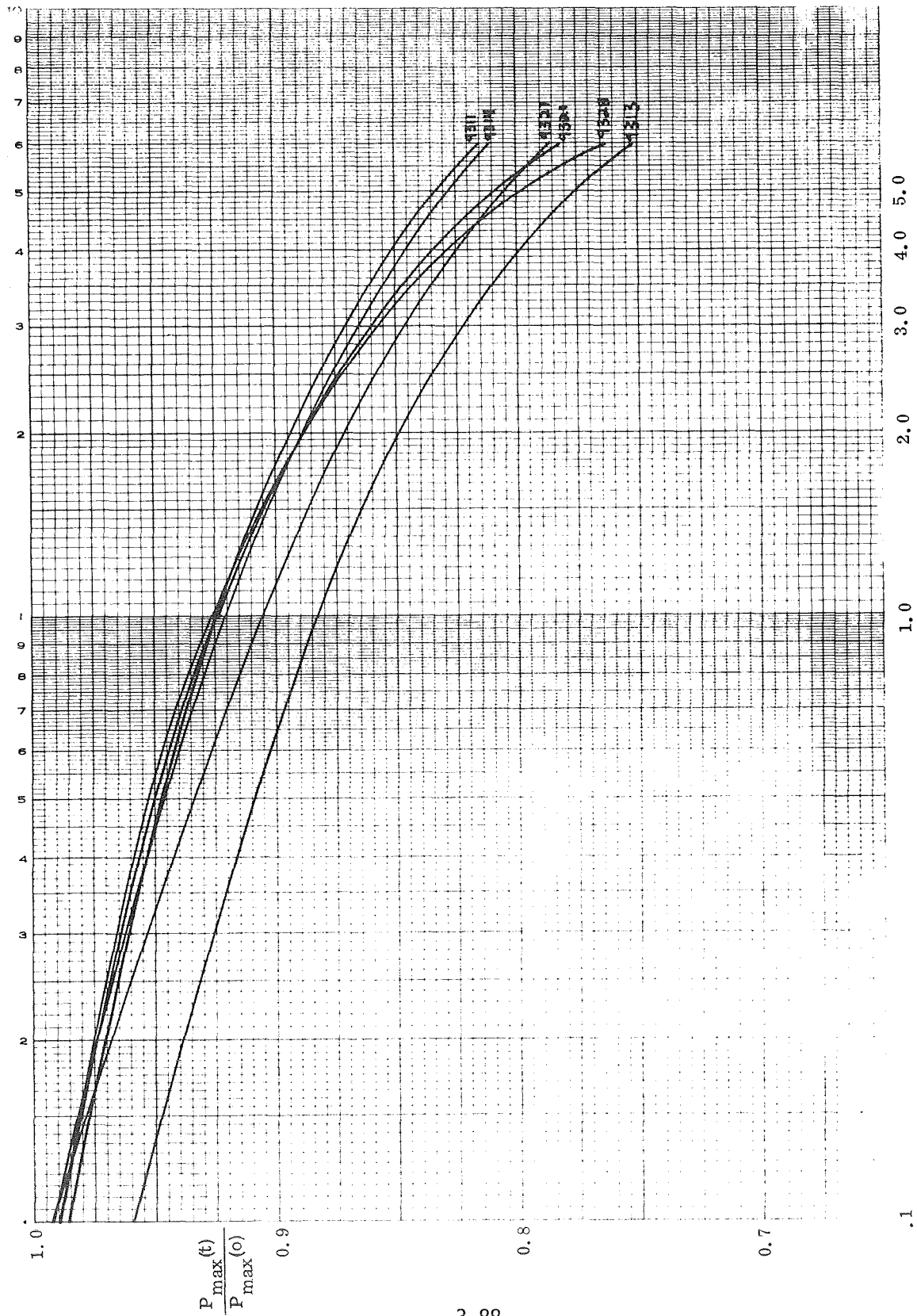


Figure 3-66 IDSCS Parameter P_m

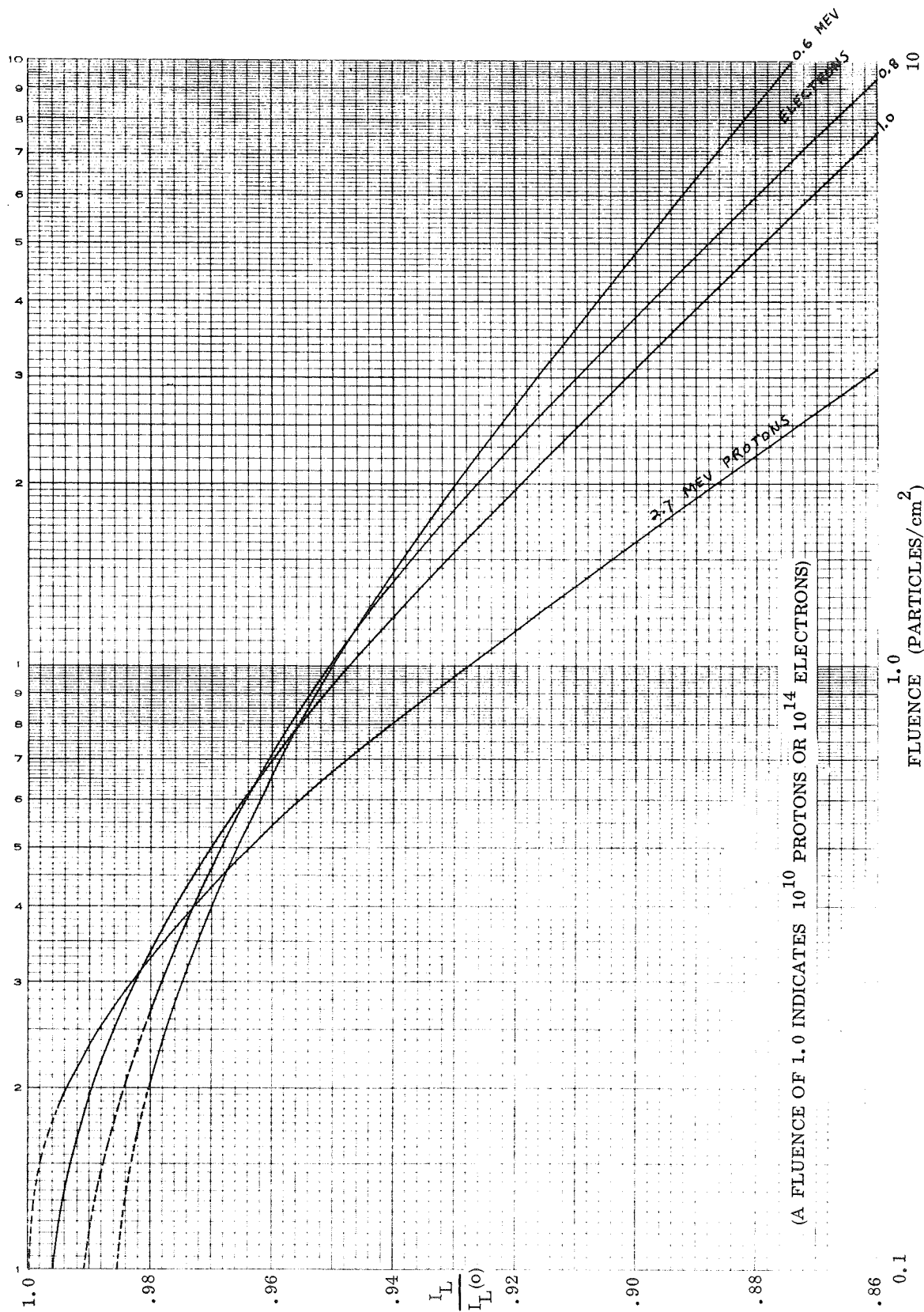


Figure 3-67 Ground-Irradiation Data Parameter I_L

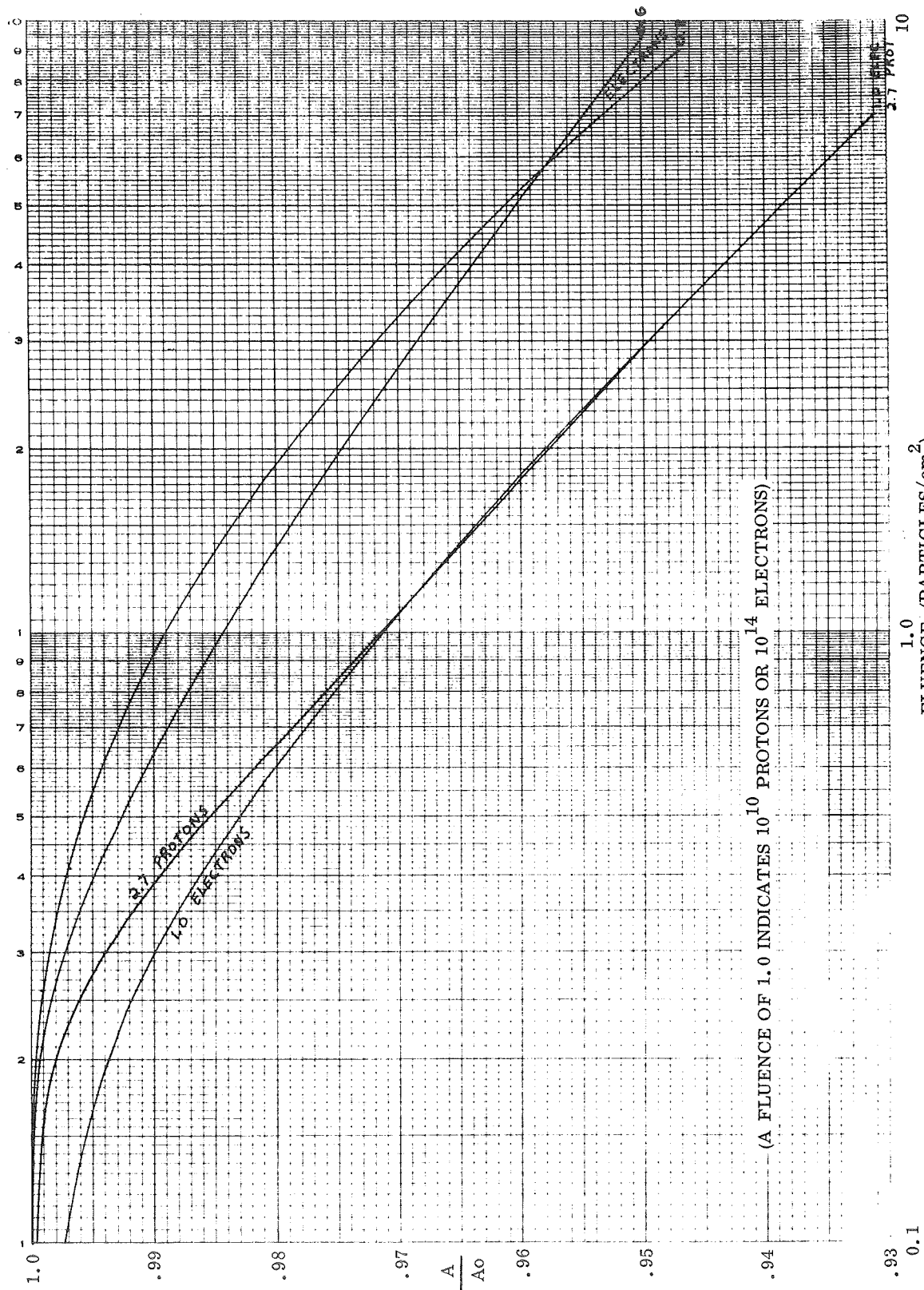


Figure 3-68 Ground-Irradiation Data Parameter A

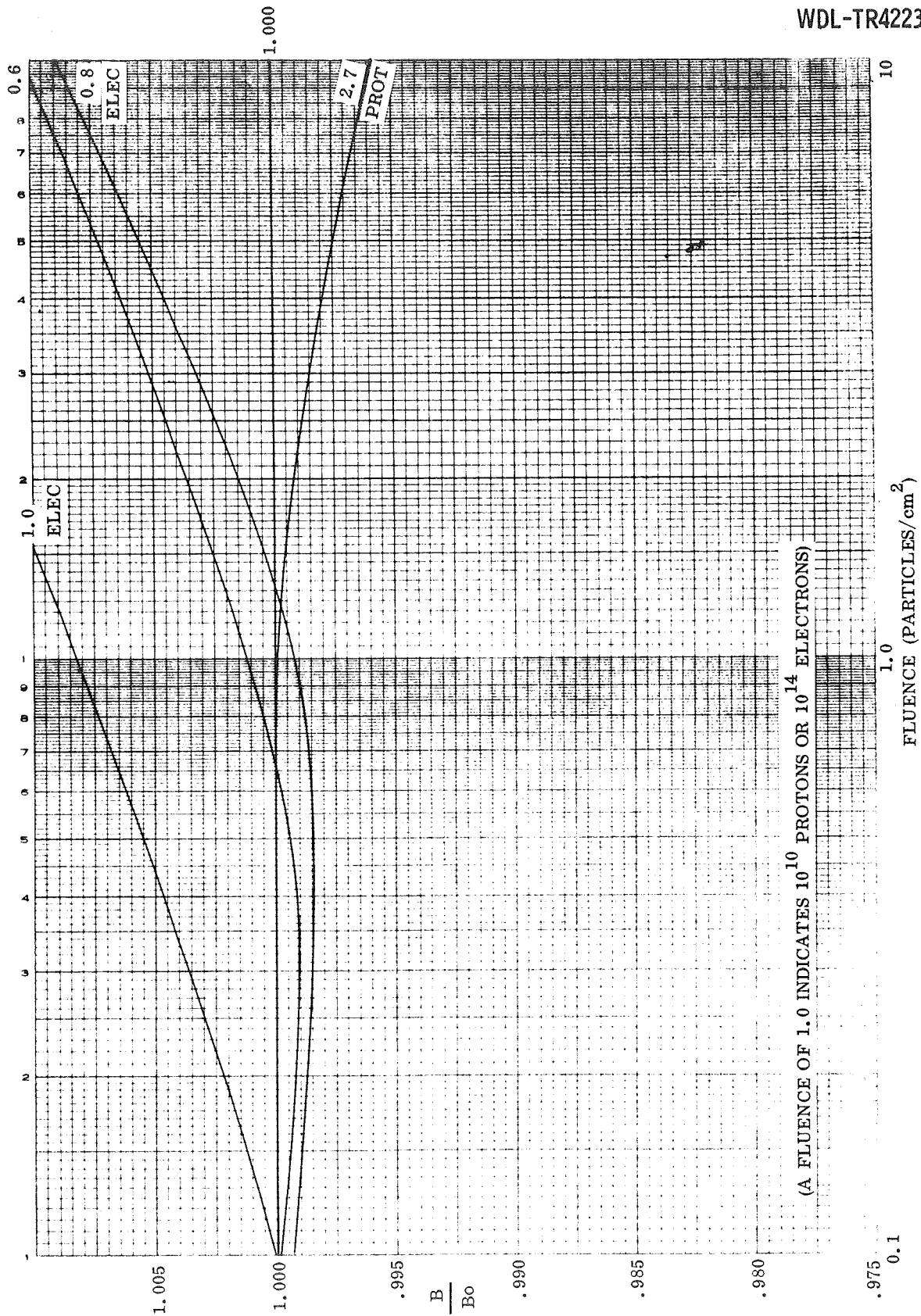


Figure 3-69 Ground-Irradiation Data Parameter B

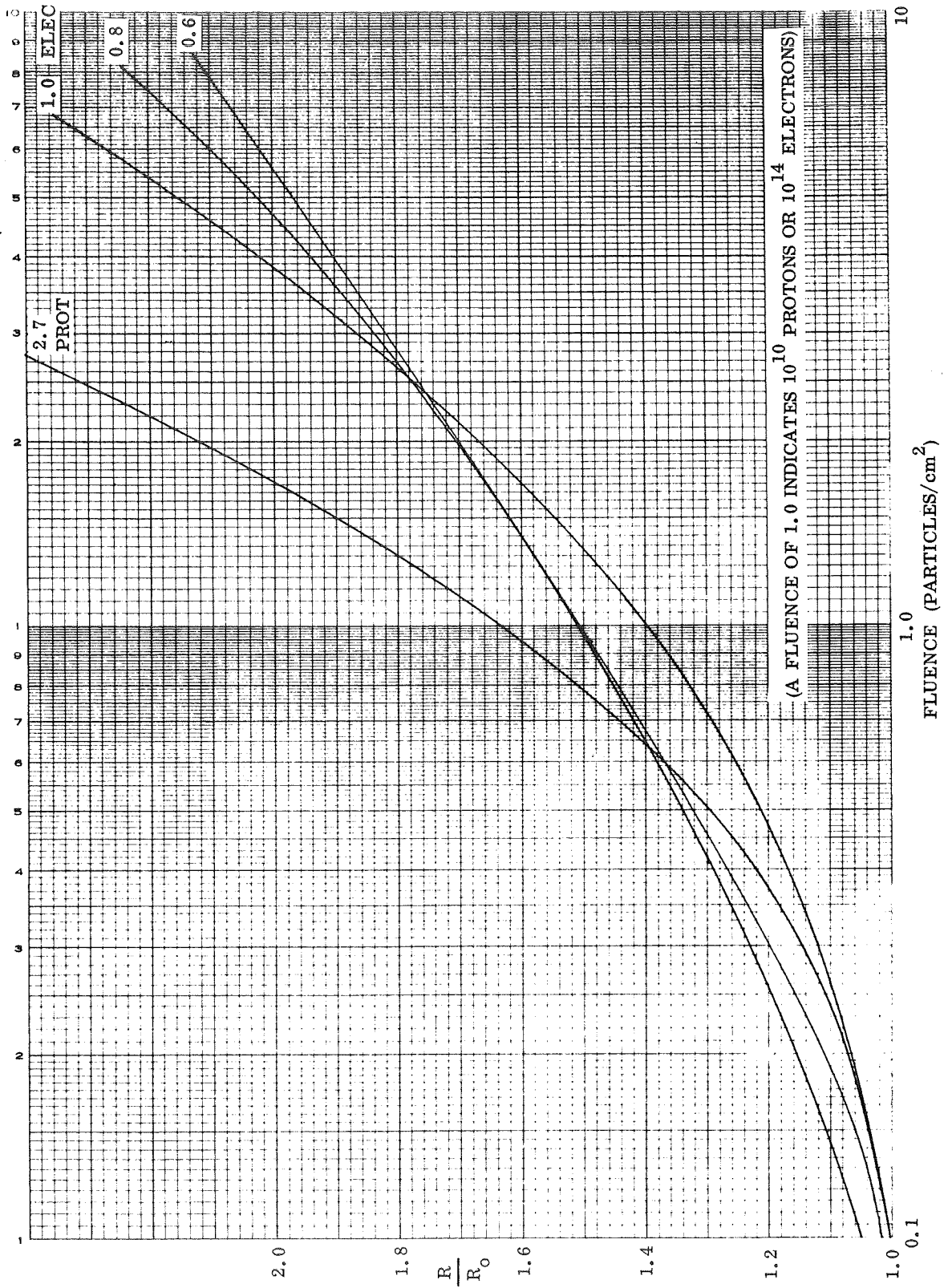


Figure 3-70 Ground-Irradiation Data Parameter R

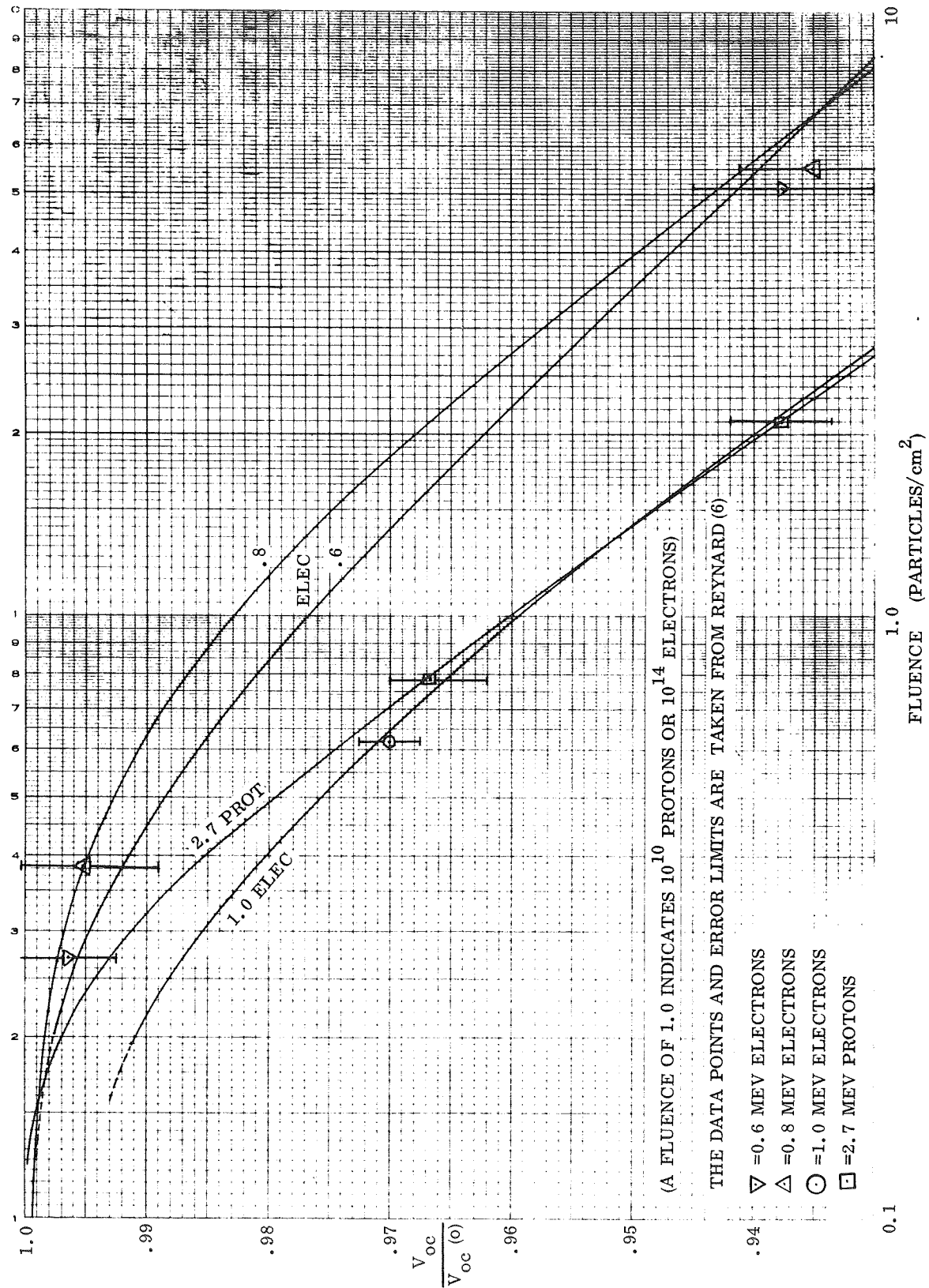


Figure 3-71 Relative Open-Circuit Voltage For Electron and Proton Irradiation

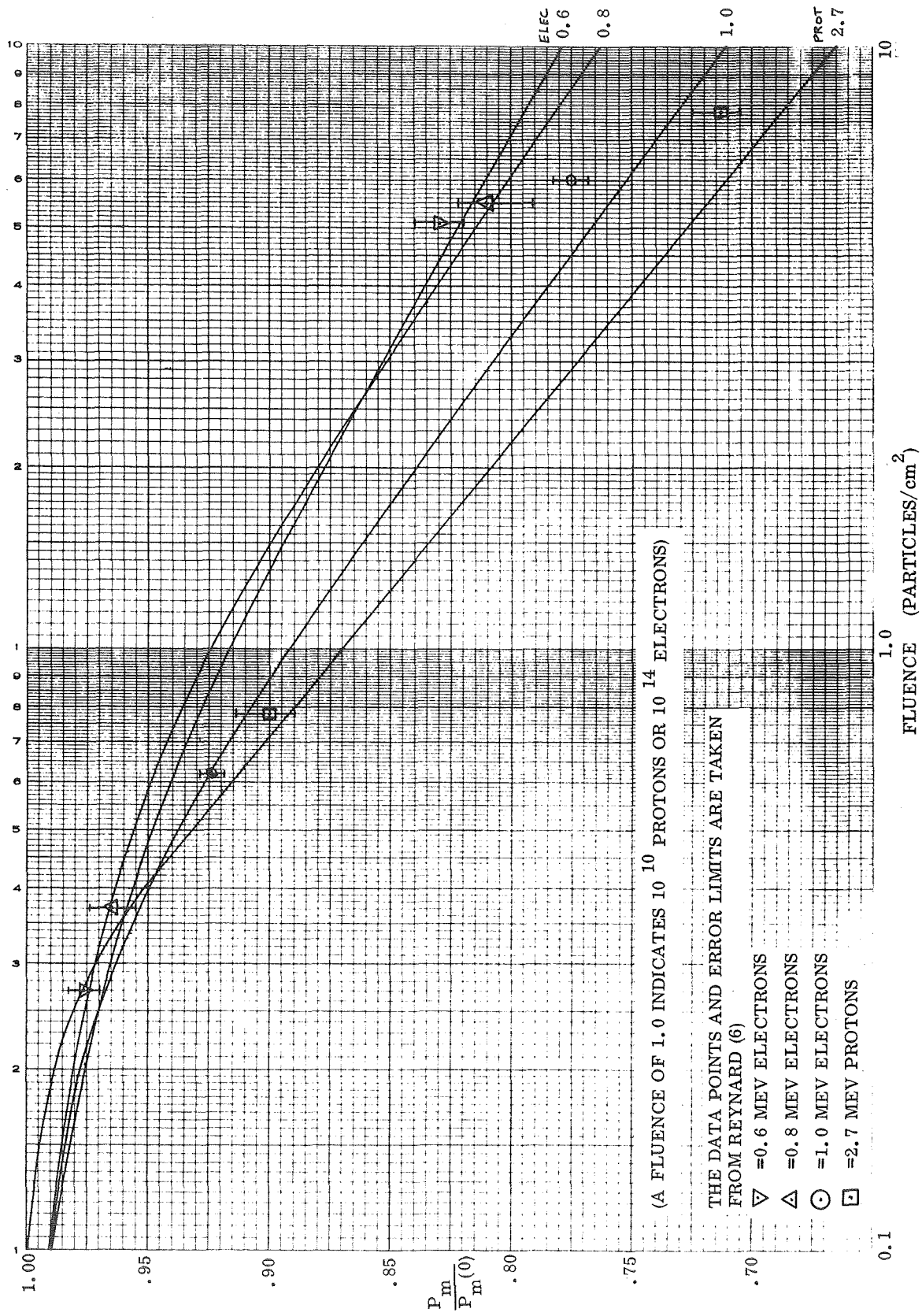


Figure 3-72 Relative Maximum Power for Electrons and Proton Irradiations

3-94

Parameterization of Noncell Losses

The parametric plots of the satellite data result directly from the regression functions derived in Section 3.4. Shunt resistance, P , has been held constant at 370 ohms. No separation of cell and noncell damage has yet been attempted in the parameterization. It is of interest, however, to examine the effects on A , B , and R of a pure light loss to the cell under the translational assumption we have been applying. As I_L lessens, V_{oc} undergoes a slight lessening also, due to the curve shift along the current axis and the negative slope at V_{oc} . The resultant parameters are plotted in Figures 3-73 and 3-74 versus I_L/I_{Lo} . The implications of a 10% coverslide darkening would be an apparent, but nonreal, increase to R/R_o of a factor of 2.2, a decrease in B/B_o of 0.987, and a decrease in A/A_o of 0.998. When corrections for various degrees of slide assembly losses are applied to the satellite parameters, a more recognizable cell degradation signature may be produced. Thus, cell and noncell losses might be distinguished by further detailed and careful study of parameter behavior.

3.7.3 Time Dependence of Noncell Losses

This section discusses another approach that was tried (with the previously published data) in an effort to separate cell from noncell degradation. The term "noncell" collectively refers to the coverslide, blue filter, anti-reflective coating, and adhesive. "Noncell degradation" refers to temporal light-energy loss due to coverslide or adhesive darkening, increased surface reflection, or spectral shifts within the coverslide assembly.

Examination of the I_{sc} degradation plots near the time-zero axis shows points somewhat higher than the fitted function; this suggests that noncell loss mechanisms might be more probable during some period near start-of-life. Three First Launch Satellites were tested in the regression to the theoretical degradation function, but with the first 100 days omitted. The results are plotted in Figure 3-75. The three curves are observed to lie very close (less than 0.7% divergence). If these curves are assumed to represent pure "cell" degradation, and the previous results to

represent "cell" plus "noncell" degradation, the difference of the two curves might represent pure "noncell" degradation. This hypothesis suggests that noncell losses on the order of 3% ($\pm 2.5\%$) take place within the first few months on orbit. Recent ground test data, in fact, appears to substantiate this observation⁽⁷⁾.

There still remains a discrepancy in that the observed 1000 day degradation is still greater than the calculated I_{sc} degradation. Obviously, the 100 day loss need not represent the total loss to the noncell components and may only reveal, for instance, the ultraviolet contribution. Trapped particulate radiation, very likely the lowest energy electrons and protons, would provide a reasonable source for long term degradation to the slide or anti-reflective coating. It is interesting to examine the updated noncell curves in the Summary Report (Figure 1-3) which were produced by removing the theoretical I_{sc} degradation from the observed total I_{sc} degradation. In the two curves shown, large losses are indicated for the first year, followed by a nearly linear degradation from that point on. The linear aspect of the noncell behavior might suggest new insights, but it must be warned that the mathematics involved may have forced its appearance because of the linear multiplier in the regression function. This need not be a disparaging observation, however, since if the function is truly a good representative of the dot data, the linear aspect could indeed be physically present. Further study might profitably be done along these lines.

(7) Communication with Dennis Curtin, COMSAT Corp, 3 Dec 1969. Bell Telephone Laboratories and RCA have tested 25 mil Corning 7940 with blue filters and various adhesives (G.E. RTV 602, Sylgard 182, and XR-6-3481). Conclusions to date indicate transmission losses ranging from 3 to 5 percent with ultraviolet irradiation with the greatest rate of change occurring during the first several hundred equivalent sun hours. Adhesives degraded less than 1%. Additional UV irradiation, 1 Mev electron and 17 Mev proton irradiation produced "no appreciable change". About 10% of all samples, unfortunately, behaved anomalously and degraded from 10 to 30 percent within the first hundred hours of UV irradiation.

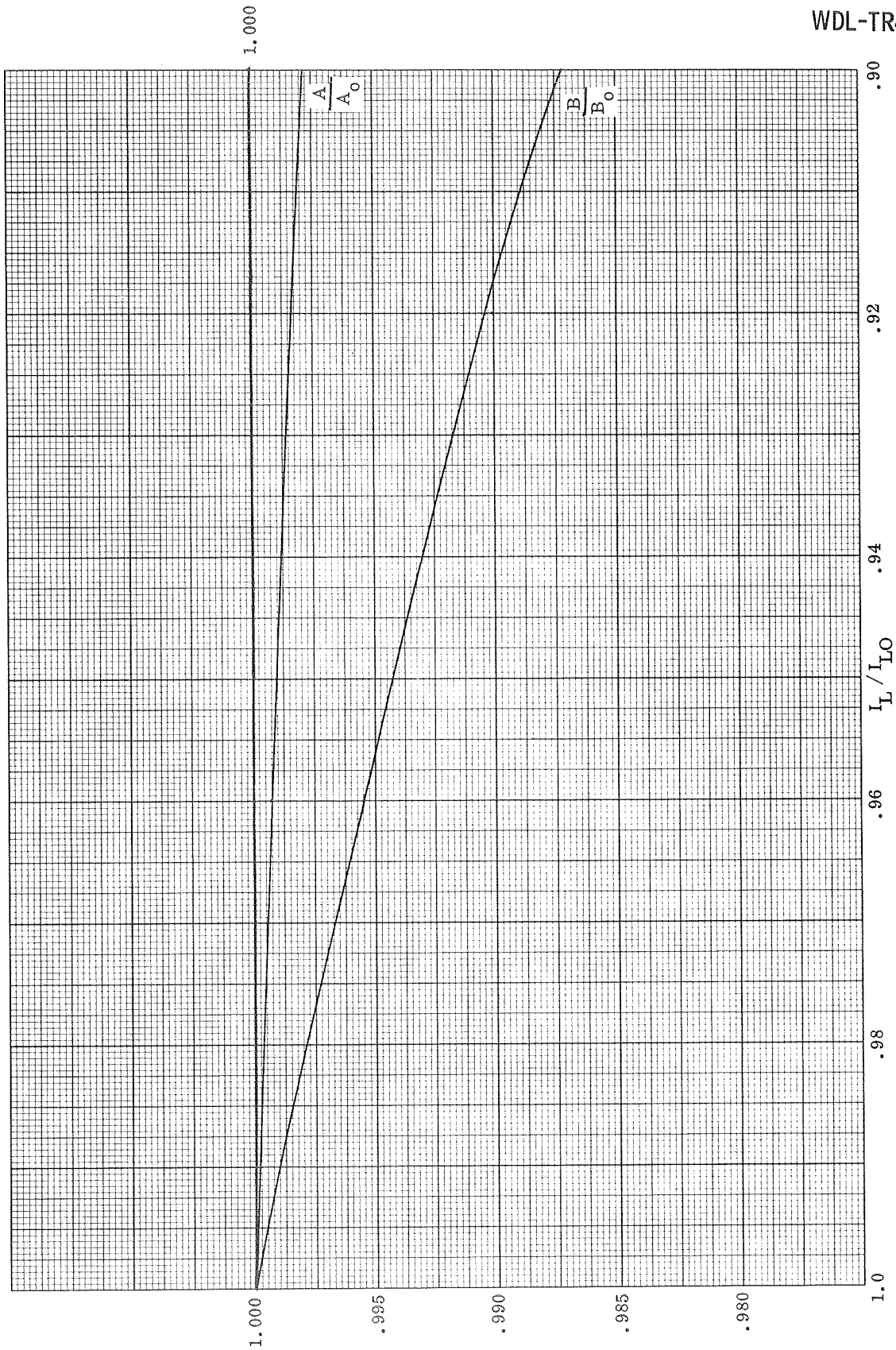
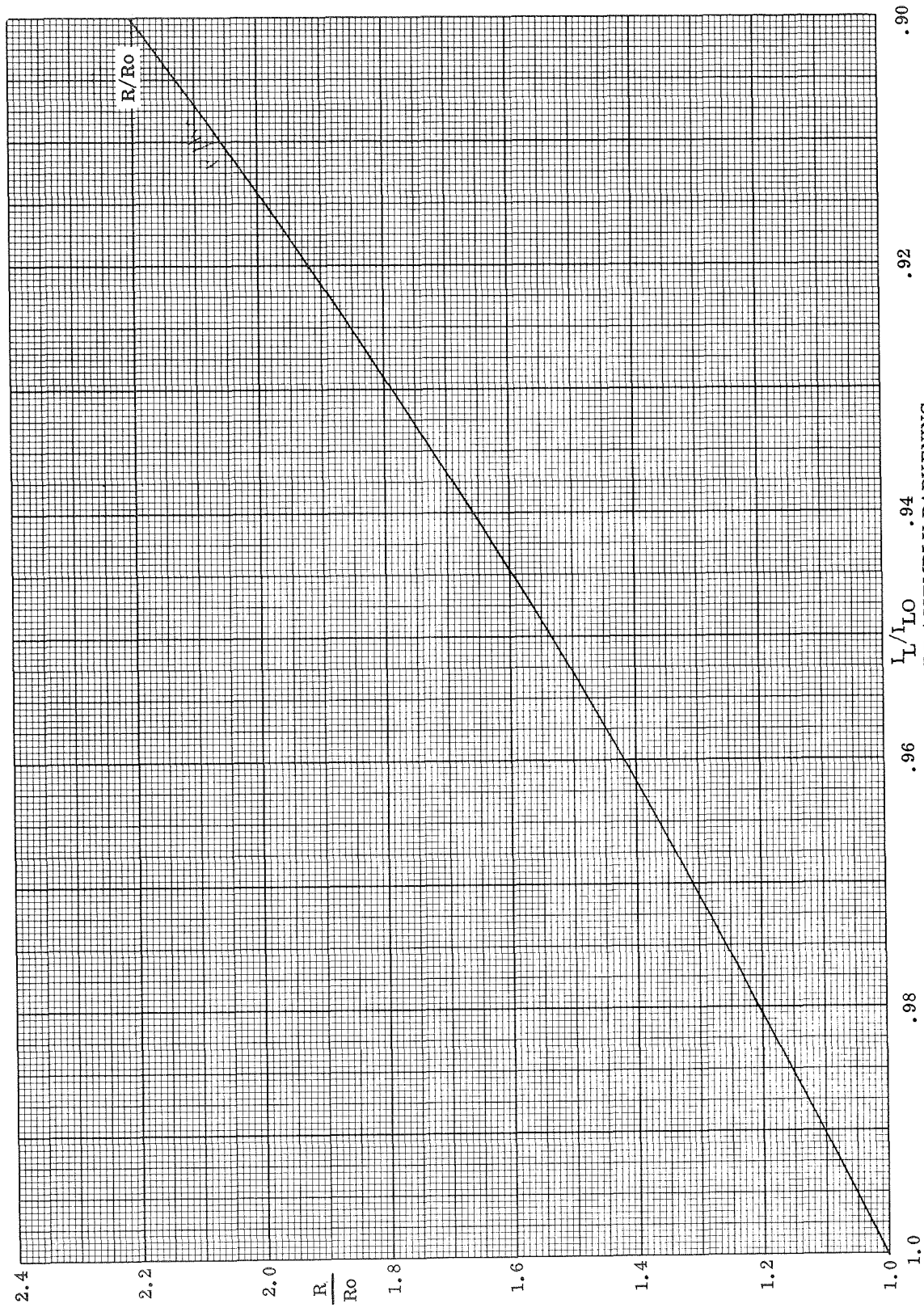


Figure 3-73 Effect on Parameters A and B of Pure Non-Cell Loss



PURE COVERSLIDE ASSEMBLY DARKENING
Figure 3-74 Effect on Parameter R of Pure Non-Cell Loss

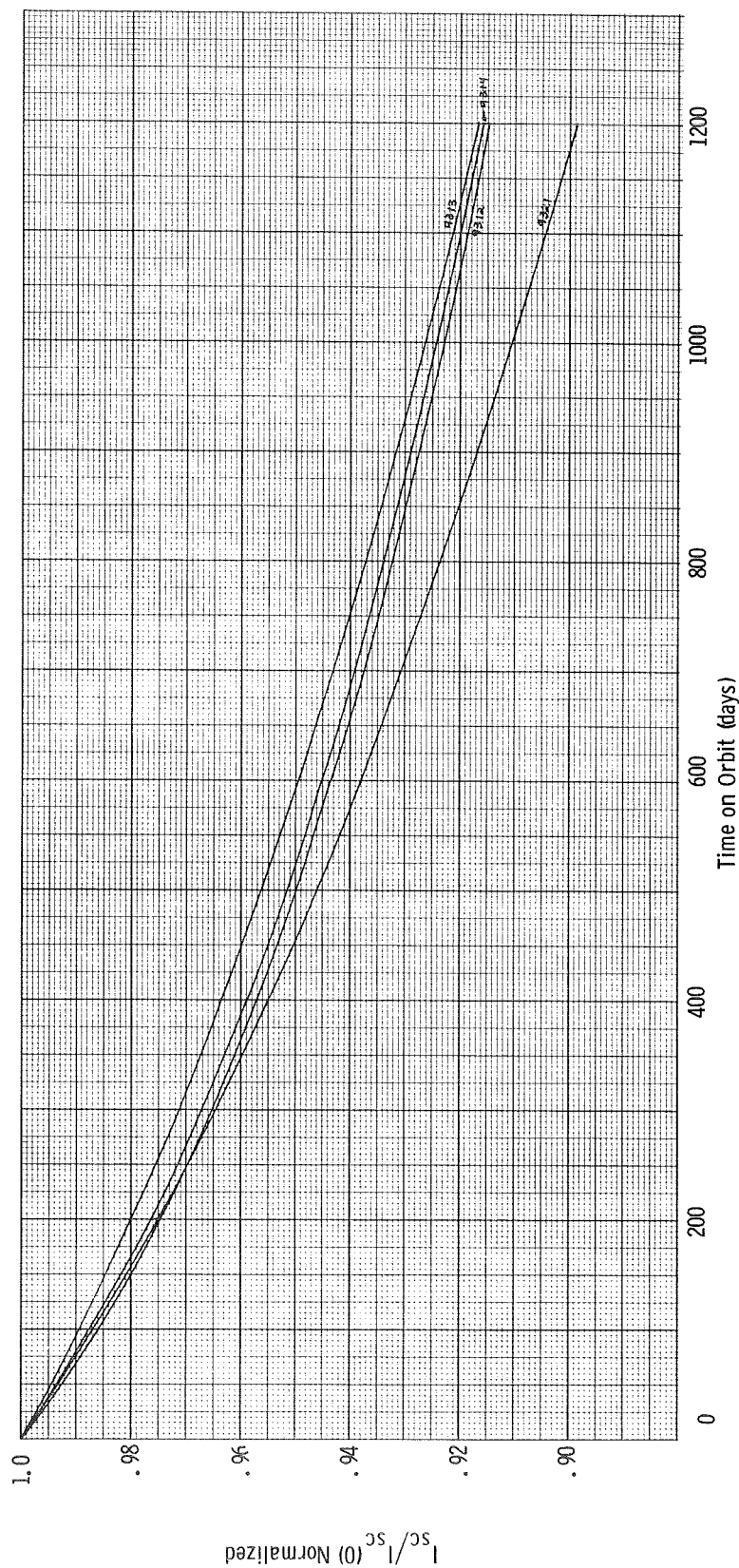


Figure 3-75 Regression Curves to Theoretical Cell Degradation Function with First 100 Days of Data Points Omitted

3.8 STUDY OF ANOMALOUS SEASONAL VARIATIONS AND VARIATIONS DUE TO CELL FAILURES

3.8.1 Seasonal Variations

A visual examination of the computer dot plots of the degradation ratios versus time has suggested that a superimposed sinusoidal variation rides on the overall trend. Three potential sources of systematic periodic error have been investigated:

- a. The Diode Intensity Factor: The solar cell equation is based on a mathematical model which, in its simplest form, is a current generator in parallel with a diode. Variation of incident light energy has been assumed to affect the I_L term only, whereas the remaining collection of terms (the diode) also varies slightly with intensity.
- b. The Cosine-Correction Factor. Lambert's Law indicates a direct equivalence between the illumination of a plane surface and the cosine of the angle between the incident light and the surface normal. In a solar cell, however, the light-generated current varies somewhat depending on where in the cell minority carriers are produced by absorbed light. The larger the incidence angle, the closer to the junction the carriers will be produced, but the higher the probability of absorption in the heavily doped surface region. The former aspect is an enhanced contribution to current and the latter, a loss. Thus, a plot of I_L versus the cosine of the angle of the incident light deviates slightly from the linear Lambert Law.
- c. Zonal Imbalance: Satellite geometry produces three distinct zones on each vehicle. During one-half of the year, the upper zone has a more favorable sun angle for producing power than the lower zone, and vice versa for the other half of the year. If, by chance, the average solar cell used in assembling the panels in one zone were slightly better, relative to the average cells used in the other zone, a periodic power output variation would result.

The Diode Intensity Factor

Two diode intensity corrections were derived from measurements made in the Philco-Ford Space Power Laboratory. The data were in the form of complete I-V curves at incident light angles varying between 0° and 80°. To avoid cosine correction effects, short-circuit current ratios were read from the curves and used as intensity ratios with no reference to the corresponding light angles. The major deviation between current as calculated from the applied solar cell equation and the data appeared between V_{oc} and $0.8 V_{oc}$ at lower intensities. This deviation suggested a correction to the cell parameter, A; A appeared to vary with the logarithm of the intensity ratio, ϕ . Plotting A versus ϕ on semi-log paper produced the relation:

$$A = A_o - .01557 \ln \phi.$$

Other experimenters have reported a diode term dependence varying with $\ln \phi$, but the above relation does not produce this. In the standard solar cell equation, the quantity I_o essentially multiplies the diode term; since $I_o \equiv \exp(-A/B)$, the diode term would effectively be multiplied by a correction factor of ϕ raised to a fixed power:

$$\phi^{0.01557/B} \simeq \phi^{0.4}.$$

A second correction factor, based on the same data, was derived in terms of A/A_o ,

$$A/A_o = 1.0433 - 0.04365 \phi + 0.032 \exp(-4.513 \phi).$$

This factor produced excellent agreement with the lab data and was subsequently computerized into the analysis program. Test cases were run on first launch satellites and the resultant square error compared with earlier runs. No improvement was observed and the correction was judged insignificant.

The Cosine Correction Factor

A number of sources were reviewed to obtain information on cosine modification functions. Data taken at Philco-Ford, at Heliotek, and at Johns Hopkins University⁽¹⁾ generally indicated a negative correction to the cosine for large angles and a positive correction for near normal angles; TRW data⁽²⁾ indicated a universal negative correction which was greatest near 70°. A reasonable general form for the Philco-Ford and Johns Hopkins data was a simple sine function modified by an additive linear function which could pivot about the 0° point. More accurate correction functions could be derived to fit any one set of data, but the variations and inconsistencies among the different sources indicated that knowledge of this function was too uncertain to warrant much added sophistication. Our function was introduced into the analysis program (modifying all individual solar cells), the program run with satellite data, and the resultant scatter measured. The parameters of the function could be varied until the sum of the square errors of the degradation ratio points about their fitted mean was minimized. Figure 3-76 shows the first result of this type of calculation with satellite No. 9312. Defining u as $\cos \theta$, the corrected u was of the following form:

$$u' = u - A \sin 2\pi u + b(1 - u).$$

The variation of A produced minimum scatter at about $A = 0.035$, with $b = 0$. Comparing the magnitude of this maximum correction to the other available data (taken on single cells in ground laboratories), we obtain the following:

-
- (1) Solar cell output as a function of Angle of Incidence, data taken by John Hopkins Applied Research Laboratories and quoted in a Heliotek information release, no date (circa 1965).
 - (2) TRW, Solar Array, Minimum Output Characteristic Computer Program, Appendix A, IOC 9361.4-237, 29 December 1964.

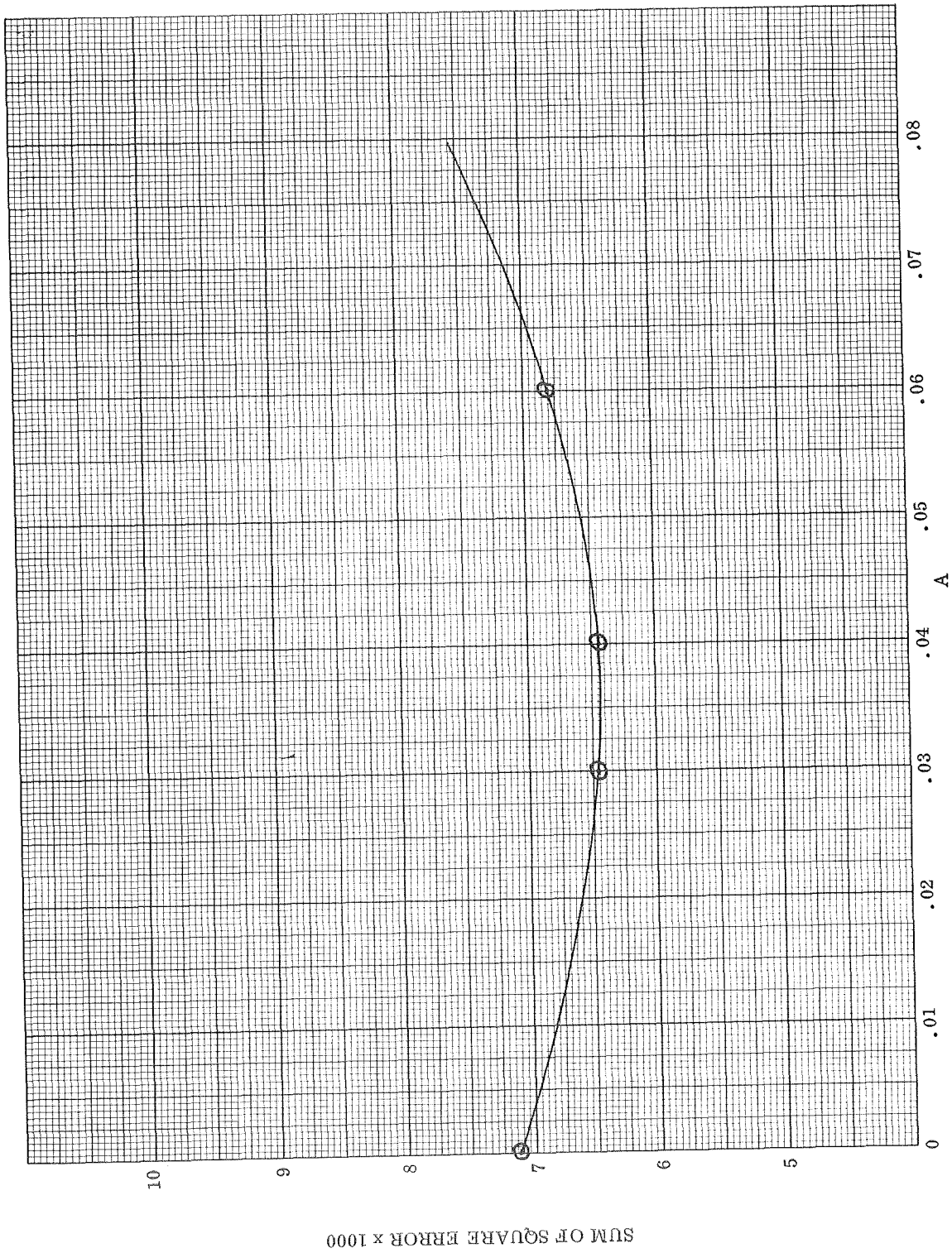


Figure 3-76 Cosine Correction Factor vs Square Error

<u>Source</u>	<u>Max. Correction to u</u>	<u>At u =</u>
This Study	-0.035	0.25
	+0.035	0.75
Philco Lab. Data	-0.034	0.23
	+0.017	0.87
Johns Hopkins/Heliotek	-0.054	0.26
	+0.030	0.77
TRW	-0.050	0.27

There appears to be some consistencies despite the variations. Time has not permitted an iteration on b or other detailed studies in this area. The 10% reduction in scatter observed in Figure 3-76 is significant, and indicates the potential of an analysis program such as this to extract subtle behavior factors from masses of crude telemetry data. However, no major changes in degradation rates, curve shapes, nor end-of-life to start-of-life ratios were effected in the overall data. The correction factor did have the effect of translating the curves slightly, in comparison to the previously published curves, and the decision was made to remove the factor from the program. If the factor had been retained, our final update would have required a complete rerun of all the previous data, instead of just the 14 or so new points.

Zonal Imbalance

The average I_L output of Zone I solar cells was adjusted mathematically to test two hypotheses: the average quality of cells might differ by a few percent between Zones I and III, and/or a cell failure or a single anomalously darkened coverslide might upset average zonal balance. The surprising 10% spread in initial array short-circuit current values (in the identically constructed 19 satellites) would indeed seem to open the possibility of an extremely probable zonal imbalance. Figure 3-77 presents the resultant square error versus an imbalance factor run on satellite No. 9312; a 3.5% imbalance is observed to reduce data scatter by 17%. Once again, the overall degradation ratio is changed

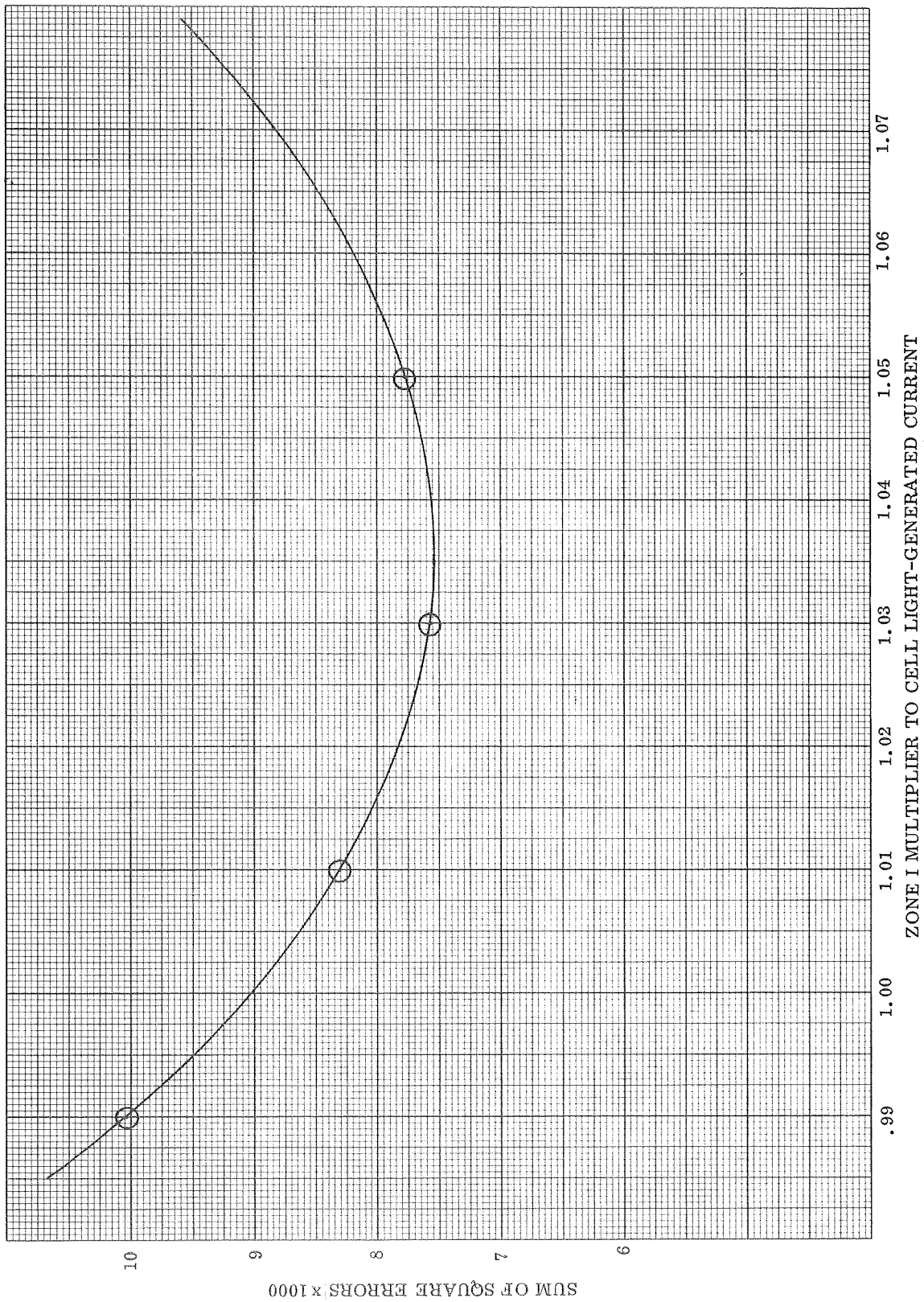


Figure 3-77 Zonal Imbalance Factor vs Square Error

insignificantly. (I_{sc}/I_{sc} (o) reads 0.4% higher at 5 years with the 3.5% imbalance.) The utility of deriving this zone factor for each satellite is thus questionable.

Data Scatter

It is interesting to note that a single cell failure or anomalously darkened cover-slide⁽³⁾ in Zones I or III would effect an approximate imbalance in average output of about

$$100 \left(1 - \frac{31}{32}\right) \% = 3.1\%.$$

This estimation is very close to the zonal imbalance factor derived above. The same cell failure situation could also cause an instantaneous maximum fluctuation of approximately

$$100 \left[1 - \frac{32 (1 + \cos 23^\circ + \cos 68^\circ)}{32 (1 + \cos 23^\circ + \cos 68^\circ)/\pi} \right] \% = 4.3\%.$$

The cosines above represent approximate zonal light incidence angles at equinox, and the fraction denominator is roughly the number of projected strings contributing current on the sunlit side. Comparing this maximum fluctuation to the scatter histograms which have been run on all the satellites as part of the regression analysis, we observe that 98% of the scatter lies within 4.3%. Moreover, the 2% collection of deviant points usually occur at eclipse period times when temperature excursion data are probable in our inputs.

These observations are mentioned to show that the consequence of a single cell or coverslide failure could explain both the sinusoidal seasonal variation and the magnitude of the data scatter. When telemetry data was inputted into the program, however, efforts were taken to use peak values only when these were clearly evident.

(3) See footnote No. 7 in Section 3.7.3 regarding anomalous darkening.

This procedure was followed to eliminate, as best as possible, the fluctuations and general effects of an array cell failure. It appears far more probable at this writing, that the actual explanation is primarily zonal imbalance with a number of contributing secondary factors that a further in-depth study could uncover. Since overall degradation results are not altered by the reduction of the scatter, there appears to be little justification for the pursuit of such a study at this time.

3.8.2 Variations Due to Cell Failures

Failure of a cell or cells produces a ripple in the control bus as the satellite rotates about its spin axis and the string containing the failed cell becomes more or less illuminated. Seasonal inclination will also vary the magnitude of this ripple component. If we consider the satellite in spherical coordinates, correlation of spin angle (rotation θ), sun angle (rotation ϕ about the equatorial axis) and a drop in control bus current can determine the relative location of a cell failure.

Excessive ripple current was noted on satellites 9316 and 9317 and was investigated to find the number of cell failures on each satellite.

Method of Study

To extract the control bus current waveform, the sample rate of the telemetry system must not be exactly related harmonically to the spin rate of the satellite. Also the spin rate must be accurately known and the ripple waveform must be repetitive.

To better see this, consider for example the case where the difference in time for one rotation and for one additional sample of telemetry data is some small Δt . Then at each sample time, the satellite will have rotated slightly more (or less) than one rotation. Thus, we will see a point on the control bus current waveform slightly displaced from the previous point. Succeeding samples would then provide a discrete tracing of the control bus current.

In actual practice, six sheets of tracing paper were scaled with current presented on the ordinate and sample number on the abscissa. Ten successive data samples were then plotted on the first sheet, the following ten samples on the succeeding sheet, and so on. The result was then a series of points, each representing some point on the assumed current waveform. Ten points cover a sample period of 18 seconds. Any two successive sheets were then used to find some periodic variation by laying one over the other, and translating one sheet along the time axis. This same Δt translation is used for each succeeding sheet and from this composite, the waveform becomes evident.

The spin rate is known to be between 2.5 Hz and 3.0 Hz. Thus, noting the period of the current waveform to be 6.2 seconds for satellite 9317 (Figure 3-78), it is seen that the spin-rate is $2.5 \text{ Hz} + 1/6.2 \text{ Hz} = 2.66 \text{ Hz}$. For satellite 9316 (Figure 3-79) the spin rate is 2.62 Hz.

The amount added to spin rate in the above calculations amounts to adding just the portion of a cycle per second that the spin rate is different from a harmonic of the sampling rate. It is correct only if the actual spin rate is between 2.5 and 3.0 Hz. (The fifth and sixth harmonics of the sampling rate).

As a test of the validity of this method, the wave shape was reconstructed using the derived spin rate for satellites 9316 and 9317 for 30 June, 30 July, and 30 August 1966. The results shown in Figures 3-80 and 3-81 give a good match to the current waveform found above.

Analysis

Analysis indicates that a single cell failure in a solar panel should result in roughly a 20% drop in panel output. If we assume that the satellites are nearly perpendicular to the sun's rays (they were actually 6° off on August 30), a single cell failure then represents about 70 ma. in a rectangular panel or around 40 ma in a trapezoidal panel. A single failure in each of two adjacent panels would then result in about 130 ma variation for a pair of rectangular panels, or about 75 ma for a pair of trapezoidal panels.

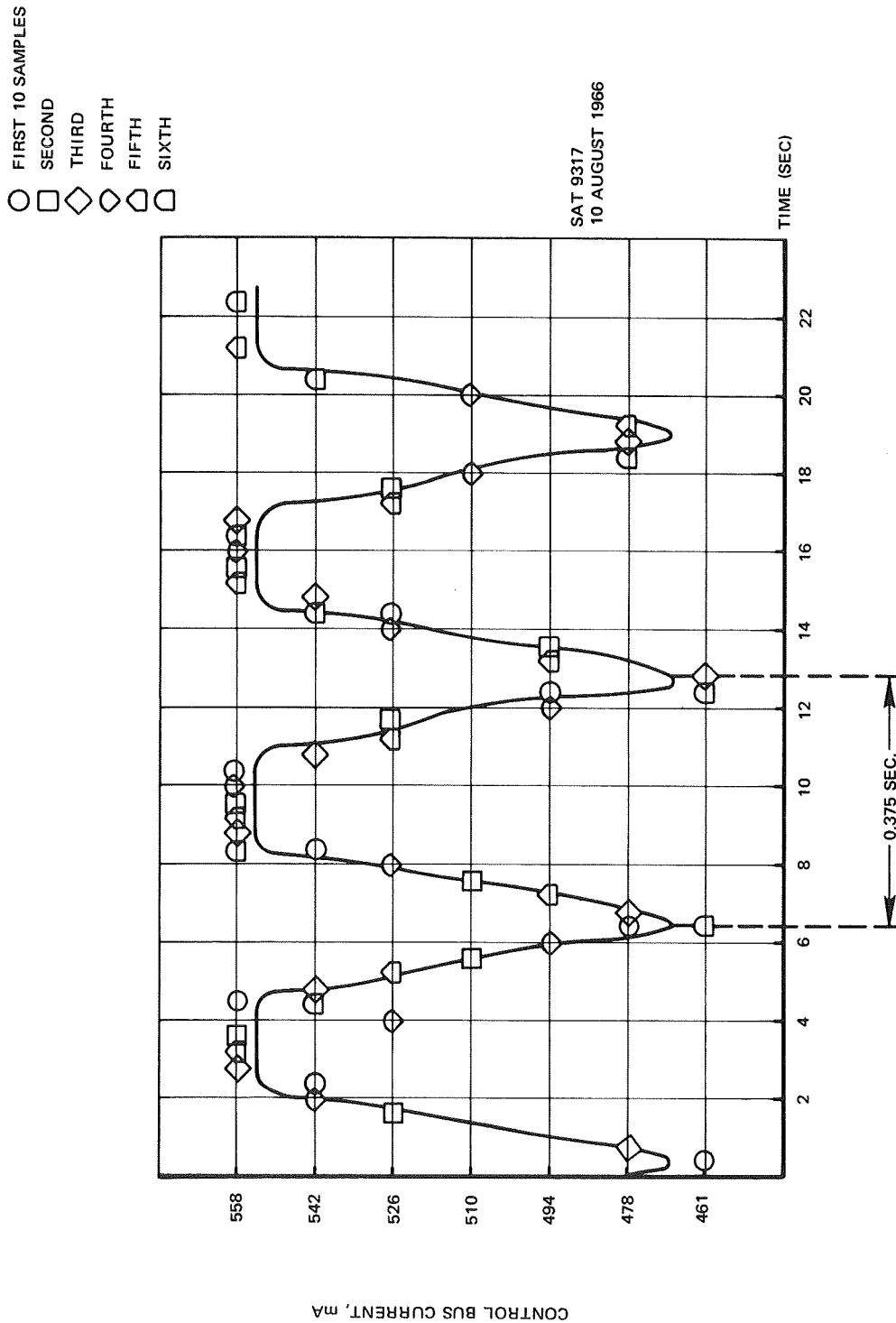


Figure 3-78 Control Bus Current Waveform for Satellite 9317

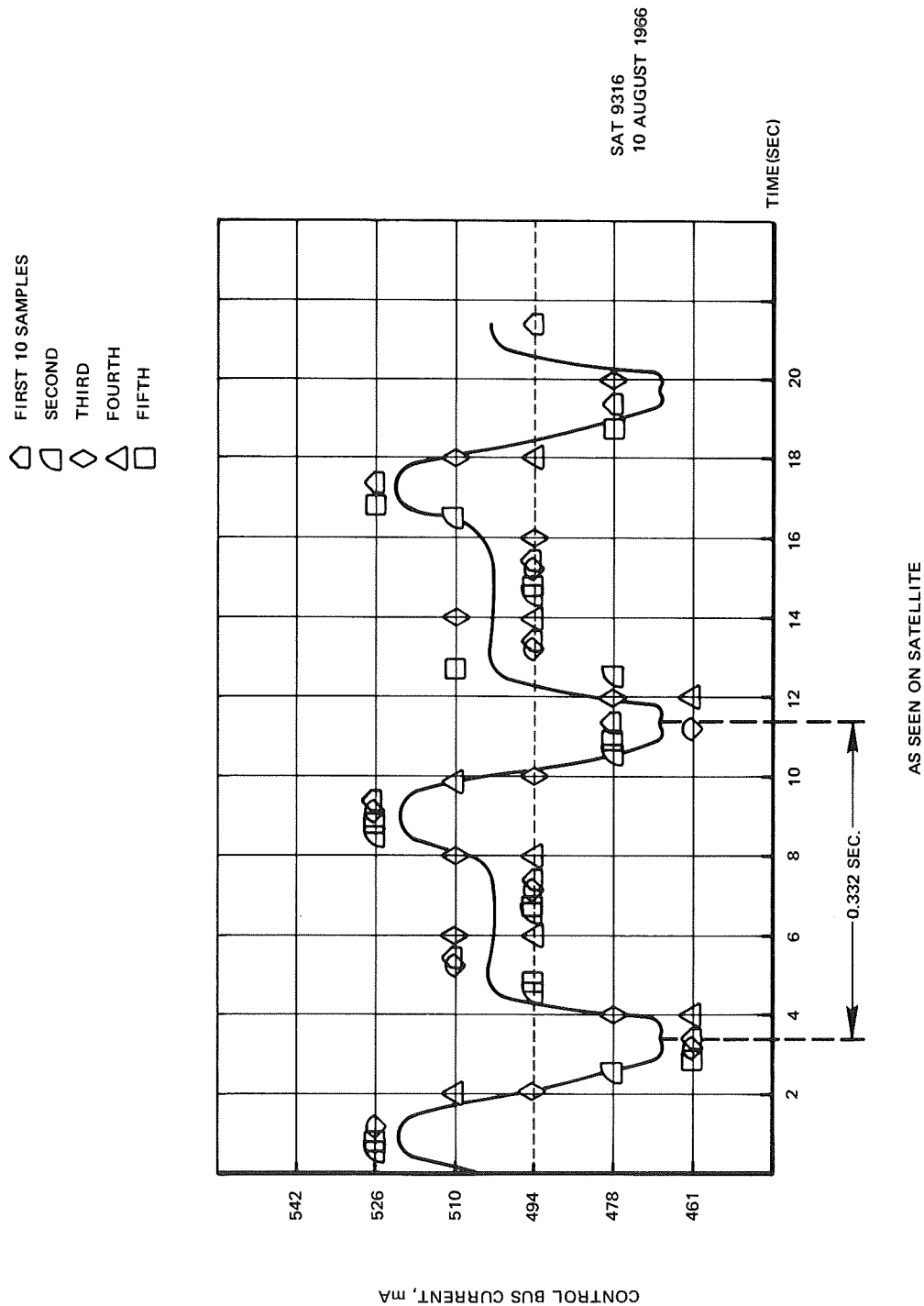


Figure 3-79 Control Bus Current Waveform for Satellite 9316

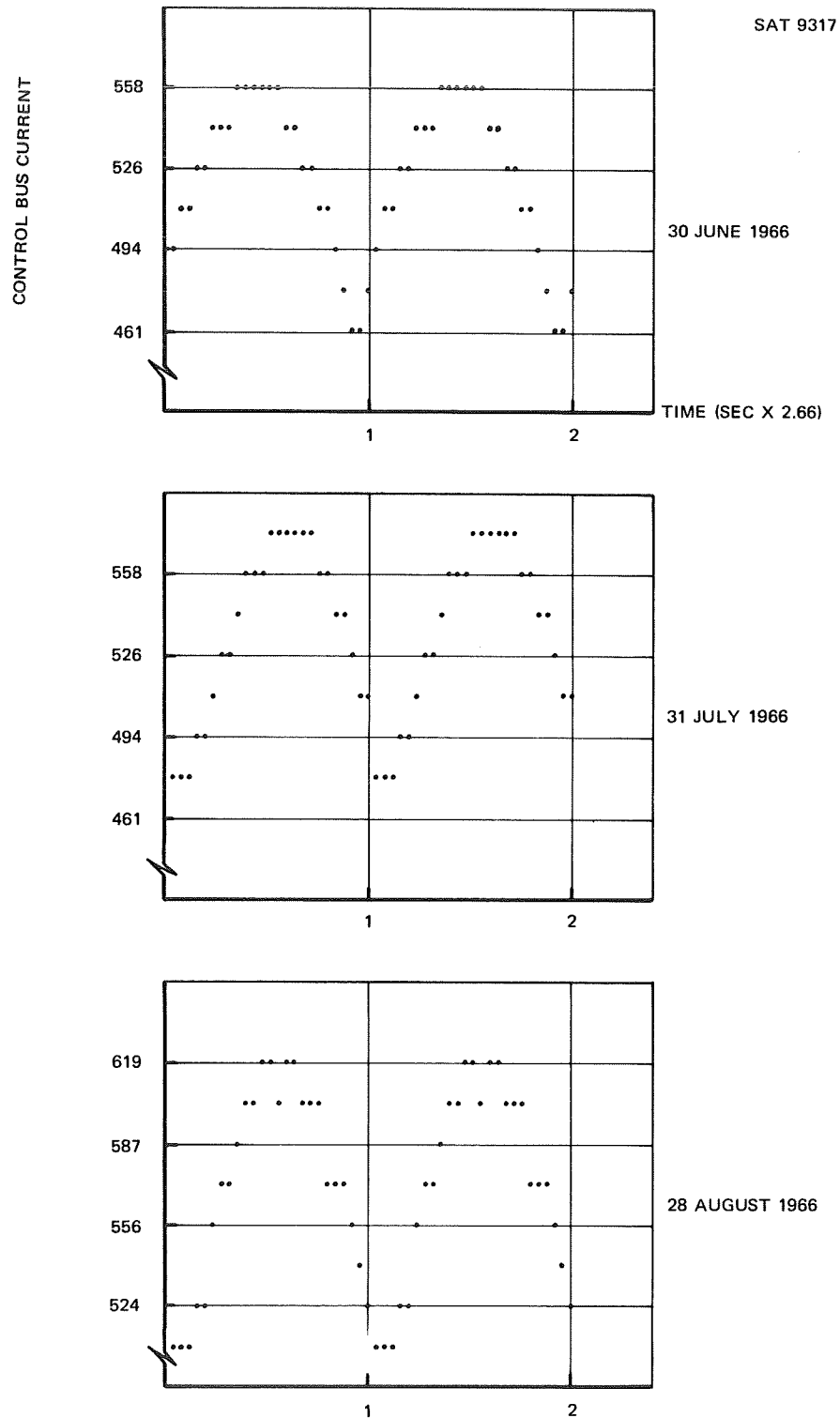


Figure 3-80 Reconstructed Control Bus Current Waveform for Sattelite 9317

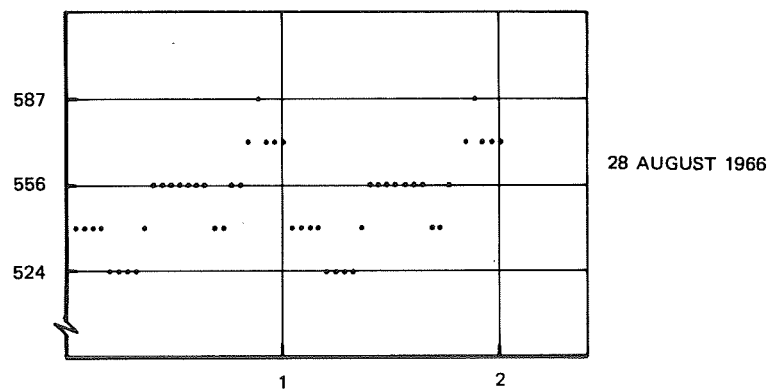
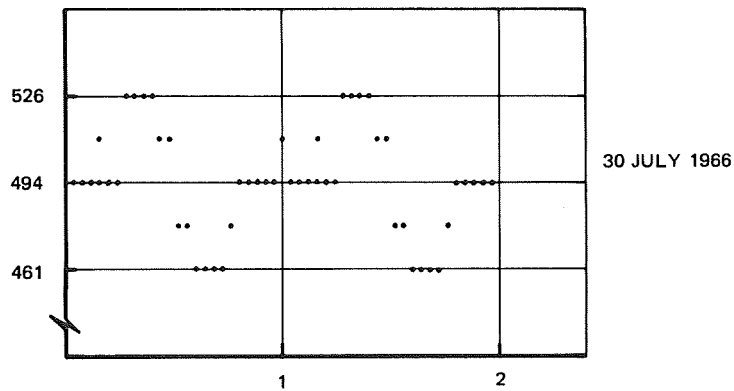
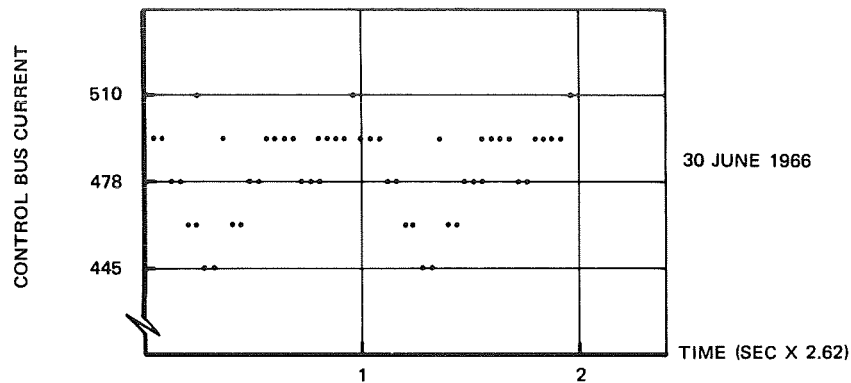


Figure 3-81 Reconstructed Control Bus Current Waveform for Sattelite 9316

In addition to the above, tests made at Philco-Ford on the Qualification Model Satellite indicate that roughly 30 ma of variation should be expected as the sunlight transfers from panel-to-panel on a "healthy" satellite. This effect has not been seen on satellites 9311 through 9315. The absence of the variation may be attributable to slow response in some part of the telemetry system, or the original measurements may not have been accurate. This has not been fully investigated.

The plot for satellite 9317 shows between 80 and 90 ma of ripple. This could indicate a single cell failure on a rectangular panel, or a failure of cells on 2 trapezoidal panels, or possibly 1 failure on a trapezoidal panel and one on a rectangular panel. Satellite 9317 had an intermittent cell in one of the trapezoidal panels before launch. However, the magnitude of the ripple current appears to have been increasing slightly since launch, whereas the satellites sun orientation has been changing so that the panel in question receives less exposure. This should decrease, rather than increase the ripple, so it is surmised that the suspect panel is not the problem.

Finally, the plot by virtue of its shape, indicates failure in 2 adjacent panels. This implies a failure in a trapezoidal panel and a rectangular panel, or a failure in 2 adjacent trapezoidal panels.

For satellite 9316, variation is on the order of 60 ma. The shape of the curve does not allow complete analysis, as it is apparently lost through quantization. Apparently, a single cell has failed in some panel, but a thorough examination of pre-flight data is needed to evaluate the curve shape.

Conclusions

The analysis indicates that 1 or 2 cells have failed in satellite 9317, and that 1 may have failed in 9316.

3.9 COMPARISON OF OTHER FLIGHT DATA

Since 1963 there have been approximately 45 satellites launched into geostationary orbits. Twenty-seven of these are IDSCS satellites, 19 of which are the subjects of this study. Barring a few exceptions, there is a sparcity of published information on the performance of the solar arrays utilized on the remaining synchronous spacecraft. An analysis of an array's performance demands sufficient information to develop a complete I-V curve; this requires data near the short-circuit current, open-circuit voltage, and knee of the I-V curve. Few satellites have had the necessary instrumentation to provide these data. One might question the economics of this type of thinking when these potential sources are available and accurate degradation data are still urgently needed for future array designs.

Figures 3-82 through 3-84 represent the short-circuit current degradation, open-circuit voltage degradation, and maximum power point degradation of the satellites considered. These include: the best- and worst-case examples of the first two IDSCS launches, GGTS, Intelsat I, Intelsat II, F-3, LES-5, LES-6, and the ATS-1 solar cell experiment. A brief summary of cell and orbital characteristics are presented in Tables 3-6 and 3-7. The ATS-1 experiment included various shield thicknesses. Cell 23 in the experiment had a 15-mil shield which most closely approximates the 20-mil shields used on IDSCS arrays. The degradation during 416.8 days (1.142 years) before core memory failure, as presented by Waddel⁽¹⁾ and Barrett and Stroud⁽²⁾, is shown in the figures. After slightly more than one year, this cell degrades in I_{sc} , V_{oc} , and P_{max} to correspond closely with worst-case degradation seen in IDSCS. Cell 21 had a 30-mil shield and showed about 2% less I_{sc} degradation than Cell 23 at a projected 1000 days, through initially Cell 21 had a higher degradation rate.

Cells 5 and 6 with 6 mil shields appear to suffer higher I_{sc} degradation rates if the data is projected beyond the active life of the experiment, but prior to 600 days,

(1) "Solar Cell Radiation Damage on Synchronous Satellite ATS-1," R. C. Waddel NASA/Goddard Space Flight Center, X-710-68-408, October 1968.

(2) "Evaluation of the performance of Solar Arrays in Intelsat Spacecraft at Synchronous Altitude," D. J. Curtin, J. F. Stockel; Comsat Corp., Wash., D. C.; 4th IECEC, Sept. 22-26, 1969, A69-42287

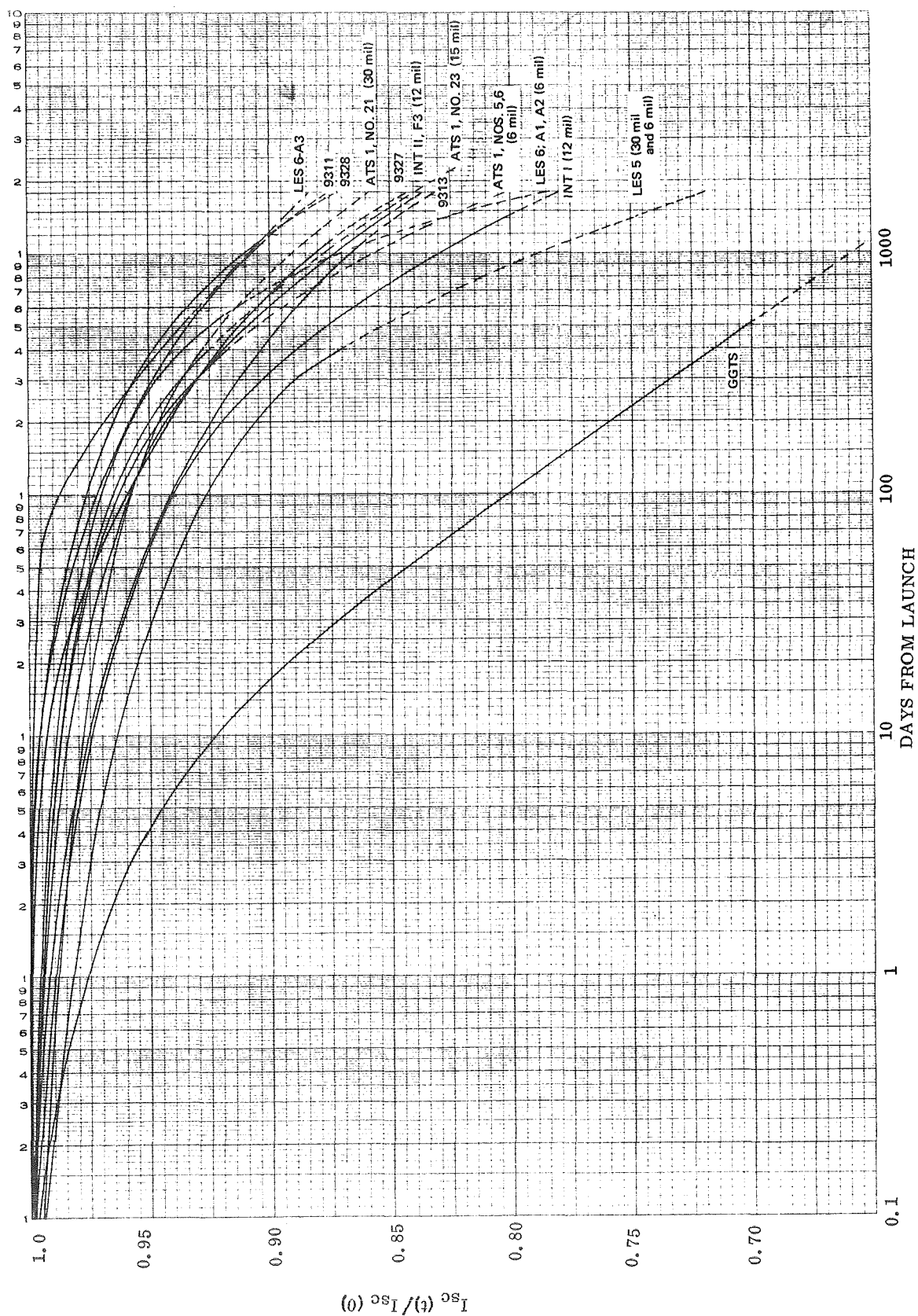


Figure 3-82 Comparison of Available Flight Data: Normalized Short-Circuit Current Degradation

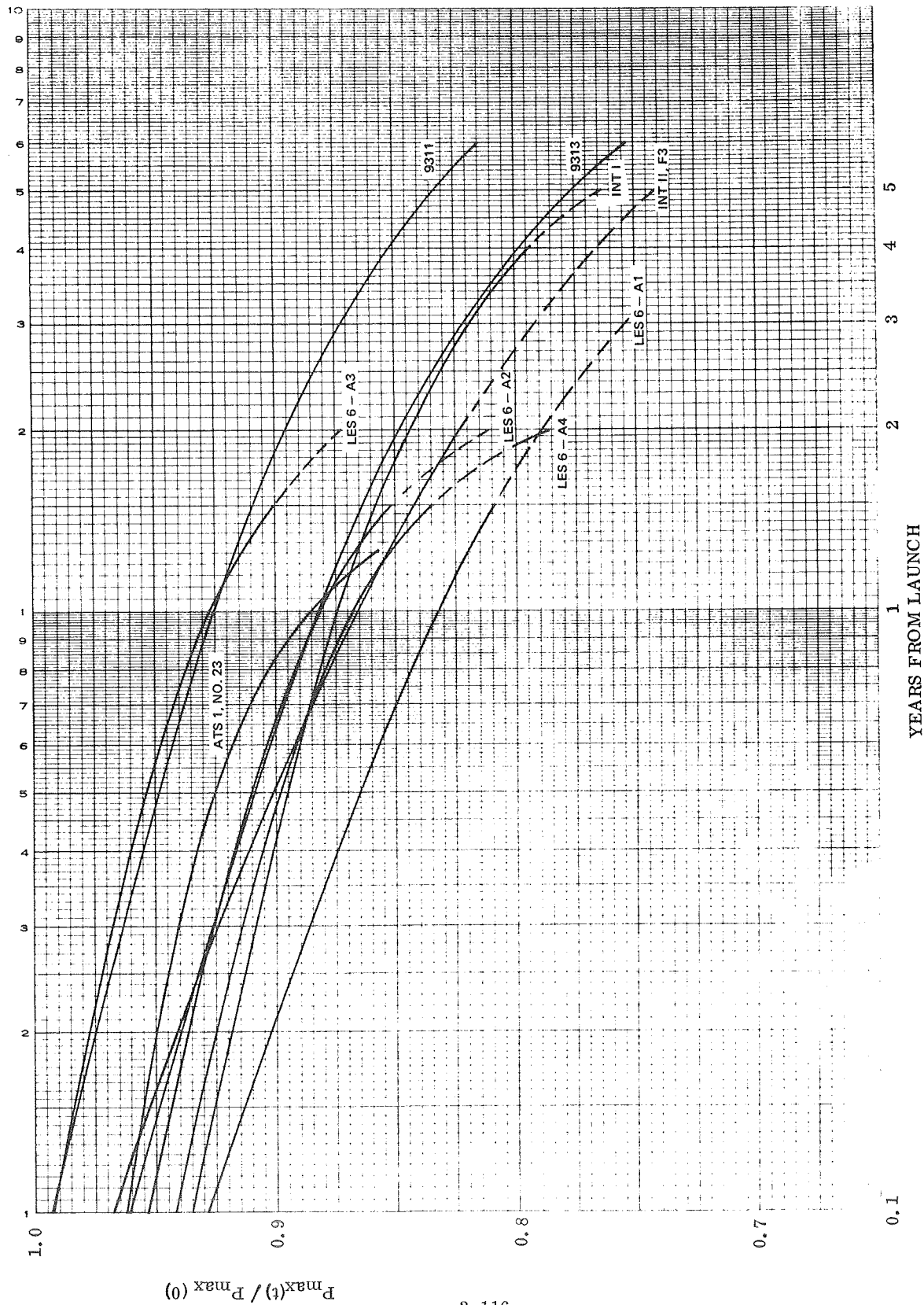


Figure 3-83 Comparison of Available Flight Data: Normalized Maximum Power Point Degradation

EUGENE DIETZGEN CO.
MADE IN U. S. A.

ND. 340R-M DIETZGEN GRAPH PAPER
MILLIMETER

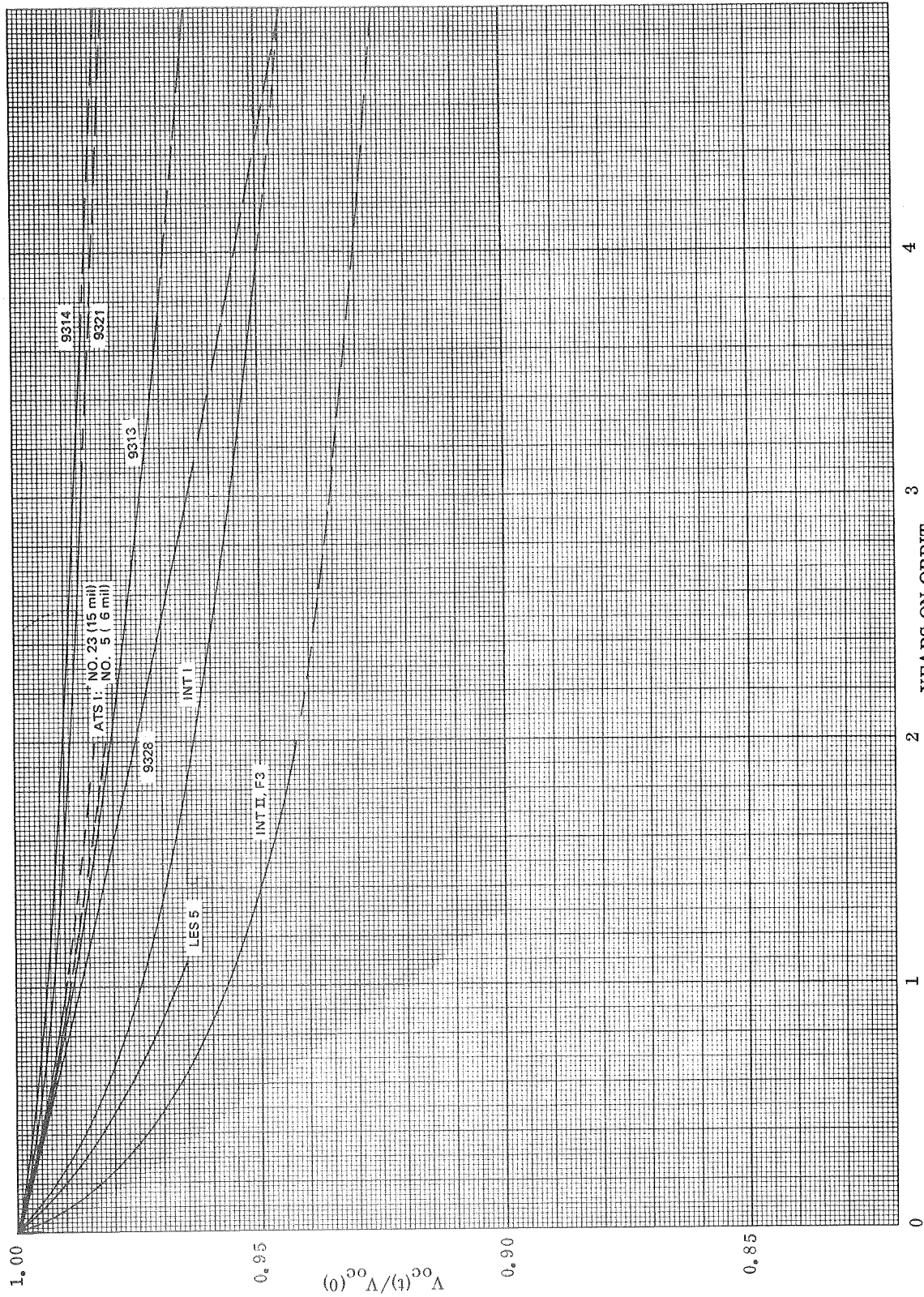


Figure 3-84 Comparison of Available Flight Data: Normalized Open-Circuit Voltage Degradation

TABLE 3-6
ORBIT CHARACTERISTICS

Satellite	Launch Date	Period (minutes)	Perigee (statute miles)	Apogee (statute miles)	Inclination (degrees)
IDSCS9311	16 June 1966	1334.7	20,913	21,053	0.1
IDSCS9312	16 June 1966	1335.3	20,923	21,066	0.1
IDSCS9313	16 June 1966	1336.6	20,927	21,088	0.1
IDSCS9314	16 June 1966	1340.8	20,935	21,194	0.0
IDSCS9315	16 June 1966	1344.0	20,949	21,258	0.1
IDSCS9316	16 June 1966	1338.6	20,936	21,139	0.2
IDSCS9317	16 June 1966	1347.6	20,948	21,350	0.0
IDSCS9321	18 June 1967	1330	20,835	21,038	0.1
IDSCS9322	18 June 1967	1331	20,854	21,031	0.0
IDSCS9323	18 June 1967	1332	20,867	21,036	0.0
IDSCS9324	18 June 1967	1333	20,875	21,063	0.0
IDSCS9325	18 June 1967	1335	20,901	21,089	0.0
IDSCS9326	18 June 1967	1337	20,923	21,128	0.1
IDSCS9327	18 June 1967	1340	20,932	21,192	0.1
IDSCS9328	18 June 1967	1343	20,935	21,275	0.0
IDSCS9331	1 July 1967	1309.8	20,509	20,846	7.2
IDSCS9332	1 July 1967	1311.6	20,542	20,857	7.2
IDSCS9333	1 July 1967	1313.5	20,582	20,866	7.2
(DATS 1)					
IDSCS9334	1 July 1967	1315	20,620	20,875	7.2
(Early Bird)					
Intelsat I	6 Apr 1965	1436.4	21,748	22,733	0.1
Intelsat II, F3	22 Mar 1967	1436.1	22,246	22,254	2.0
ATS-1	6 Dec 1966	1466	22,277	22,920	0.2
GGTS	16 June 1966	1334.2	20,913	21,051	0.1
LES-5	1 July 1967	1315	20,620	20,875	7.2
LES-6	26 Sept 1968	1431.2	22,119	22,236	3.0

TABLE 3-7
CELL CHARACTERISTICS

Spacecraft	Cell Type	Cell Resistance (ohm-cm)	Cell Classification	Cell Dimensions (cm)	Cell Contact	Contact Configuration	Cell Manufacturer	Coverslide Type	Coverslide Thickness (Mils)	Coverslide Adhesive	Preliminary Comments
INTELSAT I (EARLY BIRD)	N/P	10	Solder Dipped	1 x 2	Electroless Nickel	Bar (Shingle)	Heliotek	7940	12	GE LTV-602	Cells were shingled in five cell modules and had exposed areas at the inter-connect end of each module. Degradation in power is estimated to be greater than 2 percent per year.
INTELSAT II -F3	N/P	10	Zone Solder	1 x 2	Ag-Ti	Corner Dart	Heliotek	7940	12	GE LTV-602	Worst case exposed bare cell area was 0.01 sq. in. (0.03% of cell). Degradation in current at 26 volts is estimated to be 3.0 percent in the first 50 days.
ATS-F1 Solar Cell Experiment			Solderless	1 x 2	Ag-Ti	Bar (Silver Mesh)	Texas Instruments			Dow XR-6-3488	This is Dr. Waddell's experiment.
GGTS	N/P	10	Solderless	2 x 2 (Main) 1 x 2	Ag-Ti	Bar (Shingle)	Texas Instruments	7940	15	RTV-602	Cells are shingled but shimmed in such a way that there are 4 Mil exposed regions. In 500 days the current has degraded approximately 30%.
LES-5	N/P	10	Solderless	2 x 2 1 x 2	Ag-Ti	Bar	Texas Instruments	7940	6	RTV-602	Uses a bar inter-connect with a silver strip.
LES-6, A1, A2, A3, A4	N/P	7-14	Solderless	1 x 2	Ag-Ti		Texas Instruments	7940	6		Preliminary data is presented.

all of the cells mentioned fall within the bounds of the IDSCS best and worst-case data for I_{sc} and V_{oc} . The ATS cells tend to be closer in degradation character to the worst-case IDSCS arrays.

The LES-5 experiment⁽³⁾ showed degradation effects in I_{sc} and V_{oc} which were more severe than LES-6, ATS-5, or IDSCS. A combination of causes is suggested since I_{sc} and V_{oc} both were severely effected. Surface contamination and/or UV slide system darkening could produce the initial drop in I_{sc} of 4% over 60 days. Low energy proton damage could account for the V_{oc} losses reported, though no estimate of exposed area is given, thus confirmation is not possible. A detailed review of the entire I-V characteristic over the satellite life might prove revealing. Specifically, the degree of knee softening would shed further light on possible low-energy proton damage.

Preliminary results on the LES-6⁽⁴⁾ experimental cells A1, A2, A3, and A4 provide an interesting comparison. These cells all had shields of 6 mil Silica 7940, were silicon, n/p, blue shifted 1 x 2 cm Texas Instrument cells as used in the satellite array. Their major difference was that A3 and A4 had a 4-mil annealed beryllium-copper "window frames" to protect against low energy proton damage in normally susceptible areas. Cell A4 had no anti-reflective coating. All cells except A3 showed marked degradations in P_{max} (from 15% for A2 to 19% for A1 over 18 months); A3 showed only a 10% loss in P_{max} and less than 7% in I_{sc} over this period. This is comparable to the best IDSCS array result which also is the least degraded array/cell found in those cases considered; the 1.5-year degradation ratios for this case are 0.935 for I_{sc} , 0.91 for P_{max} , and 0.991 for V_{oc} .

Data on the Gravity Gradient Test Satellite (GGTS) indicates such poor I_{sc} performance that it must be considered anomolous and of little use in this comparison.

(3) "Solar Cell Degradation Experiments on LES-4 and -5", F. W. Sarles, L. P. Cox, Lincoln Laboratory, M.I.T., 7th Photovoltaic Conference, Nov. 68.

(4) Private communication with F. W. Sarles at Lincoln Laboratory.

Intelsat I, as reported by Curtin⁽⁵⁾, shows a slightly greater loss in P_{\max} initially than is found in the worst-case IDSCS array. At the 4-year point, however, it is within 1% of the worst-case I_{sc} and P_{\max} ratio for IDSCS arrays.

Intelsat II, F-3, shows a V_{oc} and P_{\max} loss several percent greater than found in IDSCS, while its I_{sc} loss corresponds well with the worst-case IDSCS satellites. This would seem to indicate low energy proton losses.

Since Cell 23 in the ATS-1 experiment showed good agreement with I_{sc} , V_{oc} , and P_{\max} results from the IDSCS arrays, a parametric analysis was attempted (based on 4 points) from I-V curves presented by Barrett and Stroud⁽²⁾ and the method described in Section 3.7.2 of this report. The resultant parametric variation is presented in Figures 3-85 through 3-90. The slight improvements in V_{oc} and P_{\max} within the first 3 days has not been reported elsewhere on any of the other satellites considered here. This anomaly, as well as the strange parametric trends, is not understood and is a conflict with the parametric results obtained here for the IDSCS craft.

(5) "Evaluation of the Solar Arrays in Intelsat Spacecraft at Synchronous Altitude," D. J. Curtin, J. F. Stockel; Comsat Corp., Wash., D.C.; 4th IECEC, Sept. 22-26, 1969, A69-42287.

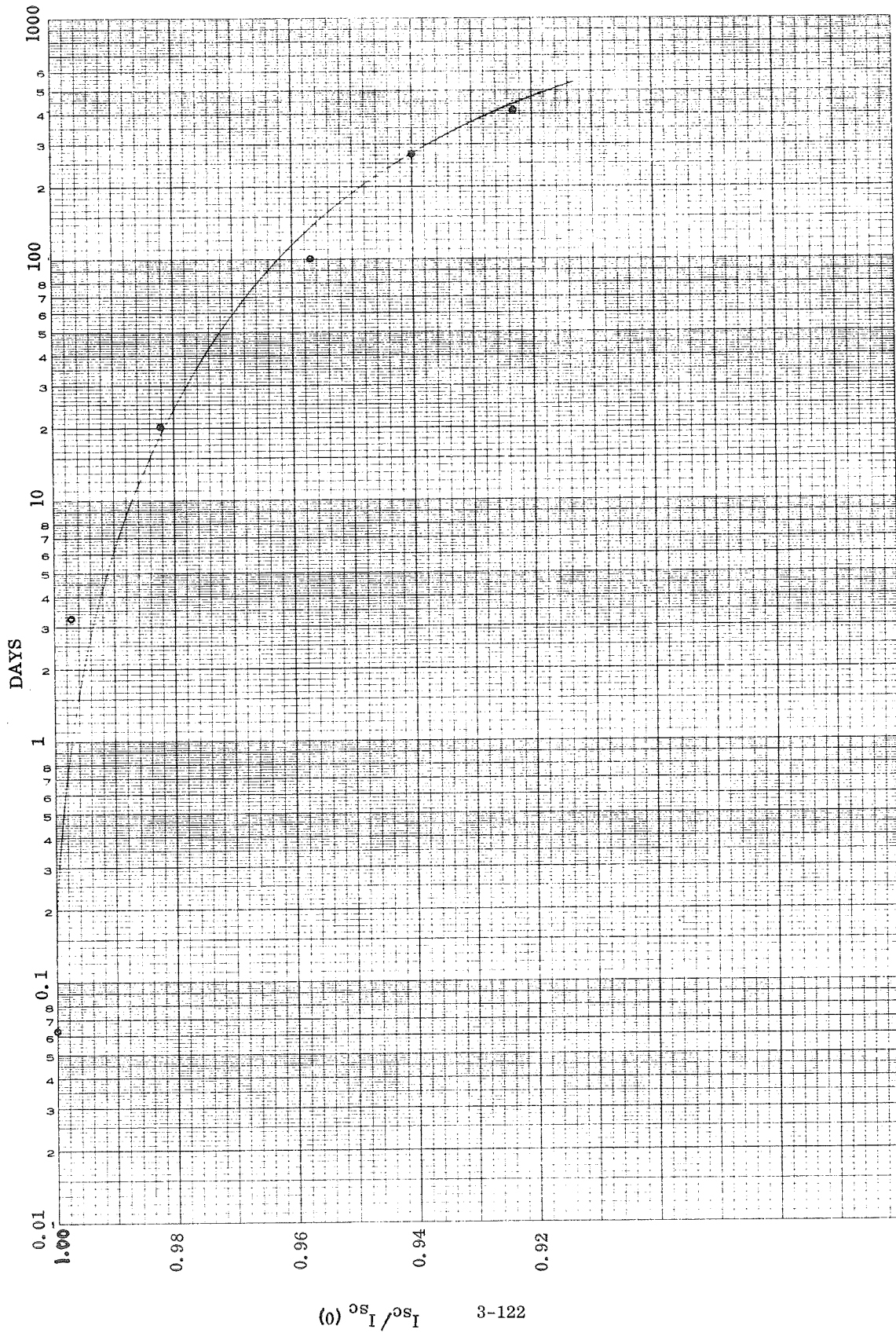


Figure 3-85 Extraction of Parameter I From ATS-1 (No. 23) Data

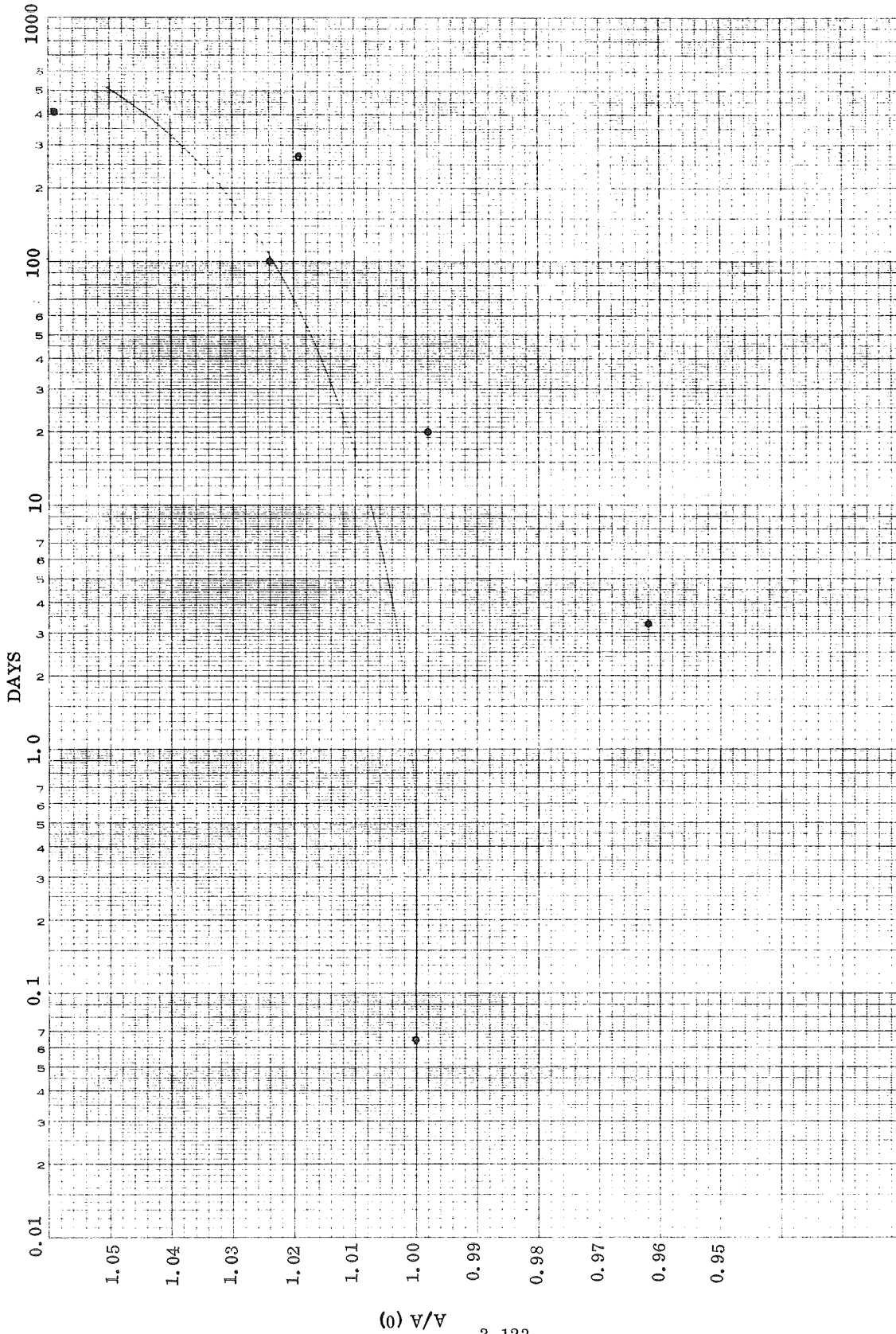


Figure 3-86 Extraction of Parameter A From ATS-1 (#23) Data

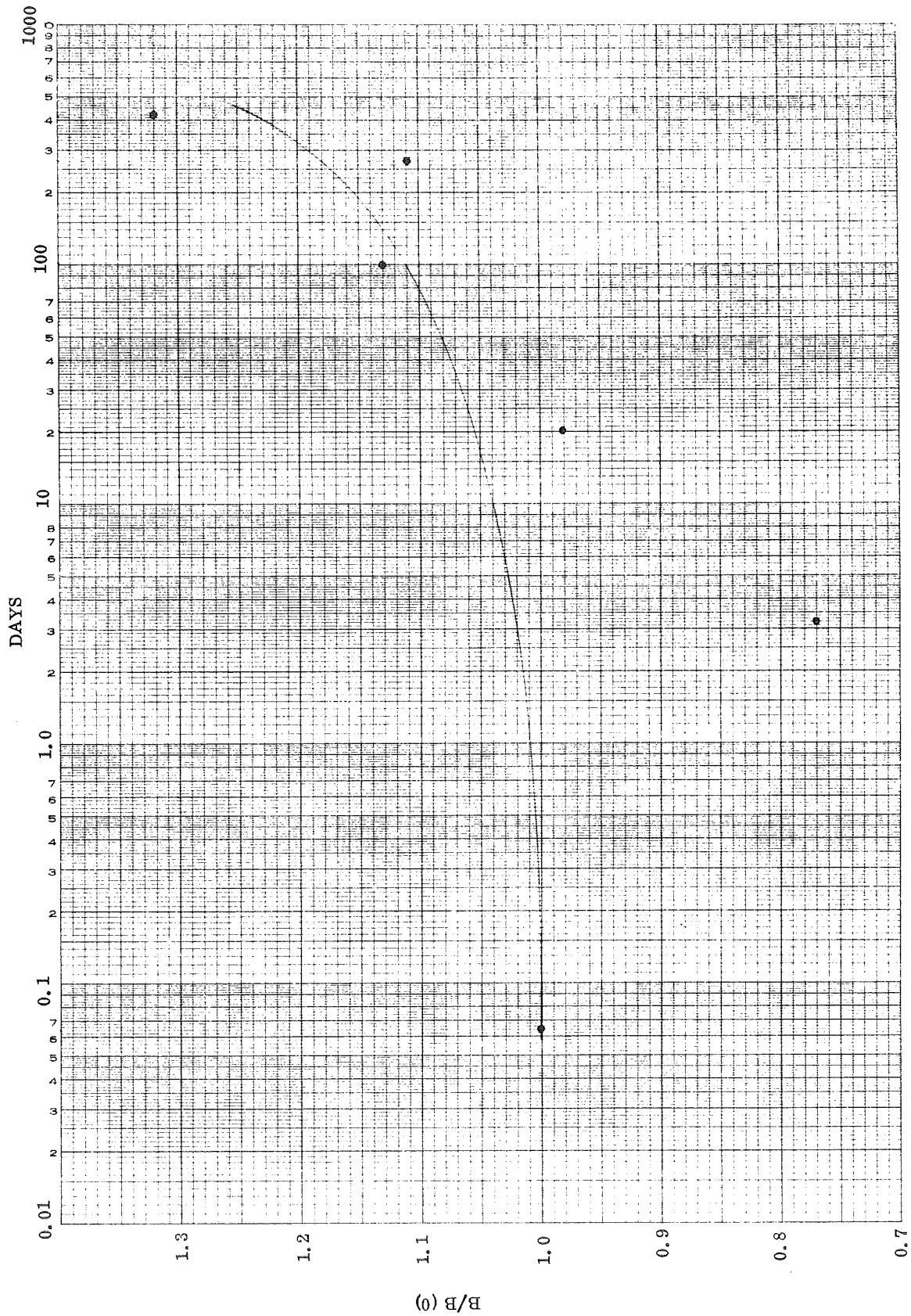


Figure 3-87 Extraction of Parameter B From ATS-1 (No. 23) Data

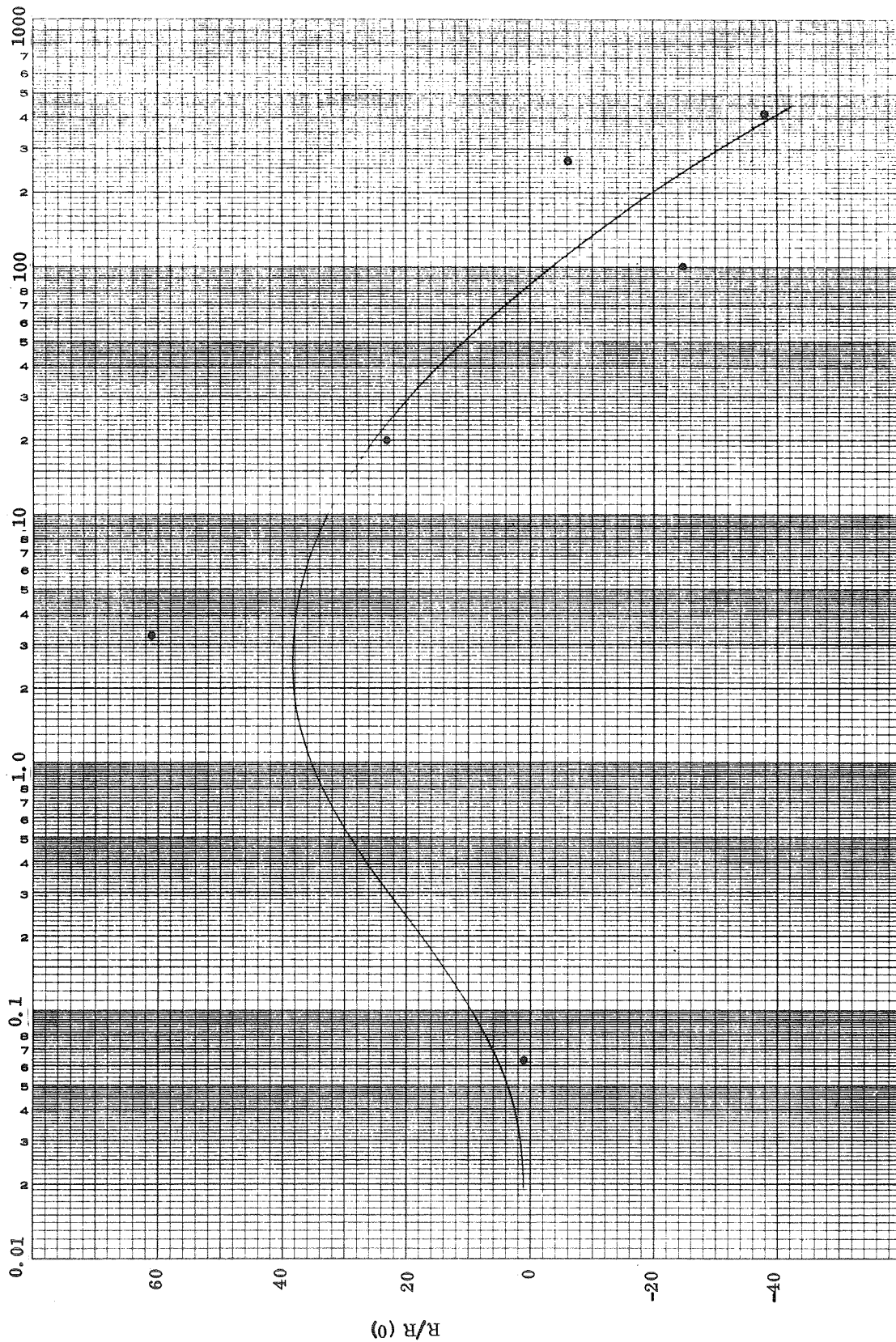
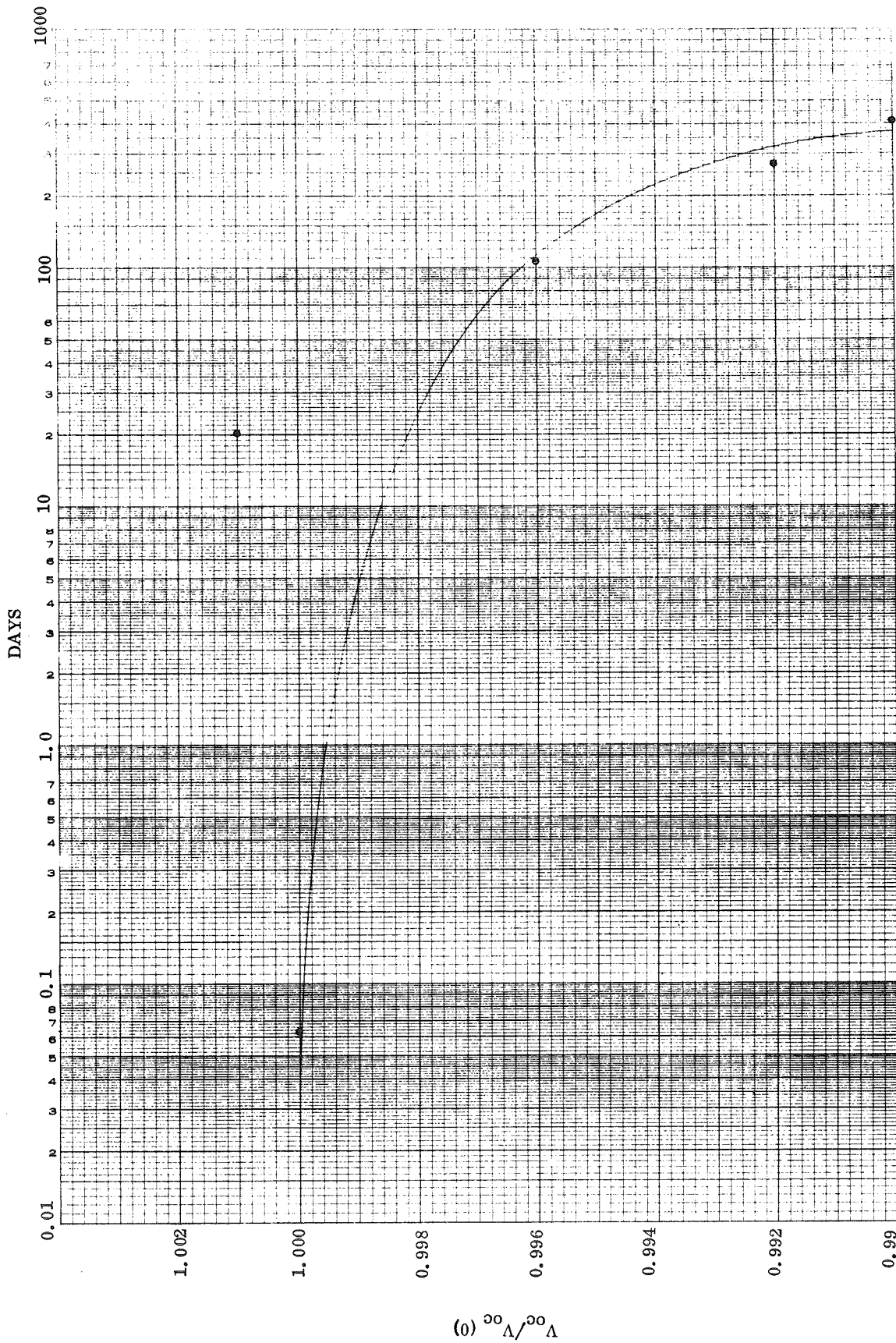


Figure 3-88 Extraction of Parameter R From ATS-1 (No. 23) Data

Figure 3-89 Extraction of Parameter V_{oc} From ATS-1 (No. 23) Data(o) $\Lambda^{\infty} / \Lambda^{\infty}$

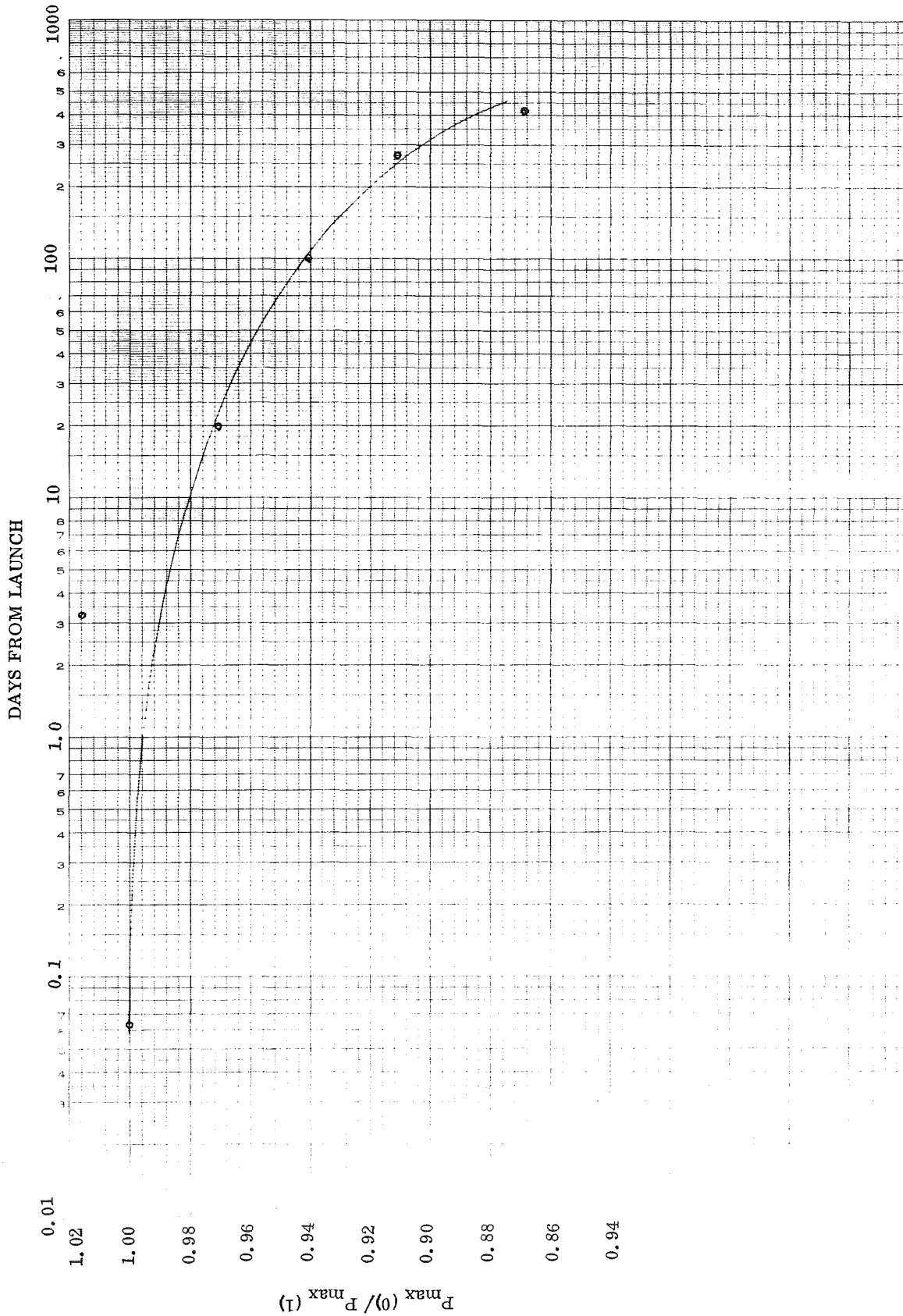


Figure 3-90 Extraction of Parameter P_{\max} From ATS-1 (No. 23) Data

SECTION 4

CONCLUSIONS AND RECOMMENDATIONS

All the available results, ground data, and calculational methods are combined to produce a consistent picture of degradation behavior with a minimum of new assumptions. From this synthesis, the final conclusions and recommendations of the study are derived.

4.1 CONCLUSIONS AND RECOMMENDATIONS

This section presents material which is a direct consequence of the stated approach and methodology of our study (c.f. sec. 2.1). To this point, we have presented the results of a telemetry data reduction, a calculation based on measured environment, and the parameterization of ground-test irradiation data. In essence, we have examined portions of both the inductive and deductive "paths" in the course of analysis and have encountered some missing links and imprecisions enroute. In this section, the authors have attempted to piece together all the facts at hand to produce a single consistent picture of behavior which is non-contradictory within all our limits of error and which requires a minimum of new assumptions regarding the missing links. There is not enough information for demonstrating the uniqueness of our conclusions, but this absence should not detract from their usefulness at this time.

Figure 4-1 indicates the general logic flow which produces the major conclusions listed below. The most surprising item is the 5-year coverslide-system loss, which ranges from 6 to 12%.

- a. Degradations projected to 5-years (on or near synchronous orbit) amount to $6\% \pm 1\%$ for I_{sc} and $2\% \pm 0.3\%$ for V_{oc} due to trapped electrons and flare protons shielded by the 20 mil coverslide and interacting with the N/P silicon solar cell beneath. The degradation levels and error bounds are those derived from ground results, the best estimation of the synchronous radiation environment, and currently accepted calculational methods.
- b. Additional cell output losses to I_{sc} are due to coverslide components which suffer transmission losses totaling $9\% \pm 3\%$ due to ultraviolet and particulate radiation. The loss figure is the mean of the Gaussian distribution of I_{sc} 5-year endpoints with the calculated I_{sc} cell degradation and uncertainty limits removed mathematically. A 2 to 5% loss to I_{sc} occurs within the first 100 days on orbit, possibly due to ultraviolet radiation.

- c. Another interaction, probably low-energy proton damage, degrades V_{oc} an additional 0 to 3% over 5 years with a random distribution over fluence. By this we mean that there exists a random distribution of exposed bare cell areas throughout the collection of satellites; the skewed gaussian distribution of V_{oc} ratios, if translated to incident low energy proton fluences, produces a nearly perfect gaussian over the fluences. Low-energy proton damage is inferred because it appears to be the only interaction capable of causing a large V_{oc} loss with a concurrent small or zero I_{sc} loss.
- d. The apparent periodic seasonal variation, superimposed on the output data in the dot plots, primarily results from a slight ($\approx 3.5\%$ in I_{sc}) difference in the output of the "average" solar cell used in the upper and lower zones of the solar array. An additional contributor is a small correction term to the Lambert Law cosine factor. The total reduction in scatter when these factors are implemented is about 27% (measured in terms of reduction in the sum of the squares of the deviations between the data points and the fitted function). A significant aspect of this phase of the study is that scatter reduction might be used to examine other buried subtleties of cell or array behavior. The criterion would be based on the fact that since there is no systematic approach for reducing true random scatter, any reduction in scatter brought about by a mathematical adjustment provides insight into related causative mechanisms.
- e. The convenient, widespread, and somewhat arbitrary use of 1 Mev equivalent electron fluences as measurements of particulate orbital environments should be discontinued. The peak damage energy for the dominant radiation type would be a far more accurate equivalence, if an equivalence must be used at all. The following table indicates the range of fluences possible with different particle energies.

	Observed Cell Degradation	1 Mev Electrons	0.8 Mev Electrons	0.6 Mev Electrons	2.7 Mev Protons
I_{sc}	0.94	1.2×10^{14}	1.38×10^{14}	1.42×10^{14}	8×10^9
V_{oc}	0.98	4.1×10^{13}	1.17×10^{14}	7.9×10^{14}	4.9×10^9

The peak damage source was shown to be trapped electrons, by a ratio of about 2.5 to 1 over flare protons, and the peak damage energy was shown to lie somewhere between 0.6 and 0.8 Mev.

- f. A useful computational technique, used throughout this study, is the definition of the solar cell equation in terms of the parameters A, B, R, and P:

$$I = I_L - \exp\left(\frac{-A}{B}\right) \left[\exp \frac{V + IR}{B} - 1 \right] - \frac{V}{P}.$$

For modern cells with shunt resistance P very large, this simplifies to the expression:

$$V = A + B \ln(I_L - I) - IR.$$

Temporal variations of these parameters for best- and worst-case satellites have been determined in this report. The parameter curves may also prove useful in identifying low-energy proton and coverslide losses.

- g. The function,

$$R = R_o \left[1 - a \ln(1 + bt) \right]$$

appears to represent the on-orbit radiation degradation ratio of cell

I_{sc} or V_{oc} over a useful range of t . Uniform flux exposures are assumed for the equation derivation, which may imply a verification that dominant degradation is due to trapped electrons rather than the more erratic flare protons.

- h. Knee rounding (or hardening) is either non-existent or within the errors of resolving the I-V curve through analysis of eclipse entrance data. Additional evidence for the absence of knee changes is present in the calculations based on the synchronous radiation environment: the peak damage energies for residual electrons and protons, 0.8 Mev and 3 Mev respectively, show no knee changes in ground-irradiation test data. A corollary to this observation is that a simple translation of the cell I-V curve along the current and voltage axes, by amounts determined from the I_{sc} and V_{oc} degradations, will suffice to define the degraded I-V curve.

Recommendations evolved as a result of this study are the following:

- a. Ground irradiation data on solar cells appears due for an update. Degradation information on 2 x 2 cm N/P silicon solar cells is needed for electron energies between 0.5 and 2.0 Mev, and for proton energies between 1 and 5 Mev. This information should be published with complete I-V curves so that parametric information can be extracted.
- b. Consistent on-orbit degradation data is sparse. The degree of variation observed in our comparison study indicates that degradation levels and mechanisms are not yet clearly defined. It is felt that no satellite should be wasted as a potential source of degradation information. This study indicates that even a few judiciously selected and accurate telemetry channels can produce significant cell performance data.

- c. Coverslide components should be carefully investigated under ultra-violet and particulate radiation. Sufficiently low electron and proton energies should be used. If possible, the source of the variable transmission loss behavior should be discovered and eliminated. Transmission losses versus slide thickness should be delineated. Surface contaminants experienced in orbital environments should be studied under irradiation. If even 2 or 3% coverslide losses could be avoided, a substantial cost saving could result from decreased solar array size or extended satellite life. Alternatively, the investment of time and money in the development of a cell with higher end-of-life output must be re-examined in the light of an improved cell/slide system approach.
- d. Degradation calculation techniques should be re-examined. The correlation of total cell damage (e.g. $\sum K\phi$) with I_{sc} or V_{oc} should be unique and unambiguous, regardless of the damage source. This aspect might be incorporated into presently accepted calculational methods by making the damage coefficient, K , flux dependent as well as energy dependent. A totally new approach, recommended by the authors, is to study energy deposition in the solar cell in defined regions (e.g., surface, junction, and base regions) and correlate it to changes in the cell equation parameters.
- e. Once modern cell and slide degradation levels and mechanisms have been well defined, the possibility opens for some group to compile a very useful design handbook which could include tables or graphs of solar cell degradations vs. altitudes, inclinations, and coverslide thicknesses. As the environment is updated, the handbook would be updated. There appears to be no reason why universally accepted environments, calculational methods, and solar cells should not be combined, once and for all. In addition, as cells and coverslide components are improved, the handbook might reflect and inspire a higher industry standard.

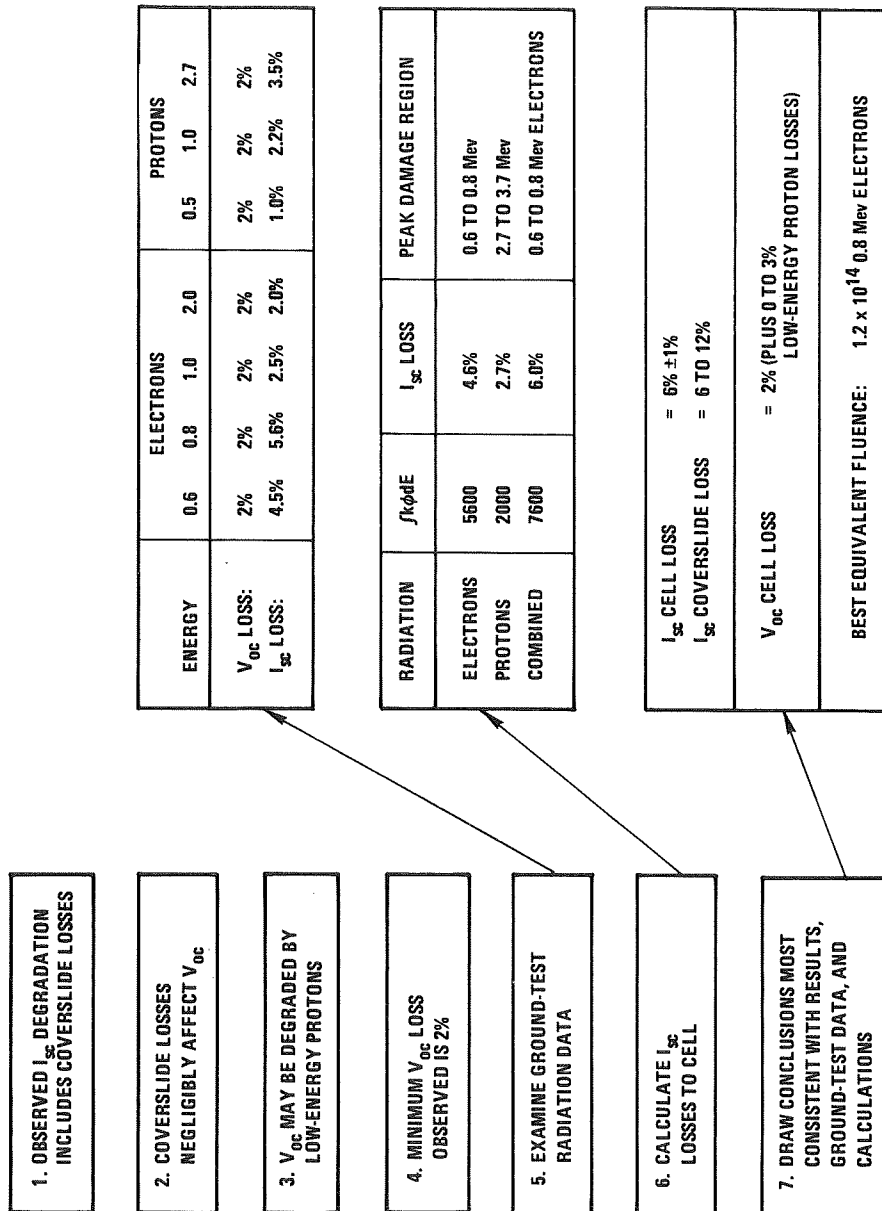


Figure 4-1 Summary of the Logic Leading to the Authors' Conclusions

APPENDICES

- A - Satellite Documentation
- B - Derivation of an Explicit Function for $I(V)$
- C - Extraction of Parameters From I-V Data
- D - Temperature Dependence of the Parameters
- E - Descriptions of Computer Programs Developed

WDL-TR4223

APPENDIX A

APPENDIX A - SATELLITE DOCUMENTATION

1.0 SATELLITE DESCRIPTION

The IDSCS satellite is an active communication repeater and is shown in Figure A-1. Its shape is a symmetrical polyhedron consisting of two octahedral truncated pyramids joined by an octagonal cylindrical center section. The height of the satellite body is 31 inches, and the diameter of the circle circumscribing the octagonal cylinder is 36 inches. The satellite weighs 97 pounds and employs passive thermal control.

It is divided into four subsystems which are described in the following paragraphs. These are:

- a. Structure
- b. Power
- c. Communication
- d. Telemetry

1.1 STRUCTURE SUBSYSTEM

The principal components of the Structure Subsystem are the structural frame, the separation equipment, and the spin-up equipment. Solar array panels cover the external surface of the structure frame. The internal surfaces of the structure provide thermal coatings for the passive thermal control required to maintain the in-orbit operating temperatures for the communication, telemetry, and power subsystems.

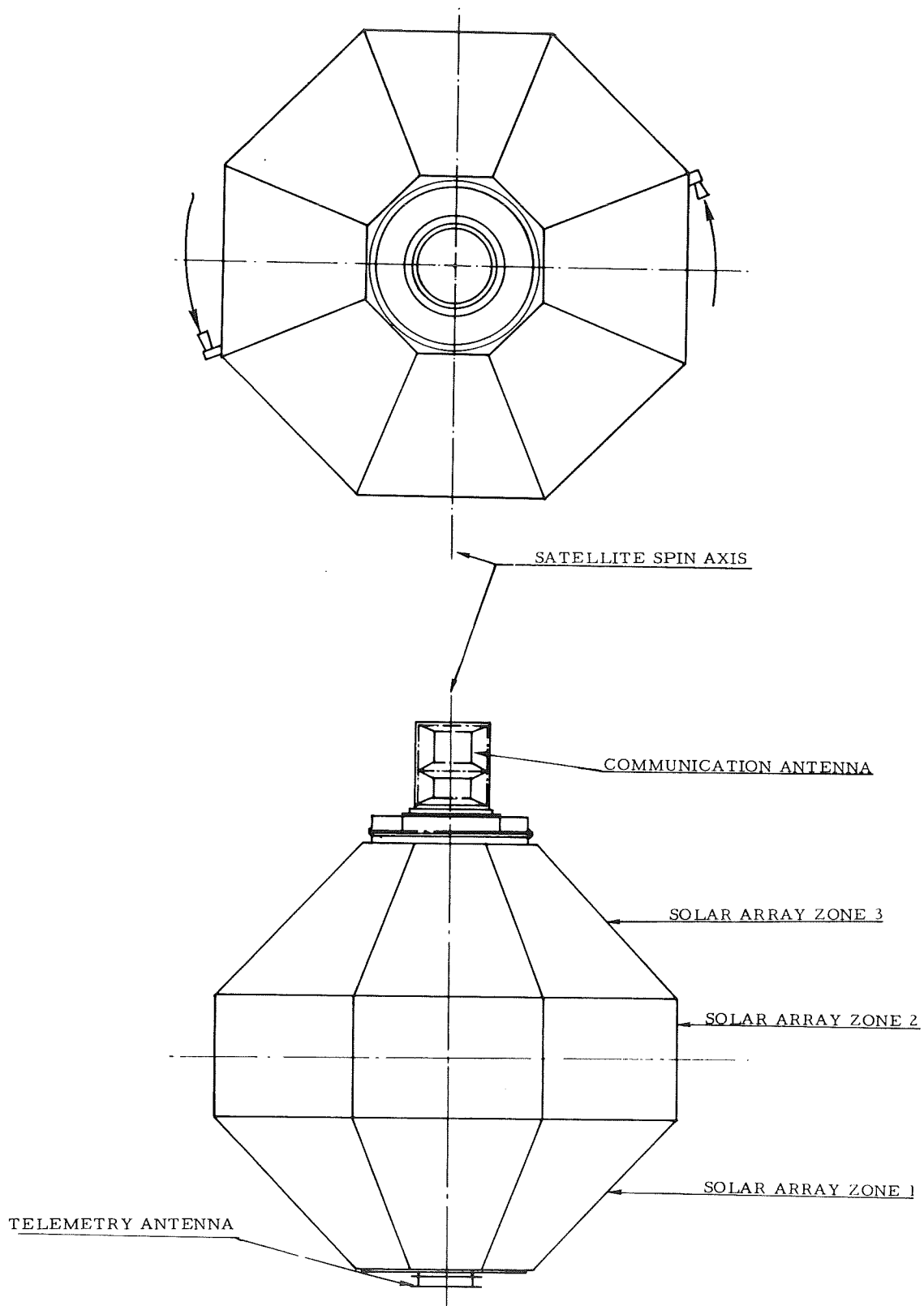


Figure A-1 Satellite Envelope Configuration

A-2

1.1.1 Structure Frame

The structure frame provides a multifaced, symmetrical outer shell consisting of two truncated, eight-sided pyramids placed on either end of an eight-sided modified cylindrical section. The spin axis passes through the vertical apices of the truncated pyramids. The basic frame consists of a central thin-gauge magnesium alloy sheet cylinder and eight equally-spaced radial webs. An aluminum end ring is attached to each end of the cylinder to provide structural attachments and to form the octagonal shape at the truncated ends of the pyramidal sections of the body. The equipment panels are constructed of sandwich sections consisting of thin aluminum alloy facing sheets attached to an aluminum alloy hexagonal core. The four intermediate stiffening webs are fabricated from thin-gauge magnesium alloy sheets and have three large, flanged lightening holes. The central cylinder provides longitudinal stiffness to the satellite in the direction of maximum bending dictated by the horizontal position during launch.

1.1.2 Separation Equipment

The satellite is separated and propelled from the dispenser by the separation equipment. Attachment, with adequate circumferential clearance for the protruding communication antenna, is provided by a vee-groove clamp through a dispenser adapter ring. On a signal, two redundant ordnance bolt cutters separate the vee-groove clamp, allowing the four matched springs of the separation equipment to propel the satellite laterally from the dispenser with an acceleration of less than two g's to a velocity of three fps. As the spring faces separate from the satellite, redundant actuators actuate the satellite spin-up equipment. A clamp retention

device prevents damage to the satellite from possible rebound of the vee-groove clamp.

Both springs and satellites are unguided during separation since the expected tipoff attitude errors are less than two degrees, which the communication antenna beamwidth has been designed to accomodate.

1.1.3 Spin-Up Equipment

The satellite is spin stabilized at 160 revolutions per minute about its axis of symmetry by the structure subsystem cold-gas spin-up equipment which is activated immediately on separation of the satellite from the dispenser. There is no active control system.

The spin-up mechanism consists of a high-pressure nitrogen gas supply reservoir located near the satellite center of gravity, two opposed nozzles located on the outer rim of the satellite, and interconnecting lines and valves.

1.2 POWER CONTROL UNIT

The power subsystem consists of the power control unit and the solar array, plus a radiation termination unit which automatically shuts off the power after six years in orbit. A summary of the Power Subsystem characteristics is shown in Table A-1.

1.2.1 Power Subsystem

A simplified block diagram of the Power Control Unit (PCU) is shown in

TABLE A-1

SUMMARY OF POWER SUBSYSTEM CHARACTERISTICS

1. Bus Regulation:	29.4 ± 0.2 VDC
2. Bus Ripple:	300 MV P-P; 0-50 KHz
3. Bus Impedance:	Less than 1Ω ; 0-50 KHz
4. Total Load:	28.75 Watts Maximum
5. Load Control:	Automatic Turn-On and Turn-Off Based on Available Power
6. Life:	Support Communications for 3 years Minimum Support Communications and Tele- metry for 1.5 Years Minimum

Figure A-2. The function of the PCU is to regulate and distribute the solar array power and to provide telemetry inputs on the performance of the electrical power subsystem. The PCU performs the following specific functions:

- a. Regulates the main power bus voltage
- b. Provides automatic disconnect and reconnect of the telemetry subsystem as dictated by the solar array power delivery capability.
- c. Provides automatic disconnect and reconnect of the communication subsystem as dictated by the solar array power delivering capability.
- d. Provides telemetry monitoring of current, voltage, and temperature to allow operational analysis of the subsystem.

Regulation is accomplished by means of a partial shunt regulator which senses bus voltage and maintains the bus at 29.4 ± 0.2 volts. The shunt is tapped near the electrical center of the solar array and requires a minimum of power to be dissipated in the regulator.

When there is insufficient power to operate both the communication and telemetry subsystems, a bus undervoltage condition occurs. This undervoltage is redundantly sensed and the telemetry load is removed by solid-state switching. Should the undervoltage condition continue to exist, as would occur during eclipse, the communications load is removed. A resistive load equal to the communications load is then substituted across the main power bus. The voltage across this dummy load is monitored, and when sufficient power becomes available to assure that the solar array can support the communication subsystem, the substitute load is removed and communications is energized. If, after energizing

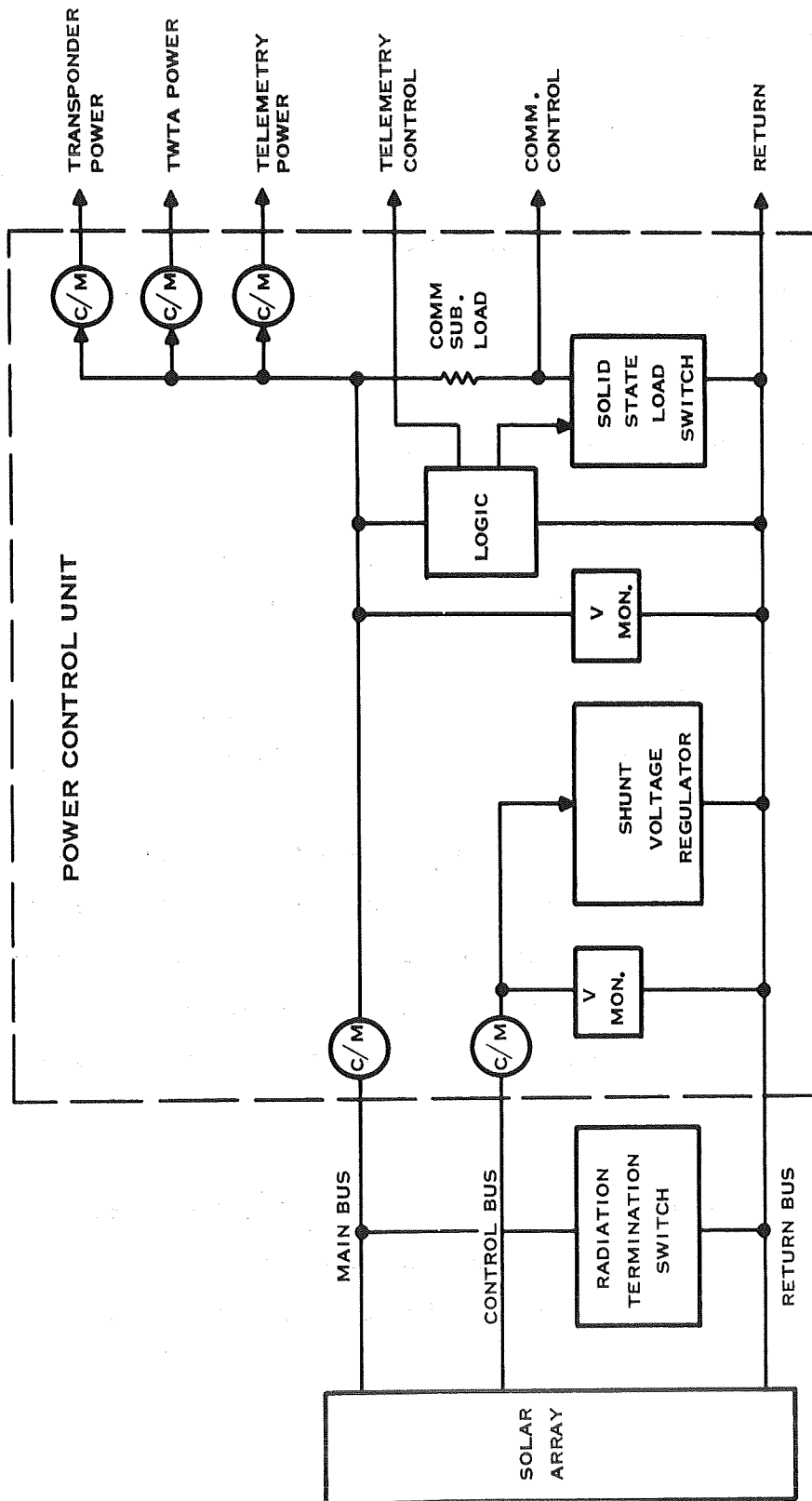


Figure A-2 Power Subsystem Block Diagram -Simplified

communications, sufficient power becomes available to support telemetry, that subsystem also is reactivated.

1.2.2 Solar Array

The solar array is designed to provide electrical power to the spacecraft during illuminated periods. The start-of-life power developed by the array is nominally 45 watts.

The system power requirements are as follows:

	<u>Watts</u>
Communication Subsystem	22.0
Telemetry Subsystem	4.5
Power Control Unit	<u>3.25</u>
Total System Consumption	29.75

The solar array is made up of 16 trapezoidal and eight rectangular panels. The trapezoidal panels have an electrical arrangement of 4 cells in parallel by 84 cells in series; the rectangular panels, 4 cells in parallel by 76 cells in series. The 24 panels are connected in parallel and electrically isolated by redundant diodes. The array is approximately center tapped to permit regulation.

The cells are 1 x 2 cm N on P gridded silicon cells with solder-dipped silver-titanium grids and electrodes. The N contact is the bar type and is located along the 1 cm edge of the cell. The cells are nominally 0.356 mm (14 mils) thick.

For purposes of thermal control and radiation protection, each cell is fitted with a coverslide. The coverslides are 0.508 mm thick (20 mils) and are made from Corning 7940 fused silica. They employ an anti-reflective coating and a blue-reflecting interference filter with a cut-on wavelength of 435 millimicrons. The coverslide is primed with Dow XR-6-3466 and bonded to the cell with Dow XR-6-3489 catalyzed 1:10.

The cells are interconnected using 0.051 mm (2 mils) dead soft copper. These interconnects are plated with 8 microns (0.3 mils) of 60/40 tin-lead to facilitate soldering into modules. The modules are ultimately bonded to a fiberglass insulator with Dow RTV-511 adhesive.

1.3 Communications Subsystem

1.3.1 Transponder

The transponder is a heterodyne repeater receiving in the 8 GHz band and transmitting in the 7 GHz band. The transponder consists of a single wide-band receiver with a 10 db noise figure and a hard limiter, two transmitters with two 3.0 watt traveling-wave-tube amplifiers, two frequency generators which generate crystal-controlled local oscillator and beacon signals, a DC-DC power converter, and a redundancy control. Figure A-3 shows the block diagram of the transponder.

The transponder receives incoming signals, consisting of a composite signal of up to four independent angle-modulated communications signals. The transponder translates the incoming signals to the transmit band and amplifies them. An internally generated beacon signal, coherently related to the local oscillator signals used in the translation process, is

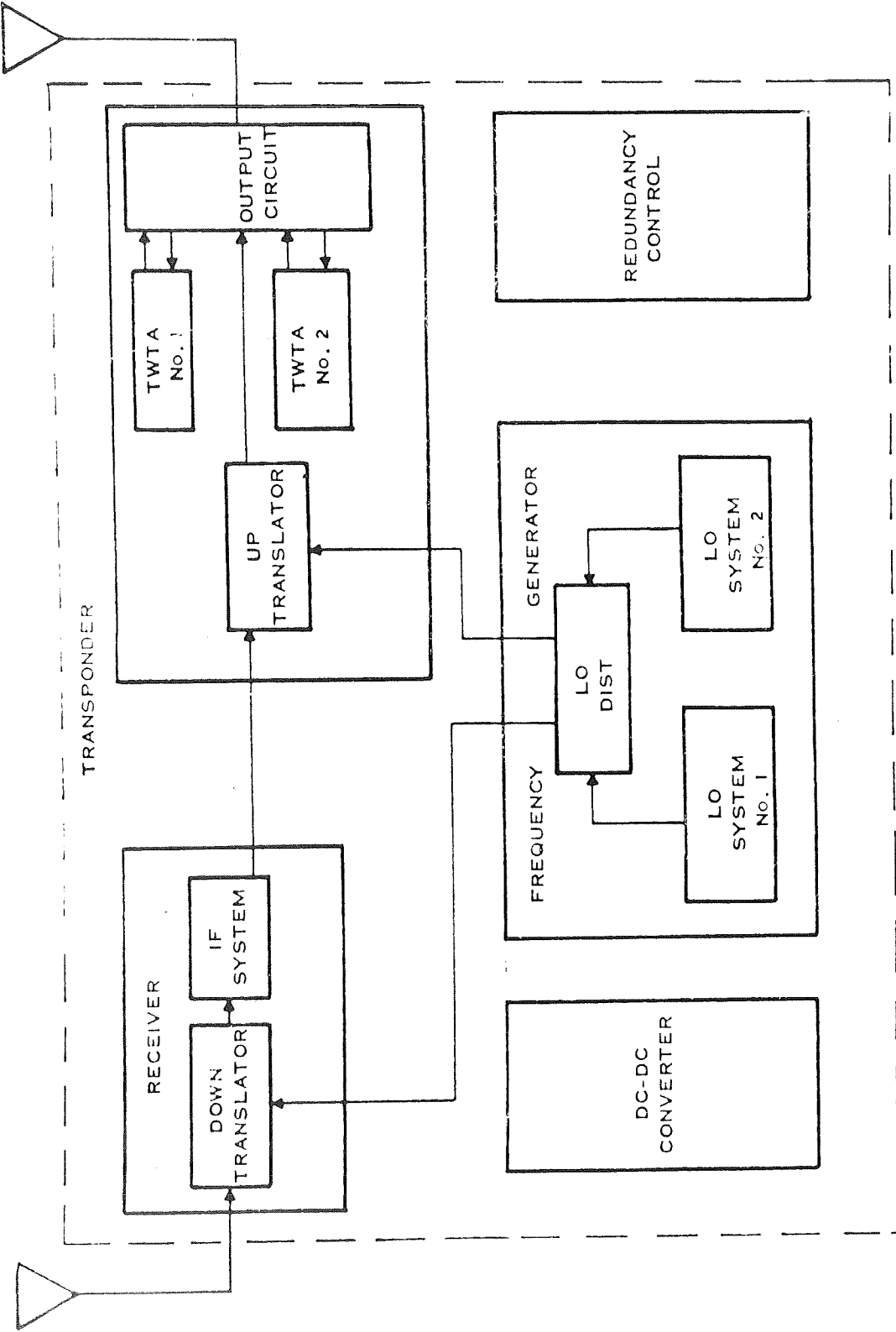


Figure A-3 Transponder Subsystem Block Diagram, Simplified

combined with the communication signals. This composite signal of communications carriers and one beacon carrier is then fed to the antenna for retransmission.

The transponder continuously transmits a 100-milliwatt beacon carrier at a frequency adjacent to the communications band. This signal is used by the ground station for acquisition and pointing the antenna at the satellite. The beacon carrier is capable of being modulated with a satellite identification signal and/or a narrow-band telemetry signal.

Coherent local oscillator signals (for the down-translator and up-translator) are generated in one of two sequentially-redundant local oscillators within the frequency generator unit and distributed as required by the local oscillator distribution subassembly. Control of the sequential local oscillator switching is accomplished by the redundancy control unit.

Regulated power is supplied to other transponder subassemblies by the DC/DC converter unit, which draws its power from the satellite power subsystem. Redundant TWTA's contain internal DC/DC converters.

The redundancy control monitors key electrical parameters, such as transmitter output power, and decides when to switch in the second frequency generator and/or TWTA.

1.3.2 Telemetry Subsystem

A simplified block diagram of the telemetry subsystem is shown in Figure A-4. Elements of the subsystem include a telemetry generator, transmitter, power converter, antenna, sun-angle sensor, and temperature sensors.

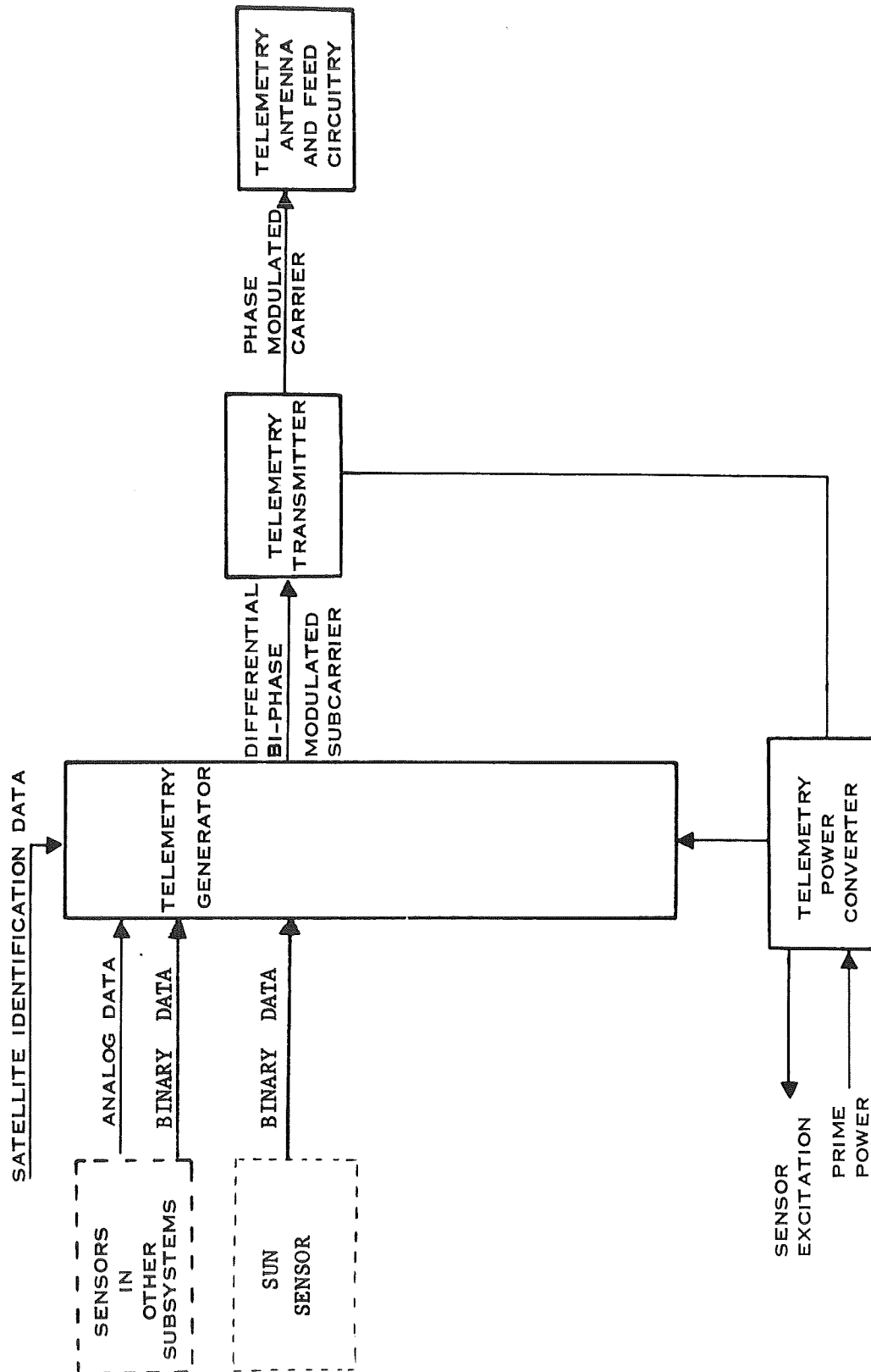


Figure A-4 Telemetry Subsystem Block Diagram - Simplified

The subsystem furnishes satellite identification, processes 56 analog telemetry signals and 18 binary signals, and transmits the data over a PCM/PSK/PM link to a 60-foot antenna at Ft. Dix, Camp Roberts, and to Air Force tracking stations. The satellite telemetry subsystem is compatible with existing ground station decommutation equipment. Detailed performance characteristics of the subsystem are listed in Table A-2.

A binary-coded input identifies up to 64 satellites. Satellite telemetry instrumentation is used to verify operational status and performance of satellite subsystems and for diagnostic analysis during malfunction conditions. Significant satellite and equipment temperatures, voltage/current/power levels, and operational status are instrumented with appropriate signal conditioning. The signals are multiplexed in the telemetry generator, analog signal levels are converted to digital signals, and the serial data stream is programmed for pulse code modulation (PCM). The PCM data are differentially biphased and modulate a crystal-controlled, phase-modulated 400-Mc transmitter. The transmitter feeds a flat plate antenna with a pattern similar to the communication antenna, but with broader coverage.

The ground data channel signal-to-noise ratio is 11 db at the bit rate of 256 bps. Using a 60-foot receiving antenna, this is well above the 6-db value considered as a minimum safe link margin.

TABLE A-2

SUMMARY OF TELEMETRY
SUBSYSTEM CHARACTERISTICS

1. Data System: Binary (NRZ) PCM
2. Number of input variables: 74 maximum
 - 18 Binary
 - 56 Analog
3. Frame synchronization: Zero plus 7-bit Barker (01110010)
4. Frame length: 64 words
5. Word length: 8 bits
6. Data quantization: 6 bits
7. Data sample rate: Once every two seconds
8. Word synchronization: 2 bits (11)
9. Frame format:
 - Frame synchronization
 - Satellite identification code
 - 18 1-bit variables
 - 56 6-bit variables
 - 3 6-bit calibration references
10. Subcarrier frequency: 1024 cps \pm 0.05%
11. Subcarrier modulation: Differential biphase
12. Bit rate: 256 bps
13. Carrier frequency: Crystal-selectable, 400 to 401.5 Mc
14. Carrier stability: $\pm 5 \times 10^{-6}$
15. Carrier modulation: Phase, ± 1.0 radian peak
16. Transmitter output power: 250 mw minimum
17. Antenna gain: 0 to -6 db, depending on aspect
18. Antenna polarization: Right-hand circular

2.0 TELEMETRY AND INSTRUMENTATION DESCRIPTION

2.1 Purpose

The basic requirements of the telemetry subsystem include data measurements, satellite identification, engineering evaluation readouts, and transmission of these signals to ground station terminals by an independent RF link.

The data measurements include sun angle and satellite temperature data. Sun angle data is used for satellite attitude determination to measure the effects of orbit injection, separation and spin stabilization errors and long-term magnetic moment effects on satellite spin axis precession. Temperatures are measured throughout the satellite, subsystems, and equipments.

Satellite identification is furnished to provide unambiguous readout of up to 64 satellites.

The engineering evaluation telemetry instrumentation monitors equipment and subsystem performance throughout the satellite. This data serves the following purposes:

- a. Operational Status Verification - Typically, the switching modes of redundancy control unit.
- b. Performance Verification - Functional parameters, together with temperature data, are instrumented to verify proper operation, adequacy of design margins, and the development/production test program in simulating the orbital environment.

- c. Degradation - The gradual shift of critical functional parameters, such as solar array output power, gives advance warning of degraded performance or increased probability of malfunction, for planning of subsequent launch schedules.
- d. Diagnostic Analysis - In the event of operational malfunction or failure, telemetry instrumentation serves to isolate the problem area, reports parameter changes in that circuit or related equipments, and furnishes information for ground test simulation of the problem. Analysis of this data leads to modifications improving the performance or reliability of subsequent equipments.

2.2 Design Philosophy

The detail design characteristics of the subsystem were selected to provide adequate telemetry data yield at minimum cost, within present technology and using existing ground station equipment wherever practical. To satisfy these goals, the frame format and synchronization techniques were chosen to conform with the Advent program using presently available ground facilities. Accordingly, the output of the telemetry generator is a serial PCM pulse train, differential bi-phase modulating a 1024 cps subcarrier at a rate of 256 bits per second. The word length is 8 bits. The first two bits are word synchronization, and the last six bits are a binary coded representation of the information, most significant bit first. The frame synchronization code (01110010) conforms to that accepted by the Advent ground decommutation equipment.

In the interest of minimizing complexity, the telemetry subsystem provides a 64-word output frame without subcommutation features. The frame total

of 64 words was chosen as ample capacity for the satellite. The telemetry instrumentation points were selected to measure critical subsystem performance requirements.

2.3 Detailed Description

2.3.1 Telemetry Generator

The generator uses integrated circuits to provide a reliable, efficient equipment with small volume and light weight. The unit was designed for 8-bit accuracy which, while not required for this application, offers inherent flexibility for future program requirements.

Design parameters are compatible with existing ground station facilities as previously described. The generator accepts up to 56 analog data inputs and 18 binary data inputs. Satellite identification inputs are inserted by a pre-wired external connector. The data input signals are time-multiplexed, analog signals are digitized, and the signals are synchronized by an internal clock oscillator. The data signals, satellite ID inputs, and internal calibration channels are programmed into a serial NRZ-PCM binary bit stream. The calibration channels are used for reference purposes in subsequent ground data reduction. The PCM data bi-phase modulates a 1024 cps subcarrier, to form the transmitter modulation signal.

2.3.2 Telemetry Transmitter

The transmitter utilizes a crystal-referenced temperature-compensated oscillator driving a buffer amplifier. The signal is frequency-multiplied,

phase modulated, with frequency doublers and power amplification as required to achieve the required 400 MHz output. Due to the requirement for selected frequencies within the operating band, provisions are made for factory tuning of the transmitter using different crystals to achieve the desired RF channel.

2.3.3 Power Converter

The DC/DC power converter is used to isolate the telemetry subsystem from electrical transients, noise in the primary power source; to eliminate ground loops; and to provide the specific voltage levels and regulation required for optimum performance and efficiency of the subsystem elements.

The converter is designed to operate over a +24 to +40 VDC primary source voltage range, in excess of the normal +24 to +30 VDC range, to permit the telemetry subsystem to monitor power source regulator malfunctions. The converter is designed for current-limiting in the event of a telemetry subsystem malfunction, so the primary communications function of the satellite will not be jeopardized. The converter uses pulse-width modulation to achieve regulation at optimum efficiency. The converter provides power for the transmitter, generator, attitude sensor, and all temperature sensors used in the satellite. Primary power to the subsystem elements is routed to the telemetry generator and distributed through the generator system interface connectors. Since temperature sensor accuracy is a direct function of reference voltage regulation, additional regulation is used for the +6 VDC supply.

2.3.4 Instrumentation

A complete listing of satellite instrumentation is shown in Table A-3. A detailed description is provided only for the sensors pertinent to this study.

2.3.4.1 Voltage Monitors

The voltage monitors are simple resistor dividers providing 0-3 volt analog output over their specified monitor range. The main bus voltage monitor is shown in Figure A-5, the control bus voltage monitor in Figure A-6. The following accuracy and stability requirements are specified:

Initial Accuracy (all conditions)	$\pm 2\%$
Stability (3 years)	$\pm 2\%$

2.3.4.2 Current Monitor

The current monitors are of the magnetic amplifier type. They derive their excitation from a common square wave inverter operating at 3 kHz. This constant volt-second excitation is impressed across the primary of the current monitor transformer. The DC current being monitored flows in the secondary of the transformer modulating the drive in the primary. The modulated drive is rectified by a full wave bridge and filtered by an output capacitor. Calibration of the current monitor is accomplished by a select-at-test load resistor. A unique feature of the design is a negative feedback winding which tends to linearize the output. A schematic of the inverter and monitors is shown in Figure A-7.

TABLE A-3
TELEMETRY INSTRUMENTATION SCHEDULE

Channel Nomenclature	Function	Normal Parameter Value	Maximum Parameter Variation	Sensor Signal Conditioner
Main bus voltage	Monitor solar array perf.	24 to 30v	24 to 50v	Resistive divider
Control bus voltage	Monitor voltage limiter perf.	0 to 15v	Full scale: 0 to 25v	Resistive divider
Main bus current	Monitor solar array perf.	1A to 1.2A	0 to 2A	Magamp
Control bus current	Monitor volt. limiter perf.	0 to 1A	0 to 1A	Magamp
TWTA primary current	Monitor TWTA performance	0.5 to 0.65A	0 to 0.8	Magamp
Transponder primary curr.	Monitor trans. performance	0.22 to 0.27A	0 to 0.5A	Magamp
Telemetry S/S primary curr.	Telemetry performance	0.15 to 0.21	0.1 to 0.3A	Magamp
Comm. on-off control status	Monitor comm. control status	0 to 1vdc off 5 to 15vdc on	N/A	Resistive divider
Power control unit temp.	Monitor operational temp.	0 to +90°C	-26 to +100°C	Temp. sensor
Solar panel zone #1 temp(hi range)	Monitor operational temp.	-18 to +50°C	-18 to +60°C	Temp. sensor
Solar panel zone #2 temp(hi range)	Monitor operational temp.	-18 to +50°C	-18 to +60°C	Temp. sensor
Solar panel zone #3 temp(hi range)	Monitor operational temp.	-18 to +50°C	-18 to +60°C	Temp. sensor
Solar panel zone #1 temp(lo range)	Monitor operational temp.	-68 to -18°C	-79 to -18°C	Temp sensor
Solar panel zone #2 temp(lo range)	Monitor operational temp.	-68 to -18°C	-79 to -18°C	Temp. sensor
Solar panel zone #3 temp(lo range)	Monitor operational temp.	-68 to -18°C	-79 to -18°C	Temp. sensor
Sun Angle Sensor	Measure sun angle to satellite spin axis	+25°	+25°	Photo diode

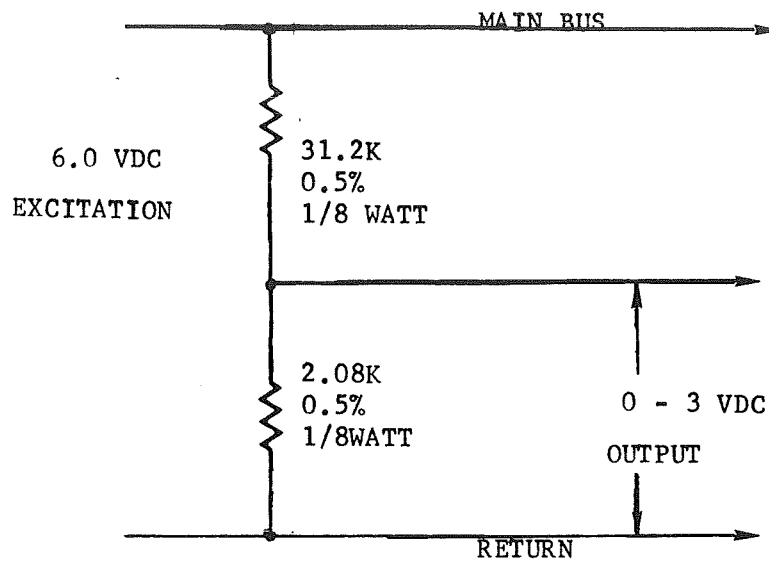


Figure A-5 Main Bus Voltage Monitor

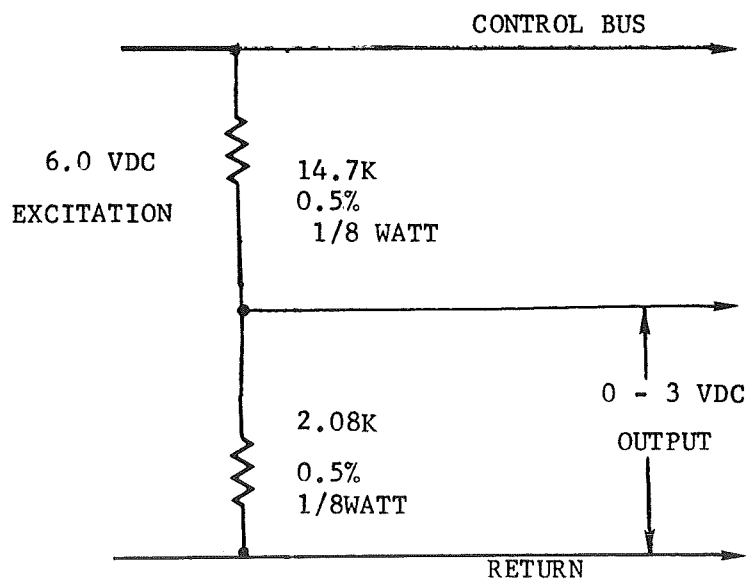


Figure A-6 Control Bus Voltage Monitor

The following accuracy and stability requirements are specified:

Initial Accuracy (all conditions)	$\pm 2\%$
Stability (3 years)	$\pm 2\%$

2.3.4.3 Temperature Monitors

Temperature monitoring is accomplished by the thermistor-resistor networks shown in Figures 4.2-4 and 3.2-5. Each of the three solar panel zones contains one of each monitor. Two are required to adequately cover the entire solar panel temperature range.

The following accuracy and stability requirements are specified:

Initial Accuracy (all conditions)	$\pm 3^{\circ}\text{C}$
Stability (3 years)	$\pm 3^{\circ}\text{C}$

2.3.4.4 Sun Angle Sensor

The following section describes the Sun Angle Sensor used in the IDCSP program. This Sun Angle Sensor measures the angle of incident sunlight with respect to the satellite spin axis and converts this angle to a digital word. It consists of two light detector heads, one mounted near each pole of the satellite, and the associated Sun Angle Sensor Electronics.

On a spin-stabilized spacecraft, the spinning action is utilized to perform a detector scanning function. The field of view of the detector head is a fan-shaped wedge, $96^{\circ} \times 3^{\circ}$. Incident solar illumination passing through

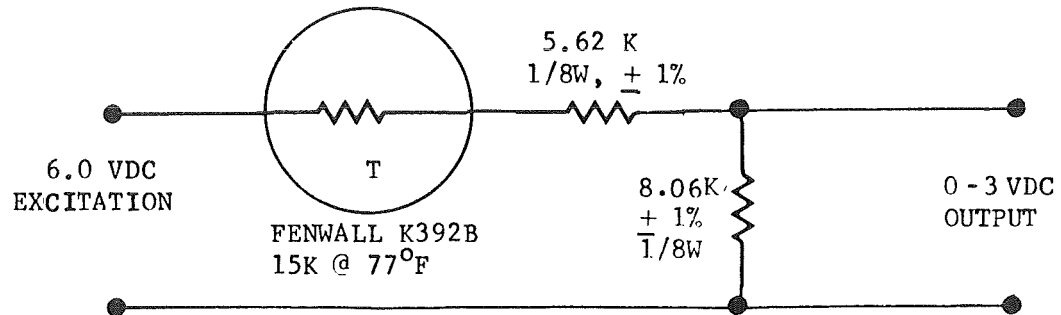


Figure A-8 Temperature Sensor (High Range)

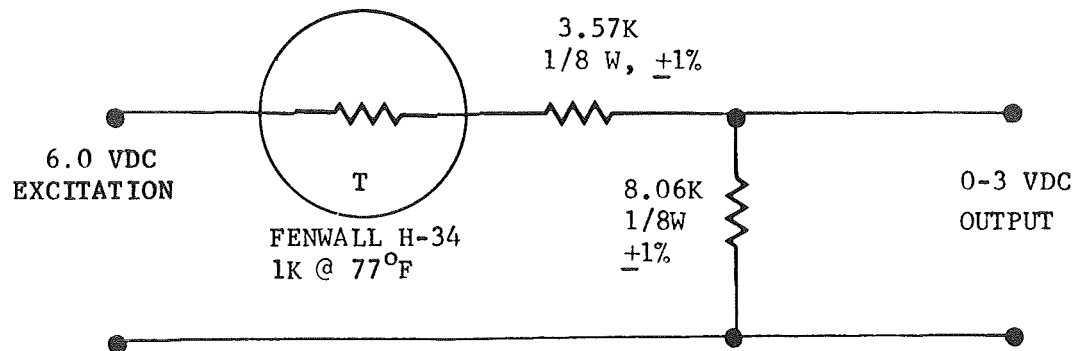


Figure A-9 Temperature Sensors (Low Range)

an optical slit and 8-bit Gray-Code mask impinges on a photosensitive semiconductor diode. When light shines on the masked diode junction, a decrease in the diode resistance changes a bias current. The resulting signal is amplified as a digitized signal which measures the angle between the sun and the plane of the sensor.

The detector signals activate the associated Sun Angle Sensor Electronics circuitry. The output signal to the Telemetry Generator is an 8-bit digital word, 7 bits representing the angle of the sun in respect to the satellite spin axis and the 8th bit indicating which of the two detectors is being energized. A "0" in the 8th bit indicates detector #1 is being energized and a "1" indicates detector #2 is operating. To eliminate the ambiguous reading when incident illumination is near 90 degrees, detector #1 is physically mounted in a plane 90 degrees away from detector #2.

The block diagram of the Sun Angle Sensor as shown in Figure A-10.

The following accuracy and stability requirements are specified:

Accuracy $\pm 0.46^{\circ}$

Stability $< 0.1^{\circ}$

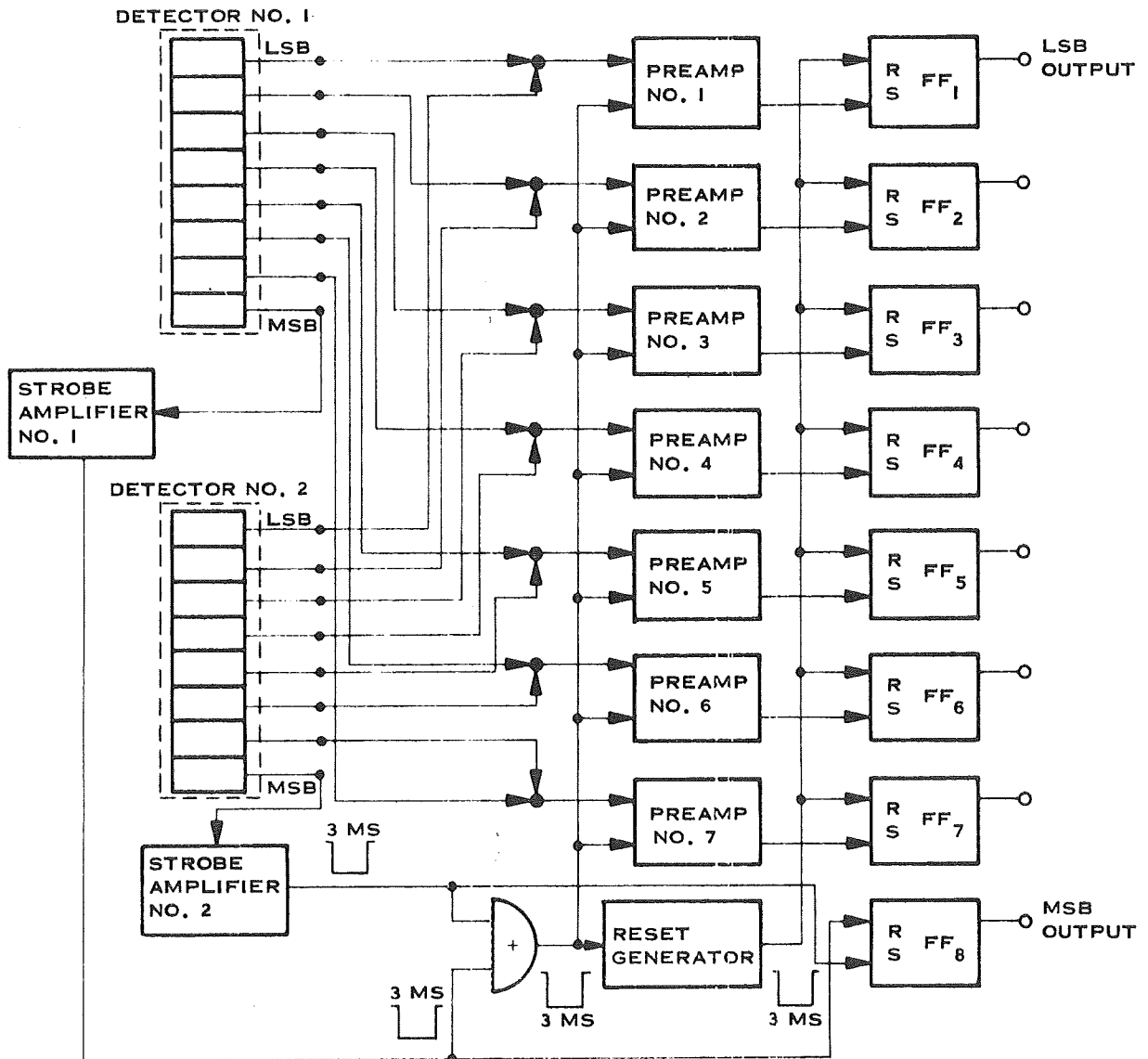


Figure A-10 Sun Angle Sensor Block Diagram

3.0 SATELLITE ORBIT DEFINITION

Three launches are considered in this study: The first (7 satellites) on 16 June 1966; the third (8 satellites) on 18 January 1967; and the multiple payload* (4 satellites) on 1 July 1967. The second launch self-aborted shortly after liftoff due to structural failure of the booster fairing. The first and third launches achieved slightly subsynchronous circular equatorial orbits. The multiple payload orbit was similar, but inclined seven degrees due to the desire to increase the total payload weight.

The nominal orbits for the three launches are given in Table A-4. The individual satellite orbits differ slightly because each has a slightly different initial velocity to insure separation and eventual distribution around the earth.

Table A-5 shows the achieved spin axis angles to the ecliptic plane for the first and third launches. Included also are the projected three-year angles. This detailed data is not available for the multiple payload, but simplified reduction of sun angle sensor data shows that spin axis angles for Satellites 9331, 9332, and 9333 are normal to the orbit plane within one degree. No sun angle data is available on 9334, the Despun Antenna Test Satellite (DATS). There is no reason to believe, however, that its attitude error exceeds one degree. A definition of angles is given in Figure A-11.

*This launch included Dodge and LES-5.

TABLE A-4
SATELLITE ORBITS

Orbital Parameter	1st Launch 16 June 1966	3rd Launch 18 Jan 1967	MPL 1 July 1967
Apogee - nautical miles	18,606	18,330	18,228
Perigee - nautical miles	18,205	18,161	18,191
Eccentricity	0.0092	0.0039	0.00086
Inclination - degrees	0.042	0.41	6.998
Period - Minutes	1,350	1,335	1,332

TABLE A-5
SATELLITE ATTITUDES

Satellite Identification	X Component Degrees	X Component Degrees	3 Year X Component Degrees	3 Year X Component Degrees
1st Launch				
9311	-1.08	-0.04	-1.50	+0.05
9312	-0.12	+0.93	-1.00	+0.78
9313	+0.22	-0.13	+1.70	0.00
9314	-0.44	-1.10	-0.44	-1.10
9315	+0.61	+0.11	+0.70	-0.40
9316	+0.79	-0.03	-0.30	+0.05
9317	+1.11	+1.02	-0.40	+0.86
3rd Launch				
9321	-1.12	-0.37	-1.12	-0.37
9322	+1.99	-0.35	+1.99	-0.35
9332	+1.10	+1.26	+1.10	+1.26
9324	+1.36	-0.57	+1.36	-0.57
9325	-0.50	+0.27	-0.50	+0.27
9326	+1.42	0.00	+1.42	0.00
9327	-1.06	+0.30	-1.06	+0.30
9328	+0.37	-1.57	+0.37	-1.57

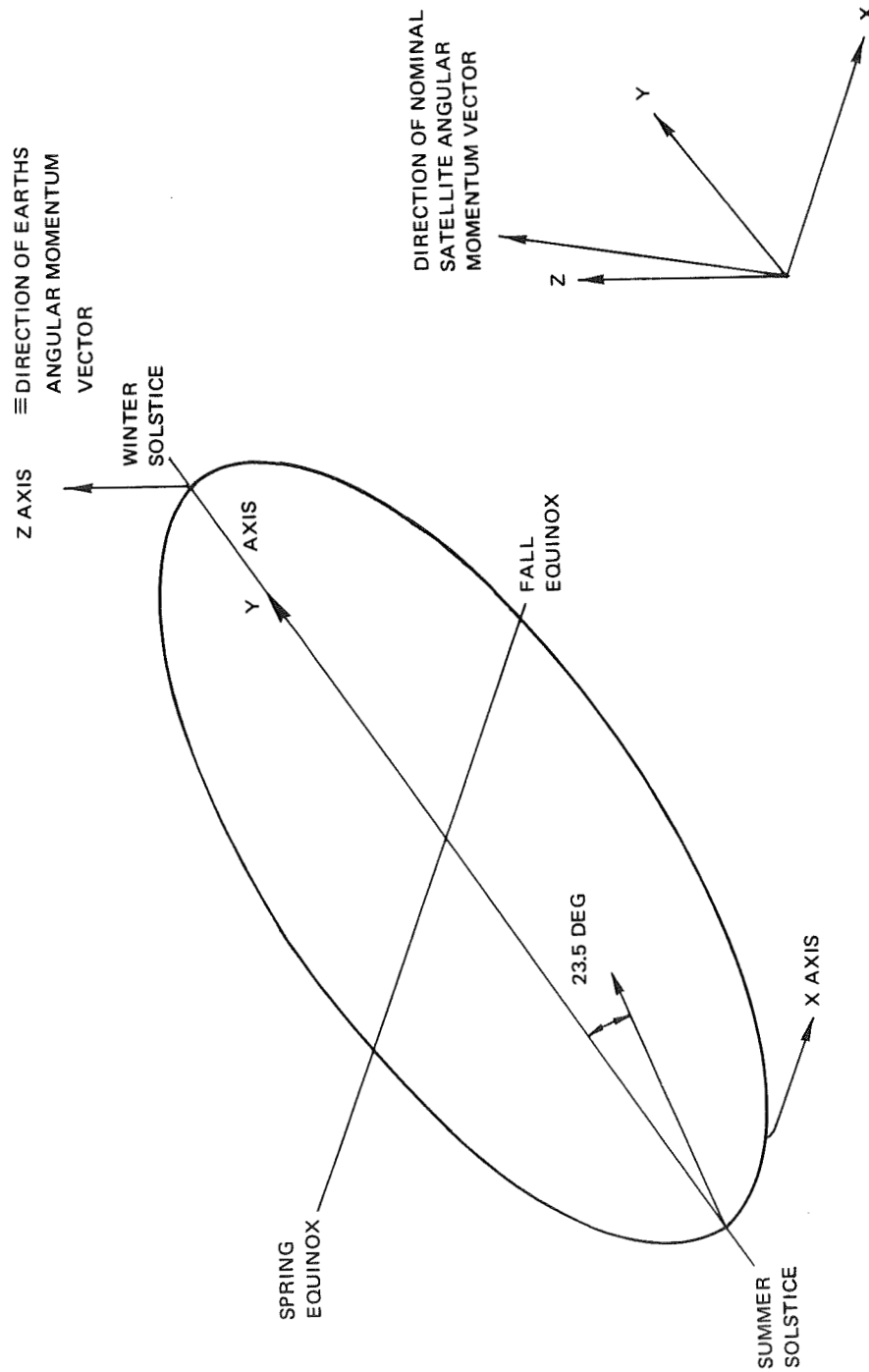


Figure A-11 Definition of Satellite Attitude Angles

WDL-TR4223

APPENDIX B

APPENDIX B DERIVATION OF AN EXPLICIT FUNCTION FOR $I(V)$

The assumed basic solar cell equation for forward characteristics is the conventional lumped-parameter version written as follows:

$$I = I_L - I_o \left[\exp \frac{(V + IR)}{B} - 1 \right] - \frac{V}{P} \quad (1)$$

where I = cell current output at voltage V when the cell is illuminated and under resistive load

I_L = light-generated current (assumed approximately proportional to the light intensity incident on the solar cell)

I_o = reverse saturation current

$B = \frac{nkT}{q}$, where k is Boltzmann's constant, T the absolute temperature, q the electron charge, and n a dimensionless constant compensating for non-ideal junction behavior ($n=1$ for an ideal diode; $n=2$ when recombination in the space charge region controls the junction current)

R = the lumped series resistance of the cell

P = the lumped parallel (shunt) resistance of the cell.

The substitutions

$$I_o = \exp(-A/B)$$

$$I' = I + \frac{V}{P}$$

produce

$$I' = I_L - \exp \frac{V(1-R/P) - A}{B} \exp \frac{I'R}{B} + I_o.$$

Since $I_o \approx 10^{-7}$, $I_L \gg I_o$, we discard I_o . The exponential containing $I'R$ is expanded to first order:

$$\exp \frac{I'R}{B} \approx 1 + \frac{I'R}{B}$$

and I' rearranged to produce

$$I'_l = \frac{I_L - E}{1 + \frac{ER}{B}}$$

where $E = \exp \frac{V(1-R/P) - A}{B}$

The second and third iterations are simply

$$I_2' = I_L - E \exp \frac{I_1' R}{B}$$

$$I_3' = I_L - E \exp \frac{I_2' R}{B} .$$

Observing the effects of typical values of I , R , and B , we find that $(1 + \frac{I'R}{B}) < \exp \frac{I'R}{B}$ and thus I_1' is greater than the true $I'(V)$. Subsequent effects of this expansion are that $I_2' < I'(\text{true})$ and $I_3' > I'(\text{true})$. Advantage is taken of this oscillatory behavior about $I'(\text{true})$ to produce our final iteration:

$$I_4' = I_L - E \exp \frac{(I_3' + I_2') R}{2B}$$

or

$$I(V) \cong I_L - E \exp \frac{(I_3' + I_2') R}{2B} - \frac{V}{P}$$

This approximate explicit relation has been compared to solutions of the exact implicit lumped-parameter equation and portions of the computer output are tabulated below. Parameter values are typical of cells applicable to this study.

$$A = 0.6641$$

$$B = 0.0423$$

$$R = 0.4$$

$$P = 367$$

$$I_L = 0.069$$

$$I_O = 1.5194251 \times 10^{-7}$$

<u>V</u>	<u>EXACT I</u>	<u>APPROX.I(V)</u>	<u>% ERROR</u>
0	.06899986	.068999708	-0.000220
0.20	.068422377	.068422225	-0.000222
0.40	.064339857	.064339958	+0.000157
0.45	.056919932	.056924937	+0.00879
0.48	.047510458	.047531384	+0.0440
0.50	.038032126	.038070307	+0.100
0.53	.017842863	.017873693	+0.173
0.55	.000073900	.000074144	+0.331

WDL-TR4223

APPENDIX C

APPENDIX C EXTRACTION OF PARAMETERS FROM I-V DATA

Parameters are extracted for two principal reasons: analysis of the parameters, per se, for the purposes of assessing cell quality or change trends due to radiation, temperature, aging, or other environmental exposures; and for the purpose of generating analytical I-V curves to duplicate original empirical curves. The former demands high statistical accuracy and requires computer techniques; the latter is less stringent and may be performed by hand or with the aid of a desk calculator. Both approaches will be discussed but only the simpler algorithms will be detailed in this appendix. The presentation will generally proceed from most simple (least guaranteed accuracy) to most complex (maximum statistical accuracy).

Five parameters (including "lumped" shunt resistance) are considered in each case. For modern cells the presence of the shunt resistance term may not be significant and simplifications will result by letting $P \rightarrow \infty$. If P is very high, normalization of the I-V curve is applicable, ($I_{\text{norm}} = I/I_L$; $V_{\text{norm}} = V/V_{\text{oc}}$). Normalization reduces the number of parameters to be extracted from three to two (assuming $I_L = I_{\text{sc}}$).

Method I: THREE POINTS, TWO SLOPES

Algorithm:

1. Measure the slope of the I-V curve at the short-circuit current point. $\frac{dV}{dI}(V=0) = -P$
2. Measure slope at open-circuit voltage point. Let $\frac{dV}{dI}(I=0) = -m$
3. Let $I_L = I_{\text{sc}}$; obtain V_{oc} ; obtain point near knee (V_k, I_k).
4. Calculate A, B, and R:

$$\text{Let } D = I_L \ln(I_L - I_k - V_k/P) - I_L \ln(I_L - V_{oc}/P) + I_k$$

$$DA = \left[mI_k (V_{oc}/P - I_L) - I_L V_k \right] \ln(I_L - V_{oc}/P) \\ + I_L V_{oc} \ln(I_L - I_k - V_k/P) + I_k V_{oc}$$

$$DB = I_L (V_k - V_{oc}) + mI_k (I_L - V_{oc}/P)$$

$$DR = m(I_L - V_{oc}/P) \left[\ln(I_L - I_k - V_k/P) - \ln(I_L - V_{oc}/P) \right] \\ - V_k + V_{oc}$$

Derivation:

Take the implicit derivative of the exact lumped-parameters cell equation.

Let

$$f = I - I_L + I_o \left(\exp \frac{V + IR}{B} - 1 \right) + \frac{V}{P}$$

$$\frac{dV}{dI} = - \frac{\frac{\partial f}{\partial I}}{\frac{\partial f}{\partial V}} = - \frac{1 + I_o \frac{R}{B} \exp \frac{IR+V}{B}}{I_o \frac{1}{B} \exp \frac{IR+V}{B} + \frac{1}{P}}$$

At $V = 0$,

$$I_{sc} = I_L - I_o \exp \frac{I_{sc} R}{B} + I_o$$

$$\frac{dV}{dI} (V = 0) = - \frac{1 + \frac{R}{B} (I_L + I_o - I_{sc})}{\frac{1}{B} (I_L + I_o - I_{sc}) + \frac{1}{P}} \approx -P \quad (1)$$

since the term in parentheses $\approx 10^{-7} - 10^{-8}$.

Similarly,

$$\frac{dV}{dI} (I = 0) = - \frac{I + \frac{R}{B}(I_L - \frac{V_{oc}}{P})}{\frac{1}{P} + \frac{1}{B}(I_L - \frac{V_{oc}}{P})} \equiv -m$$

Multiplying numerator and denominator by B, we can simplify by dropping third order terms. This is justified because measurements of the slope at this point are difficult to make with high accuracy.

$$I_L \approx 0.07 \text{ to } 0.14$$

$$B \approx 0.04$$

$$RI_L \approx 0.02 \text{ to } 0.07$$

$$V_{oc}/P \approx 0.0014 \text{ to } 0.0002$$

$$RV_{oc}/P \approx 0.0004 \text{ to } 0.0001$$

$$B/P \approx 0.0001 \text{ to } 0.00001$$

Eliminating the lowest two terms only, we obtain

$$B + RI_L \simeq m (I_L - V_{oc}/P) \quad (2)$$

Substituting $A = -B \ln I_o$ in the cell equation at $I = 0$, we obtain

$$A + B \ln (I_L - \frac{V_{oc}}{P}) = V_{oc}. \quad (3)$$

Finally, for some point near the knee, (V_k, I_k) , we evaluate the general cell equation and drop the very small term, I_o , which stands alone:

$$A + B \ln(I_L - I_k - \frac{V_k}{P}) - I_k R = V_k. \quad (4)$$

Equations 2, 3 and 4 constitute three relations in the three unknowns, A, B, and R. Using substitutions or determinants, we proceed to the explicit expressions listed in Step 4 of the algorithm.

METHOD II: FOUR POINTS, ONE SLOPE

Algorithm:

1. Measure slope at I_{sc} .

$$\frac{dV}{dI} (V = 0) = -P$$

2. Let $I_L = I_{sc}$; Obtain three points on the I-V curve, preferably two above and below the knee, and one at or near V_{oc} .
3. Calculate A, B, and R:

$$\begin{aligned} \text{Let } D = & (I_1 - I_3) \ln(I_L - I_2 - V_2/P) \\ & + (I_2 - I_1) \ln(I_L - I_3 - V_3/P) \\ & + (I_3 - I_2) \ln(I_L - I_1 - V_1/P) \end{aligned}$$

$$\begin{aligned} DA = & (V_3 I_1 - V_1 I_3) \ln(I_L - I_2 - V_2/P) \\ & + (V_1 I_2 - V_2 I_1) \ln(I_L - I_3 - V_3/P) \\ & + (V_2 I_3 - V_3 I_2) \ln(I_L - I_1 - V_1/P) \end{aligned}$$

$$DB = (I_1 - I_3)V_2 + (I_2 - I_1)V_3 + (I_3 - I_2)V_1$$

$$\begin{aligned} DR = & (V_3 - V_1) \ln(I_L - I_2 - V_2/P) \\ & + (V_1 - V_2) \ln(I_L - I_3 - V_3/P) \\ & + (V_2 - V_3) \ln(I_L - I_1 - V_1/P). \end{aligned}$$

Derivation:

The derivative at $V = 0$ to obtain P was derived under Method I above. Substituting $A = -B \ln I_o$ in the cell equation and three values of (V, I) we rearrange and produce 3 equations in the three unknowns A , B , and R .

METHOD III: PSEUDO LEAST-SQUARES METHOD

Algorithm:

1. Measure slope at I_{sc} .

$$\frac{dV}{dI}(V=0) = -P$$

2. Let $I_L = I_{sc}$; obtain N points on the I-V curve, (V_n, I_n) . Form Q groups of three different points each. The number of possible combinations of N points taken 3 at a time is:

$$Q = \frac{N!}{6(N-3)!}$$

3. Calculate A_q , B_q , and R_q for each group; $q = 1$ to Q .
4. Using the approximate explicit expression for $I(V)$ derived in Appendix A, for each group calculate S_q , the sum of the squares of the deviations of the N data points from the analytical curve generated with the parameters A_q , B_q , and R_q :

$$S_q = \sum_{n=1}^N \left[I_n - I_q(V_n) \right]^2$$

5. Determine the minimum S_q by examination, and obtain the corresponding combination of A, B, and R used in group q. These values will be the "best" parameters derivable by this method.

METHOD IV: TRUE LEAST-SQUARES METHOD

Algorithm:

1. Obtain N points on the I-V curve, (V_n, I_n) .
2. Obtain trial values of the five cell parameters, P_i , from one of the above methods, or by "educated guess". (e.g., let $P_1 = I_L$, $P_2 = A$, etc.)

3. Let $F_n(I_n, V_n, P_i) = I_n - I(V_n, P_i)$

It is desired to adjust the P_i such that

$$\sum_{n=1}^N F_n^2$$

is a minimum. Let $P'_i = P_i + \Delta P_i$ be such an adjustment. Expand each of the corresponding F'_n about their initial values:

$$F'_n = F_n + \frac{\partial F_n}{\partial P_i} \Delta P_i = \epsilon$$

Obtain the $N \times 5$ matrix, H , made up of the $\partial F_n / \partial P_i$. This may be accomplished by evaluation of the functional derivatives or by the approximate method of ratioing the difference in F_n (caused by a variation in some P_i) to the difference in P_i .

4. Let ϵ , F_n , and ΔP_i be 1×5 matrices. Then

$$\epsilon = F_n + H \Delta P_i$$

$$\sum_{n=1}^N (F'_n)^2 = \epsilon^T \epsilon$$

We desire the minimum $\epsilon^T \epsilon$, or

$$\frac{\partial}{\partial P_i} (\epsilon^T \epsilon) = 0$$

Hence,

$$\frac{\partial}{\partial P_i} (F_n + H \Delta P_i)^T (F_n + H \Delta P_i) = 0$$

or

$$H^T (F_n + H \Delta P_i) = H^T F_n + H^T H \Delta P_i = 0$$

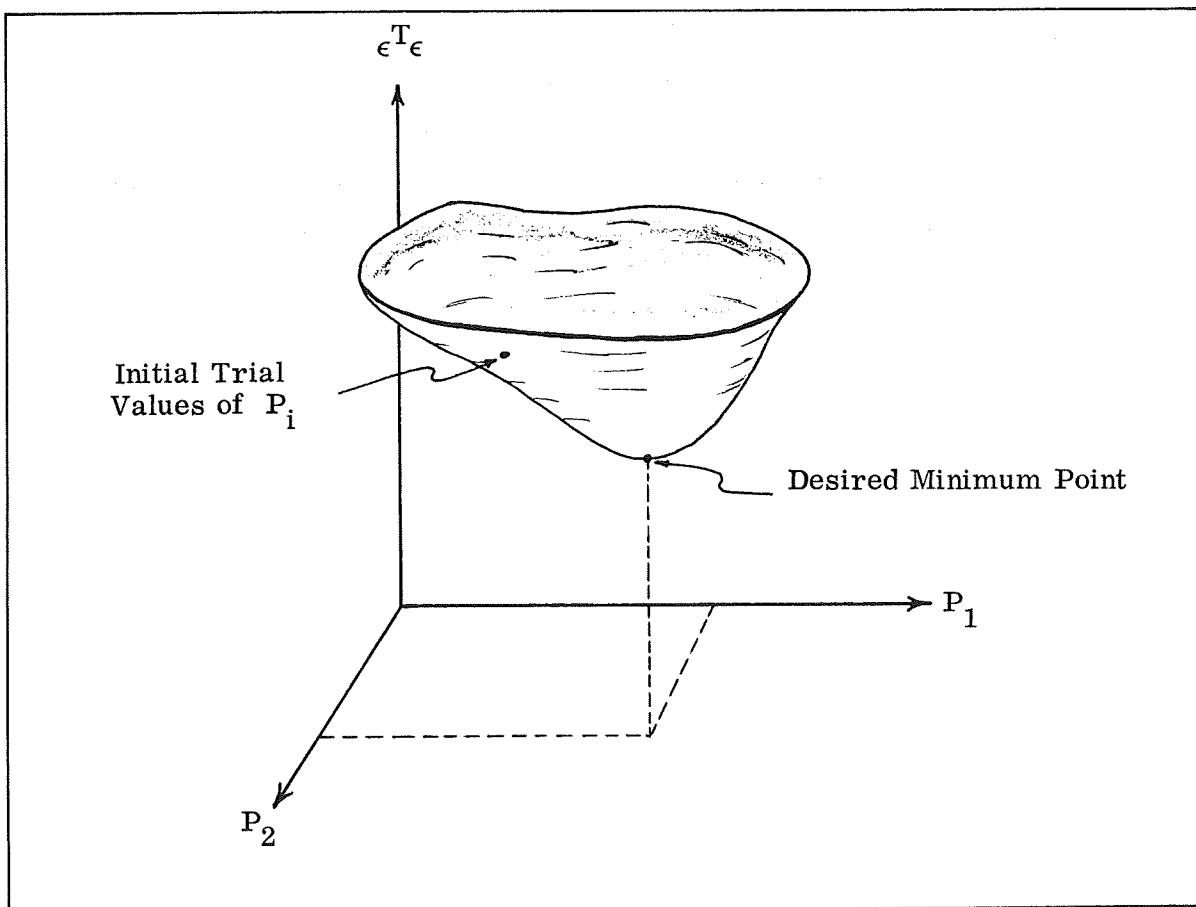
Solving for the ΔP_i matrix, the following calculation must be carried out:

$$\Delta P_i = - (H^T H)^{-1} H^T F_n.$$

5. Calculate P'_i and test $\epsilon^T \epsilon$.
6. Repeat steps 3, 4, and 5 above until $\epsilon^T \epsilon$ converges to a stable minimum value.

Derivation:

The sum of the squares of the deviations between the data points and the curve $I(V_n, P_i)$ may be visualized as a surface in six-dimensional space:



Since ϵ^T is the sum of squared quantities, it is always positive or zero. Any incorrect initial trial set of parameters will always produce a point on the surface above the desired minimum point. The convergence to the minimum point proceeds in a manner analogous to the 2-dimensional iteration scheme described at the end of Section 3.5 for the determination of cell I_{sc} and V_{oc} . The slope of the surface along a path which is the shortest distance to the minimum point is determined; the surface along that path is considered linear, and subsequent iterations aim at reaching the minimum point.

The possibility always exists, when dealing with non-linear functions, of producing anomalous values of the P_i . This phenomenon occurs when "local" minima are present on the ϵ^T surface and when the initial trial parameter set just happens to land near one of them. When the resultant P_i are obviously anomalous, the problem should be rerun with a different set of trial parameters.

WDL-TR4223

APPENDIX D

APPENDIX D

TEMPERATURE DEPENDENCE OF THE PARAMETERS

Tentative temperature functions have been assigned to each parameter on the basis of trends shown in Reynard's* 1965 data. With the absence of the raw (not redrawn) laboratory I-V curves, and an operational least-squares parameter fitting program, a number of simplifying assumptions have been made at this time:

- a. Temperature trends of each parameter have been assumed monotonic, smooth, and generally "well behaved."
- b. The constant, n , defined in Appendix A, has been treated as a true constant (even though some evidence exists that it varies at temperature extremes); hence, $B \propto T$ on an absolute temperature scale.
- c. Normal light intensity values have been assumed: 1 sun or less.
- d. The lumped-parameter solar cell equation has been assumed (c.f. Appendix B, Eqn. 1); solving for I_L at $V = 0$ produces

$$I_L = I_{sc} + \exp \frac{I_{sc} R - A}{B} - \exp \left(\frac{-A}{B} \right).$$

* D. L. Reynard, Proton and Electron Irradiation of N/P Silicon Solar Cells, Contract AF 04(647)-787, Lockheed Rpt. LMSC 3-56-65-4, 12 April 1965.

It is observed that any difference between I_L and I_{sc} is produced by the dissipative series-resistance term only. In the Reynard data, the worst-case fitted values of R produce a difference of less than 0.1 ma between I_L and I_{sc} at 200°F. This small difference justifies the use of the slope at I_{sc} as a means of determining the shunt resistance, P (see derivation in Appendix B). Hence,

$$-\frac{dV}{dI} (V=0) = P$$

- e. The variations in I_{sc} and V_{oc} with temperature have been assumed exactly linear. The rates of change are based on the Reynard cell data.
- f. The theoretical temperature dependence of I_o has not been used. Since the parameter A has been defined to replace I_o ,

$$A = -B \ln I_o,$$

its temperature dependence is derived from a combination of the other parameters.

- g. The measured and fitted temperature variations of P and R have been tentatively expressed by simplified first-order equations.

The assigned temperature variations of the five parameters, expressed as functions of parameters extracted at temperature T_o , are as follows (all temperatures are $^{\circ}\text{F}$):

$$B(T) = B(T_o) \frac{T + 460}{T_o + 460}$$

$$V_{oc}(T) = V_{oc}(T_o) \frac{0.6387 - 0.00129 T}{0.6387 - 0.00129 T_o}$$

$$I_{sc}(T) = I_{sc}(T_o) \frac{0.0663 + 0.00002941 T}{0.0663 + 0.00002941 T_o}$$

$$P(T) = P(T_o) \frac{V_{oc}(T) I_{sc}(T_o)}{V_{oc}(T_o) I_{sc}(T)} \exp \left[.00153 (T_o - T) \right]$$

$$R(T) = R(T_o) \frac{V_{oc}(T) I_{sc}(T_o)}{V_{oc}(T_o) I_{sc}(T)} \exp \left[-.00153 (T_o - T) \right]$$

$$A(T) = V_{oc}(T) - B(T) \ln \left[I_{sc}(T) - \frac{V_{oc}(T)}{P(T)} \right]$$

$$I_L(T) = I_{sc}(T) + \exp \left[\frac{I_{sc}(T) R(T)}{B(T)} - 1 \right] \exp \left[- \frac{A(T)}{B(T)} \right]$$

A family of curves based on these functions is plotted in Figure D-1. The assumed initial parameters are averaged from 12 I-V curves supplied by Heliotek in 1964 for the IDSCS array:

$$B = 0.0423$$

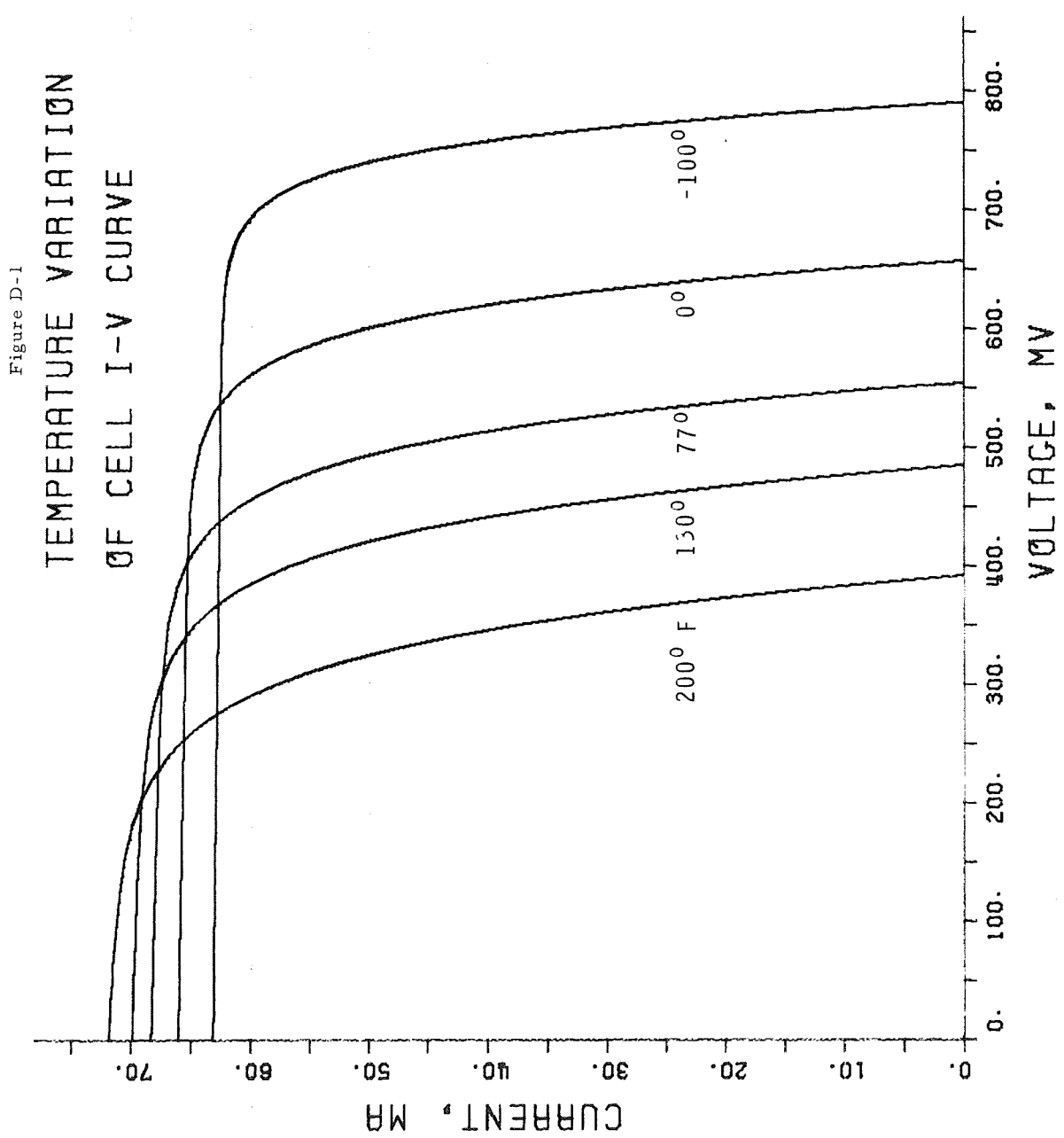
$$T_o = 82.4^{\circ}\text{F}$$

$$V_{oc} = 0.548167$$

$$I_{sc} = 0.0685083$$

$$P = 370.5$$

$$R = 0.10$$



WDL-TR4223

APPENDIX E

APPENDIX E

DESCRIPTIONS OF COMPUTER PROGRAMS DEVELOPED

The programs described in the following section were developed under this contract and are available thru the office of Science and Technology Information. They are written in FORTRAN IV for Philco-Ford's internal GE-615 system.

1.0 DEGRADATION ANALYSIS COMPUTER PROGRAM - "ANALYSIS"

Basic Design Criteria

The Following criteria were considered as a design basis for the program:

1. Easy modification to data structure to allow efficient updating as data are accumulated.
2. Easy development of hard copies of digitized flight data.
3. Block structure for versatility, maximum options in outputting level, and allowance for easy modification and expansion as the contract matures.
4. Rapid and efficient access to allow quick development.

A time-shared computer system was chosen as the facility through which the analysis would be carried out.

Program Description

The flow chart in Figure E-1 shows the implementation of the analysis described in Section 2.3.

Input Elements

There are three different types of input elements to the program:

1. Elements common to all satellites under consideration which include average solar cell equation parameters, the direction cosines which define the satellite geometry, the number of cells and their electrical combination comprising the total satellite solar array. As these elements are common, they are included as part of the analysis program.
2. Elements unique to each satellite are the flight data and the satellite number. The flight data needed in the program include:
 - a. Days from launch
 - b. Sun Angle
 - c. Main bus voltage
 - d. Main bus current
 - e. Control bus voltage
 - f. Control bus current
 - g. Temperatures of zone one, zone two, and zone three.

A data point contains all information a. through g. for one day.

The satellite number is inputted during each analysis run. Flight data, extracted from telemetry output printouts, is first punched onto paper tape (providing a hard copy of data) to digitize it and is then read into long-term disc storage files. When a satellite is analyzed, the flight data are called from disc storage and automatically included in the basic analysis program. Updating is accomplished by analyzing the new data and appending the results to the old data file.

3. Control elements are inputted during an actual run upon computer request for the needed information. The control elements

determine the number of data points analyzed, the type of analysis desired (present options are either total satellite analysis or individual cell analysis) and iteration check criteria in the computation of degradation factors.

Compute Elements (see Section 2.3 for detailed calculation)

Satellite Analysis

If only satellite analysis is specified, loop (1) of Figure E-1 will be traversed once for each data point entered. When all N points have been analyzed, the loop is exited and the theoretical power, actual power, the difference between theoretical and actual power, and the number of days from launch is outputted for each data point.

CELL Analysis

If cell analysis has been requested in the input, several data computation loops are traversed for each day analyzed.

On the first pass through the basic compute path, where satellite power is computed from the approximate solar cell equation, degradation factors are set equal to one (1). Testing the difference current and finding the difference does not meet the inputted criteria "B" forces operation through loop (2). Here the degradation factor of I_{SC} (77°F) is updated to a value less than its previous value (see 2.3 for details) and the basic compute path is entered again. The degradation factor will be reduced on successive passes around loop (2) until the difference between theoretical and actual current is less than criteria "B". When the difference is in fact less than "B", which is small enough to assure in the iteration scheme acceptable "zero" difference, the present value of the degradation factor is retained. With this degraded I_{SC} (77°F), a similar iteration through loop (3) produces a degraded V_{OC} (77°F). Both degradation factors for I_{SC} and V_{OC} are outputted and the next data point is analyzed as just described. The program is terminated either by direct command or when all data points have been analyzed.

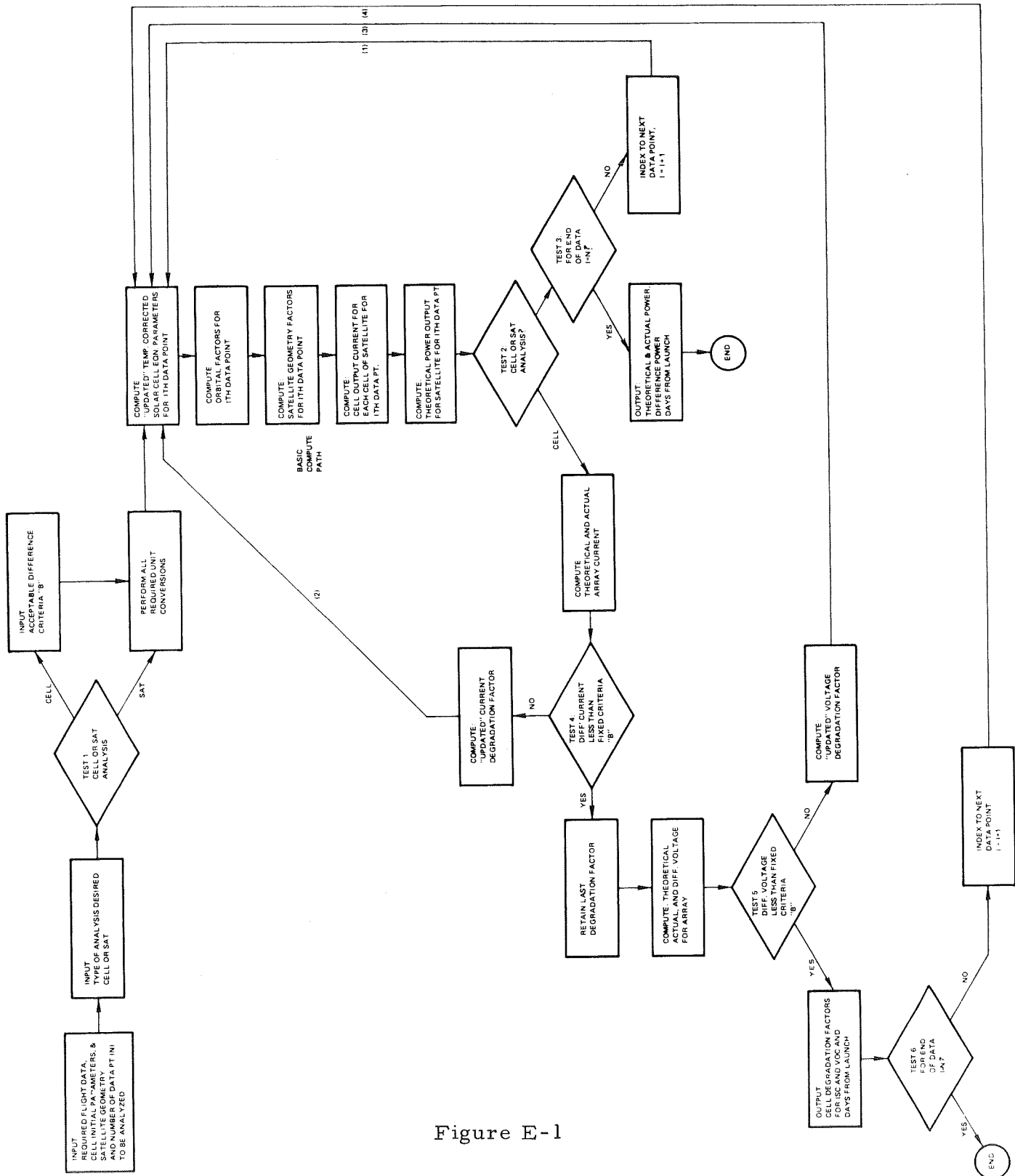


Figure E-1

Degradation Analysis Program, Simplified Flow Chart

It should be noted that safeguard alarms are built into each iteration scheme to indicate non-convergence. On no occasion has the alarm been necessary, and differences converge in seven or less iterations.

Output Elements

The analysis program provides two types of output. A tabular list of output data are generated during the run. Also a data file on the magnetic disc is developed simultaneously in a form suitable for input to the plotting routine which is used to generate plots shown in Figures 3-4 through 3-41, and to allow regression and statistical analysis to be implemented on the resulting outputted points at a later date.

Other Utility Programs

1. I-V Curve Fitting - "ARBFIT"

This program fits the lumped-parameter cell equation to three or more I-V pairs of data points. It implements the "pseudo" least-squares fit as described in Appendix C, Method 3. When more than three data pairs are inputted, the program searches for the set of three points which minimizes the square-error between all the points and the fitted cell equation. The program requires as inputs I_{SC} , P (the shunt resistance defined by the initial slope, $\frac{dV}{dI}$ at $V=0$), and the I-V pairs. The square-error associated with the fit, as well as the cell parameters are outputted.

The initial slope, P , is then recalculated from the fitted function, outputted with the original value of P , and if desired, a new fit may be obtained by rerunning with this updated value of P . For modern cells, P is probably in excess of 10,000 and any large number may be entered with little effect on the output results.

2. Maximum Power Point Locator - "PMAx"

After an I-V curve has been described analytically (using the previous program, "ARBFIT", for example), this program performs an iteration on the cell equation evaluated with inputted

parameters and finds the maximum power point on the defined curve. It eliminates the need for graphical techniques previously employed and the drawbacks associated with them.

3. Eclipse Entrace I-V Evaluation - "MATDEV" and "ECLIV"
These programs develop and utilize analytical descriptions of control bus voltage and current versus time, as the satellite enters the penumbra of the earth, to describe the I-V curve of the array near the knee region. The programs implement the technique describe in Section 2.4.

4. Statistical Programs - "CORR" and "CONLIM"
The "CORR" program evalutes the correlation coefficient described in Section 2.5 for a set of data and functional fit to this data.

The "CONLIM" program evalutes the 95% confidence limits about a fit to a set of data as described in Section 2.5.

5. Nonlinear Regression to an Arbitrary Function - "GOFIT"
This is a general regression analysis program allowing any trial function with defined first and second derivatives to be fitted to a set of data. The functional regression parameters are sought from a guessed starting point in multi-dimensional parameters space. The square error criteria is set by the user. Outputs include the final regression parameters, the square error, a histogram of error distribution, and a comparison table of original data to the fitted function evaluated at the independent variable points in the data.

Facility is also provided for extracting "stray" data points which contribute large square errors as shown in the histogram and can produce misleading fits. "GOFIT" uses the degradation function developed in Section 3.3. For further discussion of the method employed see Appendix C, Method 4.

DISTRIBUTION LIST

DISTRIBUTION LIST

National Aeronautics and Space Administration
Scientific and Technical Information
Center: Input
P. O. Box 33
College Park, Maryland 20740

National Aeronautics and Space Administration
Headquarters
New Technology Representative
Code UT
Washington, D. C. 20546

Mr. Arvin H. Smith
Headquarters
National Aeronautics and Space Administration
Code RNW
Washington, D. C. 20546

Mr. Ernst M. Cohn
Headquarters
National Aeronautics and Space Administration
Code RNW
Washington, D. C. 20546

Mr. A. M. Greg Andrus
Headquarters
National Aeronautics and Space Administration
Code SAC
Washington, D. C. 20546

Mr. Norm Mayer
Headquarters
National Aeronautics and Space Administration
OART, RV-2
Washington, D. C. 20546

Mr. Robert J. Debs
Ames Research Center
National Aeronautics and Space Administration
Code PES
Moffett Field, California 94035

Mr. Elmer R. Streed
Ames Research Center
National Aeronautics and Space Administration
Code PES
Moffett Field, California 94035

Mr. Arthur C. Wilbur
Ames Research Center
National Aeronautics and Space Administration
Code PES
Moffett Field, California 94035

Mr. Eugene Jesse
Ames Research Center
National Aeronautics and Space Administration
Code PES
Moffett Field, California 94035

Dr. Irving Weinberg
Headquarters
National Aeronautics and Space Administration
Code RRS
Washington, D. C. 20546

Dr. Sol Gilman
Electronics Research Center
National Aeronautics and Space Administration
Code CPE
575 Technology Square
Cambridge, Massachusetts 02139

Dr. Pao-Hsien Fang
Electronics Research Center
National Aeronautics and Space Administration
Code RME
575 Technology Square
Cambridge, Massachusetts 02139

Dr. Francis C. Schwarz
Electronics Research Center
National Aeronautics and Space Administration
Code TD
575 Technology Square
Cambridge, Massachusetts 02139

Dr. Douglas M. Warschauer
Electronics Research Center
National Aeronautics and Space Administration
Code RM
575 Technology Square
Cambridge, Massachusetts 02139

Mr. William R. Cherry
Goddard Space Flight Center
National Aeronautics and Space Administration
Code 716
Greenbelt, Maryland 20771

Mr. Luther W. Slifer, Jr.
Goddard Space Flight Center
National Aeronautics and Space Administration
Code 716
Greenbelt, Maryland 20771

Mr. John W. Fairbanks
Goddard Space Flight Center
National Aeronautics and Space Administration
Code 716
Greenbelt, Maryland 20771

Mr. Stephen G. McCarron
Goddard Space Flight Center
National Aeronautics and Space Administration
Code 716
Greenbelt, Maryland 20771

Mr. Edward M. Gaddy
Goddard Space Flight Center
National Aeronautics and Space Administration
Code 716
Greenbelt, Maryland 20771

Mr. Harold W. Warren
Goddard Space Flight Center
National Aeronautics and Space Administration
Code 716
Greenbelt, Maryland 20771

Dr. Ramond Waddel
Goddard Space Flight Center
National Aeronautics and Space Administration
Code 716
Greenbelt, Maryland 20771

Mr. Kenneth W. Edinger
Goddard Space Flight Center
National Aeronautics and Space Administration
Code 481
Greenbelt, Maryland 20771

Mr. Charles M. MacKenzie
Goddard Space Flight Center
National Aeronautics and Space Administration
Code 716.5
Greenbelt, Maryland 20771

Mr. John V. Goldsmith
Jet Propulsion Laboratory
4800 Oak Grove Drive
Pasadena, California, 91103

Mr. Paul Goldsmith
Jet Propulsion Laboratory
4800 Oak Grove Drive
Pasadena, California 91103

Mr. Paul Berman
Jet Propulsion Laboratory
4800 Oak Grove Drive
Pasadena, California 91103

Mr. Robert K. Yasui
Jet Propulsion Laboratory
4800 Oak Grove Drive
Pasadena, California 91103

Mr. Richard F. Greenwood
Jet Propulsion Laboratory
4800 Oak Grove Drive
Pasadena, California 91103

Mr. Walter A. Hasback
Jet Propulsion Laboratory
4800 Oak Grove Drive
Pasadena, California 91103

Mr. Donald W. Ritchie
Jet Propulsion Laboratory
4800 Oak Grove Drive
Pasadena, California 91103

Mr. Louis F. Schmidt
Jet Propulsion Laboratory
4800 Oak Grove Drive
Pasadena, California 91103

Dr. Bruce E. Anspaugh
Jet Propulsion Laboratory
4800 Oak Grove Drive
Pasadena, California 91103

Mr. L. Daniel Runkle
Jet Propulsion Laboratory
4800 Oak Grove Drive
Pasadena, California 91103

Mr. John L. Patterson
Langley Research Center
National Aeronautics and Space Administration
MS 472, Langley Station
Hampton, Virginia 23365

Mr. Robert D. Smith
Langley Research Center
National Aeronautics and Space Administration
Langley Station
Hampton, Virginia 23365

Mr. John R. Dawson
Langley Research Center
National Aeronautics and Space Administration
Langley Station
Hampton, Virginia 23365

Mr. Gerald F. Hill
Langley Research Center
National Aeronautics and Space Administration
Langley Station
Hampton, Virginia 23365

Mr. Walter E. Ellis
Langley Research Center
National Aeronautics and Space Administration
MS 472
Hampton, Virginia 23365

Mr. Gilbert A. Haynes
Langley Research Center
National Aeronautics and Space Administration
Langley Station
Hampton, Virginia 23365

Mr. Atwood R. Heath, Jr.
Langley Research Center
National Aeronautics and Space Administration
Hampton, Virginia 23365

Mr. Daniel T. Bernatowicz
Lewis Research Center
National Aeronautics and Space Administration
21000 Brookpark Road
Cleveland, Ohio 44135

Mr. Henry W. Brandhorst, Jr.
Lewis Research Center
National Aeronautics and Space Administration
21000 Brookpark Road
Cleveland, Ohio 44135

Mr. Adolph E. Spakowski
Lewis Research Center
National Aeronautics and Space Administration
21000 Brookpark Road
Cleveland, Ohio 44135

Mr. Americo F. Forestieri
Lewis Research Center
National Aeronautics and Space Administration
21000 Brookpark Road
Cleveland, Ohio 44135

Mr. C. Conger
Lewis Research Center
National Aeronautics and Space Administration
21000 Brookpark Road
Cleveland, Ohio 44135

Mr. J. D. Essary
Lewis Research Center
National Aeronautics and Space Administration
21000 Brookpark Road
Cleveland, Ohio 44135

Mr. James L. Cioni
Manned Spacecraft Center
National Aeronautics and Space Administration
Code EP5
Houston, Texas 77058

Mr. William E. Rice
Manned Spacecraft Center
National Aeronautics and Space Administration
Code EP5
Houston, Texas 77058

Mr. Charles W. Glassburn
Manned Spacecraft Center
National Aeronautics and Space Administration
Code EP5
Houston, Texas 77058

Mr. Fulton M. Plauche
Manned Spacecraft Center
National Aeronautics and Space Administration
Code EP5
Houston, Texas 77058

Mr. Ken Castle
Manned Spacecraft Center
National Aeronautics and Space Administration
Mail Code EE4
Houston, Texas 77058

Mr. W. R. Dusenberry
Manned Spacecraft Center
National Aeronautics and Space Administration
Code EP5, Bldg. 16
Houston, Texas 77058

Mr. Jimmy L. Miller
George C. Marshall Space Flight Center
National Aeronautics and Space Administration
Code R-ASTR-EPN
Marshall Space Flight Center, Alabama 35812

Mr. Lott W. Brantley
George C. Marshall Space Flight Center
National Aeronautics and Space Administration
Code PD-DO-EP
Marshall Space Flight Center, Alabama 35812

Mr. Richard J. Boehme
George C. Marshall Space Flight Center
National Aeronautics and Space Administration
Code R-ASTR-EP
Marshall Space Flight Center, Alabama 35812

Mr. O. H. Vaughn
George C. Marshall Space Flight Center
National Aeronautics and Space Administration
Code S&E-AERO-Y
Huntsville, Alabama 35812

Mr. Joseph F. Wise
Air Force Aero Propulsion Lab
Attn: (APIP-2)
Wright-Patterson AFB, Ohio 45433

Mr. David Massey
Air Force Aero Propulsion Lab
Attn: (APIP-2)
Wright-Patterson AFB, Ohio 45433

Mr. F. W. Forbes
Air Force Aero Propulsion Lab
APFT
Wright-Patterson AFB, Ohio 45433

Mr. Walter Allen
Johns Hopkins University
Charles & 34th Streets
Baltimore, Maryland 21218

Mr. Frank Sullivan
Johns Hopkins University
Charles & 34th Streets
Baltimore, Maryland 21218

Mr. Robert E. Fischell
APL-Johns Hopkins University
8621 Georgia Avenue
Silver Spring, Maryland 20910

Mr. Joseph J. Loferski
Brown University
Providence, Rhode Island 02912

Mr. Gerald L. Pearson
Stanford University
Stanford Electronics Labs
Stanford, California 94305

Mr. Richard H. Bube
Stanford University
Dept. of Materials Science
Stanford, California 94305

Dr. Frederick Morse
Dept. of Mechanical Engineering
University of Maryland
College Park, Maryland 20742

Mr. Eugene L. Ralph
Heliotek, Division of Textron Electronics
12500 Gladstone Avenue
Sylmar, California 91342

Mr. Paul Rappaport
Aerospace Systems Division
Radio Corporation of America
P. O. Box 800
Princeton, New Jersey 08540

Dr. A. G. Holmes-Siedle
Radio Corporation of America
Astro-Electronics Division
P. O. Box 800
Princeton, New Jersey 08540

Mr. Martin Wolf
Radio Corporation of America
Astro-Electronics Division
Box 800
Princeton, New Jersey 80540

Mr. Tom Wylie
Radio Corporation of America
Astro-Electronics Division
P. O. Box 800
Princeton, New Jersey 08540

Mr. George J. Brucker
Radio Corporation of America
Astro-Electronics Division
P. O. Box 800
Princeton, New Jersey 08540

Mr. Kenneth A. Ray
Lockheed Missiles and Space Company
Department 62-10
P. O. Box 504
Sunnyvale, California 94088

Mr. Dan R. Lott
Lockheed Missiles and Space Company
P. O. Box 504
Sunnyvale, California 94088

Mr. Larry G. Chidester
Lockheed Missiles and Space Company
P. O. Box 504
Sunnyvale, California 94088

Dr. A. G. Stanley
Lincoln Laboratory
Lexington, Massachusetts

Mr. E. L. Brancato
Naval Research Laboratory
4555 Overlook Avenue, S. W.
Code 6465
Washington, D. C. 20390

Mr. Richard L. Statler
Naval Research Laboratory
4555 Overlook Avenue, S. W.
Code 6465
Washington, D. C. 20390

Mr. Walter E. Allen
Applied Physics Laboratory
8621 Georgia Avenue
Silver Spring, Maryland 20910

Mr. William Goss
TRW Systems Group
One Space Park
Redondo Beach, California 90278

Mr. Hans Rauschenbach
TRW Systems Group
One Space Park
Redondo Beach, California 90278

Mr. Werner Luft
TRW Systems Group
One Space Park
Redondo Beach, California 90278

Mr. Robert Boring
TRW Systems Group
One Space Park
Redondo Beach, California 90278

Mr. Herbert Flicker
TRW Systems Group
One Space Park
Redondo Beach, California 90278

Mr. K. G. Downing
TRW Systems Group
One Space Park
Redondo Beach, California 90278

Mr. Matthew J. Barrett
Exotech, Incorporated
525 School Street, S. W.
Washington, D. C. 20024

Mr. W. J. Billerbeck
Communications Satellite Laboratories
P. O. Box 115
Clarksburg, Maryland 20734

Mr. Denis Curtin
Communications Satellite Laboratories
P. O. Box 115
Clarksburg, Maryland 20734

Mr. Joseph Haynos
Communications Satellite Laboratories
P. O. Box 115
Clarksburg, Maryland 20734

Mr. Floyd A. Blake
General Electric Company
Valley Forge Space Technology Center
P. O. Box 8555
Philadelphia, Pennsylvania 19101

Mr. Joel K. Baker
General Electric Company
Valley Forge Space Technology Center
P. O. Box 8555
Philadelphia, Pennsylvania 19101

Mr. Joseph Peden
General Electric Company
Valley Forge Space Technology Center
P. O. Box 8555
Philadelphia, Pennsylvania 19101

Mr. Kenneth Hanson
General Electric Company
Valley Forge Space Technology Center
P. O. Box 8555
Philadelphia, Pennsylvania 19101

Mr. Paul Weiner
General Electric Company
Valley Forge Space Technology Center
P. O. Box 8555
Philadelphia, Pennsylvania 19101

Mr. Dan Mager
General Electric Company
Valley Forge Space Technology Center
P. O. Box 8555
Philadelphia, Pennsylvania 19101

Mr. Fred Shore
General Electric Company
Valley Forge Space Technology Center
P. O. Box 8555
Philadelphia, Pennsylvania 19101

Mr. J. R. Davis
Westinghouse R & D
Beulah Road, Churchill
Pittsburgh, Pennsylvania 15235

Mr. Alivse Braga-Illa
Massachusetts Institute of Technology
Massachusetts Avenue
Cambridge, Massachusetts 02139

Mr. Wayne D. Brown
Hughes Aircraft Company
El Segundo Division
2060 East Imperial Highway
El Segundo, California 90009

Dr. Ray Andres
Hughes Aircraft Company
3011 Malibu Canyon Road
Malibu, California 90205

Mr. W. C. Dunkerly
Hughes Aircraft Company
El Segundo Division
2060 East Imperial Highway
El Segundo, California 90009

Mr. E. L. Suenoga
Hughes Aircraft Company
El Segundo Division
2060 East Imperial Highway
El Segundo, California 90009

Mr. John D. Gum
Spectrolab, Division of Textron Electronics, Inc.
12484 Gladstone Avenue
Sylmar, California 91342

Mr. Alfred E. Mann
Spectrolab, Division of Textron Electronics, Inc.
12484 Gladstone Avenue
Sylmar, California 91342

Mr. Robert C. Hamilton
Institute for Defense Analyses
400 Army-Navy Drive
Arlington, Virginia 22202

Mr. Peter Iles
Centralab Semiconductor Division
4501 North Arden Drive
El Monte, California 91731

Mr. K. S. Ling
Centralab Semiconductor Division
4501 North Arden Drive
El Monte, California 91731

Mr. Donald B. Bickler
Centralab Semiconductor Division
4501 North Arden Drive
El Monte, California 91731

Mr. Richard F. Julius
S. J. Industries
6009 Farrington Avenue
Alexandria, Virginia 22304

Mr. John H. Martin
Martin-Marietta Corporation
P. O. Box 179
Denver, Colorado 80201

Mr. W. Collins
Martin-Marietta Corporation
P. O. Box 179
Denver, Colorado 80201

Mr. Walter Camack
Martin-Marietta Corporation
P. O. Box 179
Denver, Colorado 80201

Mr. David Waddington
Martin-Marietta Corporation
P. O. Box 179
Denver, Colorado 80201

Mr. Harold E. Nastelin
Clevite Corporation
540 East 105th Street
Cleveland, Ohio 44108

Mr. D. Ogden
Chrysler Corporation
Dept. 4500
304 Oakwood Avenue
Huntsville, Alabama 35807

Mr. A. A. Nussberger
North American Rockwell Corp.
Space Division
12214 Lakewood Blvd.
Downey, California 90241

Dr. S. R. Pollack
Cara Corporation
101 North 33rd Street
Suite 332
Philadelphia, Pennsylvania 19104

Mr. Thomas G. Berry
Fairchild Hiller Corporation
Sherman Fairchild Technology Center
Fairchild Drive
Germantown, Maryland 20767

Mr. William King
Fairchild Hiller Corporation
Sherman Fairchild Technology Center
Fairchild Drive
Germantown, Maryland 20767

Mr. Richard R. Mandt
IBM Corporation
150 Sparkman Drive
Huntsville, Alabama 35807

Mr. Isodore M. Sachs
Optical Coating Laboratory, Inc.
2789 Giffen Avenue
Santa Rosa, California 95401

Mr. F. William Sarles
Massachusetts Institute of Technology
Massachusetts Avenue
Cambridge, Massachusetts 02139

Mr. Alan Stanley
Massachusetts Institute of Technology
Massachusetts Avenue
Cambridge, Massachusetts 02139

Mr. Ronald Stevenson
Douglas Aircraft Company
McDonnell Douglas Corporation
Headquarters
3000 Ocean Park Blvd.
Santa Monica, California 90406

Mr. A. D. Tonelli
Douglas Aircraft Company
McDonnell Douglas Corporation
Headquarters
3000 Ocean Park Blvd.
Santa Monica, California 90406

Mr. C. Shinbrot
Douglas Aircraft Company
McDonnell Douglas Corporation
Headquarters
3000 Ocean Park Blvd.
Santa Monica, California 90406

Mr. Edwin Stofel
Aerospace Corporation
Headquarters, El Segundo Technical
Operations and Laboratory Operations
Box 95085
Los Angeles, California 90045

Mr. Larry Gibson
Aerospace Corporation
Headquarters, El Segundo Technical
Operations and Laboratory Operations
Box 95085
Los Angeles, California 90045

Mr. H. J. Killian
Aerospace Corporation
Headquarters, El Segundo Technical
Operations and Laboratory Operations
Bldg. A-2, Orgn. 2413
Box 95085
Los Angeles, California 90045

Mr. R. E. Berry
Aerospace Corporation
2350 East El Segundo Blvd.
El Segundo, California 90274

Mr. Raymond A. Vineyard
Texas Instruments Incorporated
P. O. Box 4574
13500 North Central Expressway
Dallas, Texas 75222

Mr. S. Friedlander
Electro-Optical Systems, Inc.
300 North Halstead Street
Pasadena, California 91107

Mr. Keith Winsor
Electro-Optical Systems, Inc.
300 North Halstead Street
Pasadena, California 91107

Mr. W. R. Menetrey
Electro-Optical Systems, Inc.
300 North Halstead Street
Pasadena, California 91107

Mr. Detlev E. Hasselmann
Electro-Optical Systems, Inc.
300 North Halstead Street
Pasadena, California 91107

Dr. Nicholas Yannoni
AF Cambridge Research Labs
Attn: CRFE
L. G. Hanscom Field
Bedford, Massachusetts 01731

Dr. Jerry Silverman
AF Cambridge Research Labs
Attn: CRFE
L. G. Hanscom Field
Bedford, Massachusetts 01731

Mr. Henry Oman
The Boeing Company
Aero-Space Division
P. O. Box 3868
Seattle, Washington 98124

Mr. Frank Springate
The Boeing Company
Aero-Space Division
P. O. Box 3868
Seattle, Washington 98124

Mr. David R. Clarke
MS 47-08
The Boeing Company
P. O. Box 3868
Seattle, Washington 98124

Col. R. B. Griffith
SMGS
Space and Missile System Organization AFSC
Los Angeles Air Force Station
Los Angeles, California 90045

Major J. T. Artman
SMGS
Space and Missile System Organization AFSC
Los Angeles Air Force Station
Los Angeles, California 90045

Mr. Mel Creusere
Naval Ordnance Test Station
Code 3519
China Lake, California 93555

Major B. W. George
Headquarters
Air Force Systems Command
8103 Karl Road
Alexandria, Virginia 22308

Mr. Milton Knight
Naval Air Systems Command
(Air 340C)
Department of the Navy
Washington, D. C. 20360

Mr. J. L. Byers
Naval Air Systems Command
Propulsion Division (Air 53602A)
Washington, D. C. 20360

Dr. Emil Kittl
USAECON
Attn: AMSEL-KL-PA
Fort Monmouth, New Jersey 07703

PHILCO



**Philco-Ford Corporation
Western Development Laboratories Division
Palo Alto, California 94303**